Max-Planck-Institut
für Meteorologie

MAX-PLANCK-GESELLSCHAFT

International Max Planck Research School
on Earth System Modelling

Remote sensing of sea ice thickness using SMOS data

Nina Maaß

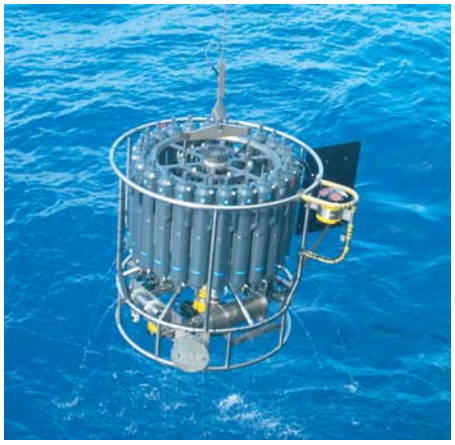

Berichte zur Erdsystemforschung 131
2013

Reports on Earth System Science

Hinweis

Die Berichte zur Erdsystemforschung werden vom Max-Planck-Institut für Meteorologie in Hamburg in unregelmäßiger Abfolge herausgegeben.

Sie enthalten wissenschaftliche und technische Beiträge, inklusive Dissertationen.

Die Beiträge geben nicht notwendigerweise die Auffassung des Instituts wieder.

Die "Berichte zur Erdsystemforschung" führen die vorherigen Reihen "Reports" und "Examensarbeiten" weiter.

Notice

The Reports on Earth System Science are published by the Max Planck Institute for Meteorology in Hamburg. They appear in irregular intervals.

They contain scientific and technical contributions, including Ph. D. theses.

The Reports do not necessarily reflect the opinion of the Institute.

The "Reports on Earth System Science" continue the former "Reports" and "Examensarbeiten" of the Max Planck Institute.

Anschrift / Address

Max-Planck-Institut für Meteorologie
Bundesstrasse 53
20146 Hamburg
Deutschland

Tel.: +49-(0)40-4 11 73-0
Fax: +49-(0)40-4 11 73-298
Web: www.mpimet.mpg.de

Layout:

Bettina Diallo, PR & Grafik

Titelfotos:
vorne:
Christian Klepp - Jochem Marotzke - Christian Klepp
hinten:
Clotilde Dubois - Christian Klepp - Katsumasa Tanaka

Berichte zur Erdsystemforschung 131/2013

Remote sensing of sea ice thickness using SMOS data

Nina Maaß

aus Henstedt-Ulzburg, Deutschland

Hamburg 2013

Reports on Earth System Science 131/2013

ISSN 1614-1199

Nina Maaß

Universität Hamburg
Institut für Meereskunde
Bundesstraße 53
20146 Hamburg

Max-Planck-Institut für Meteorologie
Bundesstraße 53
20146 Hamburg

Als Dissertation angenommen
vom Department Geowissenschaften der Universität Hamburg

auf Grund der Gutachten von
Dr. Lars Kaleschke
und
Prof. Dr. Detlef Stammer

Hamburg, den 1. Februar 2013
Prof. Dr. Jürgen Oßenbrügge
Leiter des Departments für Geowissenschaften

ISSN 1614-1199

Remote sensing of sea ice thickness using SMOS data

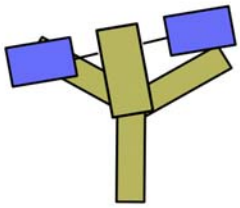

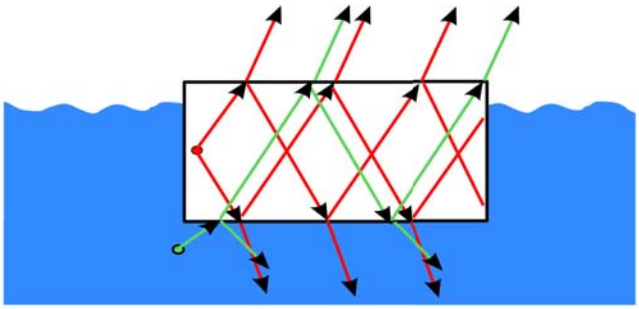

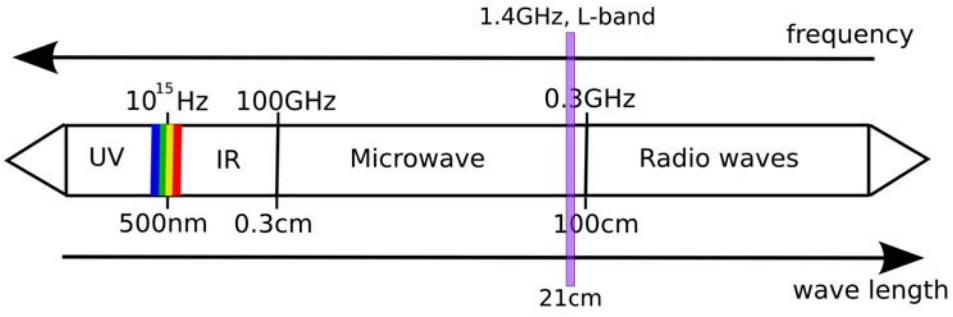

Nina Maaß

Hamburg 2013

Abstract

In this study, we investigate how ice conditions influence sea ice thickness retrieval from Soil Moisture and Ocean Salinity (SMOS) data. Additionally, we validate sea ice thicknesses retrieved in the Baltic Sea, and we examine whether it is possible to retrieve snow thickness over thick multi-year ice from SMOS data.

The European Space Agency's SMOS mission is the first passive microwave radiometer that measures at a frequency of 1.4 GHz in the L-band. Using L-band, the large penetration depth in sea ice allows us to extract information on the thickness of thin sea ice, as opposed to other microwave satellites. The accuracy of the retrieval and the maximum retrievable ice thickness depend on the ice conditions, which are mainly characterised by ice temperature T_{ice} and salinity S_{ice}. For typical Arctic conditions, ice thickness is retrievable up to about 50 cm. Here, we use a radiation model to investigate the sensitivity of the ice thickness retrieval to ice temperature and salinity. According to the model, an ice temperature change of 1°C and an ice thickness change of 1 – 3 cm cause approximately the same signal in the observed brightness temperature (for S_{ice}= 8 g/kg and ice thicknesses up to 45 cm). For typical salinities of Arctic thin ice, an ice salinity change of 1 g/kg has the same impact on brightness temperature as an ice thickness change of 0.5 – 6 cm (for T_{ice}= -7°C). Thus, the brightness temperature development above growing thin sea ice mainly indicates the ice thickness variation, and not the variations of ice temperature and salinity.

We investigate the impact of a snow layer on the ice thickness retrieval in L-band. The self-emittance of snow causes brightness temperatures to be higher for snow-covered than for snow-free ice. For typical Arctic conditions, brightness temperatures increase by 10 K at nadir view. At higher incidence angles, horizontal polarisation is even more affected, while vertical polarisation is almost unaffected. In accordance with our theoretical investigations, the root mean square deviation between simulated and observed brightness temperatures at horizontal polarisation decrease from 20.0 K, if the snow layer is neglected, to 4.4 K, if the snow layer is included in the simulations. Since dry snow is almost transparent in L-band, the brightness temperature of snow-covered sea ice is dependent on snow thickness only if the thermal insulation of snow is accounted for. Due to the stronger insulation by a thicker snow layer, brightness temperatures increase with increasing snow thickness over thick multi-year ice for cold Arctic conditions. This temperature effect allows us to retrieve snow thickness over thick sea ice. For the best simulation scenario and snow thicknesses up to 35 cm, the average snow thickness retrieved from horizontally polarised SMOS brightness temperatures agrees within 0.3 cm with the average snow thickness measured during the IceBridge flight campaign in the Arctic in spring 2012. The corresponding root mean square deviation is 5.7 cm and the correlation coefficient is r^2= 0.58.

We observe brightness temperatures over ice to increase by more than 20 K during the ice growth season in the Bay of Bothnia. We show that this brightness temperature increase is caused by increasing ice thicknesses, and not by changing ice conditions, which is the basis for a retrieval of ice thickness from SMOS. For validation with electromagnetic induction (EM) measurements in the Baltic Sea in March, 2011, the average SMOS and EM ice thicknesses agree within 0.5 cm. The root mean square deviation for the ice thicknesses of, on average 40 cm, is 7.7 cm.

Zusammenfassung

In dieser Arbeit untersuchen wir, wie die Eisdickenbestimmung aus Soil Moisture and Ocean Salinity (SMOS) Daten von den Eisbedingungen beeinflusst wird. Außerdem validieren wir die so gewonnenen Eisdicken in der Ostsee und untersuchen, ob eine Bestimmung der Schneedicke über dickem mehrjährigen Eis mit SMOS möglich ist.
Die SMOS Mission der Europäischen Raumfahrtbehörde trägt das erste passive Mikrowellenradiometer, das bei einer Frequenz von 1.4 GHz im sogenannten L-Band misst. Im Gegensatz zu den bisherigen Mikrowellensatelliten enthält im L-Band gemessene Strahlung aufgrund der hohen Eindringtiefe im Eis Informationen über die Eisdicke. Die Genauigkeit der Eisdickenbestimmung und die maximal bestimmbare Eisdicke hängen von den Eisbedingungen ab, die hauptsächlich durch die Temperatur und den Salzgehalt bestimmt werden. Für typische Bedingungen in der Arktis ist die Bestimmung der Eisdicke bis etwa 50 cm möglich. Wir benutzen ein Strahlungsmodel, um die Sensitivität der Eisdickenbestimmung bezüglich der Temperatur und des Salzgehaltes im Eis zu bestimmen. Unseren Modellberechnungen zufolge haben eine Temperaturänderung von 1°C und eine Eisdickenänderung von 1 – 3 cm etwa denselben Effekt auf die Helligkeitstemperatur (für einen Eissalzgehalt von 8 g/kg und Eisdicken bis 45 cm). Für Salzgehalte, die typisch sind für dünnes Eis in der Arktis, hat eine Salzgehaltsänderung von 1 g/kg je nach Eisdicke etwa den gleichen Einfluss auf die Helligkeitstemperatur wie eine Eisdickenänderung von 0.5 – 6 cm (für eine Eistemperatur von -7°C). Folglich spiegelt der Verlauf der Helligkeitstemperatur über wachsendem dünnen Eis hauptsächlich die Änderung der Eisdicke wieder und nicht die Änderungen der Temperatur und des Salzgehaltes im Eis.
Wir untersuchen den Effekt einer Schneedecke auf dem Eis auf die Eisdickenbestimmung im L-Band. Aufgrund der Eigenstrahlung des Schnees ist die Helligkeitstemperatur über schneebedecktem Eis höher als über unbedecktem Eis. Für typische arktische Bedingungen ist die Helligkeitstemperatur im Nadir 10 K höher. Für höhere Einfallswinkel ist der Einfluss bei horizontaler Polarisation noch höher, während die vertikale Polarisation kaum betroffen ist. Unsere theoretischen Ergebnisse stimmen mit Beobachtungen überein und die mittlere quadratische Abweichung zwischen modellierten und beobachteten Helligkeitstemperaturen verringert sich von 20.0 K bei Vernachlässigung der Schneeschicht auf 4.4 K bei Berücksichtigung der Schneeschicht in unseren Simulationen. Da trockener Schnee im L-Band nahezu transparent ist, hängt die Helligkeitstemperatur über schneebedecktem Eis nur aufgrund der thermischen Isolation durch Schnee von der Dicke der Schneeschicht ab. Über dickem mehrjährigen Eis und unter kalten Bedingungen bewirkt der stärkere Isolationseffekt einer dickeren Schneeschicht einen Anstieg der Helligkeitstemperatur mit der Schneedicke. Dieser Temperatureffekt ermöglicht die Bestimmung der Schneedicke über dickem Eis mit SMOS. Für das beste Simulationsszenario und Schneedicken bis 35 cm stimmt die aus den horizontal polarisierten SMOS Helligkeitstemperaturen gewonnene mittlere Schneedicke bis auf 0.3 cm mit der gemessenen mittleren Schneedicke überein. Die mittlere gemessene Schneedicke wurde aus Messungen während der IceBridge-Kampagne im Frühling 2012 in der Arktis bestimmt. Die mittlere quadratische Abweichung beträgt 5.7 cm und der Korrelationskoeffizient ist $r^2 = 0.58$.
Während der Eiswachstumsperiode im Bottnischen Meerbusen beobachten wir einen

Helligkeitstemperaturanstieg von mehr als 20 K über dem Eis. Wir zeigen, dass dieser Anstieg durch einen Anstieg der Eisdicke verursacht wird und nicht durch sich verändernde Eisbedingungen. Zu Validierungszwecken betrachten wir Eisdicken, die im März 2011 aus elektromagnetischen Induktionsmessungen in der Ostsee gewonnen wurden. Die ermittelte mittlere Eisdicke stimmt bis auf 0.5 cm mit der mittleren SMOS Eisdicke überein. Die mittlere quadratische Abweichung für das etwa 40 cm dicke Eis beträgt 7.7 cm.

Contents

Chapter 1

Introduction

The Soil Moisture and Ocean Salinity (SMOS) mission carries the first satellite-based passive microwave radiometer that measures radiation emitted from the Earth at a frequency of 1.4 GHz in the L-band. Using L-band, brightness temperatures measured above sea ice contain information on the ice thickness, as opposed to the brightness temperatures measured by previous passive microwave sensors that operate at higher frequencies. The reason is that radiation measured by L-band instruments originates from considerably deeper layers in the ice. Thus, brightness temperatures measured with SMOS can be used to retrieve thin sea ice thickness up to a maximum thickness. The maximum retrievable thickness of sea ice depends on the dielectric properties of the ice. Here, we investigate the impact of ice temperature and salinity on L-band brightness temperatures and consider the consequences for the ice thickness retrieval using SMOS. Furthermore, we examine how a snow layer on top of the ice influences the brightness temperature above sea ice, and whether there is a relationship between the brightness temperature and the thickness of the snow layer. Finally, we apply our ice thickness retrieval model to SMOS brightness temperatures observed in the Baltic Sea and evaluate the retrieval of ice thicknesses under rather challenging conditions.

Importance of L-band sea ice thickness retrieval

The retrieval of sea ice thickness from SMOS measurements fills a gap in the satellite-based techniques for the estimation of sea ice thickness. Altimeters measure the freeboard of sea ice, from which sea ice thickness is inferred via Archimedes' principle (Laxon et al., 2003; Kwok and Rothrock, 2009). However, the relative error of altimeter-based ice thickness measurements is large for thin sea ice (Laxon et al., 2003). The thickness of thin ice can be estimated from the ice surface temperature using thermal infrared imagery. However, this method is only applicable under cold clear-sky conditions and is strongly affected by fog and thin clouds (Yu and Rothrock, 1996). Additionally, there have been attempts to estimate ice thickness from passive microwave measurements at the 19 and 37 GHz channels by exploiting the correlation between ice surface properties and ice thickness. However, this technique is restricted to ice thicknesses less than about 10 to 20 cm (Martin et al., 2004; Tamura and Ohshima, 2011).

The retrieval of thin sea ice thickness from L-band radiometry depends on the dielectric properties of sea ice. In L-band, the dielectric properties of sea ice are

mainly determined by the brine volume fraction in the ice (Vant et al., 1978), which is primarily related to ice salinity and temperature (Cox and Weeks, 1983). The dielectric properties of sea ice determine the maximum thickness that can be retrieved with L-band instruments. For ice thicknesses smaller than this maximum value, the radiation signal observed above sea ice is a function of ice thickness. For ice thicknesses larger than this maximum value, an increase of ice thickness does not further modify the observed radiation signal. Thus, the maximum retrievable ice thickness determines what we consider here as thin ice. For example, for sea ice with a salinity of S_{ice}= 8 g/kg and a bulk temperature of T_{ice}= -5°C, the maximum retrievable ice thickness in L-band is about 50 cm, whereas sea ice thickness can be retrieved up to an ice thickness of 1.5 m for sea ice with a salinity of S_{ice}= 1 g/kg and a temperature of T_{ice}= -3°C, as can be encountered in brackish waters like the Baltic Sea (Kaleschke et al., 2010).

Sensitivity to ice conditions

Until now, a dielectric slab model for one ice layer has been used to describe brightness temperature as a function of ice thickness (Kaleschke et al., 2010). The model requires ice concentration, bulk ice temperature and bulk ice salinity as input. For the retrieval of sea ice thickness from SMOS brightness temperatures, a semi-empiric approximation of the model has been developed. In the previous studies, the tie-points of this semi-empiric approximation were assumed to be constant (Kaleschke et al., 2010, 2012), although they vary with ice temperature and salinity. Alternatively, a radiative transfer model with one ice layer and constant values for ice temperature and salinity has been used to compare simulated and measured airborne L-band brightness temperatures (Mills and Heygster, 2011). Knowledge on the influence of ice temperature and salinity is important, because only if the observed radiation signal mainly originates from ice thickness changes rather than from changes in the ice conditions, the ice thickness development is retrievable from SMOS data. Therefore, we need to quantify the impact of ice temperature and salinity and their variations on the ice thickness retrieval. In this study, we theoretically deduce the sensitivity of brightness temperature to ice temperature and salinity. We use two radiation models that are capable of treating an arbitrary number of layers. Thus, we are also able to investigate the impact of a temperature gradient within the ice as compared to a bulk ice temperature.

Snow

The one ice layer radiation model used for sea ice thickness retrieval from SMOS in previous studies (Kaleschke et al., 2010, 2012) neglects the potential presence of a snow cover on sea ice. Snow is almost transparent for microwave radiation at 1.4 GHz frequency (e.g. Hallikainen (1989); Rott and Mätzler (1987); Hall (1996)). Due to the transparency of snow, at low microwave frequencies a snow cover does not modify the radiation that originates from the underlying sea ice. However, because snow emits radiation itself and generally has a higher emissivity in L-band than ice, snow should be taken into account for L-band measurements. Additionally, snow has a thermal insulation effect on ice. The bulk ice temperature of snow-covered sea ice is generally higher than the bulk ice temperature of bare sea ice.

Here, we use the two multiple-layer models to examine the impact of a snow cover

on brightness temperatures above sea ice and the implications for the ice thickness retrieval of snow-covered sea ice. In order to test the validity of our theoretical investigations, we simulate brightness temperatures for ice and snow thicknesses measured during the National Aeronautics and Space Administration (NASA) Operation IceBridge flight campaign in spring 2012 in the Arctic. We perform simulations that neglect the snow layer and that include the snow layer. We then compare these simulated brightness temperatures with brightness temperatures measured by SMOS. Furthermore, we investigate whether there is a dependence between the brightness temperatures observed above snow-covered ice and the thickness of the snow layer on the ice. We evaluate whether SMOS has not only the potential for retrieving ice thickness over thin ice, but also the potential for estimating snow thickness over thick multi-year sea ice in the Arctic.

Information on snow thickness is required for the freeboard-based estimation of sea ice thickness from lidar and radar altimetry (Kwok and Cunningham, 2008; Giles et al., 2007). However, snow thickness observations over sea ice are scarce. The most comprehensive analysis for the Arctic Ocean is based on snow thickness and density measurements from Soviet drifting stations between 1954 and 1991 (Warren et al., 1999). However, it is not clear how well this climatology represents present-day snow conditions. First cross-basin surveys of snow thickness over Arctic sea ice have been provided by airborne radar measurements (Kwok et al., 2011). However, airborne remote sensing is spatially and temporally restricted to individual campaigns. Algorithms for the retrieval of snow thickness from passive microwave satellite measurements have been developed (Comiso et al., 2003). The snow thickness is calculated from the spectral gradient ratio of the 19 and 37 GHz vertical polarisation channels, e.g. on-board the Advanced Microwave Scanning Radiometer-EOS (AMSR-E). However, the algorithm is only applicable to dry snow conditions, and only to Antarctic sea ice and first-year ice in the Arctic (Comiso et al., 2003). Over multi-year sea ice the snow thickness cannot be retrieved unambiguously, because the microwave signature used in the algorithm is very similar for snow and multi-year ice. Thus, a method to estimate snow thickness over thick Arctic multi-year ice from SMOS brightness temperatures would improve monitoring of sea ice conditions in the Arctic from space.

Validation of SMOS sea ice thickness retrieval

The potential for the retrieval of sea ice thickness from L-band radiometry has been demonstrated for simultaneous airborne measurements of L-band brightness temperature and of ice thickness during the Pol-ICE campaign 2007 in the Baltic Sea (Kaleschke et al., 2010). The ice thicknesses retrieved from the L-band radiometer measurements were compared with ice thicknesses obtained from electromagnetic induction (EM) measurements. However, the results were interpreted rather as indications than as evidence that there is a potential for the retrieval of ice thickness from L-band radiometry. The reasons were mainly 1) the campaign was conducted under melting conditions, which hampered the thickness retrieval from L-band measurements, 2) the spatial overlap between the L-band and the EM measurements was relatively small, and 3) the radiometer was not operating at its nominal performance (Kaleschke et al., 2010). Furthermore, the different footprint sizes of airborne and

satellite-based L-band measurements affect the conclusions that can be drawn from the campaign data for SMOS applications in the Baltic Sea. The L-band measurements of the campaign had footprints of about 700 m, while SMOS L-band measurements have footprints of 35 – 50 km.

In a study on the sea ice thickness retrieval from L-band brightness temperatures measured by SMOS, ice thicknesses retrieved from SMOS data were compared with ice thicknesses as calculated with an ice growth model and with ice thicknesses as estimated from MODerate resolution Imaging Spectroradiometer (MODIS) thermal infrared imagery (Kaleschke et al., 2012). In the ice growth model, ice thickness was derived from surface air temperature using a parameterisation between ice thickness and freezing degree days (after Lebedev). The ice thicknesses retrieved from SMOS were highly consistent with the ice thickness development in the ice growth model. However, the comparison was conducted for a well defined case of quickly growing sea ice under cold conditions and only measurements of one SMOS grid point in the Arctic were considered. A further comparison of ice thicknesses derived from SMOS and from MODIS for one day gave a root mean square deviation of 10 cm and a correlation coefficient of $r^2 = 0.5$. However, the uncertainty of ice thicknesses derived from MODIS is 40 – 50% (Kaleschke et al., 2012).

Thus, further investigations of the SMOS sea ice thickness retrieval performance are needed. Here, we use one of the multiple-layer radiation models and ice thickness estimations from MODIS thermal infrared imagery to simulate brightness temperatures over growing sea ice in the Baltic Sea. These simulated brightness temperatures are compared with brightness temperatures observed by SMOS. Additionally, we compare SMOS retrieved ice thicknesses with EM ice thickness measurements from an EU SafeWin field campaign in March, 2011 in the Baltic Sea.

Outline
This work is organised as follows:

In Chapter 2, we provide the basis for the investigations presented in this thesis. We shortly introduce the SMOS mission and describe our brightness temperature data processing. Furthermore, we consider the different contributions to the brightness temperatures as measured by SMOS. Finally, we describe two radiation models that characterise the brightness temperature contribution of sea ice, and thus provide the physical basis for the retrieval of sea ice parameters from SMOS brightness temperatures.

In Chapter 3, we first examine under which conditions we can assume the temperature gradient within ice to be linear, and how brightness temperatures as simulated for a linear temperature gradient differ from brightness temperatures as simulated for a bulk ice temperature. We calculate the sensitivity of brightness temperatures to both ice temperature and ice salinity, and examine the corresponding consequences for the sea ice thickness retrieval from SMOS brightness temperatures. Finally, we consider an example case of freezing sea ice in the Arctic to compare the contributions to the observed SMOS brightness temperature caused by changes in ice temperature, ice salinity, and ice thickness.

In Chapter 4, we investigate the impact of the dielectric properties and of the thermal insulation of snow on the SMOS retrieval of ice thickness. We examine whether the brightness temperature of snow-covered sea ice depends on the thickness of the snow layer. We use airborne snow and ice thickness data to simulate brightness temperatures, and compare these with brightness temperatures measured by SMOS. Finally, we investigate the potential for a retrieval of snow thickness from SMOS brightness temperatures observed over thick Arctic sea ice.

In Chapter 5, we first simulate brightness temperatures over ice-free water in the Baltic Sea in order to estimate our model's performance over open water. Subsequently, we assess the potential of an ice thickness retrieval from SMOS brightness temperatures in the Baltic Sea by comparing simulated and measured brightness temperatures over growing sea ice. Finally, we compare ice thicknesses as retrieved with our model from SMOS brightness temperatures with ice thicknesses as measured during an EM Bird flight campaign.

In Chapter 6, we then give the main conclusions from the work presented here.

Remark: In this thesis, a citation after the full stop of the last sentence of a paragraph denotes that the citation refers to the contents of the entire paragraph.

Chapter 2

Fundamentals

In this chapter, we provide the basis for the investigations presented in this thesis. In section 2.1, we shortly introduce the SMOS mission, and in section 2.2, we describe how we process the Level 1C SMOS brightness temperature data to obtain brightness temperatures that we can use for comparison with our modelled brightness temperatures and for the retrieval of ice (and snow) thickness. The Level 1C SMOS brightness temperatures are brightness temperatures observed at the top of the atmosphere (TOA). In section 2.3, we list the contributions to brightness temperatures observed at the TOA, and describe how we deal with these contributions in this study. In section 2.4, we then describe two radiation models that characterise the brightness temperature contribution from sea ice. This contribution provides the physical basis for the retrieval of sea ice parameters from SMOS brightness temperatures.

2.1 The SMOS mission

The Soil Moisture and Ocean Salinity (SMOS) mission is an Earth Observation mission of the European Space Agency (ESA). The SMOS satellite was launched in November, 2009 and is operated on a sun-synchronous, quasi-circular orbit at an altitude of 758 km. SMOS achieves a global coverage every three days. The SMOS payload is a passive microwave 2D-interferometer: the Microwave Imaging Radiometer using Aperture Synthesis (MIRAS). MIRAS measures the microwave radiation emitted from the Earth's surface at a frequency of 1.4 GHz in the L-band. The corresponding wavelength is 21 cm. (Kerr et al., 2001)
The MIRAS instrument consists of 69 small receiver antennas that are deployed on three co-planar arms 120° apart (Y-shape). Each of the arms has a length of 4.5 m. The instrument exploits the interferometry principle and measures the phase difference of the radiation incident on the 69 antennas (McMullan et al., 2008). The technique is based on cross-correlation of observations from all possible combinations of receiver pairs. Thus, the instrument instantaneously records a whole scene. Every 1.2 seconds a two-dimensional snapshot is obtained (Figure 2.1). This snapshot contains observations under various viewing angles. The viewing angles range between 0 and 65°. From an altitude of around 758 km, the antenna covers an area of almost 3000 km

in diameter. However, due to the interferometry principle and the Y-shaped antenna, the field of view is limited to a hexagon-like shape about 1000 km across called the 'alias-free zone'. This area corresponds to observations where there is no ambiguity in the phase-difference (Camps et al., 2003).
The resolution of every brightness temperature measurement depends on the incidence angle. The resolution at the centre of the field of view (i.e. at nadir view) is about 35 km × 35 km and decreases to about 50 km × 50 km at the edge of the field of view (i.e. at incidence angles of 65°). The radiometric accuracy of single measurements is 1.8 - 2.2 K (Pinori et al., 2008).
MIRAS measures brightness temperatures at full polarisation. Thus, all parameters of the Stokes vector are provided. MIRAS records alternatively X, XY, Y, and YX polarisations. X and Y are the vertical and horizontal polarisation at the antenna reference frame. These have to be converted to the classically considered horizontal and vertical polarisation at the Earth's surface level frame (see section 2.2.1). XY is a cross polarisation, i.e. two polarisations at the same time with the different SMOS arms.

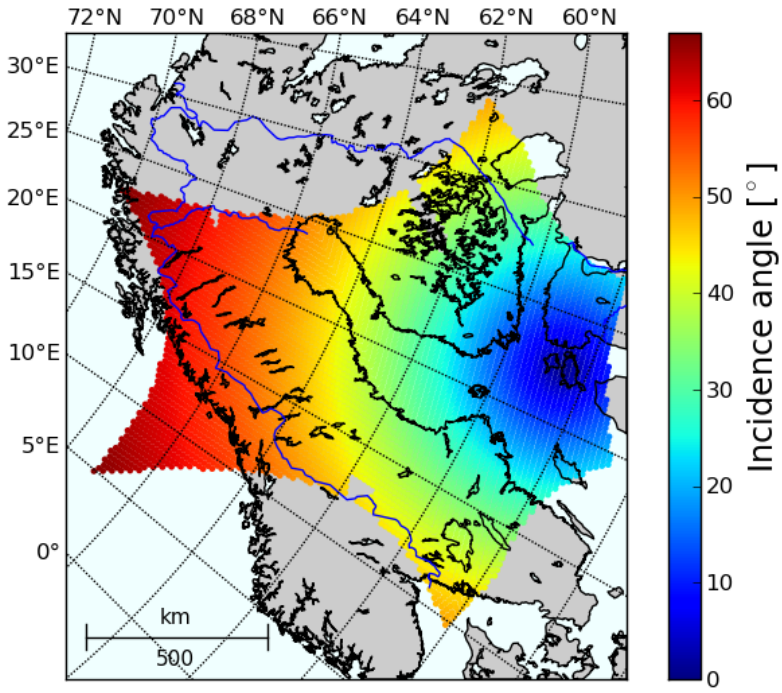

Figure 2.1: Example of the hexagon-like shaped 'alias-free' SMOS snapshot over the Baltic Sea area in Northern Europe. The colors indicate the incidence angle distribution over the snapshot.

2.2 SMOS data processing

In this study, we use SMOS Level 1C data. The Level 1C product contains multi-angular brightness temperatures at the TOA. The Level 1C data are geolocated in an equal-area grid system, the Icosahedral Snyder Equal Area projection with aperture 4, resolution 9, and shape of cells as hexagon (ISEA 4H9) (Pinori et al., 2008). The Discrete Global Grid (DGG) system ISEA 4H9 is characterised by a uniform distance of 15 km between the cells. Every grid cell is defined by a grid point number and the latitude and longitude of the grid cell's center point. The DGG systems are described in detail in Sahr et al. (2003).
Here, we describe the data processing of SMOS brightness temperatures in this study. For every SMOS grid point, we first gather all Level 1C brightness temperatures and the auxiliary data provided during one day. The latitude, the longitude, and the grid point number of the measurement are stored together with the brightness temperatures at full polarisation, the incidence angles, the Faraday rotation angles, the georotation angles, and the snapshot numbers. For every SMOS grid point, we then perform the following procedure.

2.2.1 Transformation to the Earth reference frame

On its way from the Earth's surface to the TOA, the radiation measured by SMOS is affected by an atmospheric effect called Faraday rotation. Faraday rotation is induced by ionospheric electrons. The electrons rotate the electric field while the electromagnetic waves propagate through the atmosphere. Thus, the Stokes vector components are modified. Neglecting the Faraday rotation can introduce brightness temperature errors of about 1 – 4 K (Kerr et al., 2001; Le Vine and Abraham, 2002).
The correction for Faraday rotation can be combined with the correction for the geometrical rotation from the antenna reference frame to the Earth reference frame. The Level 1C brightness temperatures, which are used in this study, are given in the antenna reference frame, and thus have to be transformed to the Earth reference frame. For the full polarisation mode, the Level 1C data provide the Stokes vector components T_X, T_Y, T_3 and T_4, as well as the georotation angle α_r, and the Faraday rotation angle ω_{Fa}. The transformation of the Stokes vector in the antenna reference frame to the Stokes vector in the Earth reference frame is calculated via the relation

$$\begin{pmatrix} T_{B,H} \\ T_{B,V} \\ T_{B,3} \\ T_{B,4} \end{pmatrix} = \begin{pmatrix} \cos^2\alpha & \sin^2\alpha & \cos\alpha\sin\alpha & 0 \\ \sin^2\alpha & \cos^2\alpha & -\cos\alpha\sin\alpha & 0 \\ -\sin(2\alpha) & \sin(2\alpha) & \cos(2\alpha) & 0 \\ 0 & 0 & 0 & 1 \end{pmatrix} \begin{pmatrix} T_X \\ T_Y \\ T_3 \\ T_4 \end{pmatrix} \quad , \tag{2.1}$$

where $\alpha = \alpha_r + \omega_{Fa}$, and $T_{B,H}$ and $T_{B,V}$ are the horizontally and vertically polarised brightness temperatures in the Earth reference frame, and $T_{B,3}$ and $T_{B,4}$ are the 3rd and 4th Stokes component in the Earth reference frame (Zine et al., 2008).
The MIRAS radiometer alternately measures one or two of the four Stokes vector components per snapshot. For the data processing of SMOS brightness temperatures

in this study, we thus use the four Stokes vector components T_X, T_Y, T_3 and T_4 from subsequent snapshots to calculate the horizontally and vertically polarised brightness temperatures for the considered SMOS grid point.
The brightness temperature intensity $T_{B,I}$, which is also used in this study, is defined as the mean of the vertical and horizontal components of the brightness temperature and is not affected by rotational effects :

$$T_{B,I} = \frac{T_X + T_Y}{2} = \frac{T_{B,H} + T_{B,V}}{2} \quad . \tag{2.2}$$

2.2.2 The RFI filter

SMOS measures radiation in L-band in a protected frequency window of 1.400 – 1.427 GHz. Nevertheless, SMOS measurements are affected by Radio Frequency Interference (RFI) that originates from radars, TV stations, and radio transmission. Due to their high level of transmitted power, L-band radars are probably the most important sources of RFI. L-band radars may interfere in an area of 80 km × 700 km. The intensity of brightness temperature contamination by RFI is not constant. In some cases, RFI occurs as a strong point source with very high brightness temperatures. The resulting brightness temperature measurements by far exceed the naturally observed brightness temperatures emitted by the Earth's surface. These measurements are unusable for any retrieval of geophysical parameters. Strong RFI sources can also corrupt the whole snapshot's brightness temperatures. In other cases, the source of RFI is weak and hard to discriminate from natural sources of L-band radiation and thus distorts the retrieval of geophysical parameters. The contamination by RFI is stronger at Y- than at X-polarisation. (Camps et al., 2010)
Until now, it is not clear how to deal most effectively with the problems caused by RFI contamination. There are several algorithms under development (e.g. Camps et al., 2010; Oliva et al., 2012; Misra and Ruf, 2012). In this study, we use the following approach. We collect all horizontally and vertically polarised SMOS brightness temperatures measured within a SMOS grid point. These brightness temperatures are sorted according to their incidence angles. In a first step, we exclude all brightness temperatures with obviously unreasonable values. The brightness temperature is defined as the physical temperature times the emissivity. Thus, the range of reasonable brightness temperature values can be estimated from the naturally occuring values of physical temperatures and emissivities of the media considered here, namely sea water, sea ice, and snow. For the regions where the occurrence of sea ice is possible (ice season in the high latitudes), we can assume that the L-band emissivity of sea water ranges between 0.2 and 0.6 (Klein and Swift, 1977), that the emissivities of sea ice and snow range between 0.4 and 1.0 (Vant et al., 1978; Tiuri et al., 1984), that the temperature of sea water ranges between -2 and 20°C, and that the temperatures of ice and snow range between -80 and 0°C. Thus, we exclude brightness temperatures that are not in the range of 50 – 280 K, because we do not expect natural radiation to take values outside of this range for sea ice applications. Due to the transformation from the antenna reference frame to the Earth reference frame, a RFI-contaminated brightness temperature at a certain polarisation (X or Y) affects the resulting brightness temperatures at both horizontal and vertical polarisation. Thus, we exclude the

brightness temperatures at both polarisations, even if only one of them is outside the 50 – 280 K range.
If, after this step, we have more than ten brightness temperatures for each polarisation and cover at least an incidence angle range of 10° per grid point, we use the remaining brightness temperatures to calculate a third order polynomial fit of the SMOS brightness temperatures as a function of incidence angle. The polynomial fit is calculated separately for the horizontal and the vertical polarisation. All brightness temperatures that deviate more than 15 K from this polynomial fit are excluded from the further analysis (Figure 2.2). As in the first step of the filter procedure, we exclude not only the affected brightness temperature at horizontal or vertical polarisation, but also the corresponding brightness temperature at the other polarisation, because it has been transformed simultaneously from the antenna reference to the Earth reference frame.
The value of 15 K for the exclusion of brightness temperatures is determined after visual inspection of example cases and is only a rough estimation. Furthermore, fitting the brightness temperatures at horizontal and vertical polarisation as a function of incidence angle by two separate third order polynomials can introduce errors, especially for low incidence angles, where horizontally and vertically polarised brightness temperatures should be nearly equal. However, applying the described RFI filter approach to SMOS data does not cause the resulting brightness temperatures to visibly differ from brightness temperatures, that were obtained for a very stringent RFI filter used for data processing in the framework of the ESA SMOSIce project. The latter RFI filter simply excludes all snapshots that contain any brightness temperature measurements higher than 300 K.

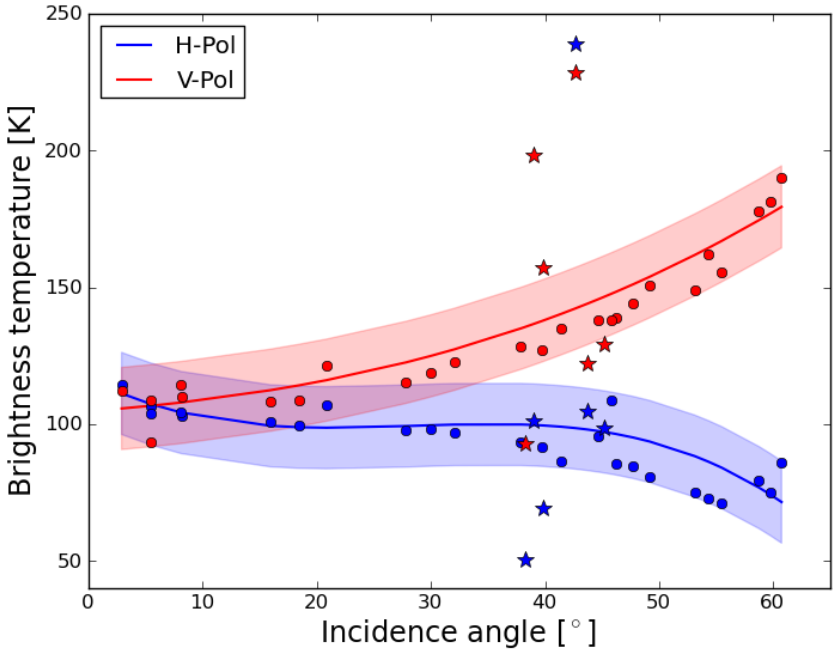

Figure 2.2: Example of our procedure to exclude RFI-contaminated SMOS brightness temperature measurements. The blue color indicates horizontal polarisation, the red color indicates vertical polarisation. The dots and stars show SMOS measurements. The lines show the polynomial fits to the SMOS measurements, the shaded areas show the range of brightness temperatures included for the further processing (± 15 K around the polynomial fit). The dots are included in the further processing, the stars are excluded from the further processing.

2.3 Brightness temperatures as seen by SMOS

The brightness temperature $T_{B,TOA}$ as observed from a radiometer like the MIRAS instrument on-board the SMOS satellite originates from radiation emitted from the Earth's surface itself $T_{B,terr}$, from radiation that is emitted by extraterrestrial sources and then reflected at the Earth's surface $(1-e_{terr})T_{B,extra}$, and from radiation emitted on the path between the Earth's surface and the radiometer $T_{B,atm}$:

$$T_{B,TOA} = T_{B,terr,TOA} + (1 - e_{terr})T_{B,extra,TOA} + T_{B,atm,TOA} \quad , \tag{2.3}$$

where e_{terr} is the emissivity of the Earth's surface, and correspondingly $(1-e_{terr})$ is the reflectivity of the Earth's surface, and the subscript TOA denotes that the considered contributions are influenced by the atmospheric particles on their way to the TOA. For the retrieval of geophysical parameters at the Earth's surface, $(1 - e_{terr})T_{B,extra,TOA}$ and $T_{B,atm,TOA}$ represent perturbing additional contributions. The SMOS Level 1C brightness temperatures used in this study are brightness temperatures at the TOA. The three main sources of additional contributions to these TOA brightness temperatures are sky radiation, sun glint, and atmospheric absorption and emission (Zine et al., 2008), which are considered in the following.

2.3.1 Sky radiation

The downwelling sky radiation that is scattered by the Earth's surface is called sky glitter. In L-band, sky radiation originates from the uniform cosmic microwave background, the line emission from hydrogen, and a continuum background (Le Vine and Abraham, 2004; Le Vine et al., 2005). The sky glitter contribution is expected to be geographically and seasonally variable and to vary from about 2 K to more than 7 K over sea surfaces (Zine et al., 2008). Due to the higher reflectivity of sea water as compared to sea ice, we expect the sky glitter contribution for sea ice to be smaller. Therefore, and because the correction for sky glitter is quite complex, we do not apply a correction for the sky glitter. Here, we only take into account the uniform and constant cosmic microwave background radiation $T_{B,cosm}$ of about 2.7 K that is reflected by the Earth's surface: $T_{B,extra}$= $T_{B,cosm}$= 2.7 K.

2.3.2 Sun glint

The sun is a very strong source of radiation in L-band. The solar radiation depends on the solar activity, and is thus time-dependent. The solar radiation reflected at the Earth's surface contributes to the TOA brightness temperature. However, the fraction of affected measurements is expected to be small. Thus, brightness temperatures are usually not corrected for sun glint; instead, affected measurements are flagged and discarded. (Zine et al., 2008)

2.3.3 Atmospheric absorption and emission

The TOA brightness temperatures $T_{B,TOA}$ are influenced by the atmosphere due to attenuation and to atmospheric self-emission. Because these two effects have opposite consequences on the TOA brightness temperature, the overall effect can be negative or positive. On the one hand, radiation originating from the Earth's surface is attenuated on its way through the atmosphere, i.e. the brightness temperature observed at the TOA is lower than the brightness temperature observed at the Earth's surface. On the other hand, atmospheric particles emit radiation themselves. This self-emission is added to the radiation of the Earth's surface. The TOA brightness temperature $T_{B,TOA}$ can thus be described by:

$$T_{B,TOA} = (T_{B,terr} + (1 - e_{terr})T_{B,extra})\mathrm{e}^{-\tau_{atm}} + T_{B,up} + (1 - e_{terr})T_{B,down}\mathrm{e}^{-\tau_{atm}} \quad , \quad (2.4)$$

where τ_{atm} is the optical thickness of the atmosphere, $T_{B,terr}$ is the upwelling brightness temperature from the Earth's surface, $T_{B,up}$ is the brightness temperature that is self-emitted by the atmosphere upward and attenuated along the upward path to the TOA, $T_{B,down}$ is the brightness temperature that is self-emitted by the atmosphere downward and attenuated along the downward path to the Earth's surface. Equation (2.4) describes how $T_{B,terr}$ is attenuated on its path upward to the TOA, and how the downwelling radiation $T_{B,down}$ is reflected by the Earth's surface, which has the reflectivity $1 - e_{terr}$, and is then again attenuated along the upward path to the TOA. Numerical simulations with the Liebe model (Liebe et al., 1993) indicate that the main contribution to both $T_{B,up}$ and $T_{B,down}$ is emission from a thin layer near the Earth's surface. Thus, their radiative contributions are almost equal. Because the difference is less than 0.01 K, they can be represented by a single value $T_{B,ud} = T_{B,up} = T_{B,down}$. (Zine et al., 2008)

The constituents of the atmosphere that have to be considered for an atmospheric correction are the dry atmosphere, water vapour, clouds, and rain. In L-band, the radiative contribution by clouds and rain is negligible, except for very deep cumulus clouds and heavy precipitation events. The by far largest radiative contribution from the dry atmosphere is assigned to molecular oxygen. Water vapour has rotational absorption lines in the microwave region. Thus, the atmospheric contributions to brightness temperatures measured at the TOA mainly originate from atmospheric oxygen and water vapour. (Zine et al., 2008)

In order to account for atmospheric absorption and emission, we calculate the total atmospheric contribution $\Delta T_{B,atm}$ for different scenarios and use the pre-calculated values of the total atmospheric contribution $\Delta T_{B,atm}$ as correction terms for simulated brightness temperatures. We calculate the correction terms $\Delta T_{B,atm}$ for different terrain brightness temperatures, terrain emissivities, incidence angles and states of the atmosphere. Thus, using equations (2.3) and (2.4), the brightness temperature at the TOA is expressed as

$$T_{B,TOA} = T_{B,terr} + (1 - e_{terr})T_{B,extra} + \Delta T_{B,atm} \quad , \quad (2.5)$$

with

$$\Delta T_{B,atm} = T_{B,TOA} - (T_{B,terr} + (1 - e_{terr})T_{B,extra}) \tag{2.6}$$

$$= (T_{B,terr} + (1 - e_{terr})T_{B,extra})(\mathrm{e}^{-\tau_{atm}} - 1) + T_{B,ud}(1 + (1 - e_{terr})\mathrm{e}^{-\tau_{atm}}) \quad . \tag{2.7}$$

The optical thickness of the atmosphere τ_{atm} is defined as

$$\tau_{atm} = \frac{1}{\cos\theta} \int_{z=0}^{\infty} \kappa(z) dz \quad , \tag{2.8}$$

where $\kappa(z)$ is the atmospheric absorption coefficient at height z, and θ is the incidence angle. For frequencies below 10 GHz, scattering effects may be ignored for most atmospheric weather conditions and we may use the expression of the brightness temperature that represents the upwelling and downwelling atmospheric radiation for a non-scattering atmosphere:

$$T_{B,ud} = \frac{1}{\cos\theta} \int_{z=0}^{\infty} \kappa(z) T(z) \mathrm{e}^{-\tau_{atm}} dz \quad , \tag{2.9}$$

where $T(z)$ is the air temperature at height z. (Ulaby et al., 1981)

Calculation of the atmospheric absorption coefficient
In this study, we calculate the absorption coefficients of water vapour $\kappa_{wv}(p)$, oxygen $\kappa_{O_2}(p)$ and nitrogen $\kappa_{N_2}(p)$ as functions of pressure p using the atmospheric absorption model developed by Rosenkranz (1998). Because it is part of the atmospheric absorption model, we here also include the radiative contribution by nitrogen, even if it is much smaller than the contributions by water vapour and oxygen. The atmospheric absorption coefficient is the sum of the contributions by water vapour, oxygen, and nitrogen:

$$\kappa(p) = \kappa_{wv}(p) + \kappa_{O_2}(p) + \kappa_{N_2}(p) \quad . \tag{2.10}$$

The atmospheric absorption model calculates the absorption coefficients $\kappa_{wv}(p)$, $\kappa_{O_2}(p)$ and $\kappa_{N_2}(p)$ at frequency f from 1. the pressure profile, 2. the temperature profile, and 3. the water vapour density profile in the atmosphere. Here, we use the following approach to derive these three profiles:

1. We use a logarithmic pressure profile with 100 pressure levels between 1013 hPa and 13 hPa described by

$$p[\mathrm{hPa}] = 1013 - 1000 \cdot \log_{10}(k) \quad , \tag{2.11}$$

   where k takes values between 1 and 10.

2. The temperature profile $T(p)$ is based on the monthly mean air temperatures from the National Centers for Environmental Prediction (NCEP) Reanalysis temperature data derived by the Climate Diagnostics Center (CDC). The monthly mean

air temperatures have been averaged over the time period from 1948 to 2011 and are provided for 17 pressure levels ranging between 1000 and 10 hPa. We use only the data for polar latitudes $\phi > 70°$. We linearly interpolate the temperatures, which are given for the NCEP pressure profile, to match the pressure profile as defined in equation (2.11).

3. The water vapour density profile is derived from the relative humidity profile. We use the monthly mean relative humidities from NCEP reanalysis data averaged from 1948 to 2011 for 8 pressure levels ranging between 1000 and 300 hPa. We use only the data for polar latitudes $\phi > 70°$. As for the temperature profile, we linearly interpolate the relative humidities given for 8 pressure levels to the pressure profile given in equation (2.11). To derive the water vapour density profile from the relative humidity profile, we first use the ideal gas law to relate the water vapour density $\rho_{wv}(p)$ to the water vapour pressure $p_{wv}(p)$:

$$\rho_{wv}(p) = \frac{p_{wv}(p) M_{wv}}{R \cdot T(p)} \quad , \tag{2.12}$$

where M_{wv}= 18.016 $\cdot 10^{-3}$ $\frac{\text{kg}}{\text{mol}}$ is the molar mass of water vapour, and R= 8.3144 $\frac{\text{J}}{\text{mol K}}$ is the gas constant. The water vapour pressure $p_{wv}(p)$ is

$$p_{wv}(p) = \phi(p) p_{sat}(p) \quad , \tag{2.13}$$

where $\phi(p)$ is the relative humidity and $p_{sat}(p)$ is the water vapour saturation pressure. The water vapour saturation pressure can be calculated using the relationship by Murray (1967):

$$p_{sat}(p)[\text{hPa}] = 100 \cdot 6.1078 \cdot e^{\frac{a(T(p) - 273.16\ \text{K})}{T(p) - b}} \quad , \tag{2.14}$$

with a= 17.2693882 and b= 35.86 K.

With the input profiles from 1. to 3., we calculate the atmospheric absorption coefficient profile $\kappa(p)$ as a function of pressure p. However, equation (2.9) requires the atmospheric absorption coefficient profile $\kappa(z)$ and the temperature profile $T(z)$ with regard to the geometric height z. Therefore, we use the barometric formula to convert pressure p to height z. The barometric formula for a constant temperature gradient $\gamma = -\frac{\partial T}{\partial z}$ in the atmosphere is

$$p = p_0 \left(\frac{T_0 - \gamma z}{T_0 - \gamma z_0} \right)^{\frac{g}{\gamma R_d}} \quad , \tag{2.15}$$

where p_0 is the pressure and T_0 is the temperature at height z_0, g= 9.81 m/s^2 is the Earth's gravitational acceleration, and R_d= 287 J/(kgK) is the gas constant of dry air. For p_0, T_0, and z_0, we here use the values p_0= 1000 hPa, the corresponding temperature $T_0 = T(p = p_0)$ from the NCEP temperature profile, and z_0= 111 m from the U.S. standard atmosphere (NOAA and Force, 1976). For the temperature gradient we use the value γ= 0.65 K/100 m, as assigned to the lowest 11 km of the U.S. standard

atmosphere (NOAA and Force, 1976). Reorganizing equation (2.15) gives the height z as a function of pressure p:

$$z = \frac{1}{\gamma}(T_0 - \left(\frac{p}{p_0}\right)^{\frac{\gamma R_d}{g}} (T_0 - \gamma z_0)) \quad . \tag{2.16}$$

Atmospheric correction of brightness temperatures

The atmospheric contributions $\Delta T_{B,atm}$ for different terrain brightness temperatures $T_{B,terr}$, terrain emissivities e_{terr}, and incidence angles, as calculated with the described approach, are given in Table A.1 in the appendix. We perform the calculations for emissivities ranging between 0.3 and 1.0. For each emissivity, we choose representative brightness temperatures, as they would be observed at realistic physical temperatures for ice and water. The incidence angles considered here are 0°, 20°, 40° and 60°. We perform the calculations for three different months. We use the monthly means of the NCEP temperature and humidity profiles for January, April and October. The values of the atmospheric contributions $\Delta T_{B,atm}$ are used as correction terms for the brightness temperature simulations in this study.

According to our calculations, the atmospheric contribution $\Delta T_{B,atm}$ to the brightness temperature as observed at the TOA ranges between -0.36 K and +5.67 K, i.e. in most cases the effect of the atmospheric self-emittance dominates over the attenuation of radiation from the Earth's surface. Note that due to the definition of $\Delta T_{B,atm}$ as a correction term that accounts for the overall effect of the atmosphere on the brightness temperature of the Earth's surface, we sometimes obtain negative values for $\Delta T_{B,atm}$, even if the brightness temperature itself can of course never be negative.

We find the following relationships regarding the different scenarios with 1. different emissivities, 2. different brightness temperatures (and thus different physical temperatures), 3. different incidence angles, and 4. different states of the atmosphere (represented here by the month of the year):

1. The atmospheric contribution decreases with increasing emissivity. The higher the emissivity e_{terr}, the lower is the reflectivity $1 - e_{terr}$. Thus, the fraction of $T_{B,down}$ that is reflected at the Earth's surface is lower and contributes less to the brightness temperature measured at the TOA. For emissivities e_{terr} higher than about 0.95 the atmospheric contribution $\Delta T_{B,atm}$ can reach negative values, i.e. the brightness temperature observed at the TOA is lower than the brightness temperature observed at the Earth's surface.

2. The atmospheric contribution $\Delta T_{B,atm}$ decreases with increasing brightness temperature of the Earth's surface, i.e. with increasing physical temperature. The higher the brightness temperature of the Earth's surface, the more radiation is attenuated by atmospheric particles on the path through the atmosphere.

3. The absolute value of the atmospheric contribution $\Delta T_{B,atm}$ increases with increasing incidence angle of the brightness temperature observation. For higher incidence angles, the path through the atmosphere is longer than for lower incidence angles. Thus, if the self-emittance of the atmosphere dominates over the attenuation of the atmosphere, the atmospheric contribution is higher for higher

incidence angles. Whereas, if the attenuation of the atmosphere dominates over the self-emittance of the atmosphere, the atmospheric contribution has higher negative values for higher incidence angles.

4. The atmospheric contributions $\Delta T_{B,atm}$ for the mean atmospheric profiles of air temperature and humidity in January, April and October are very similar. Averaged over all considered emissivities, brightness temperatures, and incidence angles, the atmospheric contributions $\Delta T_{B,atm}$ for the October values are 2.6% higher than the atmospheric contributions for the April values, and 5.9% higher than the January values, respectively.

2.3.4 The TOA brightness temperature

For sea ice applications, the terrain brightness temperature consists of the brightness temperature of sea water and the brightness temperature of sea ice. Thus, the brightness temperature at the TOA is

$$T_{B,TOA} = (1-c)(T_{B,water} + (1-e_{water})T_{B,cosm}) + c(T_{B,ice} + (1-e_{ice})T_{B,cosm}) + \Delta T_{B,atm} \quad , \tag{2.17}$$

where c is ice concentration, e_{water} is the emissivity and $T_{B,water}$ the brightness temperature of water, e_{ice} is the emissivity and $T_{B,ice}$ the brightness temperature of the ice layer.
The calculation of the brightness temperature of an ice layer $T_{B,ice}$ is described in section 2.4. The brightness temperature of sea water $T_{B,water}$ is

$$T_{B,water} = e_{water} T_{water} \quad , \tag{2.18}$$

where T_{water} is the physical temperature of water. We calculate the emissivity of water e_{water} from the Fresnel equations for a specular surface (e.g. Ulaby et al., 1981):

$$e_{water}(p = H) = 1 - \left| \frac{\cos\theta - \sqrt{\epsilon_{water} - \sin^2\theta}}{\cos\theta + \sqrt{\epsilon_{water} - \sin^2\theta}} \right|^2 \tag{2.19}$$

$$e_{water}(p = V) = 1 - \left| \frac{\epsilon_{water}\cos\theta - \sqrt{\epsilon_{water} - \sin^2\theta}}{\epsilon_{water}\cos\theta + \sqrt{\epsilon_{water} - \sin^2\theta}} \right|^2 \quad , \tag{2.20}$$

where θ is the incidence angle and ϵ_{water} is the permittivity of water. Here, the permittivity of water is calculated from empirical equations (Klein and Swift, 1977).
As mentioned before, we assume $T_{B,cosm}$= 2.7 K for the cosmic background radiation in this study and use Table A.1 to determine the atmospheric contribution $\Delta T_{B,atm}$ for given brightness temperatures, emissivities, and incidence angles, respectively.

2.4 The radiation models

In this section, we focus on the brightness temperature as observed over sea ice ($T_{B,ice}$). In order to retrieve ice thickness from SMOS brightness temperatures, we have to set up a model that describes brightness temperature as a function of ice thickness.
In previous studies (Kaleschke et al., 2010, 2012), the ice brightness temperature was determined with a radiation model based on the approach described in Menashi et al. (1993). The approach is valid for a dielectric slab of ice that is bordered by the underlying water and the air above the slab of ice. However, here we want to investigate the impact of a temperature gradient within the ice as compared to a bulk ice temperature, and the impact of a snow layer on brightness temperatures above sea ice. Thus, we need radiation models that are capable of treating multiple layers of ice, and an ice layer that is covered by a snow layer.
In general, there are two approaches to consider radiometric emission from layered media; they are called the coherent and the incoherent approach. A coherent model is based on the solutions for the Maxwell equations and accounts for both the magnitudes and the phases of the electromagnetic fields that are reflected within the layered structure of the medium. An incoherent model is an approximation of the radiometric emission. The approximation is applicable, if the coherence of the radiation is reduced as a result of irregular boundaries, finite receiver bandwith, or antenna beam width (Menashi et al., 1993).
For sea ice applications in L-band, a coherent model describes sea ice emissivity as a periodic function of sea ice thickness. If the root mean square ice thickness within the illuminated footprint varies by at least a quarter of the considered wavelength λ (for SMOS: $\lambda = 21$ cm), the periodicity averages out. Instead of a coherent signal, we then observe an incoherent signal, and sea ice emissivity can be described as a unique function of ice thickness. This incoherent behaviour is the prerequisite for the retrieval of ice thickness from L-band measurements.
Here, we use an incoherent radiation model for multiple layers as described in Burke et al. (1979). This model is referred to as the incoherent Burke model throughout the thesis. Because the Burke model makes some simplifying assumptions, we also use a coherent multiple-layer model as described in Ulaby et al. (1981) and compare the results from both models. The coherent model is referred to as the coherent Ulaby model throughout the thesis. These two models, which are used for the following analyses, are presented in the following two sections. The main differences between these two models and the model after Menashi et al. (1993), which was used in previous studies, are summarised in Table 2.1.

2.4.1 The coherent Ulaby model

In order to consider the coherent emissivity of electromagnetic radiation in a medium that consists of multiple layers, we here use a method described in Ulaby et al. (1981) that follows Kong (1975). This method gives the reflection and the transmission coefficients for a N-layer medium with plane boundaries. A sketch of a N-layer medium as it is considered here is depicted in Figure 2.3. For our sea ice applications, the

Table 2.1: Radiation models used for the calculation of L-band brightness temperatures above sea ice.

	Ulaby et al. (1981)	**Menashi et al. (1993)**	**Burke et al. (1979)**
approach	coherent	coherent/incoherent	incoherent
number of layers in medium	$N \in \mathbb{N}$	1	$N \in \mathbb{N}$
reduces to water emissivity for $d_{ice} \to 0$	yes	yes	no
based on	Maxwell equations	Fourier series expansion of coherent expression + integral over ice thickness variation	radiative transfer equation
neglects reflection terms of order > 1	no	partly	yes

semi-infinite layer on top consists of air, and the semi-infinite layer at the bottom is the sea water underneath the ice layer. The approach of this method is that the wave equation's solutions for the electric and the magnetic fields in the mth layer can be expressed as functions of the field amplitudes A_m and C_m of the mth layer, the depth z, the incidence angle on the first interface θ_0, and the z-component of the wave number in the mth layer k_{zm}, which can be expressed by

$$k_{zm} = \frac{\omega}{c_0}\sqrt{\epsilon_m - \sin^2\theta_0} \quad , \tag{2.21}$$

where ω is the frequency in radians per second, c_0 is the speed of light (in vacuum), and ϵ_m is the permittivity of the mth layer.
The wave equations for the mth and the $(m+1)$th layer are related to each other by the boundary conditions at z= -d_m. From the continuity of the tangential electric and magnetic fields we obtain two equations. In matrix form these two equations can be combined to one. Here, we consider the matrix for a horizontally polarised incident field:

$$\begin{pmatrix} A_m e^{-ik_{zm}d_m} \\ C_m e^{ik_{zm}d_m} \end{pmatrix} = B_{m(m+1)} \begin{pmatrix} A_{m+1} e^{-ik_{z(m+1)}d_{m+1}} \\ C_{m+1} e^{ik_{z(m+1)}d_{m+1}} \end{pmatrix} \quad , \tag{2.22}$$

where

$$B_{m(m+1)} = \frac{1}{2}\left(1 + \frac{\mu_m k_{z(m+1)}}{\mu_{m+1} k_{zm}}\right) \begin{pmatrix} e^{i\gamma} & R_{m(m+1)} e^{-i\gamma} \\ R_{m(m+1)} e^{i\gamma} & e^{-i\gamma} \end{pmatrix} \quad ,$$

$$\text{with } \gamma = k_{z(m+1)}(d_{m+1} - d_m) \quad ,$$

$$R_{m(m+1)} = \frac{\mu_{m+1} k_{zm} - \mu_m k_{z(m+1)}}{\mu_{m+1} k_{zm} + \mu_m k_{z(m+1)}} \quad .$$

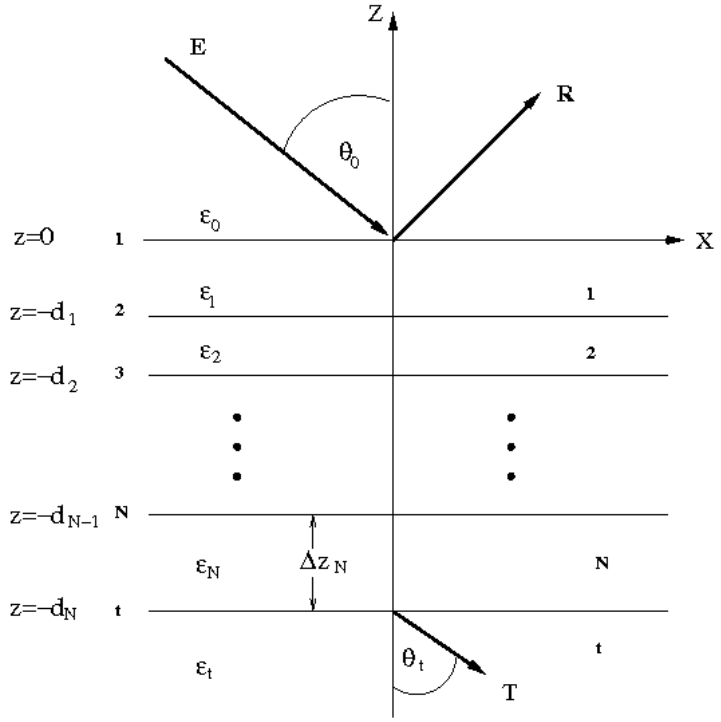

Figure 2.3: Reflection and transmission for a N-layer medium with the notations as used in the coherent model after Ulaby et al. (1981), as well as in the incoherent model after Burke et al. (1979).

$B_{m(m+1)}$ is called the backward propagation matrix, and $R_{m(m+1)}$ is the Fresnel reflection coefficient for horizontal polarisation at the boundary z= -d_m within the medium that is characterised by the permittivity ϵ_m.
The amplitudes for the incident and the reflected fields can be related to those in the first layer by B_{01}, and to those in the second layer by $B_{01}B_{12}$, etc. In the semi-infinite medium below layer N, there is only a transmitted field amplitude. The value for d_t in equation (2.22) can be an arbitrary finite number, because the d_t in the transmitted field will cancel with that in B_{Nt}. Hence, the incident and the reflected field amplitudes are related to the transmitted field amplitudes by

$$\begin{pmatrix} 1 \\ R \end{pmatrix} = B_{01}B_{12}\cdots B_{Nt}\begin{pmatrix} Te^{-ik_{zt}d_t} \\ 0 \end{pmatrix} \quad , \tag{2.23}$$

where R is the reflection coefficient and T the transmission coefficient for the N-layer medium. Equation (2.23) represents two equations with two unknowns R and T. Inserting the expression for T from the first equation into the second equation gives

$$R = \frac{B[2,1]}{B[1,1]} \quad , \tag{2.24}$$

where $B[m,n]$ is the entry of the matrix $B = B_{01}B_{12}\cdots B_{Nt}$ in the mth row and the nth column. The emissivity of the N-layer medium is then

$$e = 1 - \left|R^2\right| \quad . \tag{2.25}$$

The above described approach covers the horizontally polarised case. The solution for vertical polarisation is obtained by replacing ϵ by μ, and μ by ϵ in all equations. (Ulaby et al., 1981)
The brightness temperature at polarisation p (p= H for horizontal and p= V for vertical polarisation) of the N-layer medium is then the emissivity of the medium at polarisation p times the medium's physical temperature T_g:

$$T_{B,p} = e_p T_g \quad . \tag{2.26}$$

Here, we take the mean temperature of the considered ice and snow layers for T_g.

2.4.2 The incoherent Burke model

In order to consider the incoherent emissivity of electromagnetic radiation in a medium that consists of multiple layers, we here use a method described in Burke et al. (1979). The emission model is based on the radiative transfer equation and was originally developed for soil moisture applications of X- and L-band radiometer measurements. The model describes the radiation emitted from a stratified bare soil with N layers. The dielectric properties are assumed to be constant across the layers. A sketch of a N-layer medium as considered here is depicted in Figure 2.3. For our sea ice applications, the semi-infinite layer on top consists of air, and the semi-infinite layer at the bottom is the sea water underneath the ice layer.
The radiative transfer equation for the first layer can be written as

$$\frac{dT_p}{d(\gamma_1 z)} = -T_p + T_1 \quad , \tag{2.27}$$

where T_p is the brightness temperature at polarisation p, γ_1 is the absorption coefficient of the first layer, z is the path length, and T_1 is the physical temperature of the first layer. Equation (2.27) can be integrated from a point just below the surface to a point just above the interface between the first and the second layers. The resulting expression has two components. One accounts for the radiation emitted upward in the first layer and heading towards the surface, the other describes the upwelling radiation at the bottom of the first layer. The upwelling radiation in turn also has two components. Firstly, radiation emitted downward in the first layer that is reflected at the interface between the first and the second layers, and secondly, radiation transmitted from lower layers. The radiation field just above the surface is the radiation field just below multiplied by the transmittance of the interface.
The radiative transfer equation can then be integrated again from just below the first layer to a point just above the interface between the second and the third layer. If this procedure is repeated for N layers, we obtain the brightness temperature above the layered medium:

$$T_p(\theta_0) = \sum_{i=1}^{N} T_i (1 - e^{-\gamma_i(\theta_0)\Delta z_i})(1 + R_{p,i+1}(\theta_0) e^{-\gamma_i(\theta_0)\Delta z_i}) \cdot \prod_{j=1}^{i} (1 - R_{p,j}(\theta_0)) e^{-\sum_{j=2}^{i} \gamma_{j-1}(\theta_0)\Delta z_{j-1}} \quad , \tag{2.28}$$

where θ_0 is the angle of incidence at the first layer, T_i is the physical temperature of the ith layer, and Δz_i is the ith layer's thickness. The absorption coefficient γ_i can be expressed as

$$\gamma_i = 2\frac{\omega\alpha_{zi}(\theta_0)}{c_0} \quad , \tag{2.29}$$

where ω is the frequency in radians per second, c_0 is the speed of light (in vacuum), and

$$\alpha_{zi}(\theta_0) = \frac{\epsilon_{Ii}}{2\beta_{zi}(\theta_0)} \quad , \tag{2.30}$$

$$\beta_{zi}(\theta_0) = \sqrt{\frac{1}{2}(\epsilon_{Ri} - \sin^2\theta_0)(1 + \sqrt{1 + \frac{\epsilon_{Ii}^2}{(\epsilon_{Ri} - \sin^2\theta_0)^2}})} \quad , \tag{2.31}$$

where ϵ_{Ri} and ϵ_{Ii} are the real and the imaginary parts of the ith layer's complex permittivity, respectively.
$R_{p,i}$ is the absolute value squared of the Fresnel coefficient $\rho_{p,i}$ in the ith layer for the p polarisation:

$$\rho_{H,i} = \frac{k_{zi} - k_{z(i-1)}}{k_{zi} + k_{z(i-1)}} \quad , \tag{2.32}$$

$$\rho_{V,i} = \frac{\epsilon_{j-1}k_{zi} - \epsilon_j k_{z(i-1)}}{\epsilon_{j-1}k_{zi} + \epsilon_j k_{z(i-1)}} \quad , \tag{2.33}$$

where $k_{zi} = \beta_{zi}(\theta_0) + i\alpha_{zi}(\theta_0)$ and $\epsilon_j = \epsilon_{Ri} + i\epsilon_{Ii}$. (Burke et al., 1979)

2.4.3 Model assumptions for sea ice applications

The dielectric properties of the layers considered in the coherent Ulaby model and the incoherent Burke model are described by the permittivities of the layers. In order to calculate the brightness temperature over sea ice, we consider one or more layers of sea ice that are bounded by an infinitely thick layer of air and an infinitely thick layer of sea water. As already done in Kaleschke et al. (2010), we here use the following expressions for the corresponding permittivities.
The permittivity of air is assumed to be ϵ_{air}=1, which is the value for vacuum. For the permittivity of sea water, we use the empirical relationship by Klein and Swift (1977). For the permittivity of sea ice we use an empirical relationship that describes the ice permittivity ϵ_{ice} as a function of brine volume fraction V_b within the ice (Vant et al., 1978):

$$\epsilon_{ice} = a_1 + a_2 V_b + i(a_3 + a_4 V_b) \quad , \tag{2.34}$$

where V_b is given in ‰, and a_1, a_2, a_3, and a_4 are frequency-dependent coefficients. The empirical relationship is valid for $V_b < 70$ ‰. For the SMOS frequency of f= 1.4 GHz, we linearly interpolate the coefficients a_1, a_2, a_3, and a_4 for 1 and 2 GHz, as introduced by Vant et al. (1978) for first-year ice and multi-year ice conditions (Table 2.2). The brine volume fraction V_b can be expressed as a function of the bulk values for the ice salinity S_{ice}, the ice density ρ_{ice}, the density of the brine ρ_{brine}, and the ice

Table 2.2: Coefficients used here for the calculation of sea ice permittivity according to equation (2.34) as interpolated for f= 1.4 GHz from the values for 1 and 2 GHz (Vant et al., 1978).

	a_1	a_2	a_3	a_4
first-year ice	3.10	0.0084	0.037	0.00445
multi-year ice	3.10	0.0084	0.003	0.00435

temperature T_{ice}. For ice temperatures lower than -2°C, we use the equations given in Cox and Weeks (1983), and for higher ice temperatures (as can be encountered particularly in low-salinity sea ice), we use the equations given in Leppäranta and Manninen (1988). For the ice density ρ_{ice}, we use an expression that relates ice density to ice temperature T_{ice} (Pounder, 1965):

$$\rho_{ice} = 0.917 - 1.403 \cdot 10^{-4} T_{ice} \quad , \tag{2.35}$$

where T_{ice} is given in °C. For the brine density, we use an expression that depends on brine salinity S_{brine} (Cox and Weeks, 1983):

$$\rho_{brine} = 1 + 0.0008 S_{brine} \quad , \tag{2.36}$$

where S_{brine} is inserted in ‰. We obtain the brine salinity S_{brine} from polynomial approximations for the dependency between brine salinity and ice temperature (Vant et al., 1978).

Chapter 3

Sensitivity of brightness temperature and of ice thickness retrieval to ice conditions

In this chapter, we investigate how ice conditions influence the brightness temperature over sea ice. The dielectric properties of sea ice are described by the ice permittivity, which can be expressed as a function of relative brine volume in the ice (Vant et al., 1978). The relative brine volume mainly depends on ice temperature and salinity (Cox and Weeks, 1983).
In section 3.1, we investigate the impact of the temperature distribution within the ice column on the brightness temperature as observed above the ice column. In addition, we calculate the sensitivity of brightness temperature to bulk ice temperature, and assess the consequences for the ice thickness retrieval in L-band. In section 3.2, we calculate the sensitivity of brightness temperature to bulk ice salinity, and assess the consequences for the ice thickness retrieval in L-band. In section 3.3, we consider an example case of freezing sea ice in the Arctic and compare the contribution of increasing ice thickness to the observed brightness temperature evolution with the contributions caused by naturally occuring variations of ice temperature and salinity.

3.1 Impact of ice temperature

In order to investigate the effect of ice temperature variability on brightness temperature simulations, we set up the following investigations: In section 3.1.1, we use a simple heat conduction model to identify the conditions under which the temperature gradient within ice can be assumed to be linear. In section 3.1.2, we compare brightness temperatures as simulated for a linear temperature gradient within the ice with brightness temperatures as simulated for a bulk ice temperature. In section 3.1.3, we calculate how sensitive simulated brightness temperatures are to ice temperature changes and how this sensitivity impacts the retrieval of ice thickness from brightness temperatures. Thus, we can estimate both, the influence of changing temperature con-

ditions on the retrieval and the retrieval error introduced by the uncertainty of the ice temperature estimation.

3.1.1 Conditions for a linear temperature gradient

The radiation models used to retrieve ice thickness from SMOS data require information on the ice temperature. A possible approach is to use ice surface temperatures obtained from MODIS thermal imagery, for example. In the absence of any temperature information for the ice, ice temperature could also be estimated from air temperature, which is globally available on short terms from reanalysis data sets, for example. If only one ice layer is considered in the radiation model, a bulk ice temperature is required, whereas the models with multiple layers within the ice can be applied to an ice temperature profile. However, note that in the coherent Ulaby model the ice temperature profile is only taken into account via the permittivity profile and the permittivity's dependence on ice temperature, while for the ice temperature the mean value of the profile is used. In contrast, the Burke model contains both the temperature profile and the permittivity profile.
In order to estimate the required bulk ice temperature or ice temperature profile from the ice surface temperature, we have to make some assumptions regarding the temperature distribution within ice. If the temperature gradient within ice can be assumed to be linear, the temperature in the ice increases linearly from the surface temperature to the freezing temperature of the water underneath the ice. In order to investigate under which conditions this assumption is applicable for the retrieval of ice thickness from SMOS data, we set up a heat conduction model and simulate abrupt temperature changes at the ice surface. Thus, we can roughly estimate how long it takes for the ice system to re-establish a linear temperature gradient within ice.
The heat equation for a function $u(x, y, z, t)$ with the spatial variables x, y, z and the time variable t is

$$\frac{du}{dt} - \alpha \Delta u = 0 \quad , \tag{3.1}$$

where α is the thermal diffusivity, and Δ is the Laplace operator. For a homogeneous ice column, in which the ice temperature is assumed to vary only with depth, equation (3.1) can be written in the form

$$\rho_{ice} c_{p,ice} \frac{dT}{dt} = \kappa_{ice} \frac{d^2T}{dz^2} \quad , \tag{3.2}$$

where ρ_{ice} is the density of ice, $c_{p,ice}$ is the specific heat capacity of ice, and κ_{ice} is the heat conductivity of ice. Because we here only need to roughly estimate the time scales, we neglect the temperature dependence of the heat capacity and heat conductivity and use typical values for the above parameters: ρ_{ice}= 910 kg/m^3, $c_{p,ice}$= 2113 J/(kgK), and κ_{ice}= 2.1 W/(Km) (as used for example in Tonboe et al. (2011)).
We perform our calculations for an ice thickness d_{ice}= 50 cm and an ice thickness d_{ice}= 100 cm, respectively. These thicknesses are at and above the maximum ice thickness that is retrievable from SMOS measurements in the Arctic. The ice column is uniformly divided into 11 layers, corresponding to a vertical resolution of about 4.5 cm for the ice with d_{ice}= 50 cm, and 9.1 cm for the ice with d_{ice}= 100 cm, respectively.

The initial temperature profile is set to be at a constant temperature of -2°C for all ice layers, i.e. near the freezing temperature of Arctic water. We simulate three abrupt temperature changes at the ice surface. First, the ice surface temperature drops down from the initial value of -2°C to -10°C, followed by a further sudden drop to -30°C, and a final abrupt increase back to -2°C. In our simulations, the abrupt changes occur each after one day for the ice with d_{ice}= 50 cm, and after two days for the ice with d_{ice}= 100 cm, respectively. The bottommost layer is kept near the freezing temperature of water at -2°C throughout the simulations. The temperatures of the remaining ice layers are calculated from equation (3.2) using forward in time and central in space finite differences with a time step of 10 minutes. The simulations (Figures 3.1 to 3.4) yield that in the chosen example cases with quite large temperature changes on the ice surface, an almost linear temperature gradient within ice is established within time scales of hours.

Impact on brightness temperature

We use the coherent Ulaby model to simulate brightness temperatures for sea ice with ice temperature profiles as they occur during the simulated temperature changes (Figure 3.5). In addition, we simulate brightness temperatures for an assumed linear temperature gradient between the surface temperature and the bottom temperature at the water freezing point, and compare the resulting brightness temperatures.

We perform the simulations for the 50 cm thick ice. For the bulk ice and water salinity and the water temperature we assume typical Arctic values: S_{ice}= 8 g/kg, S_{water}= 30 g/kg, T_{water}= -1.8°C. In order to get a representative brightness temperature for 50 cm thick ice from the oscillating coherent model, we calculate the average brightness temperature for one oscillation around the ice thickness of 50 cm. At nadir, the period of the coherent oscillation is half the electromagnetic wavelength in the medium. Here, we model L-band brightness temperatures for a wavelength in vacuum of about λ_0= 21 cm. The wavelength in ice is $\lambda_{ice} = \frac{\lambda_0}{\sqrt{\epsilon_{ice}}}$. Thus, we perform the simulations for d_{ice}= 50 cm $\pm \frac{1}{2}\frac{\lambda_{ice}}{2}$ (e.g. for $d_{ice} \approx$ 50 cm $\pm$ 2.9 cm for ϵ_{ice}= 3.2).

On the first day, the ice surface temperature of the temperature simulations is at -10°C, while the remaining ice layers first have a constant temperature of -2°C and then gradually adjust their temperature until a linear temperature gradient between the ice surface and the ice bottom temperature is formed. The resulting average brightness temperature from the coherent Ulaby model is 231.5 K, while the resulting average brightness temperature is 229.9 K for ice that is assumed to have a linear temperature gradient over the 11 layers with temperatures ranging from -10°C at the surface to -2°C at the bottom. Thus, the difference between ice with a surface temperature of -10°C and a non-linear temperature gradient and ice with a surface temperature of -10°C and a linear temperature gradient is 1.6 K. However, already two hours after the change in ice surface temperature, the difference to the ice with a linear temperature gradient is only 0.5 K, and 0.3 K after four hours. On the second day with a surface temperature jump to -30°C, the brightness temperature at the end of the day, when the temperature gradient is almost linear, is 221.9 K, while the brightness temperature of the first temperature profile, when the temperature gradient is highly non-linear, is 228.5 K. The difference thus being 6.6 K, but again the difference reduces to 4.3 K two hours after the surface temperature change, and to 3.1 K after four hours. After more

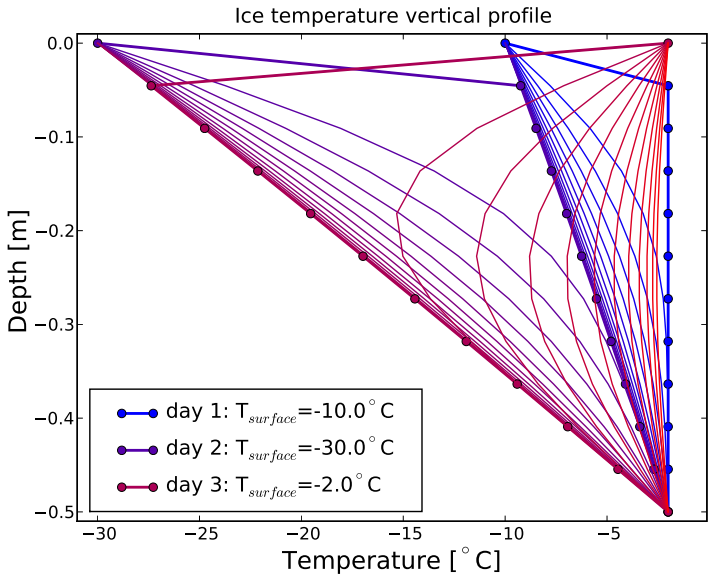

Figure 3.1: Vertical ice temperature profile for a 50 cm thick ice column with simulated abrupt temperature changes of the uppermost surface ice layer, as described in section 3.1.1. The lines with dots show the temperature profiles at the beginning of each day. The remaining lines show the temperature profiles every two hours, gradually changing their color with time from blue at the beginning of day 1, to violet at the beginning of day 2, to magenta at the beginning of day 3, and red at the end of day 3.

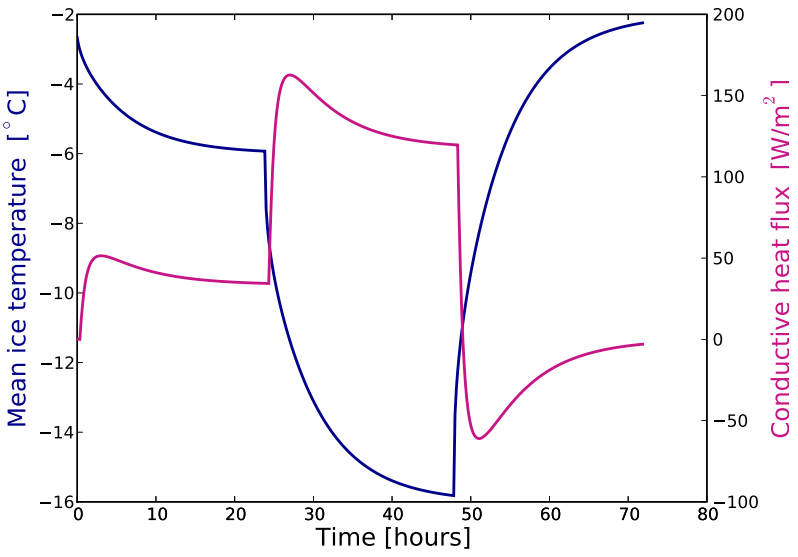

Figure 3.2: Temporal development of the mean ice temperature and the conductive heat flux within a 50 cm thick ice column with simulated abrupt temperature changes of the uppermost surface ice layer, as described in section 3.1.1.

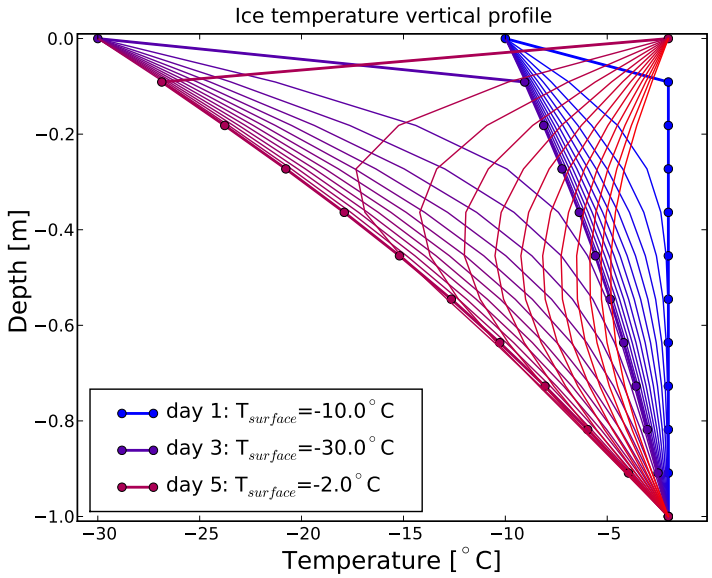

Figure 3.3: Vertical ice temperature profile for a 100 cm thick ice column with simulated abrupt temperature changes of the uppermost surface ice layer, as described in section 3.1.1. The lines with dots show the temperature profiles at the beginning of day 1, 3 and 5. The remaining lines show the temperature profiles every four hours, gradually changing their color with time from blue at the beginning of day 1, to violet at the beginning of day 3, to magenta at the beginning of day 5, and finally to red at the end of day 6.

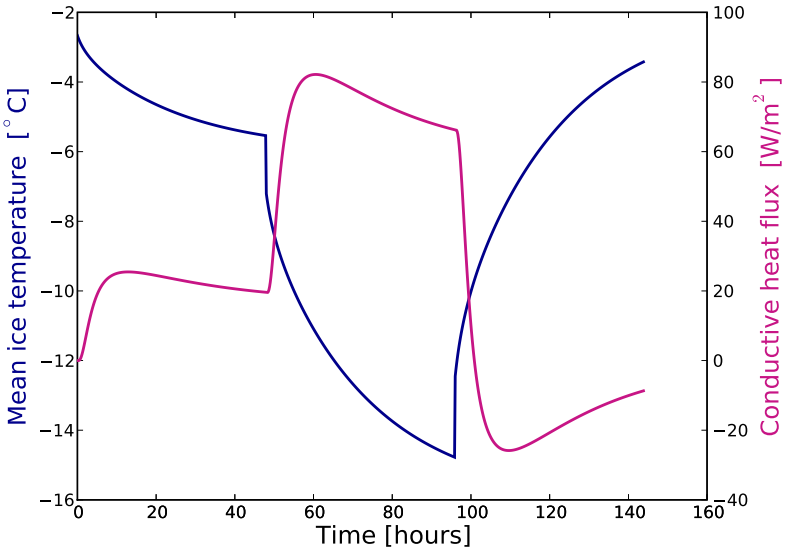

Figure 3.4: Temporal development of the mean ice temperature and the conductive heat flux within a 100 cm thick ice column with simulated abrupt temperature changes of the uppermost surface ice layer, as described in section 3.1.1.

than about eight hours, the brightness temperature difference is less than 0.5 K. For the last day, when the surface temperature abruptly increases back to -2°C, the brightness temperature of ice with a linear temperature gradient is 232.1 K, as compared to 225.3 K for the non-linear temperature gradient in the ice at the beginning of the day. The corresponding difference in the brightness temperature is 6.8 K, and 2.9 K two hours after the ice surface temperature has changed, and 1.3 K after four hours.

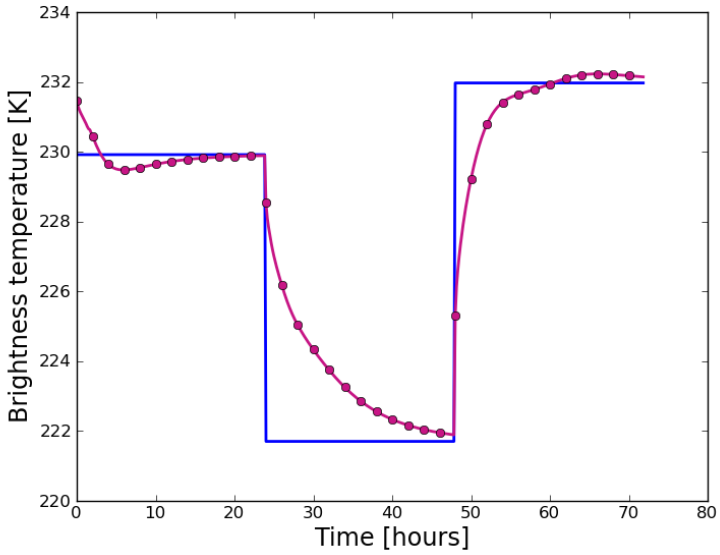

Figure 3.5: Brightness temperature at nadir view for the ice temperature profiles as calculated for Figure 3.1 (pink) and as calculated for an assumed linear temperature gradient between the temperature at the surface and at the bottom of the ice column (blue). The given brightness temperatures are simulated with the coherent Ulaby model and represent the average values for one oscillation around an ice thickness of 50 cm. The dots indicate the brightness temperature every two hours.

3.1.2 Bulk ice temperature vs. temperature gradient

In the previous section, we investigated under which conditions a linear temperature gradient within ice is a reasonable assumption. Here, we investigate how the assumption of a bulk ice temperature impacts the modelled brightness temperature as compared to a model that contains multiple layers and a temperature gradient within ice.

Multiple layers in the Burke model

As a first test of the incoherent Burke model with multiple ice layers, we assume a constant temperature for the entire ice column and gradually increase the number of layers within the ice from 1 to 100. For these isothermal conditions, we expect the brightness temperature as a function of ice thickness to be independent of the number of layers. For the coherent Ulaby model, this expected behaviour is confirmed (not

shown here). However, for the incoherent Burke model, we find that the modelled brightness temperature decreases considerably with an increasing number of ice layers (Figure 3.6). The largest difference occurs when moving from the consideration of one ice layer to the consideration of two ice layers. The more layers we add, the less any additional ice layer impacts the brightness temperature. Thus, the brightness temperature curves for 20 and 100 layers are almost identical.

Multiple layers in the Ulaby model

For the test case of an isothermal temperature profile in ice, brightness temperatures as modelled with the coherent Ulaby model are independent of the number of layers in ice (not shown here). Due to the Burke model's dependence on the number of considered layers in ice, we use the coherent Ulaby model to estimate the error that is introduced to the brightness temperature simulation by considering only one ice layer with a bulk ice temperature instead of multiple ice layers with a temperature gradient in the ice. The example case for typical Arctic first-year ice conditions shows that the brightness temperatures for the model with one ice layer are somewhat lower than for the model with multiple layers (Figure 3.7). When averaged over the ice thickness range considered here, the mean brightness temperature for one ice layer is 224.9 K, whereas the mean brightness temperature for 100 layers in the ice is 229.7 K.

We hypothesise, that one reason for the difference between the model with one ice layer and a bulk ice temperature and the model with multiple ice layers and a linear temperature gradient is the following. Ice permittivity in our models is a function of brine volume fraction (Vant et al., 1978), which is a non-linear function of ice temperature and ice salinity (Cox and Weeks, 1983). If only one ice layer is considered, the model's input value for ice temperature is the average value of the ice surface temperature and the ice bottom temperature (= the water freezing temperature). However, due to the non-linear relation between permittivity and ice temperature, the permittivity associated with the average ice temperature is not equal to the average value of the permittivity profile associated with the ice temperature profile (Figure 3.8). A possible approach to deal with this non-linearity could be to use the average permittivity of the permittivity profile as input to the radiation model, instead of the permittivity associated with the average ice temperature. However, ice emissivity is a non-linear function of ice permittivity, and the ice emissivity of the average ice permittivity is not equal to the ice emissivity associated with the ice permittivity profile. Thus, because it would be convenient to apply only the model with one ice layer for the retrieval of ice thickness, we here try to find one representative value for the ice permittivity. Because the ice permittivity in the coherent Ulaby model mainly occurs within the exponential function, we here take the logarithm of the average value of the exponentiated ice permittivity as value for the ice permittivity. We find that the effectivity of this procedure depends on ice temperature (Figure 3.9). For an ice surface temperature of T_{surf}= -5°C, the model with one ice layer and the new ice permittivity value is not very representative for the brightness temperatures of the model with 100 ice layers, whereas for an ice surface temperature of T_{surf}= -15°C, the model with one ice layer and the new ice permittivity value represents better the brightness temperature curve of the time-consuming model with 100 ice layers.

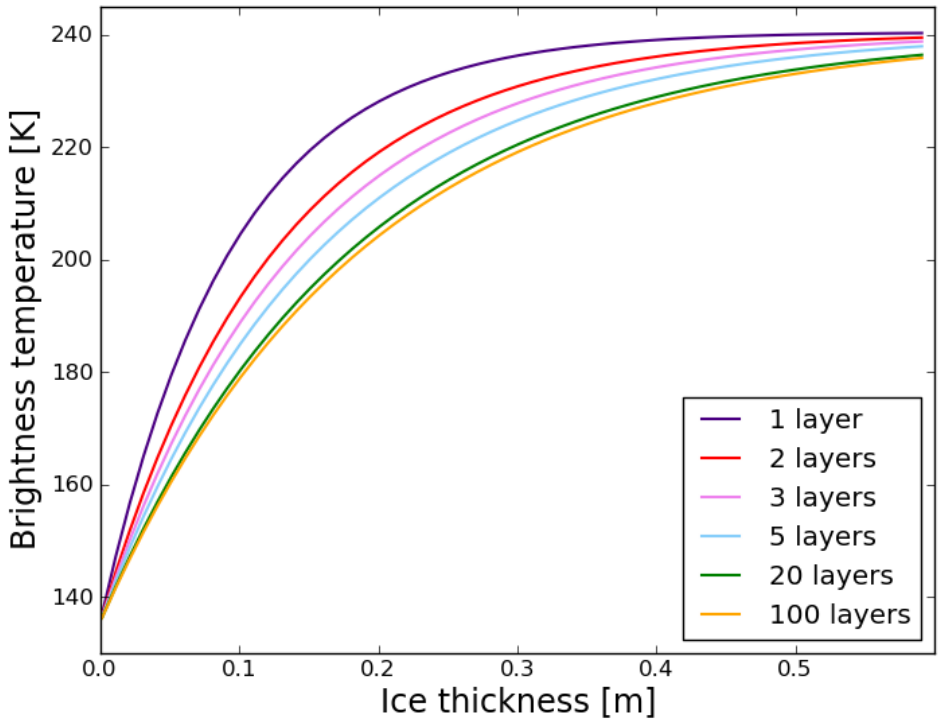

Figure 3.6: Nadir brightness temperature as a function of ice thickness as simulated with the incoherent Burke model for typical Arctic conditions (S_{water}= 30 g/kg, S_{ice}= 8 g/kg, T_{water}= -1.8°C, $T_{surface}$= -10°C). The temperature within ice is assumed to be constant for the whole ice column, i.e. the ice temperature is equal to the ice surface temperature for all ice layers. The colors indicate the number of ice layers used in the model.

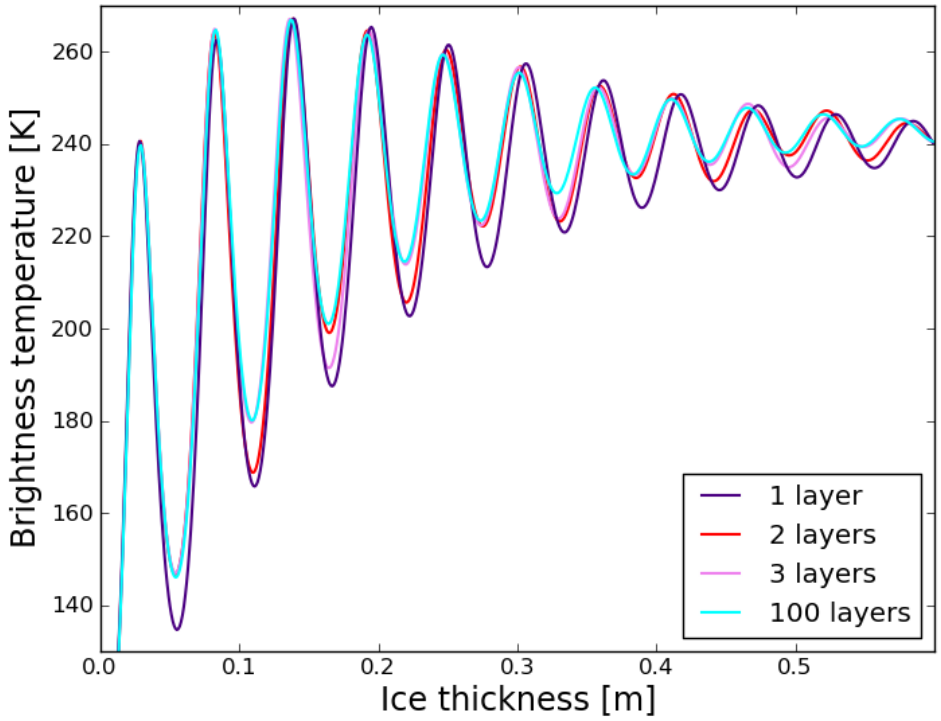

Figure 3.7: Nadir brightness temperature as a function of ice thickness as simulated with the coherent Ulaby model for typical Arctic conditions (S_{water}= 30 g/kg, S_{ice}= 8 g/kg, T_{water}= -1.8°C, $T_{surface}$= -10°C). The temperature within ice is assumed to increase linearly from the ice surface temperature to the ice bottom temperature, which is at the freezing point of sea water (here: -1.8°C). The colors indicate the number of ice layers used in the model.

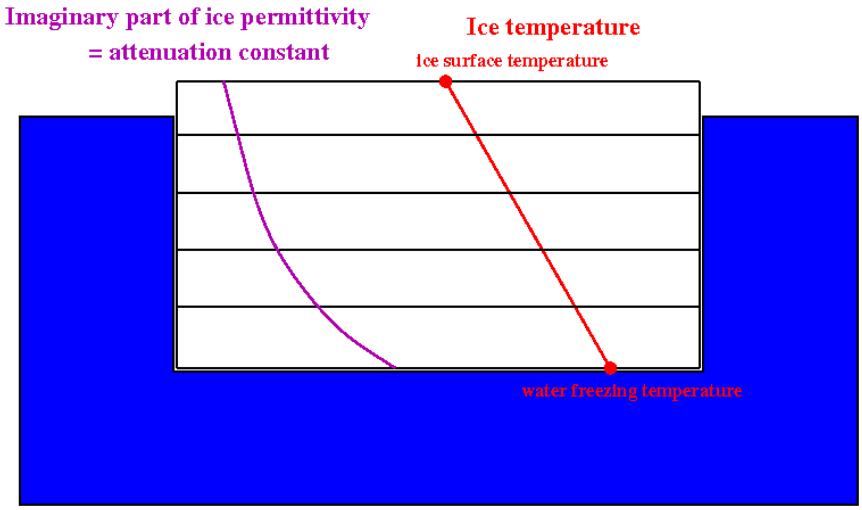

Figure 3.8: Sketch of the ice temperature profile and the related profile of the imaginary part of the ice permittivity (= attenuation constant).

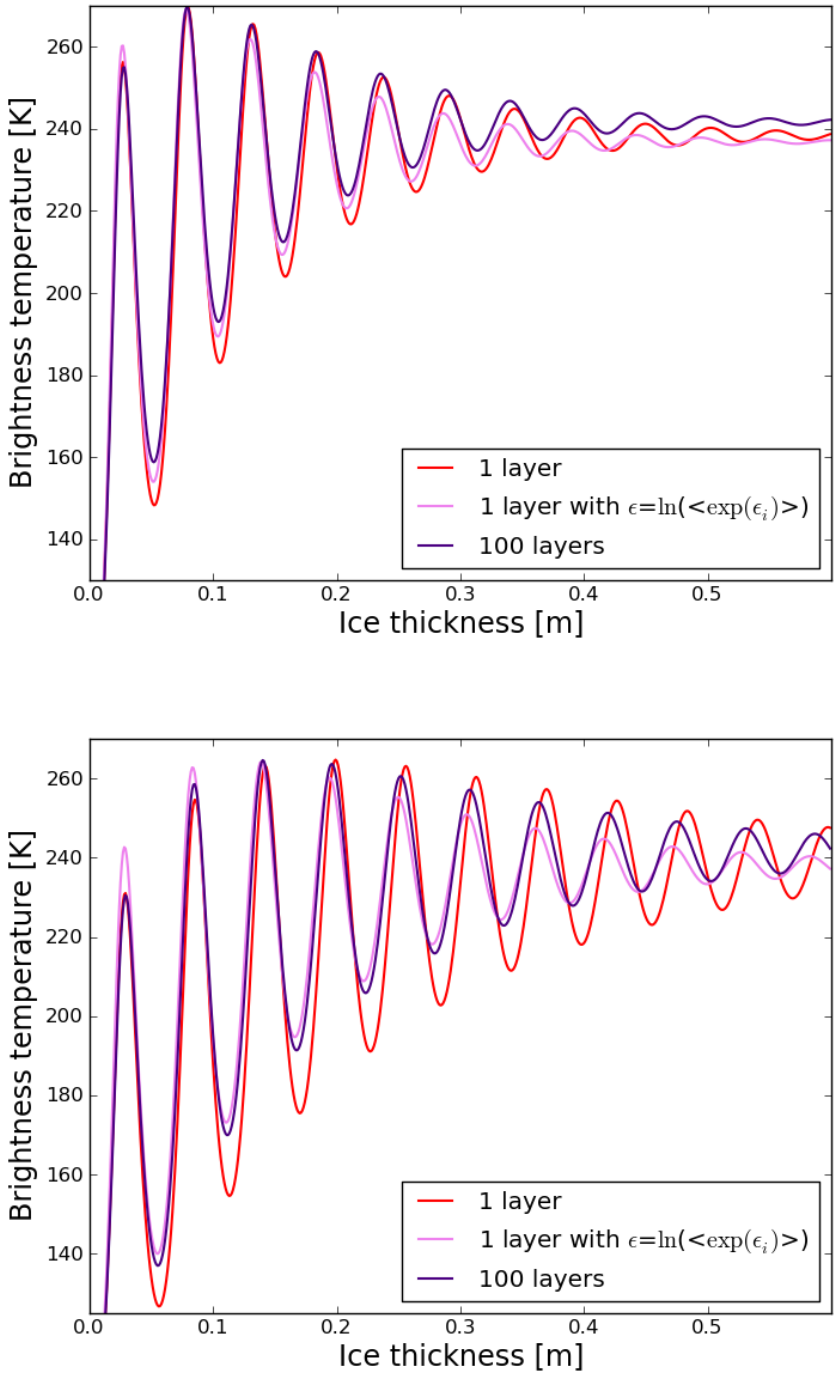

Figure 3.9: Nadir brightness temperature as a function of ice thickness as simulated with the coherent Ulaby model for typical Arctic conditions (S_{water}= 30 g/kg, S_{ice}= 8 g/kg, T_{water}= -1.8°C). The upper figure shows the results for T_{surf}= -5°C, the lower figure for T_{surf}= -15°C. Temperature within ice is assumed to increase linearly from the ice surface temperature to the ice bottom temperature, which is at the freezing point of sea water (here: -1.8°C). The red and the violet lines show the results for 1 and 100 ice layers, respectively. The pink line shows the result that is obtained, when the one-ice-layer-model is applied with a representative value for the ice permittivity (as described in section 3.1.2).

3.1.3 Sensitivity to bulk ice temperature

Here, we investigate how the bulk ice temperature and its variability impact brightness temperature simulations. We use the incoherent Burke model with one ice layer. The calculations are performed for four different ice thicknesses and three incidence angles. For ice and water salinities, we choose typical values for Arctic and for Baltic conditions. For the Arctic, water and bulk ice salinity are set to S_{water}= 30 g/kg and S_{ice}= 8 g/kg, respectively. For the Baltic, water and bulk ice salinity are set to S_{water}= 6 g/kg and S_{ice}= 1 g/kg, respectively. Water is assumed to be at the freezing point, i.e. T_{water}= -1.8°C for Arctic and T_{water}= -0.3°C for Baltic conditions, respectively. Bulk ice temperature is assumed to be the average value of the ice surface temperature and the water temperature.

Brightness temperature derivative with respect to ice temperature
First, we describe brightness temperature TB as a function of ice surface temperature T_{surf} (Figures 3.10 and 3.14). We then numerically differentiate the brightness temperature function with respect to ice surface temperature (Figures 3.11 and 3.15). The derivative $\frac{\partial TB}{\partial T_{surf}}$ is also a function of ice surface temperature and describes the change of the observed brightness temperature with a changing ice surface temperature. For $\frac{\partial TB}{\partial T_{surf}} > 0$, brightness temperatures increase with increasing ice temperature, whereas they decrease with increasing ice temperature for $\frac{\partial TB}{\partial T_{surf}} < 0$. The derivative $\frac{\partial TB}{\partial T_{surf}}$ can be used to estimate the error of the brightness temperature simulation caused by the uncertainty of the ice surface temperature estimation.
According to our model, brightness temperatures increase with increasing ice temperatures for cold conditions until a reversal point is reached, where $\frac{\partial TB}{\partial T_{surf}} = 0$. For ice temperatures higher than this reversal point, brightness temperatures decrease with further increasing ice temperatures. The ice temperature of this reversal point depends on ice thickness. For thinner ice, the reversal occurs at higher temperatures than for thicker ice. For thin ice, brightness temperatures increase with increasing ice temperature, except for very high ice temperatures. For thick ice, brightness temperatures increase only slightly with ice temperature for ice surface temperatures below -10°C, start to decrease with ice temperature for ice surface temperatures above -10°C, and decrease more strongly for warm temperatures. With thin or thick ice we here refer to ice that is thin or thick compared to the maximum retrievable ice thickness, which is about 50 cm for Arctic conditions and about 1 m for Baltic conditions.

Brightness temperature derivative with respect to ice thickness
When we differentiate the brightness temperature function with respect to ice thickness (Figures 3.12 and 3.16), the calculated derivatives $\frac{\partial TB}{\partial d_{ice}}$ clearly show how the potential for retrieving ice thickness from L-band brightness temperatures declines for increasing ice thickness. Furthermore, brightness temperature sensitivity to ice thickness decreases with increasing ice temperature for all ice thicknesses. The only exception is found for thin ice under Baltic conditions (Figures 3.16). In this case, the brightness temperature sensitivity increases with increasing ice temperature up to a surface ice temperature of about -5°C. For further increasing temperature the

sensitivity then reduces rapidly.
The derivative $\frac{\partial TB}{\partial d_{ice}}$ can be used to estimate the ice thickness retrieval's uncertainty for different ice temperature and ice thickness conditions. For example, if radiometric uncertainty is considered to be 2 K, and we require an ice thickness accuracy of 5 cm, we should apply the ice thickness retrieval only in the regime with $\frac{\partial TB}{\partial d_{ice}} > 2$ K/5 cm= 0.4 K/cm. For the Arctic conditions, this requirement is fulfilled for all ice surface temperatures, if the ice is 15 cm thick, and for ice surface temperatures below about -9°C, if the ice is 30 cm thick, for example. For the Baltic conditions, this requirement is fulfilled for ice surface temperatures below about -0.5°C, -3°C, and -10°C, if the ice thickness is 25 cm, 50 cm, and 75 cm, respectively.

Impact of the ice temperature on the retrieval
The derivatives $\frac{\partial TB}{\partial T_{surf}}$ and $\frac{\partial TB}{\partial d_{ice}}$ can be used to estimate the impact of ice temperature variability on the ice thickness retrieval:

$$\frac{\partial d_{ice}}{\partial T_{surf}} = \frac{\partial TB}{\partial T_{surf}} \left(\frac{\partial TB}{\partial d_{ice}} \right)^{-1} \quad . \tag{3.3}$$

For both Arctic and Baltic conditions, the ice thickness retrieval for thin ice is only very slightly affected by ice surface temperature (Figures 3.13 and 3.17). The thicker the ice is, the more the ice thickness retrieval is influenced by ice temperature. The ice thickness retrieval's sensitivity to ice surface temperature has a positive sign for cold conditions, that is we would retrieve too high ice thicknesses, if we assumed too high values for the ice surface temperature. The ice thickness retrieval's sensitivity to ice temperature then increases with increasing ice surface temperature until a reversal point. At this reversal point, $\frac{\partial d_{ice}}{\partial T_{surf}}$ shows a deep drop and reaches very high negative values for further increasing ice temperatures, that is we would retrieve too small ice thicknesses, if we assumed too high values for the ice surface temperature. This reversal point originates from the change of sign for $\frac{\partial TB}{\partial T_{surf}}$ at a certain ice surface temperature. The temperature of this reversal point is at higher temperatures for thinner ice than for thicker ice, and the reversal generally occurs at higher temperatures for the Baltic than for the Arctic ice conditions. For example, for the Arctic conditions at nadir view, the reversal point occurs at T_{surf}= -2.8°C for an ice thickness of 15 cm, and at T_{surf}= -9.6°C for an ice thickness of 60 cm, respectively. Below this reversal point, the ice thickness retrieval's sensitivity to ice temperature is about 1 – 2 cm per 1 K of ice temperature change for ice thicknesses up to 30 cm, about 1 – 3 cm per 1 K of ice temperature change for ice thicknesses of 45 cm, and about 2 – 10 cm per 1 K of ice temperature change for ice thicknesses of 60 cm for the Arctic conditions.
The sensitivity of brightness temperature to ice surface temperature, the sensitivity of brightness temperature to ice thickness, and the sensitivity of the ice thickness retrieval to ice surface temperature are given in the Tables A.2 to A.7 in the appendix. In the Tables, we give the sensitivities for different ice thicknesses and ice surface temperatures for Arctic and Baltic conditions, respectively. The given values are the mean sensitivities for the brightness temperature intensity averaged over incidence angles θ= 0 – 40°. These brightness temperatures are used in the sea ice thickness processing procedure as performed in the framework of the ESA SMOSIce project. The corresponding reversal points are given in the Tables A.14 and A.15 in the appendix.

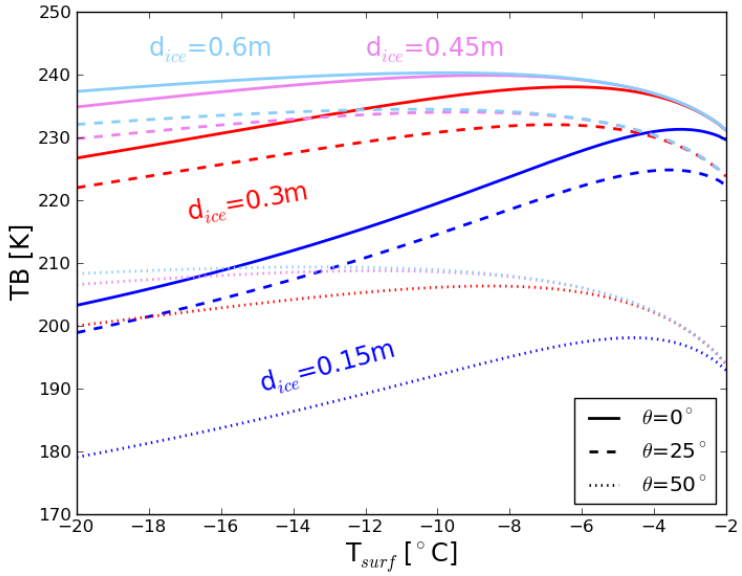

Figure 3.10: Horizontally polarised brightness temperature TB as a function of ice surface temperature T_{surf} according to the incoherent Burke model for one ice layer. The ice is assumed to be at typical Arctic conditions (S_{water}= 30 g/kg, S_{ice}= 8 g/kg, T_{water}= -1.8°C). The four colors indicate the different ice thicknesses, the line styles indicate the incidence angles.

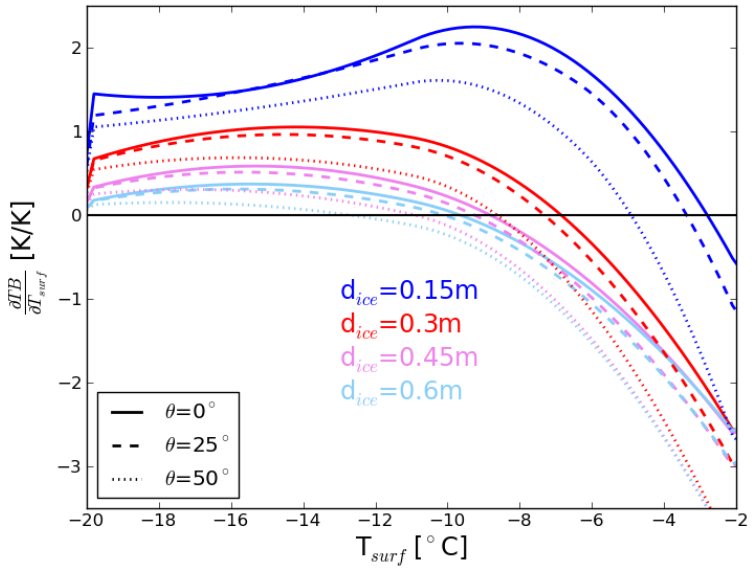

Figure 3.11: Derivative of horizontally polarised brightness temperature TB with respect to ice surface temperature T_{surf} as a function of T_{surf} according to the incoherent Burke model for one ice layer. For the assumed ice conditions and the explanation of the lines see caption of Figure 3.10.

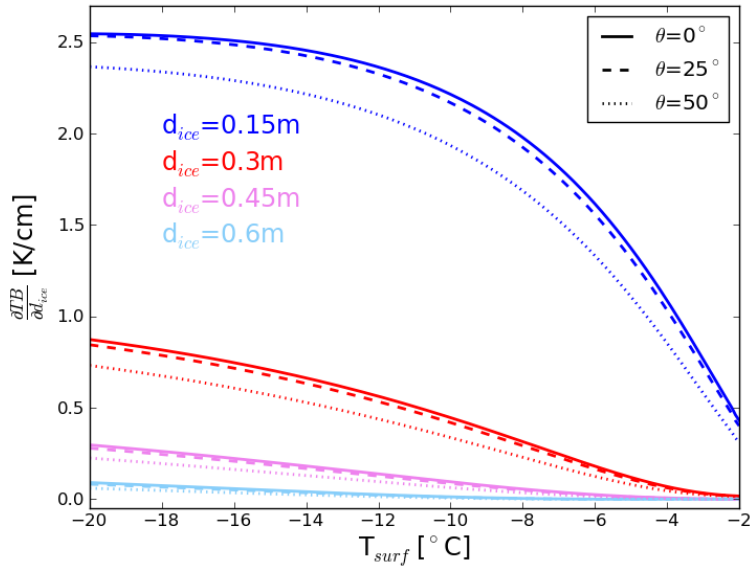

Figure 3.12: Derivative of horizontally polarised brightness temperature TB with respect to ice thickness d_{ice} as a function of ice surface temperature T_{surf} according to the incoherent Burke model for one ice layer. For the assumed ice conditions and the explanation of the lines see caption of Figure 3.10.

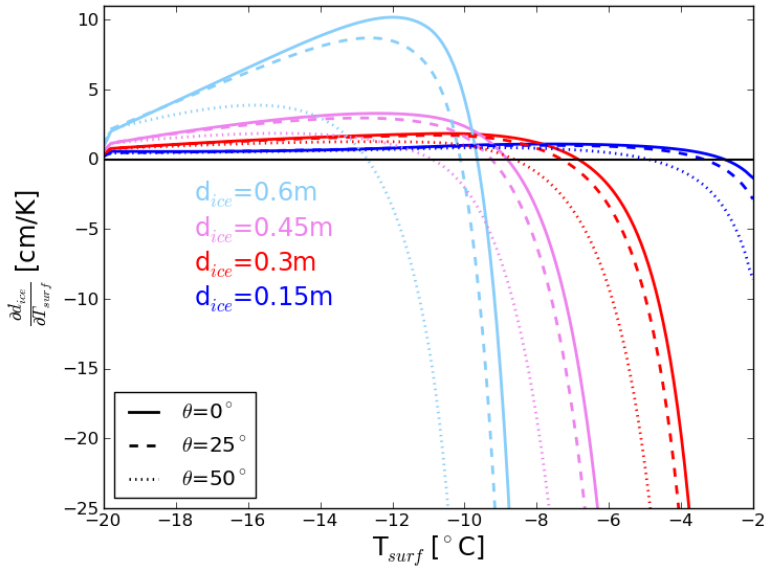

Figure 3.13: Derivative of ice thickness d_{ice} with respect to ice surface temperature T_{surf} as a function of T_{surf}, when the horizontally polarised brightness temperature is described as a function of ice thickness following the incoherent Burke model for one ice layer. For the assumed ice conditions and the explanation of the lines see caption of Figure 3.10.

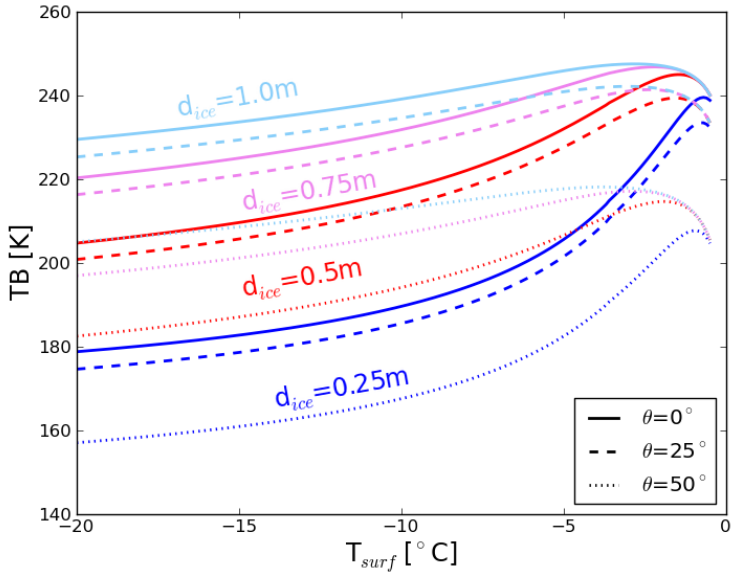

Figure 3.14: Horizontally polarised brightness temperature TB as a function of ice surface temperature T_{surf} according to the incoherent Burke model for one ice layer. The ice is assumed to be at typical Baltic conditions (S_{water}= 6 g/kg, S_{ice}= 1 g/kg, T_{water}= -0.3°C). The four colors indicate the different ice thicknesses, the line styles indicate the incidence angles.

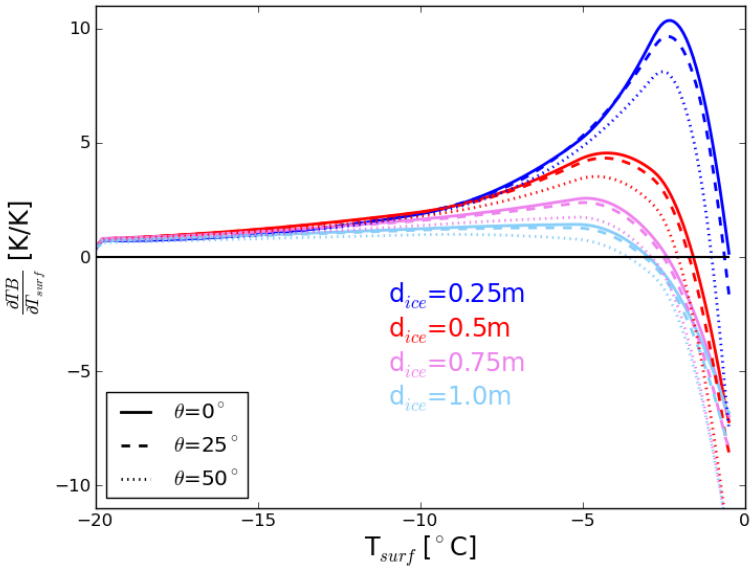

Figure 3.15: Derivative of horizontally polarised brightness temperature TB with respect to ice surface temperature T_{surf} as a function of T_{surf} according to the incoherent Burke model for one ice layer. For the assumed ice conditions and the explanation of the lines see caption of Figure 3.14.

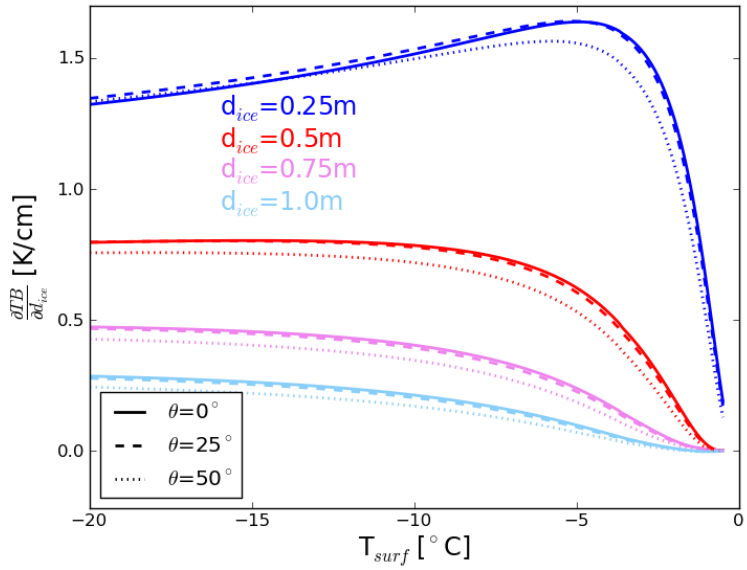

Figure 3.16: Derivative of horizontally polarised brightness temperature TB with respect to ice thickness d_{ice} as a function of ice surface temperature T_{surf} according to the incoherent Burke model for one ice layer. For the assumed ice conditions and the explanation of the lines see caption of Figure 3.14.

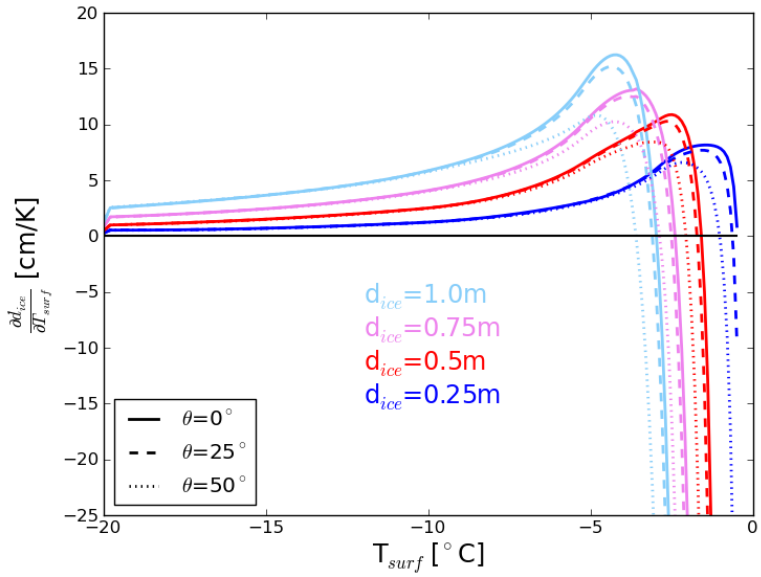

Figure 3.17: Derivative of ice thickness d_{ice} with respect to ice surface temperature T_{surf} as a function of T_{surf}, when the horizontally polarised brightness temperature is described as a function of ice thickness following the incoherent Burke model for one ice layer. For the assumed ice conditions and the explanation of the lines see caption of Figure 3.14.

3.2 Sensitivity to bulk ice salinity

Similarly to the approach for investigating the effect of temperature variability on brightness temperature simulations, we here investigate how ice salinity and its variability impact brightness temperature simulations. We again use the incoherent Burke model with one ice layer. As for the analysis of temperature sensitivity, the calculations are performed for four different ice thicknesses and three incidence angles. For Arctic conditions water salinity is assumed to be S_{water}= 30 g/kg, and the bulk ice temperature is assumed to be T_{ice}= -7°C; for Baltic conditions we assume S_{water}= 6 g/kg and T_{ice}= -3°C. Water is assumed to be at the freezing point, i.e. T_{water}= -1.8°C for Arctic and T_{water}= -0.3°C for Baltic conditions, respectively.

Brightness temperature derivative with respect to ice salinity
First, we describe brightness temperature as a function of ice salinity (Figure 3.18 and 3.22). We then numerically differentiate the brightness temperature function with respect to ice salinity (Figure 3.19 and 3.23). The derivative $\frac{\partial TB}{\partial S_{ice}}$ is also a function of ice salinity and describes the change of the observed brightness temperature with a changing salinity. For $\frac{\partial TB}{\partial S_{ice}} > 0$, brightness temperatures increase with increasing ice salinity, whereas they decrease with increasing ice salinity for $\frac{\partial TB}{\partial S_{ice}} < 0$. The derivative $\frac{\partial TB}{\partial S_{ice}}$ can be used to estimate the error of the brightness temperature simulation caused by the uncertainty of the ice salinity estimation.
According to our model, under Arctic conditions the brightness temperature for ice salinities $S_{ice} > 5$ g/kg and ice thicknesses $d_{ice} \geq 45$ cm is only very slightly sensitive to ice salinity changes; for thinner ice, the sensitivity is somewhat higher. In contrast, brightness temperature sensitivity to ice salinity is very high for all ice thicknesses, if ice salinity is low. For the Arctic conditions and ice salinities $S_{ice} < 5$ g/kg, brightness temperatures vary by up to more than 20 K for ice salinity variations of 1 g/kg. However, ice salinities $S_{ice} < 5$ g/kg are seldom found in Arctic sea ice with ice thicknesses below 60 cm, which are the retrievable thicknesses. According to an empirical relationship between ice salinity and ice thickness in the Arctic (Cox and Weeks, 1974), sea ice with a thickness ranging from 15 cm to 60 cm has typically ice salinities ranging from S_{ice}= 11.3 g/kg to S_{ice}= 6.9 g/kg.
Compared to the Arctic conditions, brightness temperatures under the Baltic conditions are even more sensitive to ice salinity for low ice salinities. For an ice salinity S_{ice}= 1 g/kg, which is a value often used for Baltic applications, an ice salinity variation of 1 g/kg causes a brightness temperature variation of about 8 K for an ice thickness d_{ice}= 100 cm, and even 26 K for an ice thickness d_{ice}= 25 cm.

Brightness temperature derivative with respect to ice thickness
When we differentiate the brightness temperature function with respect to ice thickness (Figure 3.20 and 3.24), the calculated derivatives $\frac{\partial TB}{\partial d_{ice}}$ again clearly show how the potential for retrieving ice thickness from L-band brightness temperatures declines with increasing ice thickness. The brightness temperature's sensitivity to ice thickness first increases with increasing salinity, reaches a maximum value, and then decreases with further increasing ice salinity. The salinity value associated with the maximum sensitivity to ice thickness depends on ice thickness and ranges from S_{ice}= 0 g/kg for

d_{ice}= 60 cm to S_{ice}= 4.5 g/kg for d_{ice}= 15 cm under Arctic conditions, and from S_{ice}= 0 g/kg for d_{ice}= 100 cm to S_{ice}= 1 g/kg for d_{ice}= 25 cm under Baltic conditions.
The derivative $\frac{\partial TB}{\partial d_{ice}}$ can also be used to estimate the ice thickness retrieval's uncertainty for different ice salinity and ice thickness conditions. For example, if the radiometric uncertainty is assumed to be 2 K, and we require an ice thickness accuracy of 5 cm, we should consider the ice thickness retrieval only in the regime with $\frac{\partial TB}{\partial d_{ice}} > 2$ K/5 cm= 0.4 K/cm. For the Arctic conditions, this requirement is fulfilled for all ice salinities considered here, if the ice is 15 cm thick, and for ice salinities below about 9 g/kg, if the ice is 30 cm thick, for example. For the Baltic conditions, this requirement is fulfilled for all ice salinities considered here, if the ice is 25 cm thick and for ice salinities $S_{ice} < 2$ g/kg, if the ice is 50 cm thick, for example.

Impact of ice salinity on the retrieval
The derivatives $\frac{\partial TB}{\partial S_{ice}}$ and $\frac{\partial TB}{\partial d_{ice}}$ can be used to estimate the impact of ice salinity variability on the ice thickness retrieval:

$$\frac{\partial d_{ice}}{\partial S_{ice}} = \frac{\partial TB}{\partial S_{ice}} \left(\frac{\partial TB}{\partial d_{ice}} \right)^{-1} \quad . \tag{3.4}$$

For the Arctic conditions, the ice thickness retrieval for thin ice (d_{ice}= 15 cm) is only slightly affected by ice salinity (Figure 3.21).
Based on the empirical relationship between ice salinity and ice thickness (Cox and Weeks, 1974), we can state the following for Arctic conditions. For the range of salinities that is generally associated with a certain ice thickness, the sensitivity of the retrieved ice thickness is always below 10 cm thickness variation per ice salinity variation of 1 g/kg. For example, according to the empirical relationship, ice with a thickness of d_{ice}= 45 cm has an ice salinity of roughly S_{ice}= 7 g/kg. Our sensitivity study predicts $\left| \frac{\partial d_{ice}}{\partial S_{ice}} \right| < 10 \ \frac{\text{cm}}{\text{g/kg}}$ to be valid for d_{ice}= 45 cm, if the salinity is 3 g/kg< S_{ice} < 12 g/kg. Thus, this statement is true for our example of ice with a thickness of d_{ice}= 45 cm. Accordingly, the statement $\left| \frac{\partial d_{ice}}{\partial S_{ice}} \right| < 10 \ \frac{\text{cm}}{\text{g/kg}}$ is valid for the ice thicknesses considered here, if we assume that the corresponding ice salinities are close to the ice salinities related to the considered ice thickness via the empirical relationship by Cox and Weeks (1974). For typical Arctic conditions, an ice salinity change of 1 g/kg mostly has the same impact on brightness temperature as an ice thickness change of 0.5 – 6 cm, depending on the ice thickness. For the Baltic conditions, the ice thickness retrieval's sensitivity to ice salinity is considerably higher.
As for the sensitivity to ice temperature in section 3.1.3, we give the sensitivities of brightness temperature and of the ice thickness retrieval to ice salinity, as well as the corresponding reversal points in the Tables A.8 to A.13, and in the Tables A.16 and A.17 in the appendix, respectively.

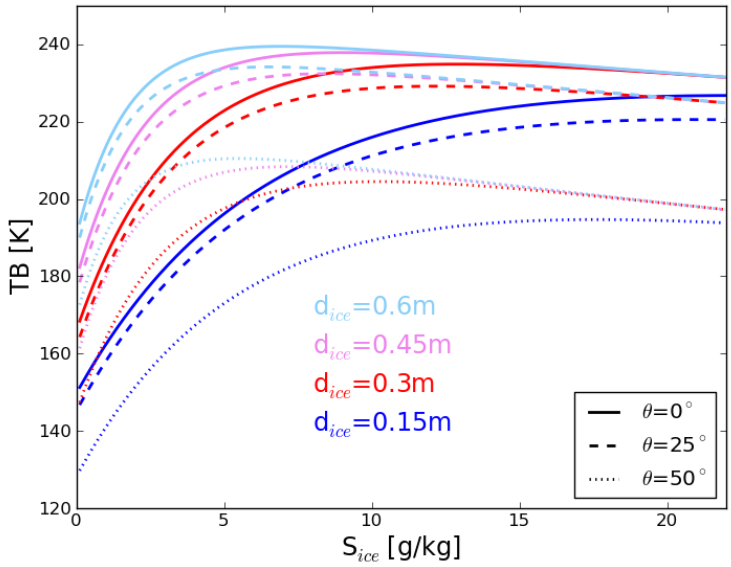

Figure 3.18: Horizontally polarised brightness temperature TB as a function of ice salinity S_{ice} according to the Burke model for one ice layer. The ice is assumed to be at typical Arctic conditions (S_{water}= 30 g/kg, $T_{surface}$= -15°C, T_{water}= -1.8°C). The four colors indicate the different ice thicknesses, the line styles indicate the incidence angles.

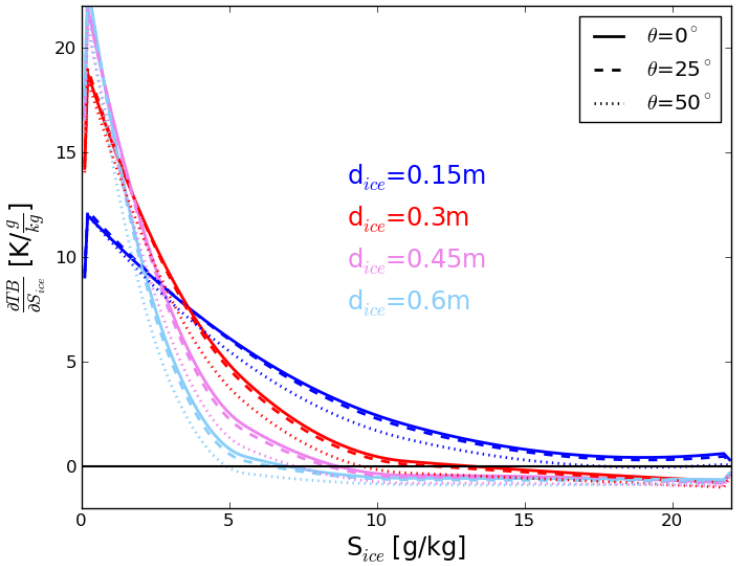

Figure 3.19: Derivative of horizontally polarised brightness temperature TB with respect to ice salinity S_{ice} as a function of S_{ice} according to the Burke model for one ice layer. For the assumed ice conditions and the explanation of the lines see caption of Figure 3.18.

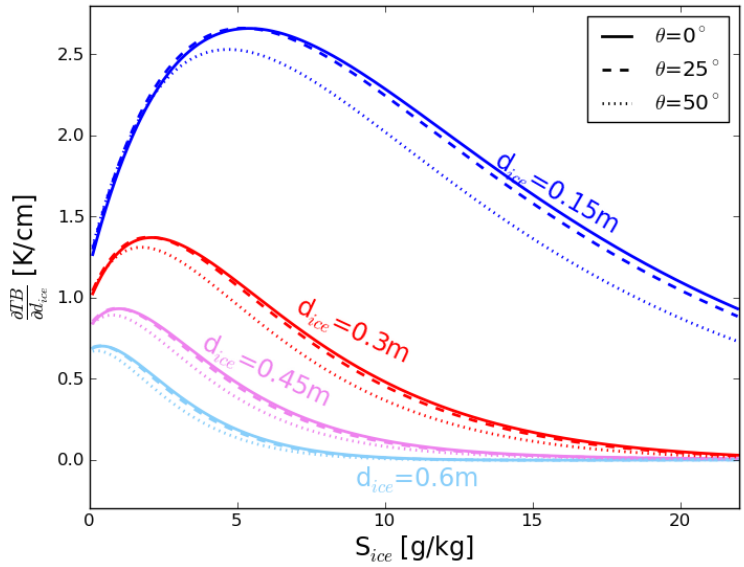

Figure 3.20: Derivative of horizontally polarised brightness temperature TB with respect to ice thickness d_{ice} as a function of ice salinity S_{ice} according to the Burke model for one ice layer. For the assumed ice conditions and the explanation of the lines see caption of Figure 3.18.

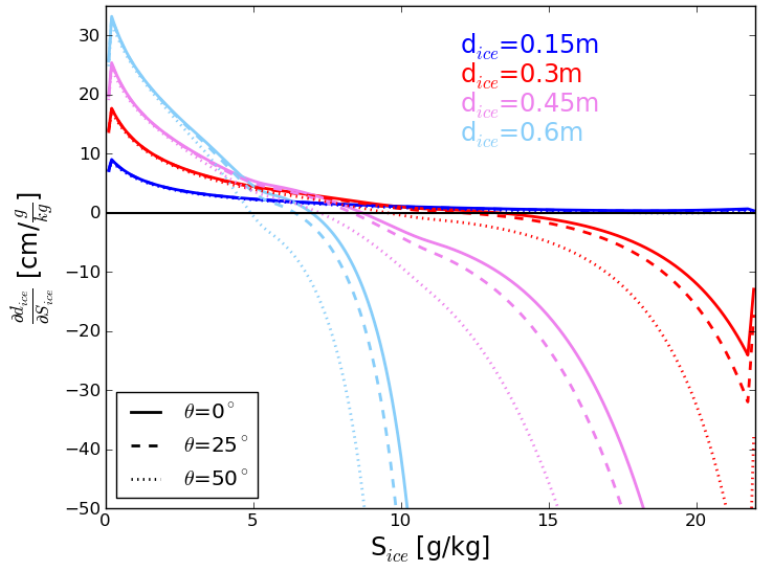

Figure 3.21: Derivative of ice thickness d_{ice} with respect to ice salinity S_{ice} as a function of S_{ice}, when the horizontally polarised brightness temperature is described as a function of ice thickness following the Burke model for one ice layer. For the assumed ice conditions and the explanation of the lines see caption of Figure 3.18.

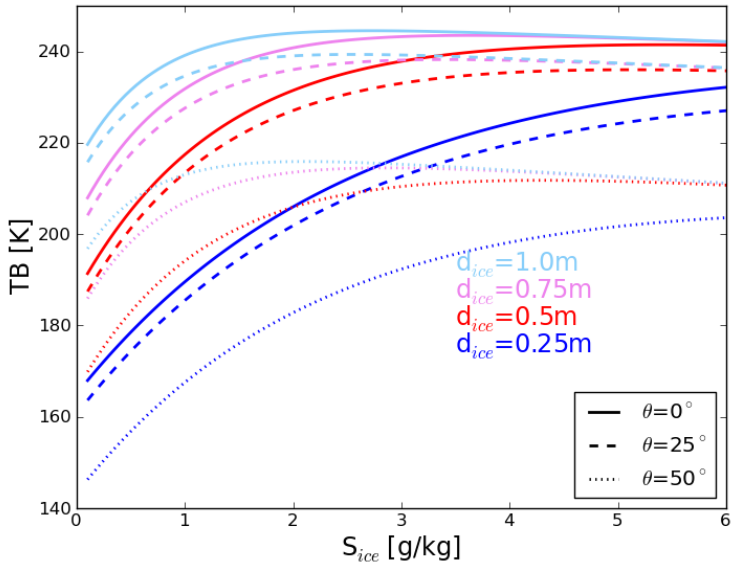

Figure 3.22: Horizontally polarised brightness temperature TB as a function of ice salinity S_{ice} according to the Burke model for one ice layer. The ice is assumed to be at typical Baltic conditions (S_{water}= 6 g/kg, $T_{surface}$= -10°C, T_{water}= -0.3°C). The four colors indicate the different ice thicknesses, the line styles indicate the incidence angles.

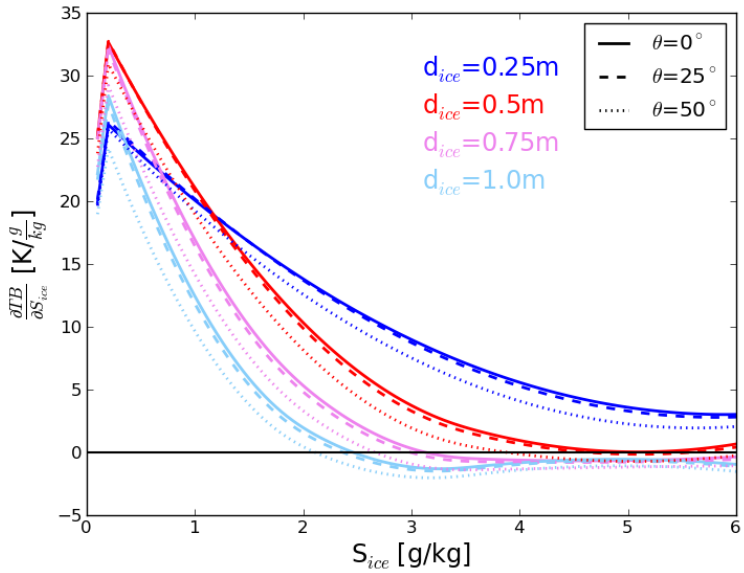

Figure 3.23: Derivative of horizontally polarised brightness temperature TB with respect to ice salinity S_{ice} as a function of S_{ice} according to the Burke model for one ice layer. For the assumed ice conditions and the explanation of the lines see caption of Figure 3.22.

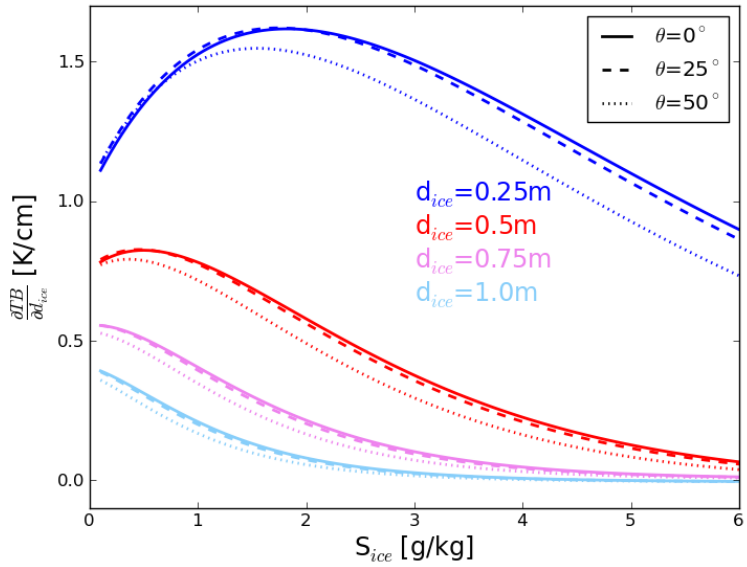

Figure 3.24: Derivative of horizontally polarised brightness temperature TB with respect to ice thickness d_{ice} as a function of ice salinity S_{ice} according to the Burke model for one ice layer. For the assumed ice conditions and the explanation of the lines see caption of Figure 3.22.

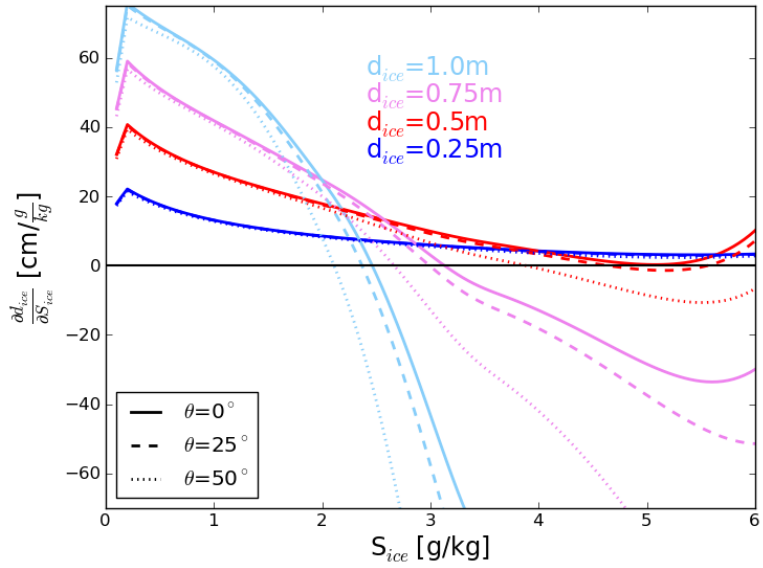

Figure 3.25: Derivative of ice thickness d_{ice} with respect to ice salinity S_{ice} as a function of S_{ice}, when the horizontally polarised brightness temperature is described as a function of ice thickness following the Burke model for one ice layer. For the assumed ice conditions and the explanation of the lines see caption of Figure 3.22.

3.3 Comparison of the impact by ice temperature, salinity, and thickness

Here, we consider an example case of freezing sea ice in the Laptev Sea to investigate how observed SMOS brightness temperature changes are related to estimated changes of ice temperature, salinity, and thickness. Thus, we aim to compare the contributions of these three ice parameters to the brightness temperature under realistic conditions.

Freezing sea ice in the Laptev Sea

We examine sea ice that is forming and gradually growing in October and November, 2010 in the Laptev Sea. We here consider the SMOS grid point at 77.5°N and 137.5°E, which is the grid point analysed in Kaleschke et al. (2012). They estimate the variability of the ice parameters that influence the observed brightness temperatures from the surface air temperature time series from NCEP reanalysis data (Kalnay et al., 1996) and from ice concentration data from AMSR-E observations (Cavalieri et al., 2004). The ice concentration time series indicates that the considered area is ice-free until the 20th October, and that on the 20th October ice is formed, and that the ice cover is almost closed after two days and stays closed for the following weeks. Kaleschke et al. (2012) use the Lebedev sea ice thickness parameterisation to estimate ice thickness from observed surface air temperatures (Maykut, 1986). The Lebedev parameterisation of sea ice thickness is based on cumulative freezing degree days: d_{ice}= $1.33\Theta^{0.58}$ [cm], where $\Theta = \int (T_f - T_a)dt$ are the cumulative freezing degree days, and T_a and T_f are the surface air temperature and the freezing point of sea water (here: T_f= -1.9 °C), respectively. For the examined case, the Lebedev parameterisation describes the sea ice growth reasonably; the ice thicknesses calculated from the freezing degree days and the ice thicknesses as retrieved from SMOS agree well (Kaleschke et al., 2012).

Here, we consider the situation in the Laptev Sea from 22nd October to 15th November, 2010, because this is the main ice growth period. According to the Lebedev parameterisation, the ice thickness increases from 0 to about 34 cm during this time period. In order to estimate the ice salinity variability associated with this ice thickness increase, we use an empirical relationship between ice salinity and ice thickness for Arctic first-year ice (Cox and Weeks, 1974). The ice salinities that correspond to the estimated ice thickness range of 0 – 34 cm are between 14.2 and 7.6 g/kg. Assuming that the ice temperature is the average value of the air surface temperature and the water temperature at freezing point, we estimate the variability of ice temperature from NCEP reanalysis data. The ice temperature for the considered time period from 22nd October to 15th November takes values between -12.4 and -2.4°C.

Variability of the intensity

Ice thickness in Kaleschke et al. (2012) is retrieved using an approach for the radiation model that is based on Menashi et al. (1993). Thus, we here also use the incoherent radiation model based on Menashi et al. (1993) to simulate how the variability of ice thickness, ice temperature, and ice salinity impact brightness temperature (Figure 3.26). As the ice thickness increases from 0 to 34 cm, the brightness temperature

increases by 143 K, whereas the brightness temperature increases only by 31 K for the ice temperature increasing from -12.4 to -2.4°C, and by 16 K for the ice salinity increasing from 7.6 to 14.2 g/kg. The brightness temperature change caused by the variability of the temperature corresponds to about 21%, and the brightness temperature change caused by the variability of salinity corresponds to about 11% of the brightness temperature change associated with the variability of ice thickness. Hence, according to the radiation model, the ice thickness change is the main contributor to the temporal development of the brightness temperature signal.

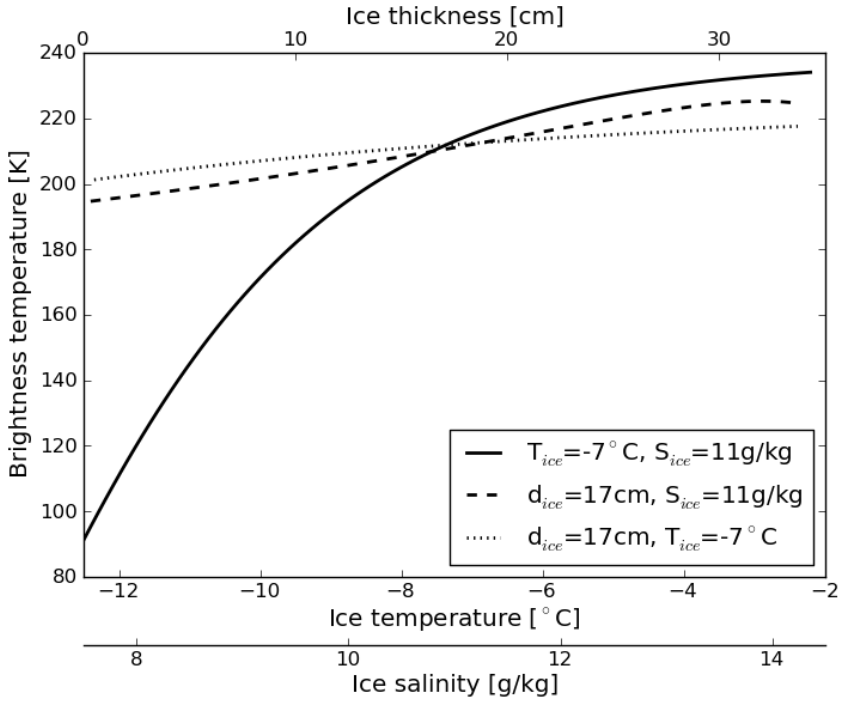

Figure 3.26: Change of brightness temperature intensity at an incidence angle θ= 30° as a function of ice thickness, bulk ice temperature, and bulk ice salinity simulated with the radiation model for one ice layer based on Menashi et al. (1993). In each case, two parameters are kept constant at an average value (see figure legend), while the remaining third parameter varies within the estimated range of values (see x-axis) for the situation in the Laptev Sea during 22nd October and 15th November, 2010.

Variability of the polarisation difference

There are attempts to retrieve ice thickness from SMOS brightness temperatures using the polarisation difference $TB_V - TB_H$ (Heygster et al., 2012). Thus, we here perform the above described analysis also for the polarisation difference at an incidence angle θ= 30° (Figure 3.27). As the ice thickness increases from 0 to 4 cm, the polarisation difference first increases and then decreases with a further increasing ice thickness from 4 to 34 cm. Thus, the polarisation difference between about 0 and 10 cm ice thickness is not a unique function of ice thickness. The overall variability of the polarisation difference related to the change of ice thickness is 4.8 K, whereas the variabilities related to the ice temperature and salinity changes are about 3.6 K and 0.8 K, respectively. Thus, the brightness temperature changes

caused by the variabilities of temperature and salinity correspond to about 74% and 16% of the brightness temperature change caused by the variability of ice thickness. The polarisation difference is hence considerably more affected by ice temperature variations than the intensity.

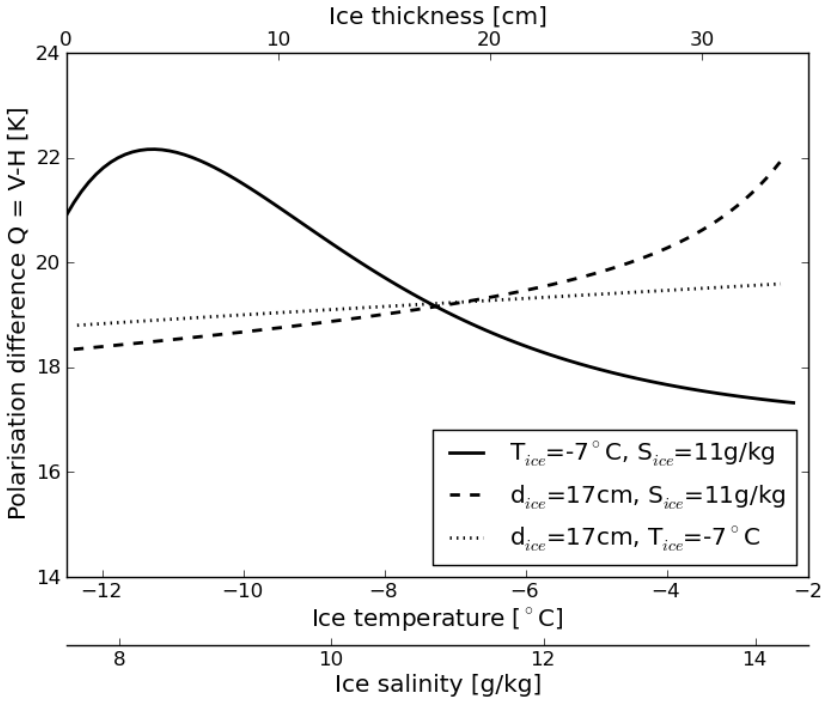

Figure 3.27: Change of brightness temperature polarisation difference at an incidence angle θ= 30° as a function of ice thickness, bulk ice temperature, and bulk ice salinity simulated with the incoherent Menashi model with one ice layer. In each case, two parameters are kept constant at an average value (see figure legend), while the remaining third parameter varies within the estimated range of values (see x-axis) for the situation in the Laptev Sea during 22nd October and 15th November, 2010.

3.4 Summary and Discussion

In this chapter, we investigated the impact of ice temperature and ice salinity on simulated brightness temperatures and on the ice thickness retrieval from L-band brightness temperatures. First, we assessed whether the temperature gradient within ice can be assumed to be linear for our ice thickness retrieval purposes. We investigated how the brightness temperature simulations for one ice layer and a bulk ice temperature compare with the brightness temperature simulations for multiple layers in the ice and a temperature gradient. We calculated the sensitivities of brightness temperature to ice temperature and ice salinity and their impact on the retrieval of ice thickness. Finally, we compared the impact of ice temperature and ice salinity on brightness temperature with the impact of ice thickness using an example case of freezing sea ice in the Laptev Sea.

Conditions for a linear temperature gradient
We used a simple heat conduction model and simulated temperature changes at the ice surface. The surface temperature took values between -2 and -30°. We found that even for sudden large changes of the ice surface temperature, the temperature distribution within ice adjusted to the new situation within a time scale of hours for ice thicknesses of 50 cm and 1 m. Sudden large changes of the ice surface temperature caused temperature gradients in ice to be highly non-linear. The brightness temperatures over 50 cm thick ice with such non-linear temperature gradients differed by up to 6.8 K from the corresponding brightness temperatures over linear temperature gradients, if the ice surface temperature was assumed to be equal in both cases. However, according to our simple heat conduction model, ice temperatures within the 50 cm thick ice adjusted quite quickly to the new temperature conditions. Two hours after the surface temperature change, brightness temperature differences were below 4.3 K, and two more hours later below 3.1 K for all cases considered here. After more than about eight hours, brightness temperature differences were less than 0.5 K.
These results reflect maximum deviations, because the ice considered here is 50 cm thick, and thus represents the maximum retrievable ice thickness for Arctic conditions; for thinner ice a linear temperature gradient would be achieved even more rapidly after changes of the ice surface temperature. Furthermore, the temperature changes considered here were quite large and are probably less pronounced in most cases observed in nature, particularly for ice covered by an insulating snow layer.
For an ice column of 50 cm thickness, the temperature gradient within ice can reasonably well be assumed to be linear for our purposes, because the time the ice temperature needs to adjust to changing conditions at the surface is in the same order of magnitude as the expected temporal deviation between SMOS measurements and possibly available surface temperature information.

Bulk ice temperature vs. linear temperature gradient
As a first test, we simulated brightness temperatures for an increasing number of layers within an isothermal ice column. For a constant ice temperature in all layers, we expected brightness temperatures to be independent of the number of layers within ice. This expectation was confirmed by the coherent Ulaby model. However,

brightness temperatures as simulated with the incoherent Burke model decreased with an increasing number of layers in ice. The reason for this obviously unphysical behaviour of the incoherent Burke model is that this model is calculated from the solution of the radiative transfer equation and neglects higher order reflection terms. Thus, every additional layer within the ice leads to the disregard of that part of the radiation that is associated with multiple reflections and refractions at the different layer boundaries. The Burke model has been widely used for soil moisture applications with multiple layers in the past (e.g. Jackson and O'Neill, 1986; Goodberlet and Mead, 2012). There are mainly two reasons why neglecting the higher order reflection terms is more applicable for describing radiation in soils than in sea ice: 1) Both the real and the imaginary part of the permittivity can take higher values in soils as compared to sea ice. Higher values of the permittivity's imaginary part indicate higher attenuation within the medium, and after multiple reflections only a small fraction of the radiation's original energy is preserved. Higher values of the permittivity's real part also reduce the impact of the higher order reflection terms. 2) The range of permittivities that is associated with different soil types, soil temperatures, and moisture contents is broader than the range of values sea ice takes for different ice conditions. The reflectivity between two media whose permittivities differ distinctly is higher than the reflectivity between two media with similar permittivities. The higher reflectivity results in a higher fraction of the original radiation to be reflected at the first interface between two layers. This reflection at the first interface is described by the first-order reflection term. Thus, neglecting higher order reflection terms influences modelled brightness temperatures less, if the considered layers differ more in their dielectric properties, i.e. in their permittivities. Furthermore, the more the dielectric properties within the considered medium differ from each other, the more important it is to account for the different properties of the layers, instead of reducing the number of layers in order to minimize the impact of neglecting the higher order reflection terms. Thus, the Burke model is more suitable for modelling radiation in and above soil layers than in and above sea ice. For sea ice applications, the Burke model can be unsuitable, if more than one layer within the ice is considered.

Thus, we used the coherent Ulaby model for the further investigations regarding the difference between the implementation of a temperature gradient and of a bulk ice temperature in the model. According to the coherent Ulaby model, brightness temperatures for multiple ice layers and a linear temperature gradient in the ice were on average about 5 K higher than brightness temperatures for one ice layer and a bulk ice temperature. We showed that one reason for this is the non-linear relationship between ice temperature and ice permittivity, because the ice permittivity that is related to the average ice temperature (= the bulk ice temperature for the one-ice-layer-model) is not equal to the average ice permittivity of the temperature profile. Thus, we introduced a value for the ice permittivity that was obtained from the ice permittivity profile associated with the considered temperature profile. Using this value in the model with one ice layer and a bulk ice temperature improved the model performance towards the results for the multiple layer model and a temperature gradient, if the ice surface temperature was T_{surf}= -15°C, but not if the ice surface temperature was T_{surf}= -5°C.

Thus, this approach was a first step towards an improvement of a radiation model

that uses only one ice layer. Due to the more time-consuming calculations associated with a model with multiple layers, a model with only one ice layer would be preferred for an ice thickness retrieval using SMOS data. However, here we did not take into account the salinity variations within the ice column; ice salinity was assumed to be constant over the ice column. Various forms of salinity profiles in ice have been observed (e.g. Weeks and Lee, 1962; Cox and Weeks, 1974), often for example a C-shaped salinity profile with higher ice salinities near the surface and near the bottom of the ice column, and lower salinities in the middle parts of the ice column. The ice permittivity, as calculated here, depends on the brine volume fraction, which depends on ice temperature and salinity. Thus, even if we introduced an ice permittivity value for the one-ice-layer-model that is more representative with regard to ice temperature variation within ice, we would not account for ice salinity variation in ice. Furthermore, the coherent Ulaby model accounts for different ice permittivities due to different temperatures in the ice layers. However, the temperature of the ice column is assumed to be constant over the considered ice layers (see equation (2.26)), and we used the average ice temperature for the calculations, thus introducing a probably small but not determined uncertainty to the investigations. Hence, we suggest that further investigations towards the determination of a representative value for the ice permittivity are needed, in order to improve the performance of a radiation model with one ice layer and bulk values for ice temperature and salinity.

Sensitivity to ice temperature and salinity

In order to investigate the sensitivity of brightness temperature to ice temperature and salinity, we here differentiated the brightness temperature function as obtained from the incoherent Burke model with respect to ice temperature, ice salinity, and ice thickness. We considered the corresponding derivatives for four different ice thicknesses and three different incidence angles. For the remaining parameters we assumed typical values.

We found that for all ice temperatures and all ice salinities, brightness temperatures increase with increasing ice thickness. Thus, if ice temperature and salinity are known, brightness temperature is a unique function of ice thickness, and we can retrieve the ice thickness from the observed brightness temperature for all ice temperatures and salinities. As expected, brightness temperature sensitivity to ice thickness was higher for thinner ice than for thicker ice.

Regarding the sensitivity of brightness temperature to ice temperature, we found that the sensitivity is higher for thinner ice than for thicker ice. According to our calculations, brightness temperatures first increased with increasing ice temperature, but started to decrease with a further increasing ice temperature, when a certain ice temperature was reached. This critical ice temperature depended on ice thickness and was higher for thinner ice than for thicker ice. For Arctic conditions at nadir view, the reversal point occurred at T_{surf}= -2.8°C for an ice thickness of 15 cm, and at T_{surf}= -9.6°C for an ice thickness of 60 cm, respectively.

A possible reason why we observed this reversal point is that the brightness temperature, which is defined as the physical temperature times the emissivity, is dominated by temperature for lower ice temperatures and by emissivity for higher ice temperatures. For colder conditions, the increasing ice temperature dominates and causes the

brightness temperature to increase, while, for warmer ice conditions, the decreasing ice emissivity dominates and causes the brightness temperature to decrease. For warmer conditions, the brine volume fraction within ice increases more rapidly with increasing ice temperature than for colder conditions. Thus, an increasing ice temperature under warm conditions modifies the permittivity of ice more strongly by increasing both the phase constant and the attenuation constant.

Regarding the brightness temperature sensitivity to ice salinity, we found that for low ice salinities, brightness temperatures strongly increased with increasing ice salinity. The rate of increase reduced rapidly with further increasing salinity until it reached very low values. For thicker ice this value was even slightly negative, i.e. brightness temperatures decreased with increasing ice salinity. Except for ice salinities $S_{ice} <$ 4 g/kg, the sensitivity to ice salinity was higher for thinner ice than for thicker ice (for T_{ice}= -7°C, θ= 0°). Thus, thinner ice is more sensitive to both, ice salinity and ice temperature.

For the retrieval of ice thickness from SMOS data, it is important to know whether the main brightness temperature variability over sea ice originates from the variability of ice thickness or from variations of the other ice parameters, e.g. temperature and salinity. For the investigated case with S_{ice}= 8 g/kg, an ice temperature change of 1 K caused approximately the same change in the brightness temperature signal as the one caused by an ice thickness change of about 1 – 3 cm for ice thicknesses up to 45 cm and ice surface temperatures colder than -8°C. Regarding the impact by ice salinity, we observed roughly three different regimes (for T_{ice}= -7°C). For low ice salinities ($S_{ice} <$ 5 g/kg), the brightness temperature sensitivity to salinity changes was very high. However, thin first-year ice in the Arctic usually has higher salinity values. For salinities 5 g/kg$< S_{ice} <$ 10 g/kg, an ice salinity change of 1 g/kg caused approximately the same change in the brightness temperature signal as the one caused by an ice thickness change of about 3 – 6 cm, depending on ice thickness. For higher ice salinities ($S_{ice} >$ 10 g/kg), brightness temperature was almost independent of ice thickness for ice thicker than 30 cm. Thus, if the ice salinity is $S_{ice} >$ 10 g/kg, a retrieval would only be possible for ice thinner than 30 cm. In contrast, at 15 cm ice thickness and $S_{ice} >$ 10 g/kg, an ice salinity change of 1 g/kg corresponded to a brightness temperature change as caused by an ice thickness change of only about 0.5 cm.

Here, we showed the results of our sensitivity studies for brightness temperatures at nadir view and at two incidence angles at horizontal polarisation. We have also calculated the sensitivities for vertical polarisation. These sensitivities of brightness temperature and ice thickness retrieval to ice temperature and ice salinity for Arctic conditions are depicted in the Figures A.1 to A.4 in the appendix. The brightness temperatures at vertical and at horizontal polarisation show a very similar behaviour. The main differences are that brightness temperature sensitivity to ice temperature is somewhat higher at vertical polarisation, and thus ice temperature has a slightly higher impact on ice thickness retrieval. At vertical polarisation, the reversal points occur at higher ice temperatures than at horizontal polarisation. Furthermore, the range of salinities, for which the impact of ice salinity on the ice thickness retrieval is low, is somewhat broader at vertical than at horizontal polarisation.

According to our sensitivity studies, for ice thickness retrieval applications, L-band

brightness temperatures over thin Arctic ice are sensitive enough to ice thickness variations, when compared to ice temperature and salinity variations. The brightness temperature supplies information on ice thickness within a certain accuracy, which can be specified using our model and assumptions about the ice temperature and salinity and their expected variations.

Comparison of the impact by ice temperature, salinity, and thickness
In order to compare the impact of ice temperature, salinity, and thickness on the brightness temperatures under realistic conditions, we examined an example case of freezing sea ice in the Laptev Sea. For the considered case, we found that the increasing ice thickness caused the brightness temperature signal above sea ice to increase by 143 K, while the estimated ice temperature and salinity variations caused the brightness temperature to vary only by 31 K (21%) and 16 K (11%), respectively. Thus, the ice thickness was the main contributor to the increasing brightness temperatures, as they were observed by SMOS. The analysis also showed that for the polarisation difference, the relative contributions of ice temperature and salinity variations as compared to the contribution of ice thickness variation were higher than for the brightness temperature intensity.

Chapter 4

Impact of snow on brightness temperature and the potential for snow thickness retrieval

Here, we investigate the impact of a potential snow cover on brightness temperatures above sea ice. In contrast to the coherent Ulaby model, the incoherent Burke model neglects higher order reflection terms. This simplification particularly affects the modelled brightness temperatures, when the attenuation of the considered medium is low, or when the layers are thin. Dry snow is assumed to be almost transparent in L-band (e.g. Rott and Mätzler, 1987; Hall, 1996), i.e. the attenuation of dry snow is low. Thus, we need to investigate whether neglecting the higher order reflection terms is applicable, when a snow layer is considered. Therefore, we here use both the coherent Ulaby model and the incoherent Burke model to investigate the impact of snow on the modelled brightness temperatures.
In section 4.1, we shortly introduce the properties of snow that are important for the simulation of brightness temperatures in L-band. In section 4.2, we investigate the impact of the dielectric properties of snow on brightness temperatures above sea ice. First, we add a snow layer of constant thickness on top of the sea ice. Subsequently, we investigate whether the brightness temperature of snow-covered sea ice depends on the thickness of the snow layer. In section 4.3, we investigate how the modelled brightness temperatures above sea ice are influenced, when the ice is covered by a snow layer of typical thickness, as observed in the Arctic and in the Baltic Sea. Snow has two different effects on brightness temperatures over sea ice. Firstly, the impact by the dielectric properties of snow. Secondly, the impact by the thermal insulation of a snow cover and the resulting higher ice temperatures. We investigate these two effects of snow separately and compare their contributions with each other. In section 4.4, we compare our brightness temperatures modelled for snow-covered sea ice with brightness temperatures measured by SMOS. Finally, we investigate the potential for a retrieval of snow thickness from SMOS brightness temperatures observed over thick Arctic sea ice.

4.1 Properties of snow

The implementation of an additional layer in our radiation models requires information on the permittivity, the thickness, and the physical temperature of this layer. We present the empirical model we use for the snow permittivity (section 4.1.1), the empirical formulas we use to estimate snow thickness (section 4.1.2), and a simple heat conduction model that allows us to calculate the bulk temperatures of the snow layer and the snow-covered ice layer (section 4.1.3).

4.1.1 Permittivity of snow in L-band

For the snow permittivity, we use a polynomial fit obtained for snow permittivity measurements at microwave frequencies ranging between 840 MHz and 12.6 GHz. Based on these measurements, it is suggested that the permittivity of snow mainly depends on snow density and snow wetness and that the permittivity is practically independent of the structure of snow. For dry snow with a density ρ_d, the real and the imaginary part of the snow permittivity are

$$\epsilon_{R,d} = 1. + 1.7\rho_d + 0.7\rho_d^2 \tag{4.1}$$

$$\epsilon_{I,d} = 1.59 \cdot 10^6 (0.52\rho_d + 0.62\rho_d^2)(\frac{1}{f} + 1.23 \cdot 10^{-14}\sqrt{f}) e^{0.036(T-273.15)} \quad , \tag{4.2}$$

where f is the frequency of the electromagnetic radiation, T is the temperature of snow in °C, and ρ_d is given in g/cm^3. (Tiuri et al., 1984)
The frequency dependence of the permittivity of wet snow is the same as that for water. Thus, the polynomial fit for the permittivity of wet snow contains the permittivity of pure water ϵ_{water}. For wet snow with a wetness by volume W_v, the real and the imaginary part of the snow permittivity are

$$\epsilon_{R,w} = \epsilon_{R,d} + (0.1W_v + 0.8W_v^2)\,\mathrm{Re}\{\epsilon_{water}\} \tag{4.3}$$

$$\epsilon_{I,w} = -(0.1W_v + 0.8W_v^2)\,\mathrm{Im}\{\epsilon_{water}\} \quad , \tag{4.4}$$

where $\mathrm{Re}\{\epsilon_{water}\}$ and $\mathrm{Im}\{\epsilon_{water}\}$ denote the real and the imaginary part of the permittivity of pure water, respectively. (Tiuri et al., 1984)
For the permittivity of pure water, we use the same equations as for the permittivity of sea water (Klein and Swift, 1977) and assume a salinity of S_{water}=0 g/kg.

4.1.2 Snow thickness

The snow thickness for Arctic applications is estimated from an empirical relationship between ice thickness d_{ice} and snow thickness d_{snow} (Doronin, 1971):

$$d_{snow} = 0 \text{ cm} \qquad \text{for} \quad d_{ice} < 5 \text{ cm} \tag{4.5}$$

$$d_{snow} = 0.05 d_{ice} \qquad \text{for} \quad 5 \text{ cm} \leq d_{ice} \leq 20 \text{ cm} \tag{4.6}$$

$$d_{snow} = 0.10 d_{ice} \qquad \text{for} \quad d_{ice} > 20 \text{ cm}. \tag{4.7}$$

For the Baltic Sea, we use an empirical relationship based on Finnish ice breaker thickness measurements from 2006 to 2010 (Mäkynen, 2012):

$$d_{snow} = 0 \text{ cm} \qquad \text{for } d_{ice} < 6 \text{ cm} \tag{4.8}$$

$$d_{snow} = 0.22 d_{ice} - 1.3 \text{ cm} \qquad \text{for } d_{ice} \geq 6 \text{ cm}. \tag{4.9}$$

4.1.3 Snow temperature

Snow has a thermal insulation effect on ice. The bulk ice temperature of snow-covered sea ice is generally higher than the bulk ice temperature of bare sea ice. In order to include the effect of thermal insulation by snow, we here assume a balance of heat fluxes at the snow-ice-interface. We account for the different thermal conductivities of ice and snow to calculate the bulk temperature of the snow layer and the snow-covered ice layer. We assume that the temperature at the bottom of the ice is at the freezing point of water (i.e. T_{bottom}= T_{water}= -1.8°C for Arctic and T_{bottom}= T_{water}= -0.3°C for Baltic conditions), and that the temperature gradients within ice and snow are linear. We assume that at the snow-ice-interface the ice temperature equals the snow temperature: $T_{ice}(z = d_{ice})$= $T_{snow}(z = d_{ice})$= T_{si} with T_{si} being the snow-ice-interface temperature, and d_{ice} being the ice thickness. Here, z denotes the vertical distance from the ice-water-interface. Thus, z is z= 0 at the ice-water-interface, $z = d_{ice}$ at the snow-ice-interface, and $z = d_{ice} + d_{snow}$ at the snow surface. We assume that thermal conduction is continuous through the snow-ice-interface (Maykut and Untersteiner, 1971):

$$k_{ice}\gamma_{ice}(z = d_{ice}) = k_{snow}\gamma_{snow}(z = d_{ice}) \quad , \tag{4.10}$$

where

$$\gamma_{ice}(z^*) = \left.\frac{\partial T_{ice}(z)}{\partial z}\right|_{z=z^*} \tag{4.11}$$

$$\gamma_{snow}(z^*) = \left.\frac{\partial T_{snow}(z)}{\partial z}\right|_{z=z^*} \quad , \tag{4.12}$$

and k_{ice} and k_{snow} are the thermal conductivities of ice and snow, respectively. Because we assume linear temperature gradients within the ice and the snow layer, $\gamma_{ice}(z) = \gamma_{ice}$ and $\gamma_{snow}(z) = \gamma_{snow}$ are constant values. The surface temperature T_{surf} and the snow-ice-interface temperature T_{si} are then described by

$$T_{surf} = T_{si} + \gamma_{snow} d_{snow} \tag{4.13}$$

$$T_{si} = T_{water} + \gamma_{ice} d_{ice} \quad . \tag{4.14}$$

If we know the surface temperature T_{surf}, we can solve this system of equations with the three equations (4.10), (4.13), and (4.14) and the three unknowns γ_{ice}, γ_{snow}, and T_{si}. The bulk ice and snow temperatures T_{ice} and T_{snow} are then

$$T_{ice} = 0.5(T_{si} + T_{water}) \tag{4.15}$$

$$T_{snow} = 0.5(T_{si} + T_{surf}) \quad . \tag{4.16}$$

For the thermal conductivity of snow we use a constant climatological value of k_{snow}= 0.31 $\frac{\mathrm{W}}{\mathrm{mK}}$ (Yu and Rothrock, 1996), and for the thermal conductivity of ice we use a parameterisation accounting for ice temperature and salinity (Untersteiner, 1964):

$$k_{ice} = 2.034\frac{\mathrm{W}}{\mathrm{Km}} + 0.13\frac{\mathrm{W}}{\mathrm{kgm}^2}\frac{S_{ice}}{T_{ice} - 273.} \quad . \tag{4.17}$$

To simplify the calculations we use the mean temperature of the snow and ice column T_{mean}=0.5(T_{surf}+T_{water}) instead of the ice temperature T_{ice} in equation (4.17).
From equations (4.10), (4.13), and (4.14) we get the following expressions for the ice and snow temperatures:

$$T_{ice} = T_{water} + \frac{1}{2}K(T_{surf} - T_{water})k_{snow}d_{ice} \tag{4.18}$$

$$T_{snow} = \frac{1}{2}(T_{water} + T_{surf} + K(T_{surf} - T_{water})k_{snow}d_{ice}) \tag{4.19}$$

where $K = (k_{ice}d_{snow} + k_{snow}d_{ice})^{-1}$.

4.2 Impact of dielectric properties of snow

As a first test, we implement a very thin and a rather thick snow layer on top of the sea ice in our radiation models. Thereafter, we investigate how the thickness of the snow layer impacts the modelled brightness temperatures. Here, we account only for the dielectric properties of the snow layer and use equations (4.1) – (4.4) to calculate the snow permittivity.

4.2.1 Impact of a snow layer with constant thickness

We compare the effect of a 1 mm and a 50 cm thick snow layer on the brightness temperatures as modelled with the incoherent Burke model and as modelled with the coherent Ulaby model. Regarding the coherent Ulaby model, we have to take into account that the coherent brightness temperature signal oscillates with the thickness of the considered layers. When we add a snow layer on top of the ice layer, these oscillations occur for both the variation of the ice layer thickness and the variation of the snow layer thickness. If we add a snow layer with a fixed thickness on top of the sea ice, the resulting brightness temperature represents the brightness temperature at a certain phase of this coherent oscillation. The resulting brightness temperature thus corresponds to the brightness temperature caused by the considered specific combination of the snow layer and the ice layer thickness, but the brightness temperature is not necessarily representative for snow layers with similar thicknesses. Thus, when modelling a 50 cm thick snow layer with the coherent Ulaby model, we perform the simulation for each ice thickness for a range of snow thicknesses around 50 cm and take the average brightness temperature as a representative value. At nadir, the period of the coherent oscillation is half the electromagnetic wavelength in the medium. We model L-band brightness temperatures for a wavelength in vacuum

of about λ_0= 21 cm. The wavelength in snow is $\lambda_{snow}= \frac{\lambda_0}{\sqrt{\epsilon_{snow}}}$. Thus, we perform the simulations for d_{snow}= 50 cm $\pm \frac{1}{2}\frac{\lambda_{snow}}{2}$ (i.e. for $d_{snow} \approx$ 50 cm $\pm$ 4.05 cm).
We do the simulations for typical Arctic sea ice conditions. Water salinity is assumed to be S_{water}= 30 g/kg, and water temperature is at the corresponding freezing temperature T_{water}= -1.8°C. Bulk ice salinity is assumed to be S_{ice}= 8 g/kg, and the surface temperature is T_{surf}= -15°C.

Results for dry snow
Here, we consider a layer of dry snow with a density of ρ_{snow}= 350 kg/m^3 and a wetness of W_v= 0%. According to the coherent Ulaby model, the very thin layer of dry snow (d_{snow}= 1 mm) has a negligible effect on brightness temperatures above sea ice at nadir view, as well as for both horizontal and vertical polarisation at an incidence angle θ= 50° (Figures 4.1 to 4.3). For the 50 cm thick snow layer of dry snow, brightness temperatures increase at nadir view, and at an incidence angle θ= 50° at horizontal polarisation, whereas the brightness temperatures at θ= 50° at vertical polarisation are unaffected by the snow layer.
According to the incoherent Burke model, brightness temperatures at nadir view and at θ= 50° at horizontal polarisation increase already for a snow layer of 1 mm thickness. For snow layer thicknesses of dry snow as considered here (d_{snow}= 1 mm and d_{snow}= 50 cm), the brightness temperatures modelled with the incoherent Burke model are independent of snow layer thickness. In accordance with the coherent Ulaby model, brightness temperatures at vertical polarisation are not influenced by a snow layer, neither for d_{snow}= 1 mm, nor for d_{snow}= 50 cm.
For both models, the brightness temperature increase at nadir view and at θ=50° at horizontal polarisation is higher for thicker ice than for thinner ice. Thus, the snow layer impacts the maximum brightness temperature that is reached, when the brightness temperature signal saturates for thick ice. In both models, for d_{snow}= 50 cm the maximum brightness temperature (averaged over the oscillations) increases by about 10 K at nadir view and by 25 K at θ= 50° at horizontal polarisation as compared to snow-free ice.
For comparison, at nadir view, the brightness temperature of an infinitely thick layer of ice would be about 240 K, while the brightness temperature of an infinitely thick layer of snow would be about 260 K. The corresponding snow-covered thick ice here has a brightness temperature of 250 K (for both models). At an incidence angle θ= 50° at horizontal polarisation, the brightness temperature of an infinitely thick layer of ice would be about 210 K, while the brightness temperature of an infinitely thick layer of snow would be about 250 K. The corresponding snow-covered thick ice here has a brightness temperature of 235 K (for both models). At vertical polarisation, the brightness temperature of an infinitely thick layer of ice would be about 260 K, and 265 K for an infinitely thick layer of snow. Thus, brightness temperatures modelled for snow-covered sea ice at nadir view and at horizontal polarisation take approximately the average value of the brightness temperatures over infinitely thick bare sea ice and over infinitely thick dry snow. At vertical polarisation, these two values are very similar and our models show no impact on brightness temperatures, when we add a layer of dry snow of up to 50 cm thickness.

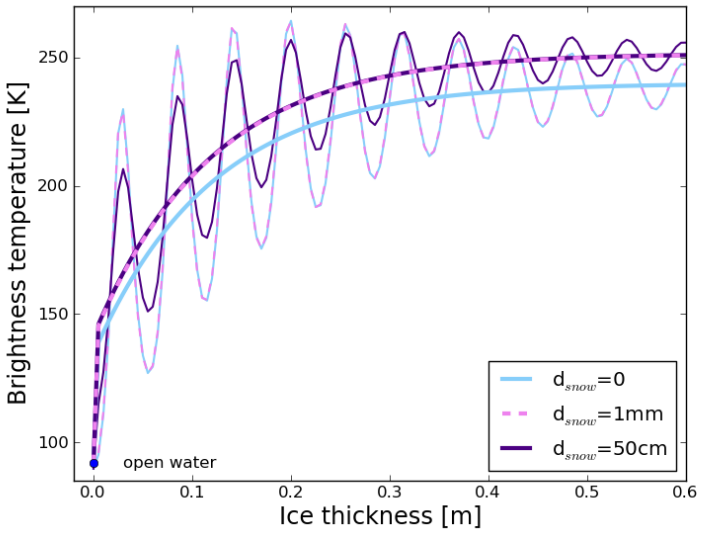

Figure 4.1: Brightness temperature at nadir view as a function of ice thickness according to the incoherent Burke model (thick lines) and the coherent Ulaby model (thin lines) for three different scenarios with dry snow (ρ_{snow}= 350 kg/m^3, W_v= 0%): 1) The light blue curves show the brightness temperatures as modelled for snow-free sea ice, 2) the pink dashed curves show the brightness temperatures as modelled for sea ice covered with a 1 mm thick snow layer, and 3) the purple curves show the brightness temperatures as modelled for sea ice covered with a 50 cm thick snow layer (average over d_{snow}= 50 cm ± 4.05 cm). The model assumptions are: S_{water}= 30 g/kg, S_{ice}= 8 g/kg, T_{surf}= -15°C, T_{water}= -1.8°C.

Results for wet snow

For comparison, we here consider a snow layer with a higher density than in the previous case (here: ρ_{snow}= 500 kg/m^3) and a volumetric fraction of 5% of liquid water (W_v= 5%), called wet snow in our study. We show only the results for brightness temperatures at nadir view (Figure 4.4). According to the coherent Ulaby model, a very thin layer (d_{snow}= 1 mm) of wet snow has a negligible effect on brightness temperatures at nadir view. For the incoherent Burke model, brightness temperatures increase, when we add a 1 mm thick layer of wet snow on top of the ice. The resulting brightness temperatures for the 1 mm thick layer of wet snow are very similar to the brightness temperatures we obtained for dry snow. For the 50 cm thick layer of wet snow brightness temperatures increase considerably in both models. The brightness temperatures reach quite quickly the maximum brightness temperature value of 250 K, which corresponds to the brightness temperature of an infinitely thick layer of wet snow.

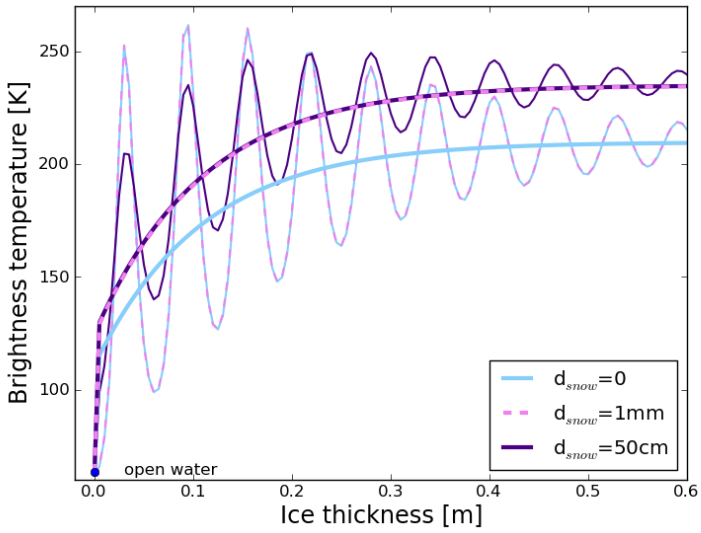

Figure 4.2: For figure description see caption of Figure 4.1, but here we show the results for horizontally polarised brightness temperatures at an incidence angle θ= 50°.

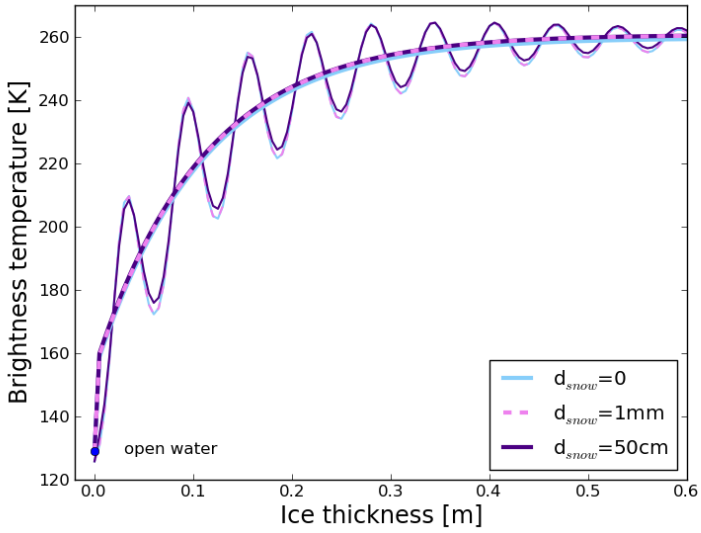

Figure 4.3: For figure description see caption of Figure 4.1, but here we show the results for vertically polarised brightness temperatures at an incidence angle θ= 50°.

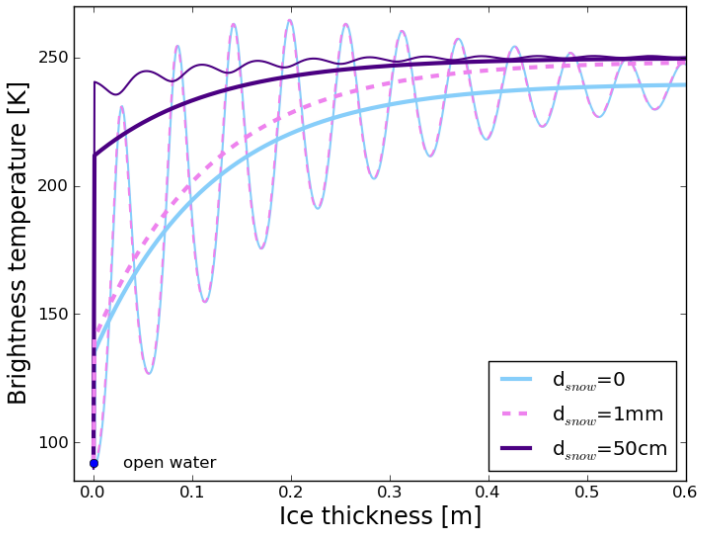

Figure 4.4: For figure description see caption of Figure 4.1, but here we show the results for wet snow (ρ_{snow}= 500 kg/m^3, W_v= 5%).

4.2.2 Impact of an increasing snow thickness

In the previous section, we found that brightness temperatures of snow-covered sea ice with different ice thicknesses and a layer of dry snow of constant thickness are not affected by an increase of the snow layer thickness from 1 mm to 50 cm, when modelled with the incoherent Burke model. We investigate whether brightness temperatures over sea ice with a constant ice thickness depend on the thickness of the snow layer. We use the coherent Ulaby and the incoherent Burke model to simulate brightness temperatures above an ice layer with thickness d_{ice}= 4 m that is covered by a snow layer whose thickness increases from 0 to 1 m for wet snow and from 0 to 100 m for dry snow, respectively. As in the previous section, we here perform the simulations for every snow thickness for a range of ice thicknesses around the chosen constant value of d_{ice}= 4 m (here: average over d_{ice}= 4 m ± 2.625 cm). We simulate brightness temperatures for nadir view and for an incidence angle θ= 50° at horizontal and at vertical polarisation. The model assumptions are the same as in the previous section.

Results

For dry snow conditions, the incoherent brightness temperature and the average value of the coherent brightness temperature depend only very slightly on snow thickness for all incidence angles and polarisations (Figure 4.5(a)). The corresponding brightness temperatures of infinitely thick ice are 260 K at nadir view, 250 K at θ= 50° at horizontal polarisation, and 265 K at θ= 50° at vertical polarisation. With increasing snow thickness the incoherent brightness temperatures and the average values of the coherent brightness temperatures increase towards these values. However, the slope is very flat; for an increase of snow thickness from 0 to 10 m, the brightness temperatures increase only by 1.3 K, 2.7 K, and 0.7 K at nadir view, horizontal polarisation at θ=

50°, and vertical polarisation at θ= 50°, respectively.
For wet snow conditions, brightness temperatures of infinitely thick ice are already reached for thinner snow layers than under dry snow conditions (Figure 4.5(b)). Thus, the brightness temperature increase is slightly higher for smaller snow thicknesses. For an increase of snow thickness from 0 to 1 m, brightness temperatures increase by 1.4 K, 1.9 K, and 0.8 K at nadir view, horizontal polarisation at θ= 50°, and vertical polarisation at θ= 50°, respectively. However, the dependence of brightness temperature on snow thickness is still very small.

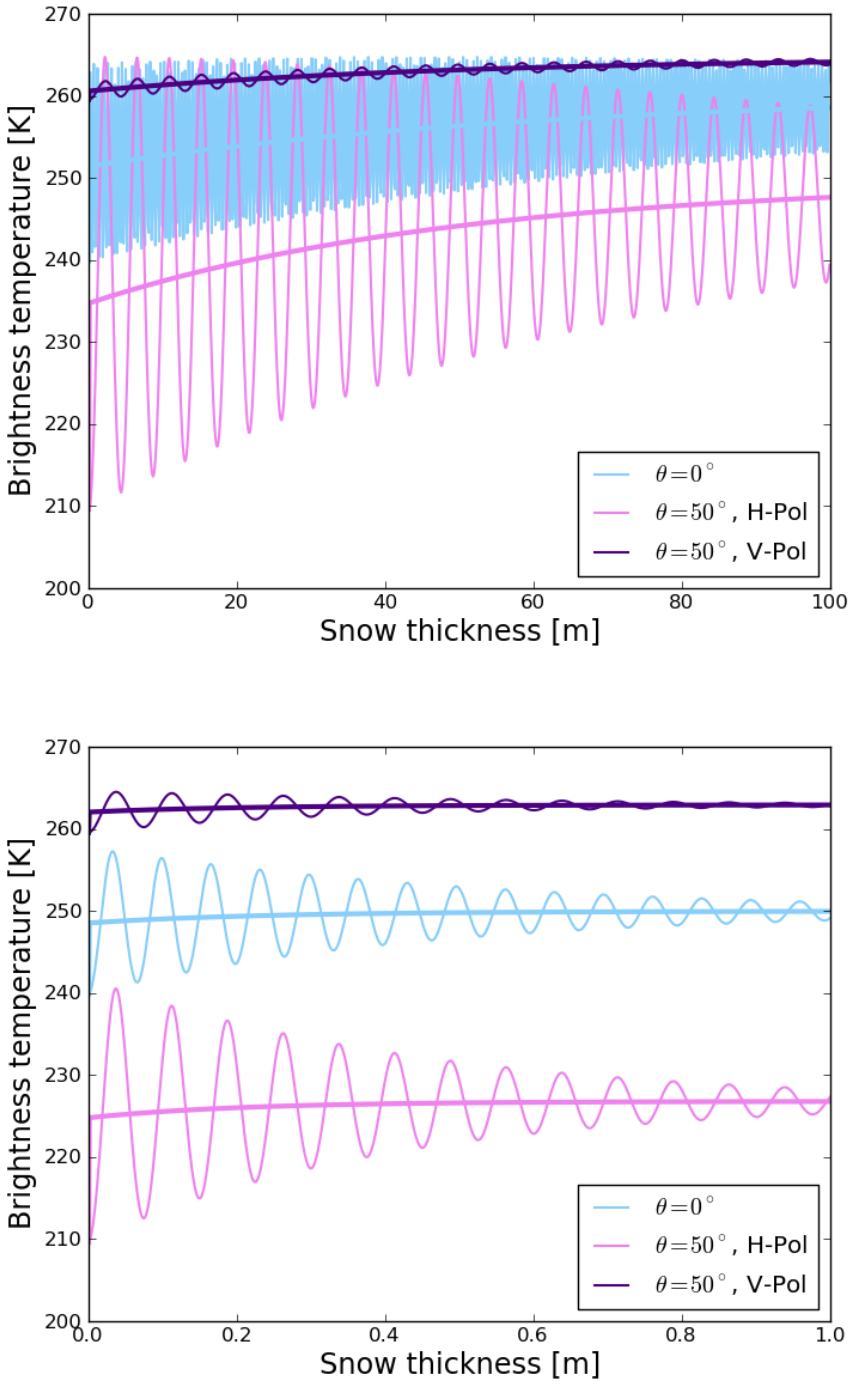

Figure 4.5: Brightness temperature over a constant ice thickness d_{ice}= 4 m (average over d_{ice}= 4 m ± 2.625 cm) as a function of snow thickness according to the coherent Ulaby (thin line) and the incoherent Burke model (thick line). We show the results for nadir view, and for horizontal and vertical polarisation at an incidence angle θ= 50°. The upper figure shows the results for dry snow (ρ_{snow}= 350 kg/m^3, W_v= 0%), and the lower figure for wet snow (ρ_{snow}= 500 kg/m^3, W_v= 5%). Note the different range of snow thicknesses at the x-axes. The model assumptions are: S_{water}= 30 g/kg, S_{ice}= 8 g/kg, T_{surf}= -15°C, T_{water}= -1.8°C.

4.3 Comparison of the impact by thermal insulation and by dielectric properties of snow

We investigate the impact of a snow layer with a realistic thickness on brightness temperatures over sea ice. We simulate brightness temperatures for typical snow thicknesses as observed in the Arctic and in the Baltic Sea (see section 4.1.2). For Arctic conditions water salinity is assumed to be S_{water}= 30 g/kg and the surface temperature is assumed to be T_{surf}= -15°C; for Baltic conditions we assume S_{water}= 6 g/kg and T_{surf}= -10°C. Water is again assumed to be at freezing temperature, thus T_{water}= -1.8°C for Arctic and T_{water}= -0.3°C for Baltic conditions, respectively. Simulations are performed for brightness temperatures at nadir view and at an incidence angle θ= 50° at horizontal and at vertical polarisation. In order to investigate the impact of the snow cover on the brightness temperatures due to the dielectric properties of snow separately from the impact due to the thermal insulation effect of snow, we compare three different scenarios for the brightness temperature as a function of ice thickness:

1. Bare sea ice without a snow cover.
2. Sea ice covered with snow, where snow thickness is an empirical function of ice thickness, as given in the equations (4.5) – (4.9). Bulk snow and ice temperatures are as calculated from equations (4.19) and (4.18), respectively.
3. Bare sea ice without a snow cover, but a bulk ice temperature as if the thermal insulation effect of snow was present. To calculate the bulk ice temperature, we use equation (4.18), the snow thickness being the same as in 2.

Results
The results of our investigations for a dry snow layer with a density of ρ_d= 350 kg/m^3 and a wetness W_v= 0% are shown in Figures 4.6 to 4.8. Due to the steps in the equations that relate snow thickness and ice thickness (given in section 4.1.2), we observe jumps in the incoherent brightness temperature signal, while the coherent brightness temperature oscillations for snow-covered sea ice consist of two oscillations that are superimposed. One oscillation is caused by variation of ice thickness, while the other is caused by snow thickness variation. Because snow and ice thickness are related via an empirical relationship, we obtain two oscillations that appear to have two different periods in terms of the ice thickness. At nadir, the oscillations have a period of half the wavelength of the electromagnetic radiation in the medium. Here, we consider L-band radiation with a wavelength in vacuum of about λ_0= 21 cm. The wavelength in sea ice is λ_{ice}= $\frac{\lambda_0}{\sqrt{\epsilon_{ice}}}$. Thus, at nadir view, the maximum amplitudes of the oscillations caused by increasing ice thickness occur about every $\frac{\lambda_{ice}}{2} \approx 5.25$ cm of ice thickness increase for typical Arctic conditions. The period of the additional oscillations caused by the snow layer at nadir view is also half the wavelength within the medium. The wavelength in snow is λ_{snow}= $\frac{\lambda_0}{\sqrt{\epsilon_{snow}}}$. Thus, the oscillation period in snow is about 8.1 cm at nadir view for typical Arctic conditions. However, the snow thickness is only about 10% of the ice thickness for Arctic conditions, and about 20% of the ice thickness for Baltic conditions. The brightness temperatures here are shown as a function of ice thickness.

Thus, at nadir view, the maximum amplitudes of the superimposed oscillations caused by the increasing snow layer thickness occur only about every 10 × 8.1 cm= 81.0 cm (Arctic conditions), or about every 5 × 8.1 cm= 40.05 cm (Baltic conditions) of ice thickness increase.

We state that, although the incoherent Burke model neglects higher order reflection terms, the modelled brightness temperatures represent the average values of the coherent oscillations as modelled with the coherent Ulaby model. For all considered cases (Arctic and Baltic conditions, nadir view, and θ= 50° at horizontal and at vertical polarisation) a snow layer causes the modelled brightness temperatures to increase. Under Baltic conditions, the higher ice temperatures caused by the thermal insulation effect of snow contribute more to this brightness temperature increase than under Arctic conditions. The main reason for this is that, according to the empirical relationship used here, the snow layer on Baltic sea ice is thicker than the snow layer on Arctic sea ice. The thickness of the snow thus has an impact on brightness temperatures, although in the previous section, we found that the thickness of the snow layer does not impact brightness temperatures, if we consider only the dielectric properties of snow. However, a thicker snow layer has a higher insulation effect and thus the bulk ice temperature under a thick snow layer is higher than under a thin snow layer.

At nadir view, the thermal insulation effect contributes to approximately half of the brightness temperature increase under Baltic conditions (Figure 4.6(b)). The temperature contribution is higher for small ice thicknesses and declines with increasing ice thickness. Under Baltic conditions, at horizontal polarisation (θ= 50°) the relative contribution of the increased ice temperature to the overall brightness temperature increase is smaller than at nadir view (Figure 4.8(a)). At vertical polarisation, the increased ice temperature under the snow cover is solely responsible for the brightness temperature increase (Figure 4.8(b)). For Arctic conditions, our models give very similar results. However, as mentioned before, the impact by thermal insulation and thus the overall impact is smaller than under Baltic conditions (Figures 4.6(a) and 4.7). We do not show the results for wet snow (ρ_d= 500 kg/m^3 and W_v= 5%) here. However, they are very similar to the presented results for dry snow.

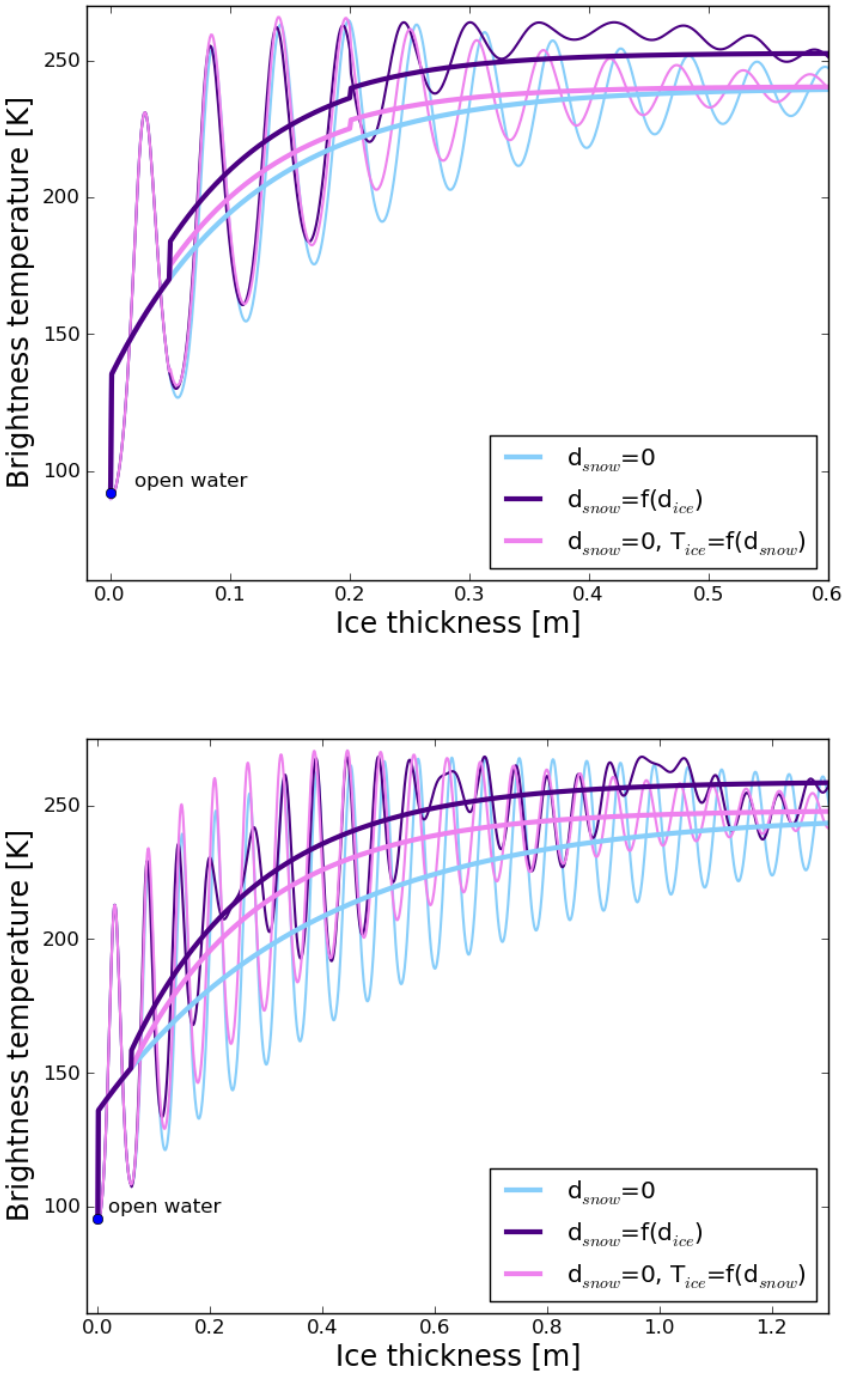

Figure 4.6: Brightness temperature at nadir view as a function of ice thickness according to the incoherent Burke model (thick lines) and the coherent Ulaby model (thin lines) for three different scenarios with dry snow (ρ_{snow}= 350 kg/m^3, W_v= 0%): 1) The light blue curves show brightness temperatures as modelled for snow-free sea ice, 2) the purple curves show brightness temperatures as modelled for snow-covered sea ice, and 3) the pink curves show brightness temperatures as modelled for snow-free sea ice with ice temperatures, as if the snow cover was present (see section 4.3). The upper figure shows the results for Arctic conditions (S_{water}= 30 g/kg, S_{ice}= 8 g/kg, T_{surf}= -15°C, T_{water}= -1.8°C), the lower figure for Baltic conditions (S_{water}= 6 g/kg, S_{ice}= 1 g/kg, T_{surf}= -10°C, T_{water}= -0.3°C).

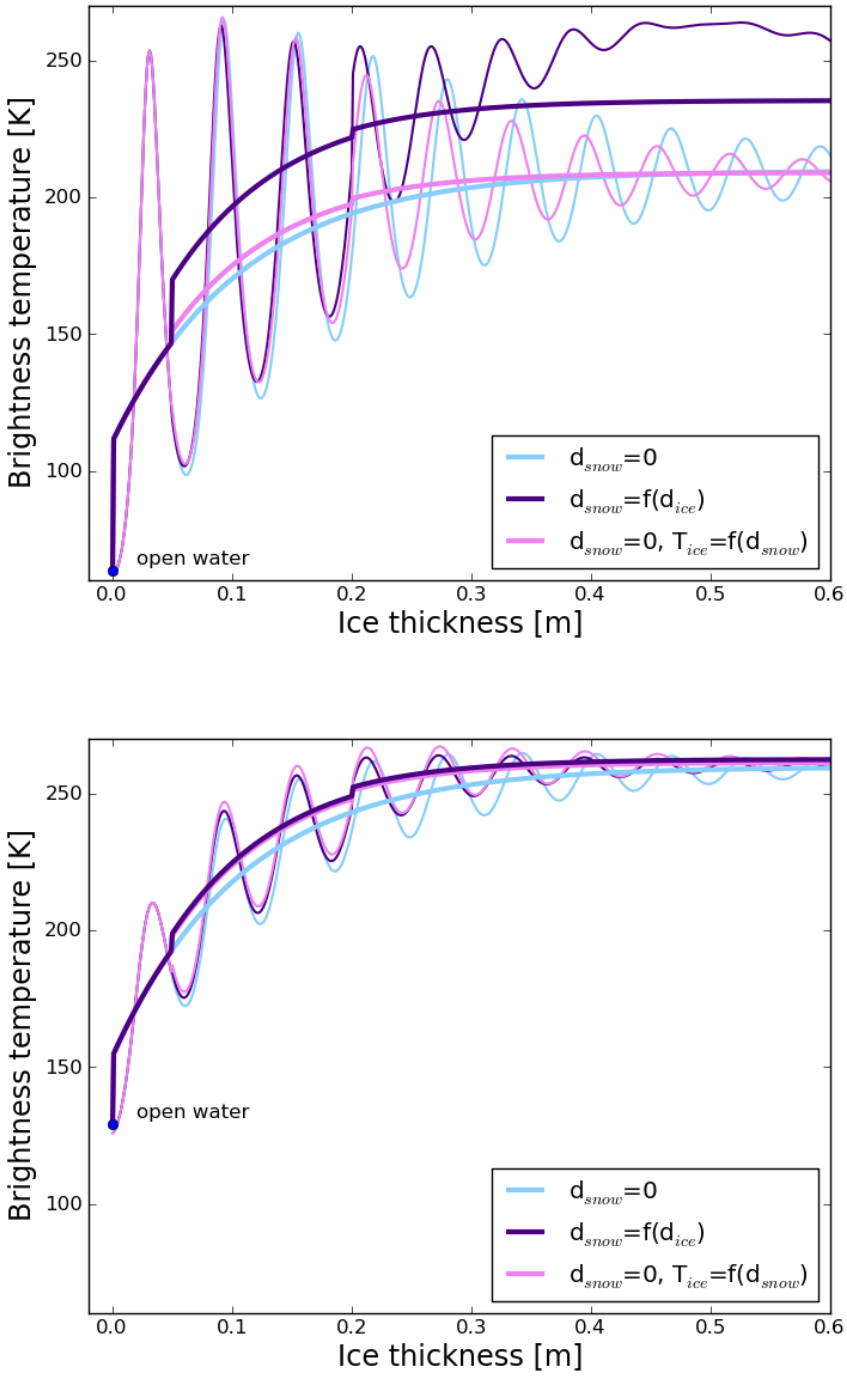

Figure 4.7: Horizontally polarised (upper figure) and vertically polarised (lower figure) brightness temperature at an incidence angle θ= 50° as a function of ice thickness according to the incoherent Burke model (thick lines) and the coherent Ulaby model (thin lines) for three different scenarios with dry snow (ρ_{snow}= 350 kg/m^3, W_v= 0%): 1) The light blue curves show brightness temperatures as modelled for snow-free sea ice, 2) the purple curves show brightness temperatures as modelled for snow-covered sea ice, and 3) the pink curves show brightness temperatures as modelled for snow-free sea ice with ice temperatures, as if the snow cover was present (see section 4.3). Here, we show the results for Arctic conditions (S_{water}= 30 g/kg, S_{ice}= 8 g/kg, T_{surf}= -15°C, T_{water}= -1.8°C).

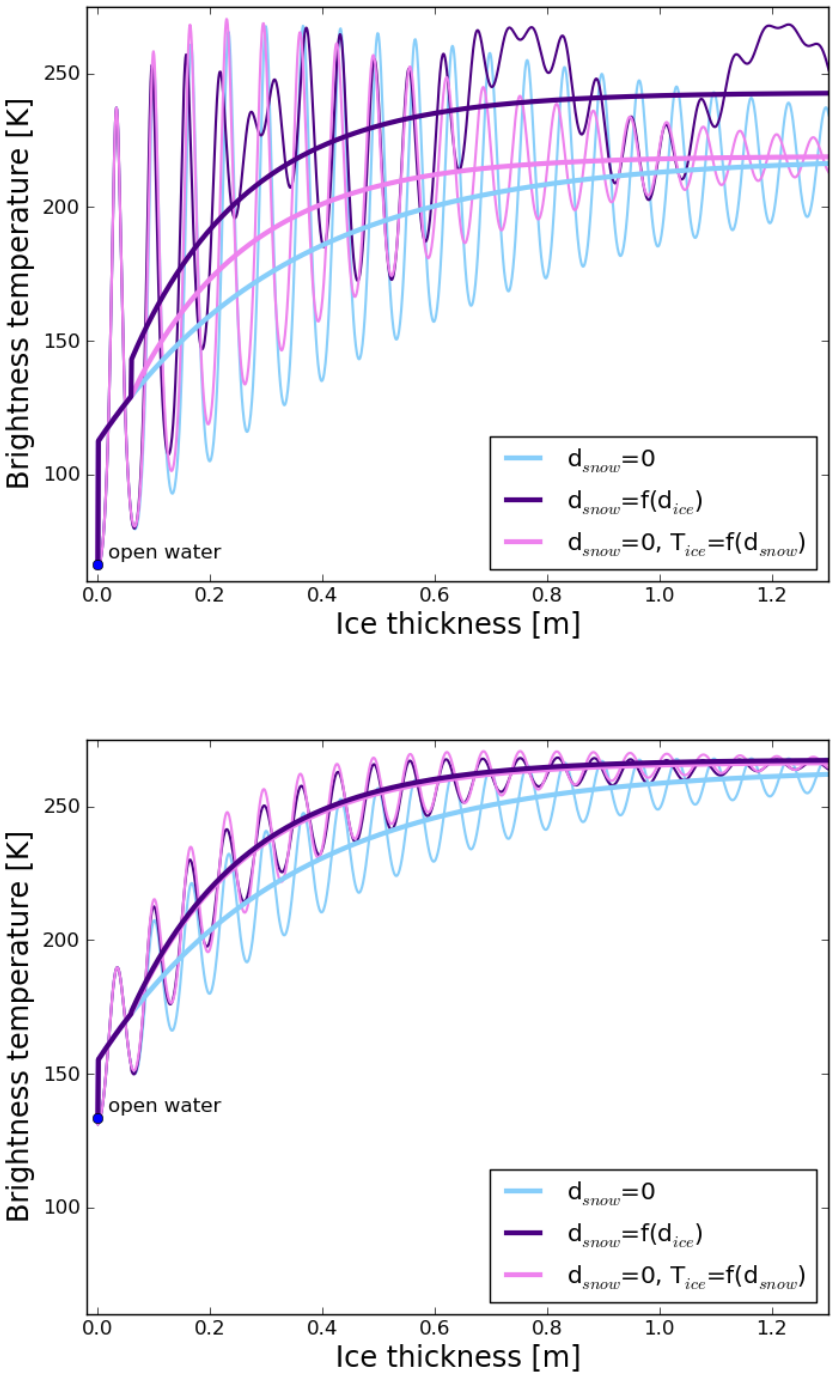

Figure 4.8: For figure description see caption of Figure 4.7, but here we show the results for Baltic conditions (S_{water}= 6 g/kg, S_{ice}= 1 g/kg, T_{surf}= -10°C, T_{water}= -0.3°C).

4.4 Comparison with observations and the potential for snow thickness retrieval

In order to test the validity of our theoretical considerations, we use the incoherent Burke model to simulate brightness temperatures over snow-covered sea ice, and compare these brightness temperature simulations with SMOS brightness temperature measurements. Additionally, we investigate whether brightness temperatures as observed by SMOS over thick Arctic sea ice depend on snow thickness and whether there is a potential for retrieving snow thickness from SMOS observations.

4.4.1 The IceBridge flight campaign

For simulation of brightness temperatures we use ice and snow thicknesses measured during the NASA Operation IceBridge mission (Kurtz et al., 2012). We use the data from the flight campaign that took place from 14th March to 2nd April, 2012 in the Arctic. The NASA IceBridge Sea Ice Freeboard, Snow Depth, and Thickness (IDCSI2) data set contains derived geophysical data products including sea ice thickness retrieved from the Airborne Topographic Mapper (ATM) laser altimeter, and snow depth retrieved from the IceBridge snow radar. Simultaneously, the ice surface temperature was measured by a KT19.85 infrared pyrometer alongside the ATM instrument. The IceBridge flight tracks and the measured ice and snow thicknesses are depicted in Figure 4.9.

IceBridge sea ice thickness
The footprint size of the ATM laser altimeter is about 1 m $\times$ 268 m. In spring 2009, airborne ATM laser altimeter measurements and temporally and spatially coincident in-situ sea ice thickness measurements were conducted on sea ice north of Greenland (GreenArc campaign). The mean sea ice thickness retrieved from laser altimeter data and the mean in-situ sea ice thickness agreed within 5 cm, while the modal values agreed within 10 cm. From this analysis, the uncertainty associated with IceBridge sea ice thickness estimates is assumed to be 40 cm. (Farrell et al., 2012)
The average ice thickness of all IceBridge ice thickness measurements obtained between 14th March and 2nd April, 2012 is about 4 m, and the flight tracks were mainly located over multi-year ice. Only a very small fraction of the measurements was carried out over ice thicknesses below 1 m ice thickness. Thus, the IceBridge measurements are not suitable for a validation of ice thickness retrieval from SMOS brightness temperatures. However, we here use the IceBridge measurements to examine whether we can use our radiation model to realistically simulate L-band brightness temperatures over snow-covered thick sea ice.

IceBridge snow thickness
The footprint size of the IceBridge snow radar is about 15 m $\times$ 16 m. The GreenArc campaign served also as a validation for the IceBridge snow thicknesses. The mean snow thickness retrieved from radar data and the mean in-situ snow thickness agreed within 1 cm, while the modal values agreed within 2 cm (Farrell et al., 2012). The

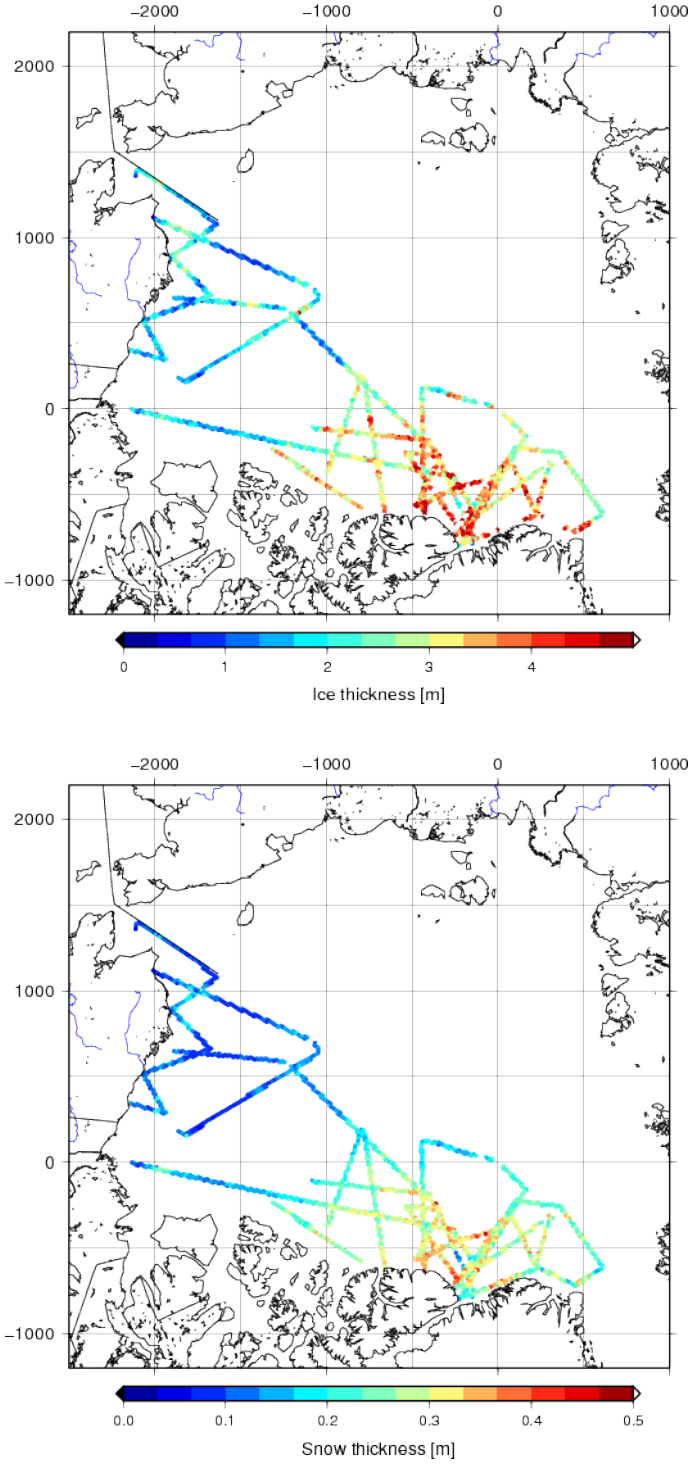

Figure 4.9: Ice thicknesses (upper figure) and snow thicknesses (lower figure) as measured during the IceBridge flight campaign in the Arctic from 14 March to 2 April, 2012. The thicknesses shown here are the average values of all thickness measurements located within a SMOS grid cell. The map is given in polar stereographic projection.

correlation coefficient between the snow thicknesses was r= 0.7, i.e. r^2= 0.49 (Farrell et al., 2012). The agreement between airborne and in-situ measurements was very good over level ice, while the observed differences were larger over multi-year ice, particularly at pressure ridges. In these regions, snow thicknesses differed by up to 20–60 cm (Farrell et al., 2012). A comparison of GreenArc snow thicknesses with climatological snow thicknesses (Warren et al., 1999) revealed a difference of 0.3 cm for the mean values (Kurtz and Farrell, 2011).

IceBridge ice surface temperature
The footprint size of the KT19.85 infrared pyrometer is about 40 m (Kurtz, 2012). Here, we use the KT19.85 temperature data (Krabill, 2012) to estimate the surface temperature of (snow-covered) sea ice. However, the uncertainty of the surface temperature data is unknown (Kurtz, 2012).

4.4.2 Brightness temperature simulations

General model assumptions
We compare two different brightness temperature simulations with brightness temperatures measured by SMOS. One simulation is performed with the incoherent Burke model with one ice layer and the ice thickness information from IceBridge measurements. In this simulation we neglect a potential snow cover. The other simulation is performed with the incoherent Burke model with one ice layer that is covered by one layer of snow; the ice and snow layer thicknesses are taken from the IceBridge measurements.
We simulate brightness temperatures for every SMOS grid cell that contains at least 50 single IceBridge measurements. For the simulations, we use the mean values of all IceBridge ice and snow thickness measurements that are located within the SMOS grid cell as model input for ice and snow thickness. Ice salinity is estimated from ice thickness using an empirical relationship between ice salinity and ice thickness in the Arctic (Cox and Weeks, 1974):

$$S_{ice}[\mathrm{g/kg}] = 14.24 - 19.39 d_{ice}[\mathrm{m}] \qquad \text{for } d_{ice} \leq 0.4 \text{ m} \tag{4.20}$$

$$S_{ice}[\mathrm{g/kg}] = 7.88 - 1.59 d_{ice}[\mathrm{m}] \qquad \text{for } d_{ice} > 0.4 \text{ m}. \tag{4.21}$$

This empirical relationship was determined for ice thicknesses up to d_{ice}= 4 m. For thicker ice we use the value for d_{ice}= 4 m, which is S_{ice}= 1.52 g/kg. Water salinity is assumed to be S_{water}= 33 g/kg. Water temperature is assumed to be at the freezing temperature of Arctic sea water, i.e. T_{water}= -1.8°C. Ice and snow temperatures are estimated from the KT19 ice surface temperatures measured during the IceBridge flight campaign. For the snow-free simulations, we use the mean value between the KT19 ice surface temperature and the water temperature as model input for the ice temperature. For the simulations that include a snow layer, we use equations (4.18) and (4.19) to calculate ice and snow temperatures for the model from KT19 ice surface temperatures. As model input for ice concentration, we use ice concentrations that have been retrieved from the 85 GHz channel of SSMIS using the ARTIST Sea Ice (ASI) algorithm (Kaleschke et al., 2001; Spreen et al., 2008). The ice concentration

data are given on a polar stereographic grid with 12.5 km grid resolution. The data are 5-day median filtered in order to mitigate unrealistic short-term sea ice concentration variations due to weather effects. For snow density we assume a value of ρ_{snow}= 260 kg/m^3, which is the mean snow density determined from in-situ measurements during the GreenArc campaign (Farrell et al., 2012). According to the IceBridge surface temperatures, we had freezing conditions during the campaign. Thus, we expect the ice to be covered by dry snow and assume a snow wetness of W= 0% in the model. For the calculation of ice permittivity, we use the equations for multi-year ice (Table 2.2).

Modifications

Additionally to the above described approach for the simulation of brightness temperatures, we do two simulations with the following constraints and changes. Ice concentration has a large impact on the modelled brightness temperatures. The difference between the brightness temperature of thick ice (for our purposes: d_{ice} > 0.5 m in the Arctic) and water is typically in the order of 100 K. An error of only 5% in the ice concentration would thus cause an error in the brightness temperature of about 0.05 × 100 K= 5 K. The uncertainty of ASI ice concentrations is higher for low ice concentrations than for high ice concentrations. The theoretically expected standard deviation of ice concentration is about 25% for ice concentrations around c_{ice}= 0%, about 13% for c_{ice}= 50%, and about 6% for c_{ice}= 100% (Spreen et al., 2008). A comparison with in-situ data and high-resolution satellite data revealed a standard deviation of almost 5% for ice concentrations c_{ice} > 90% (Andersen et al., 2007). Thus, we also consider simulations that are constrained to pixels that have an almost closed ice cover. For these simulations we use only pixels with ice concentrations $c_{ice} \geq$ 95%, and set the ice concentration in the model to c_{ice}= 100%.

Furthermore, the pixels included in our analysis are constrained with respect to the ice surface temperature. Because we do not know how reliable the KT19 surface temperature information is, we also perform simulations for a fixed surface temperature. Therefore, we calculate the average surface temperature from all KT19 measurements that are included in our analysis. As model input for the surface temperature we then use this average value and include only pixels with surface temperatures that are within one standard deviation of the average surface temperature. The average surface temperature for all pixels with ice concentrations $c_{ice} \geq$ 95% is $< T_{surf} >$= -32.8°C, and the standard deviation is $\sigma_{T_{surf}}$= 4.5°C.

Thus, we here compare SMOS brightness temperatures with brightness temperature simulations that neglect and that include a snow layer

1) for all ice concentrations and surface temperatures; ice concentration and surface temperature are variable,

2) only for almost completely ice-covered cases ($c_{ice} \geq$ 95%), but for all surface temperatures; the ice concentration is set to c_{ice}= 100%, surface temperature is variable, and

3) only for almost completely ice-covered cases ($c_{ice} \geq$ 95%) and only for surface temperatures within one standard deviation of the average surface temperature (-37.3°C< T_{surf} < -28.3°C); the ice concentration is set to c_{ice}= 100%, the surface temperature is set to the average value T_{surf}= -32.8°C.

4.4.3 Comparison of modelled and observed brightness temperatures

For the comparison with simulated brightness temperatures, we use all SMOS brightness temperatures with incidence angles θ between 0 and 60°. For each SMOS pixel we average the measured brightness temperatures θ= 0° – 10°, for the remaining incidence angles we average the brightness temperatures over 5° incidence angle intervals, i.e. for 10° – 15°, 12.5° – 17.5°, 15° – 20°, ..., 55° – 60°. The simulations are calculated for the corresponding mean incidence angles θ= 5°, 12.5°, 15°, 17.5°, ..., 57.5°.
The results for 1) all ice concentrations and all ice surface temperatures are shown in the Figures 4.10 to 4.13, and the results for 3) the pixels constrained to closed ice cover cases and a surface temperature within one standard deviation of the average value are shown in the Figures 4.14 to 4.17. The root mean square deviations, the mean deviations, and the correlation coefficients between the simulated and the measured brightness temperatures, as well as the corresponding numbers of compared data points for all simulation scenarios 1) – 3) are given in Table 4.3.

1) Results for all ice concentrations and ice surface temperatures
For this simulation scenario, the simulations that neglect and that include a snow layer differ considerably for horizontal polarisation, while the impact of a snow layer is smaller for the simulations at vertical polarisation. For both polarisations, the modelled brightness temperatures increase, when a snow layer is added. Contemporaneously, the range of brightness temperatures decreases, when a snow layer is added.
At horizontal polarisation, brightness temperatures at low incidence angles ($\theta < 15°$) increase by about 13 K, when a snow layer is added, while brightness temperatures at high incidence angles ($\theta > 50°$) increase by about 26 K, when a snow layer is added. The range of brightness temperatures for different incidence angles decreases from about 60 K, when neglecting the snow cover, to about 47 K, when including the snow cover.
In contrast to the results at horizontal polarisation, including a snow layer causes the simulated brightness temperatures at vertical polarisation to increase more for lower incidence angles than for higher incidence angles. At vertical polarisation, brightness temperatures at low incidence angles ($\theta < 15°$) increase by about 10 K, when a snow layer is added, while brightness temperatures at high incidence angles ($\theta > 50°$) increase only by about 3 K, when a snow layer is added. The range of values decreases from about 35 K, when neglecting the snow cover, to about 28 K, when including the snow cover.
At horizontal polarisation, including the snow layer considerably reduces the deviations between simulated and measured brightness temperatures (Table 4.3). When neglecting the snow layer, the simulations underestimate the measured brightness temperatures on average by 22.9 K, as compared to an average underestimation by 4.4 K, when the snow layer is included. The root mean square deviation decreases from 24.6 K for the simulations without a snow cover to 7.8 K, when including the snow layer. The correlation coefficients are rather similar, being r^2= 0.44, when the snow is neglected, and r^2= 0.38, when the snow layer is included.

At vertical polarisation, the simulations that neglect the snow cover on average underestimate the measured brightness temperatures by 5.8 K, while the measured brightness temperatures are overestimated by 2.1 K for the simulations that include the snow cover. The root mean square deviation of the brightness temperatures reduces from 8.6 K, when snow is neglected, to 5.6 K, when snow is included. The correlation coefficient is relatively low for both scenarios, r^2= 0.25, when snow is neglected, and r^2= 0.19, when snow is included.

2) Results for the closed ice cover cases and all surface temperatures
When we consider only the pixels that are almost completely ice-covered ($c_{ice} \geq 95\%$), the number of data points for the comparison reduces from N= 22798 to N= 17756. Compared to the scenario 1) simulations, the mean deviations and the root mean square deviations decrease, and the correlation coefficients increase for scenario 2), except for the mean deviation and the root mean square deviation for the simulations with snow at vertical polarisation, which increase slightly (Table 4.3).

3) Results for the closed ice cover cases and a fixed surface temperature
Here, we consider only the pixels that are both, almost completely ice-covered and have a surface temperature that is within one standard deviation of the average surface temperature, i.e. pixels with -37.3°C< T_{surf} <-28.3°C. These conditions are fulfilled by N= 12084 data points. Compared to scenarios 1) and 2), the root mean square deviations for scenario 3) decrease, and the correlation coefficients increase.
At horizontal polarisation, the root mean square deviation between simulated and measured brightness temperatures is 20.0 K, when the snow layer is neglected, and decreases to 4.4 K, when the snow layer is included. The correlation coefficient is r^2= 0.58 without snow, and r^2= 0.61 with snow.
At vertical polarisation, the correlation coefficient is r^2= 0.39 for both the simulations without snow and the simulations with snow. The corresponding root mean square deviations are 5.2 K for the simulations without snow, and 7.4 K for the simulations with snow.

4.4.4 Brightness temperatures for different snow thicknesses

The results of the comparison between measured and modelled brightness temperatures suggest that brightness temperatures observed by SMOS are influenced by the presence of a snow layer on top of the ice. According to the results from sections 4.2 and 4.3, brightness temperatures over snow-covered sea ice are independent of snow layer thickness, if only the dielectric properties of the snow layer are considered. However, due to the thermal insulation effect of snow, there is an indirect effect of snow thickness on brightness temperatures. A thicker snow layer isolates the ice layer more from the usually colder atmosphere than a thinner snow layer. In order to investigate this indirect impact of snow layer thickness on observed brightness temperatures, we divide the pixels that contain IceBridge measurements into five snow thickness classes and consider the corresponding SMOS brightness temperatures. We choose the snow thickness classes such that each class is represented by approximately the same amount

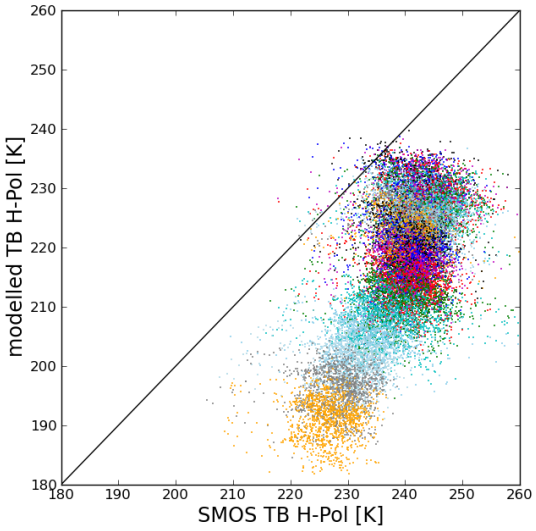

Figure 4.10: Horizontally polarised brightness temperatures as measured by SMOS and as modelled for IceBridge **ice thicknesses** using the model for **one ice layer**. The colors indicate the incidence angle increasing from 0° at the upper right corner to 60° at the lower left corner of the data cloud. The root mean square deviation between the brightness temperatures is 24.6 K, the correlation coefficient is r^2= 0.44 (for N= 22798).

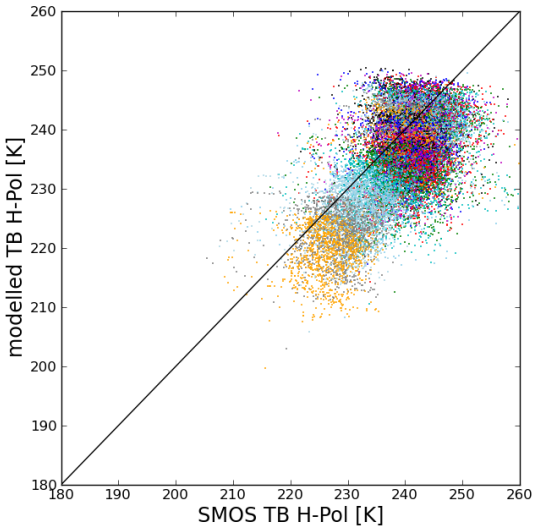

Figure 4.11: Horizontally polarised brightness temperatures as measured by SMOS and as modelled for IceBridge **ice and snow thicknesses** using the model for **one ice and one snow layer**. The colors indicate the incidence angle increasing from 0° at the upper right corner to 60° at the lower left corner of the data cloud. The root mean square deviation between the brightness temperatures is 7.8 K, the correlation coefficient is r^2= 0.38 (for N= 22798).

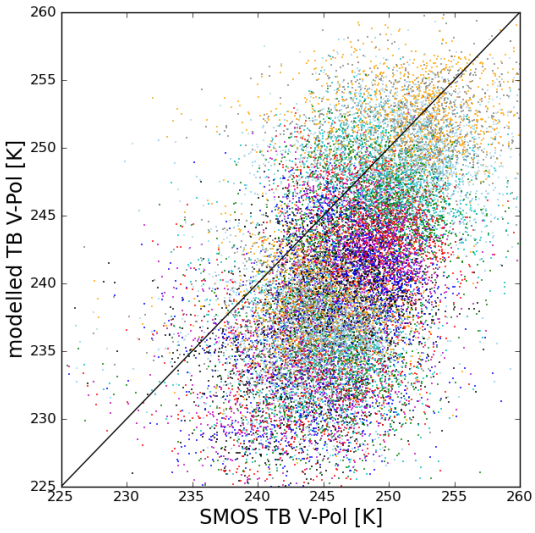

Figure 4.12: Vertically polarised brightness temperatures as measured by SMOS and as modelled for IceBridge **ice thicknesses** using the model for **one ice layer**. The colors indicate the incidence angle increasing from 0° at the lower left corner to 60° at the upper right corner of the data cloud. The root mean square deviation between the brightness temperatures is 8.6 K, the correlation coefficient is r^2= 0.25 (for N= 22798).

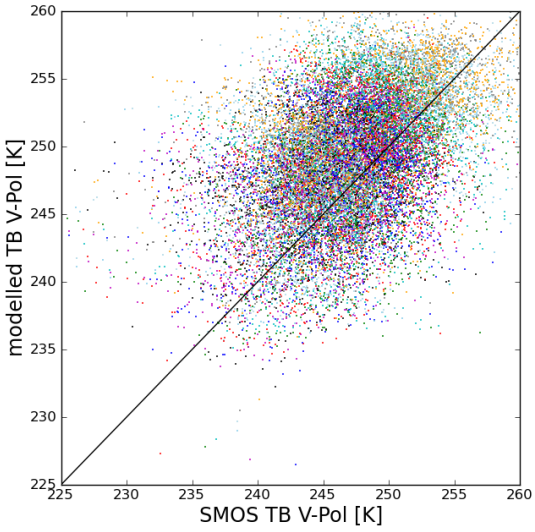

Figure 4.13: Vertically polarised brightness temperatures as measured by SMOS and as modelled for IceBridge **ice and snow thicknesses** using the model for **one ice and one snow layer**. The colors indicate the incidence angle increasing from 0° at the lower left corner to 60° at the upper right corner of the data cloud. The root mean square deviation between the brightness temperatures is 5.6 K, the correlation coefficient is r^2= 0.19 (for N= 22798).

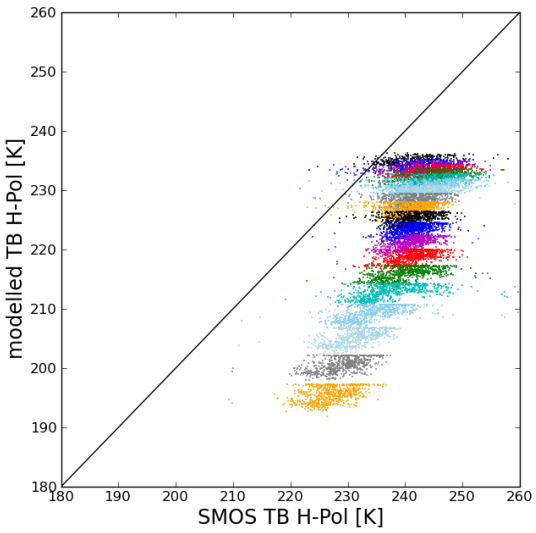

Figure 4.14: Horizontally polarised brightness temperatures as measured by SMOS and as modelled for IceBridge **ice thicknesses** using the model for **one ice layer**. The colors indicate the incidence angle increasing from 0° at the upper right corner to 60° at the lower left corner of the data cloud. Only data points with $c_{ice} \geq 95\%$ and -37.3°C< T_{surf} <-28.3°C are included. The root mean square deviation between the brightness temperatures is 20.0 K, the correlation coefficient is r^2= 0.58 (for N= 12084).

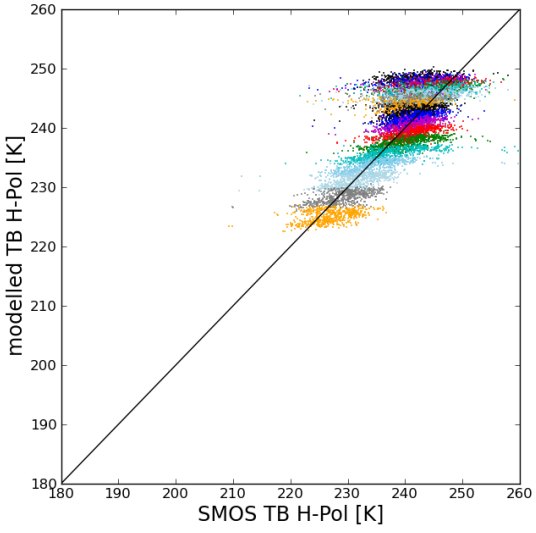

Figure 4.15: Horizontally polarised brightness temperatures as measured by SMOS and as modelled for IceBridge **ice and snow thicknesses** using the model for **one ice and one snow layer**. The colors indicate the incidence angle increasing from 0° at the upper right corner to 60° at the lower left corner of the data cloud. Only data points with $c_{ice} \geq 95\%$ and -37.3°C< T_{surf} <-28.3°C are included. The root mean square deviation between the brightness temperatures is 4.4 K, the correlation coefficient is r^2= 0.61 (for N= 12084).

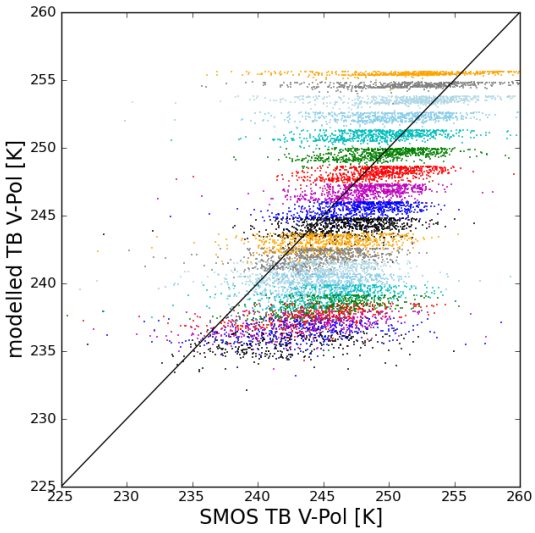

Figure 4.16: Vertically polarised brightness temperatures as measured by SMOS and as modelled for IceBridge **ice thicknesses** using the model for **one ice layer**. The colors indicate the incidence angle increasing from 0° at the lower left corner to 60° at the upper right corner of the data cloud. Only data points with $c_{ice} \geq 95\%$ and -37.3°C< T_{surf} <-28.3°C are included. The root mean square deviation between the brightness temperatures is 5.2 K, the correlation coefficient is r^2= 0.39 (for N= 12084).

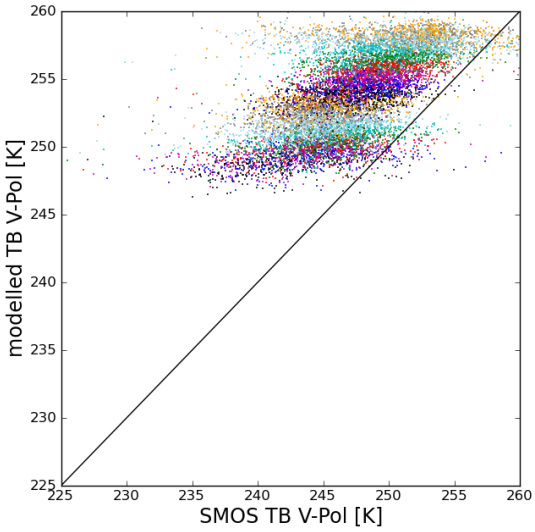

Figure 4.17: Vertically polarised brightness temperatures as measured by SMOS and as modelled for IceBridge **ice and snow thicknesses** using the model for **one ice and one snow layer**. The colors indicate the incidence angle increasing from 0° at the lower left corner to 60° at the upper right corner of the data cloud. Only data points with $c_{ice} \geq 95\%$ and -37.3°C< T_{surf} <-28.3°C are included. The root mean square deviation between the brightness temperatures is 7.4 K, the correlation coefficient is r^2= 0.39 (for N= 12084).

Table 4.1: Root mean square deviations RMSD, mean deviations MD, and correlation coefficients r^2 for simulated brightness temperatures and brightness temperatures as measured by SMOS for horizontal and vertical polarisation. The columns f(c_{ice}), f(T_{surf}) and $c_{ice} \geq 95\%$, f(T_{surf}) and $c_{ice} \geq 95\%$, $\Delta T_{surf} < 1\sigma_{T_{surf}}$ give the results for the simulation scenarios that are described in section 4.4.2 and indicated with 1) and 2) and 3), respectively.

			f(c_{ice}), f(T_{surf})	$c_{ice} \geq 95\%$, f(T_{surf})	$c_{ice} \geq 95\%$, $\Delta T_{surf} < 1\sigma_{T_{surf}}$
H-Pol	RMSD [K]	no snow	24.6	20.1	20.0
		snow	7.8	5.2	4.4
	MD [K]	no snow	22.9	18.3	18.5
		snow	4.4	-1.1	-0.9
	r^2	no snow	0.44	0.49	0.58
		snow	0.38	0.50	0.61
V-Pol	RMSD [K]	no snow	8.6	5.8	5.2
		snow	5.6	7.9	7.4
	MD [K]	no snow	5.8	1.8	2.0
		snow	-2.1	-6.7	-6.5
	r^2	no snow	0.25	0.28	0.39
		snow	0.19	0.26	0.39
Data points N			22798	17756	12084

of pixels. The snow thickness classes are 1) d_{snow}= 4 – 12 cm, 2) d_{snow}= 12 – 20 cm, 3) d_{snow}= 20 – 26 cm, 4) d_{snow}= 26 – 32 cm, and 5) d_{snow}= 32 – 44 cm. Each of the classes 1 – 5 contains between 128 and 282 pixels. For each class, we collect all SMOS brightness temperatures of the pixels with an average snow thickness in the corresponding snow thickness range. All SMOS brightness temperatures are then averaged over incidence angle ranges of 5° (except for the incidence angles averaged over θ= 0 – 10°), as was done in the previous section 4.4.3.
For comparison, we not only consider the observed brightness temperatures, but also simulate brightness temperatures for the snow thickness classes 1 – 5. Here, we again use the incoherent Burke model and fixed values for ice concentration, ice thickness, ice salinity, and ice surface temperature. We use only pixels with $c_{ice} \geq 95\%$ and set the ice concentration in the model to c_{ice}= 100%. For ice thickness in the model, we use the average value of all IceBridge ice thickness measurements with $c_{ice} \geq 95\%$, which is $< d_{ice} >$= 4 m. According to equation (4.21), the ice salinity of 4 m thick ice is S_{ice}= 1.52 g/kg, which is thus used in the model. For the surface temperature, we use the average value of all KT19 values, i.e. $< T_{surf} >$= -32.8°C.

Results

The observed and simulated brightness temperatures at vertical and horizontal polarisation for the five snow thickness classes are shown in Figure 4.18. The corresponding mean brightness temperatures, averaged over the whole incidence angle range, are

given in Table 4.2.

The observed brightness temperature
In general, the observed brightness temperatures for all incidence angles increase with increasing snow thickness for both horizontal and vertical polarisation. When averaged over the whole incidence angle range, brightness temperatures at horizontal polarisation increase by 1.1 K from snow thickness class 1 to 2. Brightness temperatures increase by 2.9 K from snow thickness class 2 to 3, by additional 0.9 K for snow thickness class 4, and another 0.6 K for snow thickness class 5.
At vertical polarisation, there is a clear increase of brightness temperatures averaged over the whole incidence angle range by 1.6 K from snow thickness class 1 to 2, and by 2.7 K from 2 to 3. However, the vertically polarised brightness temperatures for snow thickness classes 3 – 5, i.e. for snow thicknesses d_{snow}= 20 – 44 cm, are very similar. When averaged over the whole incidence angle range, the brightness temperatures for these three snow thickness classes differ by only 0.3 K.
Brightness temperatures increase more pronouncedly from snow thickness class 2 to 3, than from 1 to 2. This reflects the fact, that the average snow thickness of snow thickness class 1 is 10.2 cm, while the average snow thicknesses of 2 and 3 are 15.3 cm and 23.4 cm, respectively. Thus, snow thickness from 1 to 2 increases on average by 5.1 cm, while snow thickness from 2 to 3 increases on average by 8.1 cm. For the other cases, the increase of brightness temperatures with increasing snow thickness is smaller for higher snow thicknesses.

Comparison of modelled and observed brightness temperature
When we compare the observed brightness temperatures with the modelled brightness temperatures, we find a good agreement for horizontal polarisation, when averaged over the whole incidence angle range, while there is a systematic overestimation of brightness temperatures by the model at vertical polarisation. For low incidence angles $\theta < 20°$, observed brightness temperatures are about 5 – 8 K lower than the modelled brightness temperatures. This is in accordance with reports about problems with the SMOS brightness temperature processor that cause brightness temperatures for low incidence angles to be some K too low (Manuel Martin-Neira, personal communication, 27th September, 2012).
When averaged over the whole incidence angle range, at horizontal polarisation the mean deviation between the model and the observations is 2.1 and 2.0 K for the snow thickness classes 1 and 2, respectively; the mean deviation for the snow thickness classes 3 – 5 is between 0.2 and 0.4 K. Thus, brightness temperatures are on average slightly overestimated by the model, when compared to the observations. At vertical polarisation, we find mean deviations between the model and the observations between 4.2 and 6.2 K for the five snow thickness classes.

4.4.5 Potential for snow thickness retrieval using SMOS

The results from the previous sections suggest that observed brightness temperatures at vertical polarisation are less affected by the presence of a snow cover than the brightness temperatures at horizontal polarisation. Furthermore, with our radiation

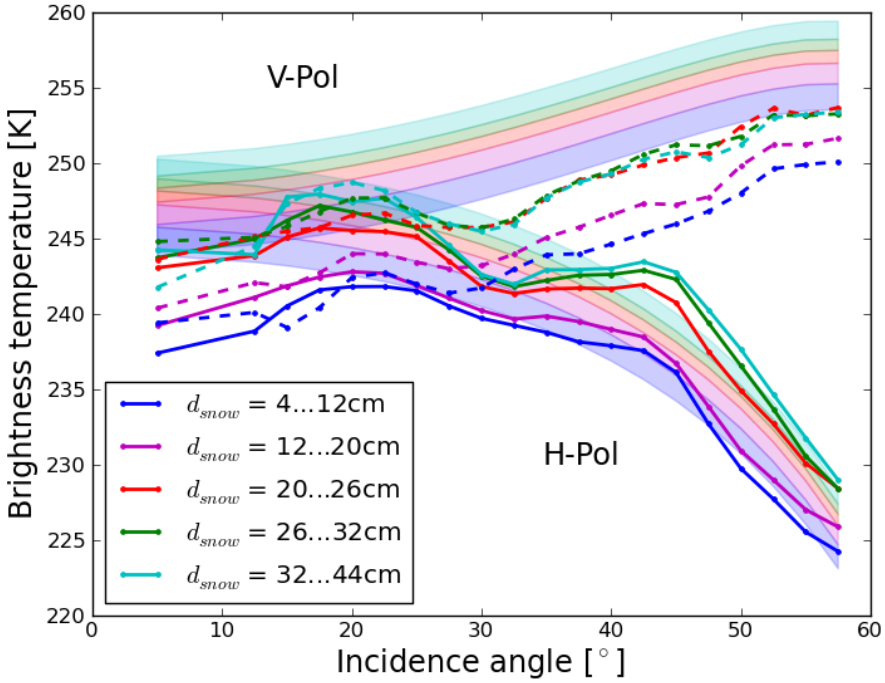

Figure 4.18: Brightness temperatures as simulated and as measured by SMOS for the snow thickness classes 1 – 5 as given in the figure legend. The shaded areas indicate the brightness temperature simulations, the lines indicate the averaged brightness temperature measurements. The solid lines indicate horizontal polarisation, the dashed lines indicate vertical polarisation.

Table 4.2: Average snow thicknesses and brightness temperatures averaged over incidence angle range 0 – 60° as simulated (TB_{mod}) and as observed by SMOS (TB_{obs}) at horizontal and at vertical polarisation for the snow thickness classes 1 – 5.

		4 – 12 cm	12 – 20 cm	20 – 26 cm	26 – 32 cm	32 – 44 cm
$< d_{snow} >$ [cm]		10.2	15.3	23.4	29.0	35.0
H-Pol	TB_{obs} [K]	236.6	237.7	240.6	241.5	242.2
	TB_{mod} [K]	238.7	239.7	241.0	241.7	242.4
V-Pol	TB_{obs} [K]	244.0	245.6	248.3	248.7	248.5
	TB_{mod} [K]	250.2	251.2	252.5	253.3	254.0

model simulated and observed brightness temperatures for snow-covered thick sea ice agree considerably better for horizontal than for vertical polarisation. Thus, we here investigate whether horizontally polarised brightness temperatures as observed by SMOS have the potential for the retrieval of snow thickness over thick Arctic sea ice. For comparison, we also consider the retrieval as obtained from vertically polarised brightness temperatures. As mentioned earlier, a potential retrieval of snow thickness would exploit the fact that the temperature of ice depends on the thickness of the snow cover. The retrieval would thus be an indirect method to derive snow thickness from SMOS brightness temperatures.
In order to investigate how successfully we can retrieve snow thickness over thick sea ice from SMOS, we use different simulation scenarios to simulate brightness temperatures at both horizontal and vertical polarisation over a range of incidence angles. In these simulation scenarios, we use fixed values for all model input parameters and perform the simulations for different snow thicknesses (d_{snow}= 5, 6, 7, ..., 55 cm). These simulated brightness temperatures are then compared with observed SMOS brightness temperatures over a range of incidence angles. The retrieved snow thickness is the snow thickness that is related with the simulation that has the lowest root mean square deviation between the simulated and the observed brightness temperatures.

The model scenarios
For the retrieval procedure, we need to assume fixed values for the model input parameters ice surface temperature, ice salinity, ice thickness, ice concentration, snow density, and water temperature and salinity. Water salinity is again assumed to be S_{water}= 33 g/kg, and the water temperature is assumed to be at the corresponding freezing temperature T_{water}= -1.8°C. As long as the values assumed for water temperature and salinity are in a reasonable range of values, the chosen values influence only very slightly the resulting brightness temperatures. The agreement between modelled and observed brightness temperatures in section 4.4.3 is highest for the cases, where we constrain our analyses to SMOS pixels that are almost completely ice-covered ($c_{ice} \geq$ 95%) and whose surface temperature is within a certain range (-37.3°C< T_{surf} <-28.3°C). Thus, we use only these pixels for our attempt to retrieve snow thickness, and assume an ice concentration c_{ice}= 100% and use a constant surface temperature for our simulations.
Because the remaining model input parameters are only roughly estimated in section 4.4.3, we here assume different values for these parameters in the different scenarios. We perform the simulations for 14 different scenarios. The settings of these scenarios are given in Table A.18 in the appendix. In section 4.4.3, the ice surface temperature is assumed to be T_{surf}= -32.8°C, the ice salinity is S_{ice}= 1.52 g/kg, the ice thickness is d_{ice}= 4 m, and the snow density is ρ_{snow}= 260 kg/m^3. In the scenarios here, the surface temperature takes values between -40.15 and -33.15°C, the ice salinity is 1.52 or 2.5 g/kg, the ice thickness is between 3 and 5 m, and the snow density takes values between 200 and 320 kg/m^3. Additionally, we consider simulations over the incidence angle range 15 – 50° or 15 – 60°. The simulated brightness temperatures are then compared to SMOS brightness temperatures only using data from the day on which the corresponding IceBridge measurements took place, or additionally from the day before and after that day. Thus, in the latter comparison we average the SMOS

brightness temperatures over three days.

Results

The root mean square deviations and the correlation coefficients between the IceBridge snow thicknesses and the snow thicknesses retrieved from SMOS brightness temperatures for the 14 simulation scenarios are shown in Figure 4.19. The corresponding minimum, maximum, and mean values for the root mean square deviations and the correlation coefficients are given in Table 4.3. The values for all simulation scenarios are given in the Tables A.19 and A.19 in the appendix.
The results from the previous sections suggest that the sensitivity of brightness temperature to snow thickness decreases with increasing snow thickness. Thus, the accuracy of a potential snow thickness retrieval from SMOS brightness temperatures is expected to be higher for lower snow thicknesses. Therefore, we here also compare only the SMOS retrieved snow thicknesses $d_{snow} < 35$ cm with IceBridge snow thickness measurements. For these lower snow thicknesses, only the results for horizontal polarisation are depicted in Figure 4.19 and Table 4.3, because for vertical polarisation almost all retrieved snow thicknesses are below 35 cm, even if they are not explicitly constrained to these values.

Comparison of snow thicknesses for the different scenarios

At vertical polarisation, the root mean square deviations and the correlation coefficients between the IceBridge and the SMOS snow thicknesses show an approximately linear relationship (Figure 4.3). Lower correlation coefficients coincide with higher root mean square deviations, and higher correlation coefficients coincide with lower root mean square deviations. For the 14 simulation scenarios for vertical polarisation, the correlation coefficients r^2 take values between 0.03 and 0.35, on average we obtain a correlation coefficient $r^2 = 0.19$. The root mean square deviations between the IceBridge and the SMOS snow thicknesses range between 12.48 and 17.28 cm, the average value being 15.19 cm.
At horizontal polarisation, there is no coincidence between high correlations and low root mean square deviations, or low correlations and high root mean square deviations. For the 14 simulation scenarios for horizontal polarisation, the correlation coefficients r^2 take values between 0.51 and 0.64, on average we obtain a correlation coefficient $r^2 = 0.59$. The root mean square deviations between the IceBridge and the SMOS snow thicknesses range between 10.95 and 18.02 cm, the average value being 12.89 cm. Thus, all correlation coefficients for horizontal polarisation are higher than for vertical polarisation. The range of correlation coefficients is smaller at horizontal than at vertical polarisation, while the range of root mean square deviations is broader at horizontal than at vertical polarisation. However, the minimum and the mean values of the root mean square deviations for horizontal polarisation are smaller than for vertical polarisation.
If we consider only pixels for which the retrieval from horizontally polarised SMOS brightness temperatures gives snow thicknesses $d_{snow} < 35$ cm, the correlation coefficients slightly decrease, compared to the case, when we consider all snow thicknesses. The maximum correlation coefficient is $r^2 = 0.58$, and the average is $r^2 = 0.52$. The

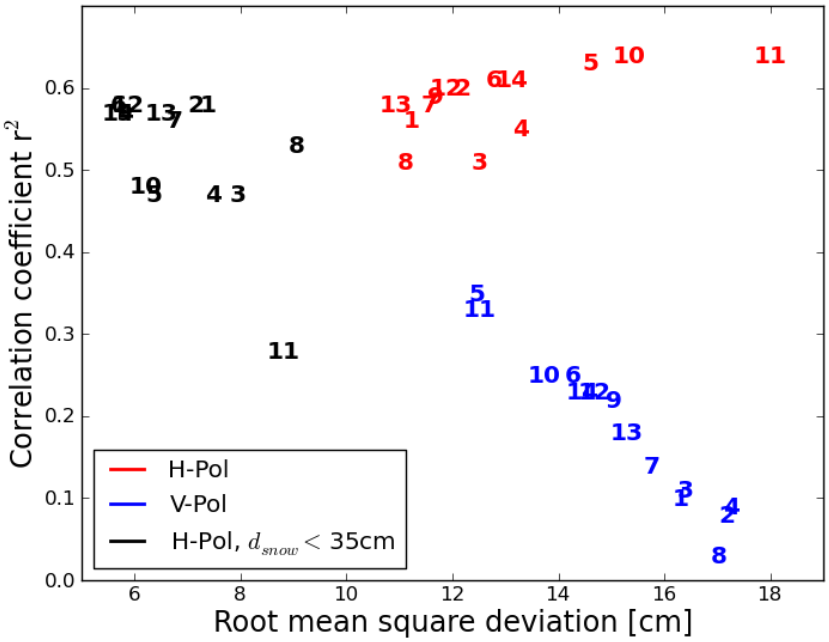

Figure 4.19: Correlation coefficients r^2 and root mean square deviations for the IceBridge snow thicknesses and the snow thicknesses retrieved from SMOS brightness temperatures for 14 different simulation scenarios. The numbers give the scenario number. The settings of the scenarios are given in Table A.18 in the appendix. The red and blue numbers show the results for the consideration of all snow thicknesses. The red numbers indicate horizontal, the blue numbers vertical polarisation. The black numbers indicate the results for horizontal polarisation, when only snow thicknesses $d_{snow} < 35$ cm (as retrieved from SMOS) are considered.

Table 4.3: Minimum, maximum, and mean root mean square deviations RMSD and correlation coefficients r^2 for the IceBridge snow thicknesses and the snow thicknesses as retrieved from SMOS brightness temperatures for the 14 simulation scenarios given in Table A.18 in the appendix. The values are given for the retrieval with horizontally and with vertically polarised brightness temperatures, as well as for horizontally polarised brightness temperatures, when only retrieved snow thicknesses $d_{snow} < 35$ cm are considered.

		MIN	MAX	MEAN
RMSD [cm]	H-Pol	10.95	18.02	12.89
	V-Pol	12.48	17.28	15.19
	H-Pol ($d_{snow} < 35$ cm)	5.71	9.07	6.93
r^2	H-Pol	0.51	0.64	0.59
	V-Pol	0.03	0.35	0.19
	H-Pol ($d_{snow} < 35$ cm)	0.28	0.58	0.52

minimum correlation is r^2= 0.26, but except for the one simulation scenario that has this low value, all other correlation coefficients r^2 take values between 0.47 and 0.58. The root mean square deviations are between 5.71 and 9.07 cm, the average value being 6.93 cm.

Comparison of snow thicknesses for one of the scenarios

We choose the simulation scenario no. 6 for a comparison between IceBridge and SMOS snow thicknesses. For this simulation scenario, the root mean square deviation is lowest, when we consider only snow thicknesses retrieved to be $d_{snow} < 35$ cm. For this simulation, the ice surface temperature is assumed to be T_{surf}= -38.15°C, the ice salinity is S_{ice}= 1.52 g/kg, the ice thickness is d_{ice}= 4 m, and the snow density is ρ_{snow}= 260 kg/m^3. We consider simulations over the incidence angle range 15 – 50°, and we use SMOS brightness temperatures averaged over three days.

The comparison for all snow thicknesses shows a good average agreement for snow thicknesses up to about 30 – 35 cm and an overestimation of snow thicknesses for thicker snow layers (Figure 4.20). The average snow thickness from the SMOS retrieval is $< d_{snow} >$= 26.5 cm, while the average IceBridge snow thickness is $< d_{snow} >$= 20.4 cm. The correlation coefficient for the snow thicknesses of this simulation scenario is r^2= 0.61, and the root mean square deviation is 12.79 cm.

If we consider only snow thicknesses retrieved to be $d_{snow} < 35$ cm (Figure 4.21), the correlation coefficient for the snow thicknesses of this simulation scenario is r^2= 0.58, and the root mean square deviation is 5.71 cm. The average snow thickness from the SMOS retrieval is $< d_{snow} >$= 16.9 cm, and the average IceBridge snow thickness is $< d_{snow} >$= 17.2 cm. Thus, the average snow thicknesses differ by only 0.3 cm.

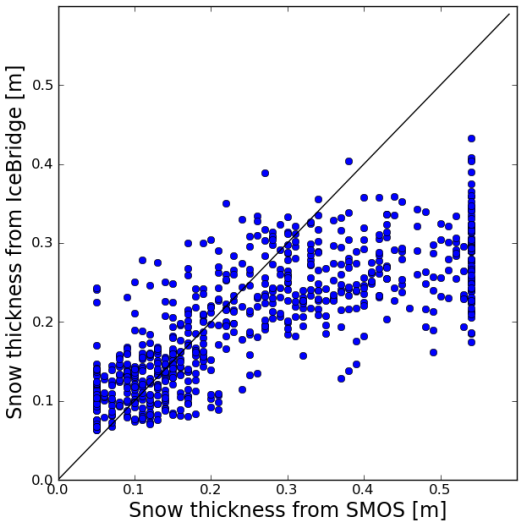

Figure 4.20: Snow thicknesses as retrieved from horizontally polarised SMOS brightness temperatures versus coincident snow thicknesses as measured during the IceBridge campaign. Here, we show the results for the simulation with θ= 15 – 50°, T_{surf}= -38.15°C, ρ_{snow}= 260 kg/m^3, d_{ice}= 4 m, and S_{ice}= 1.52 g/kg (simulation scenario no. 6).

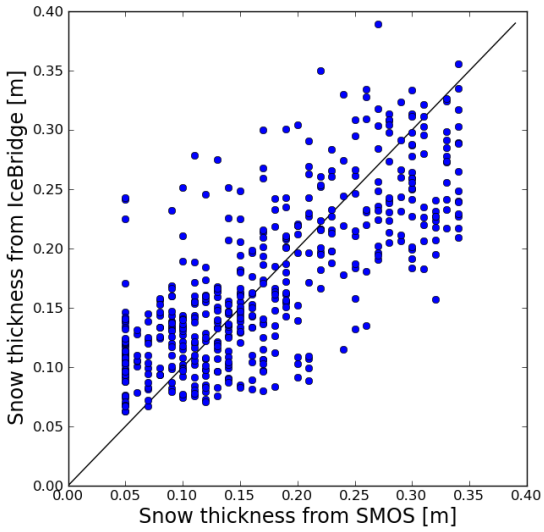

Figure 4.21: For figure description see caption of Figure 4.20, but here we show only the snow thicknesses for that the retrieval from SMOS brightness temperatures gives snow thicknesses $d_{snow} < 35$ cm.

4.5 Summary and Discussion

In this chapter, we investigated the impact of a potential snow layer on L-band brightness temperatures, the consequences for an ice thickness retrieval from SMOS brightness temperatures, and the potential to estimate snow thickness above thick Arctic sea ice from SMOS brightness temperatures. We used the coherent Ulaby model and the incoherent Burke model to simulate brightness temperatures of snow-covered sea ice, and to theoretically examine the influence of a snow layer on sea ice brightness temperatures. The incoherent Burke model was then used to simulate brightness temperatures for ice and snow thicknesses measured during a flight campaign in the Arctic. We compared these simulations with brightness temperatures measured by SMOS, and investigated the impact of the snow layer's thickness on observed brightness temperatures. Finally, we used the flight campaign data to evaluate the potential to estimate snow thickness from SMOS brightness temperatures.

Dielectric properties of snow
First, we added a snow layer on top of a layer of sea ice in both the coherent Ulaby and the incoherent Burke model. A very thin layer of snow (d_{snow}= 1 mm) had an impact on brightness temperatures as modelled with the incoherent Burke model, but not on brightness temperatures as modelled with the coherent Ulaby model. For a rather thick snow layer of 50 cm thickness, we obtained consistent results from both models. The incoherent Burke model represented the average brightness temperatures of the oscillating signal in the coherent Ulaby model. We observed this consistency of the models also when we increased the thickness of the snow layer on top of an ice layer of constant thickness. One of our aims was to investigate whether the incoherent Burke model, which is based on the radiative transfer equation, is suitable for the implementation of a snow layer on ice, although the Burke model neglects higher order reflection terms. We expected this negligence to have a higher impact for thin layers and for media with low attenuation. However, our model comparison showed that the incoherent Burke model represents well the average brightness temperatures of snow-covered sea ice as modelled with the coherent Ulaby model, which accounts for higher order reflection terms. As for the transition from open water to a very thin ice layer, the incoherent Burke model does not reduce to the value of snow-free ice for very thin snow layers. Thus, the incoherent Burke model is not suitable for modelling very thin ice (approximately below 1 – 2 cm), and, as was confirmed in this study, not for very thin snow layers on ice.
In L-band frequencies, dry snow is almost transparent. Thus, snow modifies only very slightly the brightness temperature of the underlying sea ice that would be observed, if the snow layer was not present. Nevertheless, the presence of a snow layer modifies brightness temperatures above sea ice, because the snow layer emits radiation itself. In L-band, the emissivity of snow is generally higher than the emissivity of sea ice. In accordance with these considerations, our brightness temperatures modelled for snow-covered sea ice were higher than brightness temperatures of snow-free sea ice. For our model assumptions and negligence of the thermal insulation by snow, the presence of a snow layer on ice caused brightness temperatures to increase by 10 K at nadir view. At horizontal polarisation, the brightness temperature increase caused

by snow increased with increasing incidence angle and reached 25 K at θ= 50°. In contrast, at vertical polarisation, the increase of brightness temperatures due to the presence of a snow cover decreased with increasing incidence angle. At θ= 50°, the vertically polarised brightness temperatures of snow-covered and snow-free sea ice were almost identical. The resulting brightness temperatures were similar for dry and wet snow, if the snow thickness had values typically observed on thin sea ice. For thick layers of wet snow (here: d_{snow}= 50 cm), brightness temperatures were almost independent of ice thickness and took the values for an infinitely thick layer of wet snow.
When we considered only the dielectric properties of snow, brightness temperatures as modelled with both radiation models were almost independent of snow thickness. With increasing snow thickness, brightness temperatures converged to the brightness temperatures of an infinitely thick snow layer. However, this increase was very small. The brightness temperatures of sea ice covered by dry snow increased only by 0.7 to 2.7 K for an increase of snow thickness by 10 m for the incidence angles and polarisations considered here. For wet snow, the brightness temperatures that would be observed over an infinitely thick layer of snow were reached already for thinner snow layers. However, the dependence on snow thickness was still very small, and brightness temperatures increased by 0.8 to 1.9 K for an increase of snow thickness by 1 m.

Thermal insulation by snow
Additionally to its dielectric properties, a snow layer modifies brightness temperatures above sea ice due to the thermal insulation effect of snow. The bulk ice temperature of snow-covered ice is usually higher than the bulk ice temperature of bare sea ice. In order to investigate the effect of thermal insulation by snow on brightness temperatures, we assumed snow thicknesses as they have been observed during field campaigns and used a simple heat conduction model to estimate the snow and ice temperatures. The thickness of the snow layer was assumed to be about 10% of the ice thickness for the Arctic, and 20% for the Baltic Sea. To calculate the bulk snow and ice temperatures from the snow surface temperature, we assumed the snow-ice-column to be in thermal equilibrium and used typical values for the thermal conductivities of ice and snow.
We found that, for all considered cases, the increased ice temperatures due to thermal insulation by snow increased the modelled brightness temperatures. At higher incidence angles at vertical polarisation, only the thermal insulation effect of snow caused an increase of brightness temperatures, while the presence of a snow cover had almost no impact, when the temperature effect was neglected. At lower incidence angles and at horizontal polarisation, the brightness temperature increase caused by the higher ice temperatures due to thermal insulation of snow added on the increase by the dielectric properties of snow. The contribution to the brightness temperature increase by the dielectric properties was higher than the contribution by thermal insulation. Due to the higher snow thicknesses assumed for Baltic Sea ice, the brightness temperature increase due to thermal insulation was higher for the Baltic than for the Arctic sea ice.
Regarding the observed increase of brightness temperatures due to thermal insulation

of snow, we have to pay regard to the ice temperature assumed for our model simulations. According to our sensitivity studies in section 3.1.3, brightness temperatures increase with increasing ice temperatures for ice temperatures up to a reversal point. The ice temperature of this reversal point depends on ice salinity and ice thickness. The ice salinities in the investigations in section 3.1.3 and in the snow-related investigations here were equal (S_{ice}= 8 g/kg). For this ice salinity, the reversal point occured at an ice surface temperature of about -3°C for an ice thickness of 15 cm, and at an ice surface temperature of about -10°C for an ice thickness of 60 cm. For ice surface temperatures higher than these values, brightness temperatures decreased for further increasing ice surface temperatures. Our brightness temperature simulations for the investigation of the snow impact were performed for an ice surface temperature of T_{surf}= -15°C. Thus, if we had considered a higher ice surface temperature, the thermal insulation effect of snow could have caused a decrease of brightness temperature. Because the contribution of the dielectric properties of snow was higher than the contribution by thermal insulation of snow, the overall effect of a snow layer would still be an increase of the brightness temperature of snow-covered ice compared to the brightness temperature of snow-free ice.
The coherent Ulaby model showed two superimposed oscillations in brightness temperature, one caused by variation of ice thickness, the other by variation of snow thickness. As for the model results in the first section, the incoherent Burke model represented well the average value of the oscillating brightness temperature modelled with the coherent Ulaby model.

Comparison of simulated and observed brightness temperatures
In order to test the validity of our results from the theoretical investigations, we used snow and ice thickness measurements from the IceBridge flight campaign in spring 2012 in the Arctic to simulate brightness temperatures and compared these simulated brightness temperatures with brightness temperatures measured by SMOS. The IceBridge measurements were mainly taken over thick multi-year ice. Thus, they were not suitable for the validation of sea ice thickness retrieval from SMOS. However, the ice and snow thickness information was used here to validate the capability of the incoherent Burke model to realistically simulate brightness temperatures.
For the comparison of simulated and measured brightness temperatures, we calculated the root mean square deviations and the correlation coefficients between the brightness temperatures. The smaller the root mean square deviation, the better our model represents brightness temperatures as measured with SMOS. We should be careful, when we consider the correlation coefficient, because a high correlation between the brightness temperatures does not necessarily mean that the model and the observations agree well. A high correlation here means, that the brightness temperatures can be related to each other without large errors, when a certain linear function is used, which is not necessarily the identity function. Provided that there is a relationship between the two quantities, a high correlation and a contemporaneous high root mean square deviation would mean, that our model does not represent the observations well, even if the two independent data sets are highly related with each other.
For comparison with brightness temperatures observed with SMOS, we neglected the snow cover in one simulation and included the snow cover in the other simulation.

At horizontal polarisation, brightness temperatures modelled for a snow cover on ice agreed considerably better with the observed SMOS brightness temperatures than the brightness temperatures modelled for snow-free sea ice. For the simulations with snow, the mean deviation and the root mean square deviation decreased, while the correlation remained approximately constant. At vertical polarisation, the difference between simulations without and with a snow cover was considerably smaller. A result that confirmed the findings from the previous sections.
The simulations were performed for different constraints concerning the ice concentration and the ice surface temperature of the included pixels. In one scenario we considered only pixels that were almost completely ice-covered ($c_{ice} \geq 95\%$) and that had a surface temperature within one standard deviation of the average surface temperature measured during the IceBridge campaign. For this scenario, ice concentration and ice surface temperature were set to constant values. At vertical polarisation, brightness temperatures were less affected by these constraints than at horizontal polarisation. At vertical polarisation, the mean deviation and the root mean square deviation between the SMOS observations and the snow simulations even increased slightly, when we constrained the compared data accordingly. The root mean square deviations between the simulated and the measured brightness temperatures at vertical polarisation ranged between 5.2 and 8.6 K. However, the correlation coefficient r^2 increased from 0.25 (without snow) and 0.19 (with snow) to 0.39, when we considered only pixels with high ice concentrations and certain surface temperatures.
At horizontal polarisation, the agreement between simulated and measured brightness temperatures improved considerably, when we excluded pixels with low ice concentrations and ice surface temperatures outside the defined range and used constant values instead. For both, the simulations that neglect a snow layer and the simulations that include a snow layer, the mean deviation and the root mean square deviation decreased, while the correlation coefficient increased. For the simulations that include a snow layer, the mean deviation decreased from +4.4 to -0.9 K, the root mean square deviation decreased from 7.8 to 4.4 K, and the correlation coefficient r^2 increased from 0.38 to 0.61. For these constrained pixels, the root mean square deviation between simulated and measured brightness temperatures decreased from 20.0 K, when the snow layer was neglected, to 4.4 K, when the snow layer was included in the simulations. The mean deviation decreased from 18.5 K (without snow) to -0.9 K (with snow). The correlation coefficients were very similar for the simulations without snow (r^2= 0.58) and with snow (r^2= 0.61).
The reasons for the deviations between simulated and observed brightness temperatures are mainly the remaining uncertainties for the ice and snow thicknesses, the ice concentration, the ice temperature, and the ice salinity. While we had information on the former ice parameters, the ice salinity was only roughly estimated from the ice thickness using an empirical relationship between ice salinity and thickness. The IceBridge measurements were mainly taken over thick sea ice. The average value was 4 m and there were only very few measurements over sea ice with a thickness lower than 1 m. At these high ice thicknesses, ice thickness itself does not have a large impact on brightness temperature, whereas the salinity of thick sea ice is usually low, and, according to our studies in section 3.2, brightness temperature sensitivity to ice

salinity variations is very high for sea ice with low salinities. Hence, knowledge on ice salinity is more crucial for thick multi-year ice with low salinities, as considered here, than for thin first-year ice with high salinities.

Dependence of brightness temperatures on snow thickness
According to our model calculations in section 4.2, the brightness temperature of snow-covered sea ice is almost independent of the snow layer's thickness, as long as the thermal insulation effect of snow is neglected. However, the thickness of the snow layer has an impact on the temperature of the underlying sea ice. Usually, the underlying sea ice is warmer for thicker snow layers. In order to investigate whether this snow thickness dependence due to thermal insulation of snow is observed in SMOS brightness temperatures, we defined five snow thickness classes for the snow thicknesses measured during the IceBridge campaign (d_{snow}= 4 – 44 cm). We showed that, in accordance with our theoretical considerations, the corresponding averaged SMOS brightness temperatures for all considered incidence angles (θ= 0 – 60°) increased with increasing snow thickness. From the snow thickness class with d_{snow}= 4 – 12 cm to the snow thickness class with d_{snow}= 32 – 44 cm, SMOS brightness temperatures increased by 5.6 K at horizontal polarisation, and by 4.5 K at vertical polarisation. The observed increases were somewhat higher than the modelled increases of 3.7 K at horizontal, and 3.8 K at vertical polarisation. When averaged over the incidence angle range (θ = 0 – 60°), the modelled and the observed brightness temperatures for the five snow thickness classes differed by 0.2 – 2.1 K at horizontal polarisation, while at vertical polarisation the model overestimated the averaged observed brightness temperatures by about 5 – 8 K.

Retrieval of snow thickness from SMOS
The observed increase of brightness temperatures with increasing snow thickness raised the question, whether we can retrieve information on snow thickness over thick multi-year sea ice from SMOS brightness temperatures, especially from horizontal polarisation, which is influenced more by a snow layer. The approach to retrieve snow thickness from measured brightness temperatures used here was the following: We assumed constant values for all ice parameters except snow thickness and simulated brightness temperatures for a range of snow thicknesses. Subsequently, we calculated the difference between the modelled and the measured brightness temperatures. The retrieved value for snow thickness was then the snow thickness for which the simulations had the lowest deviation from the measured brightness temperatures.
For the attempt to retrieve snow thickness from SMOS brightness temperatures, we set up different simulations that assumed different constant values for the model input parameters surface temperature, ice salinity, ice thickness, and snow density. Additionally, we used different incidence angle ranges and averaged brightness temperatures over one day or three days of SMOS data. For the model input parameters we assumed values within a range that is likely to occur in nature. Thus, we were able to estimate how the retrieval would perform under the least suitable and under the most suitable assumptions for the above mentioned ice parameters, if we had no exact information on ice conditions. Ideally, we would have performed the simulations for all possible combinations of the ice parameters that were varied here. However, we think

that the 14 selected scenarios representatively cover the range of conceivable settings and the corresponding results. The surface temperatures were varied only over a range of 7°C here, because we can assume that for the retrieval of snow thickness from SMOS brightness temperatures, we would have at least some information on ice temperature, for example from air temperatures, which are quite easily available from observations or near real-time reanalysis data.

When compared to snow thickness measurements from the IceBridge campaign, we obtained better results for the retrieval of snow thickness from brightness temperatures at horizontal polarisation than from brightness temperatures at vertical polarisation, as was expected from the previous findings. For horizontal polarisation, the correlation coefficients r^2 for the 14 considered simulation scenarios ranged between 0.51 and 0.64; the average value was 0.59. Thus, the correlation coefficients obtained here were higher than the correlation coefficient of $r^2 = 0.49$, which was obtained for comparison of IceBridge snow thicknesses and field measurements in a previous study (Farrell et al., 2012). Here, the root mean square deviations between the snow thicknesses ranged between 11.0 and 18.0 cm; the average value was 12.9 cm. We observed that for higher snow thicknesses, the SMOS retrieval overestimated snow thickness. Thus, in a second comparison we considered only snow thicknesses that, according to the SMOS retrieval, were lower than 35 cm. For these snow thicknesses, the root mean square deviations for the 14 simulation scenarios ranged between 5.7 and 9.1 cm; the average value was 6.9 cm. When we used the simulation scenario for that the SMOS snow thickness retrieval had the highest agreement with IceBridge snow thicknesses, the resulting average snow thicknesses differed only by 0.3 cm for $d_{snow} < 35$ cm; the average snow thickness retrieved from SMOS was 16.9 cm, as compared to 17.2 cm for the average IceBridge snow thickness.

Here, we used a retrieval method based on discretized snow thickness values. More continuous results would have been obtained, if we used a gradient method, for which the deviation between simulated and observed brightness temperatures quickly approaches towards minimum values. Thus, we would not have to compare simulated and observed brightness temperatures for the entire snow thickness range and could resolve snow thicknesses on a finer scale. However, as the accuracy of the snow thickness retrieval is in the order of several cm, the results from a retrieval approach giving finer resolved snow thicknesses would not differ from our findings here. Though, such a gradient based retrieval approach could be more advisable for large-scale retrieval of snow thickness.

A conceivable reason for the observed dependence between snow thickness and brightness temperature is that brightness temperature actually depends on ice thickness (even if the ice is very thick). If this was the case, we would possibly observe a dependence between snow thickness and brightness temperature, because snow thickness is related to ice thickness, as it has been observed in the Arctic, e.g. by Doronin (1971), who found that snow thickness was on average 10% of ice thickness (for ice thicknesses $d_{ice} > 20$ cm). In order to exclude this possibility, we tried to retrieve ice thickness with the same approach as for the snow thickness (not shown here). The results confirmed that brightness temperatures cannot be mainly attributed to ice thickness, as the correlation between ice thicknesses was negative with $r^2 \approx 0.2$, and root mean square deviations were almost 4 m.

Here, the retrieval exploited the SMOS measurement principle of observing brightness temperatures not only under one incidence angle but for a range of incidence angles. We want to stress, that the retrieval was not successful, when we considered only single SMOS measurements or SMOS brightness temperatures from certain incidence angles. One reason is that the SMOS brightness temperatures have a relatively high variability. Thus, we need to average over as many measurements as possible in order to extract any information from the brightness temperatures. A second reason is, that with our radiation model we succeeded to simulate brightness temperatures averaged over a range of incidence angles such that they agreed well with SMOS measurements. However, the SMOS brightness temperatures showed some oscillations, when considered as a function of incidence angle. Using our model, at the present state, we were not able to reproduce these oscillations with increasing incidence angle, but only the average brightness temperature over the incidence angle range. These observed oscillations could be related to roughness effects on the ice and snow surface, which are not taken into account by our model.

To conclude, even if the retrieval of snow thickness from SMOS brightness temperatures is only based on the indirect effect, that ice that is covered by a thicker snow layer is warmer than ice covered by a thinner snow layer, we indeed are able to reasonably estimate the snow thickness over thick multi-year sea ice from SMOS brightness temperatures at horizontal polarisation.

Chapter 5

SMOS sea ice thickness retrieval in the Baltic Sea

In this chapter, we evaluate the ice thickness retrieval from SMOS brightness temperatures in the Baltic Sea. We choose the Baltic Sea for our validation approach because of the availability of ice thickness information for this region. However, the Baltic Sea area is challenging for SMOS ice thickness retrievals, because in this land-enclosed basin, the land impact is relatively high and has mainly two implications. On the one hand, a large fraction of the observed brightness temperatures is influenced by land surfaces. On the other hand, we expect more artificial sources of L-Band radiation (RFI) than in the Arctic. Both effects mainly restrict the availability of usable brightness temperature data. We expect that, if the ice thickness retrieval with SMOS succeeds in a challenging region like the Baltic Sea, the ice thickness retrieval from SMOS brightness temperatures is probably also applicable in other regions.
In section 5.1, we give a short overview of the characteristics of ice in the Baltic Sea. In the following two sections, we use the incoherent Burke radiation model to simulate brightness temperatures in the Baltic Sea. We compare these modelled brightness temperatures with brightness temperatures measured by SMOS. In section 5.2, we compare brightness temperatures over ice-free water in order to evaluate how well the brightness temperature of sea water is represented by our model. In section 5.3, we compare simulated and measured brightness temperatures over growing ice in the Baltic Sea. We use ice thickness maps from the Finnish Meteorological Institute (FMI) to estimate ice thickness, and thus assess the potential for ice thickness retrieval from SMOS brightness temperatures in the Baltic Sea. In section 5.4, we then compare ice thicknesses as retrieved with our model from SMOS brightness temperatures with ice thicknesses measured during an EM Bird flight campaign.

5.1 Baltic Sea ice

The Baltic Sea is a semi-enclosed brackish seawater basin of the Atlantic Ocean (Figure 5.1) and is located in Northern Europe. The Baltic Sea has a surface area of about 400 000 km^2 and a mean depth of 54 m. The surface water salinity ranges from 25 g/kg

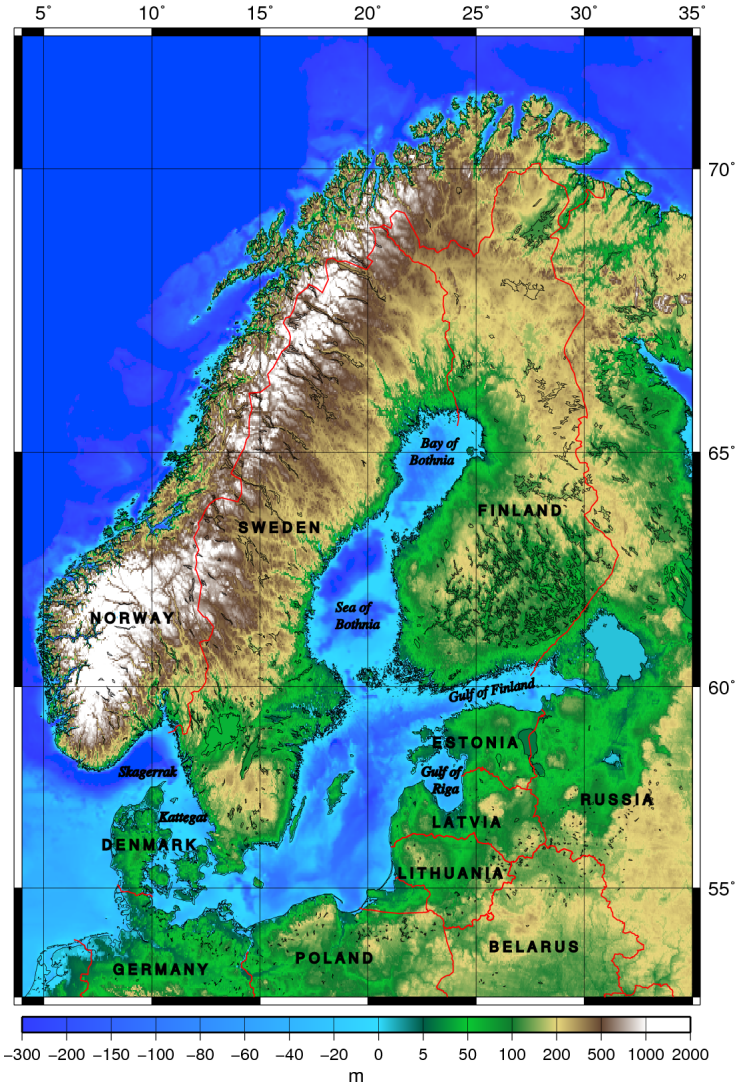

Figure 5.1: The topography of the Baltic Sea and its adjacent countries.

in the Danish Straits, to 9 g/kg in the Southern Baltic Sea, to less than 1 g/kg in the innermost parts of the Gulf of Finland and the Bay of Bothnia, and to zero in river mouths. The mean salinity is about 7 g/kg. (Leppäranta and Myrberg, 2009).
The Baltic Sea is ice-covered for 5 – 7 months every year. The maximum annual ice extent is highly variable and ranges between 12 and 100 % of the whole Baltic Sea area (Seinä and Palosuo, 1996). On average, the ice cover begins to form in the middle of November. The ice formation usually starts on the northern coast of the Bay of Bothnia and then progresses southward. On average, the Bay of Bothnia freezes over in the middle of January, and about one month later the Sea of Bothnia, the Gulf of Finland, and the Gulf of Riga are completely ice-covered as well. On average, melting starts in March, and in early May ice is only found in the Bay of Bothnia, where it melts completely by the end of May or beginning of June. (Leppäranta and Myrberg, 2009)
Ice in the Baltic Sea occurs as fast ice and drift ice. The coastal archipelago areas

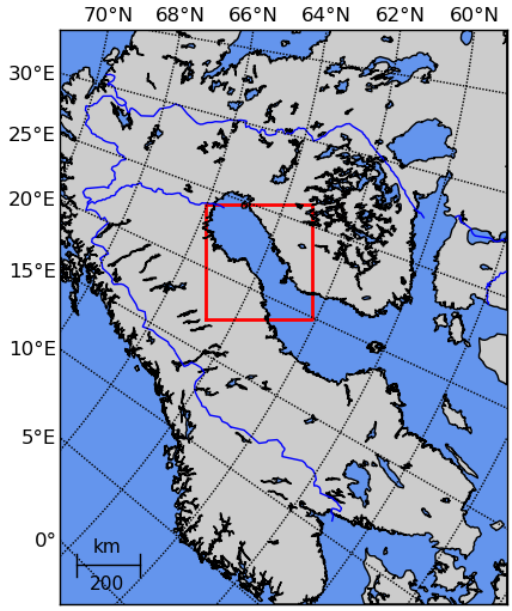

Figure 5.2: The Baltic Sea area in polar stereographic projection. The red box indicates the area in the Bay and Sea of Bothnia that we choose for the investigations in this chapter.

are covered by fast ice, i.e. the ice is attached to islands and shoals. Fast ice forms a very stable ice cover. Even a thin land-fast sea ice cover is not broken up by wind and waves (Palosuo, 1963). In contrast, the drift ice further offshore shows a highly dynamic behaviour due to forcing by wind and currents. The motion of drift ice results in an uneven and broken ice field with distinct floes (several kilometers in size), leads and cracks, brash ice barriers, rafted ice, and ice ridges (Mäkynen and Hallikainen, 2005). The thickness of level Baltic Sea ice is less than 120 cm (Leppäranta and Hakala, 1992), while ice ridges can pile up 2 m above the water level and can have total ice thicknesses of up to 12 – 17 m (Hallikainen, 1992).
Salinity of Baltic Sea ice typically takes values between 0.2 and 2 g/kg (Hallikainen, 1992). Despite the low surface water salinities, ice formed in the Baltic Sea resembles sea ice formed in more saline oceans, with preferred horizontal c-axis, jagged grain boundaries, and a grain substructure with brine layers (Palosuo, 1961; Kawamura et al., 2001). If the surrounding water has a salinity higher than about 0.6 g/kg, the ice formed has these sea ice characteristics (Palosuo, 1961). Thus, in the Baltic Sea only ice formed close to river estuaries has the characteristics of freshwater ice.
Figure 5.2 shows the Baltic Sea region in polar stereographic projection and the area of consideration for the following investigations.

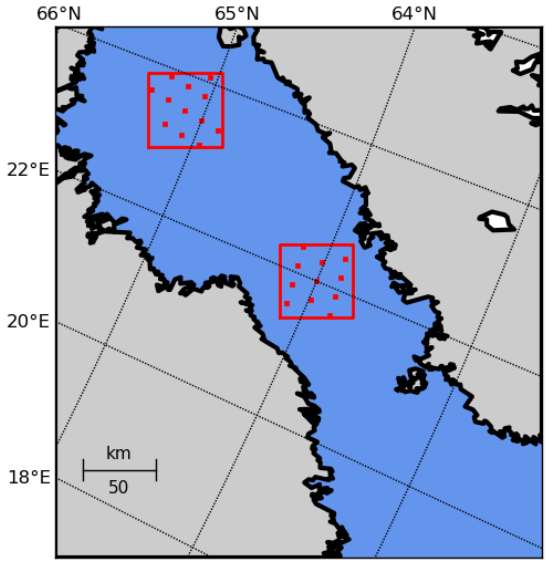

Figure 5.3: The red square boxes indicate the two areas in the Bay of Bothnia selected for the comparison of brightness temperatures as simulated with our model and as measured by SMOS over open water from 1st October to 30th November, 2010. The red points indicate the centre positions of SMOS measurements located within the boxes.

5.2 Brightness temperatures over open water

We investigate whether our radiation model is able to reasonably reproduce brightness temperatures as observed by SMOS over ice-free water. We analyse SMOS brightness temperatures measured between 1st October and 30th November, 2010 in two areas, one located in the northern part, and the other in the southern part of the Bay of Bothnia (see Figure 5.3). According to Finnish ice charts and a visual inspection of optical MODIS images, these areas were ice-free during the examined time period. The measured brightness temperatures are then compared with modelled brightness temperatures.

We expect that brightness temperatures over open water are modelled more realistically and more easily than brightness temperatures over areas that contain sea ice. Here, we use the good reproducibility of water brightness temperatures to also investigate whether the brightness temperature corrections for atmospheric effects and for the cosmic background radiation, included in our radiation model (section 2.3), improve the model's performance.

In L-band, brightness temperatures of open water are mainly influenced by water temperature and water salinity. Additionally, the wind-induced roughness of the sea surface impacts the brightness temperature. However, the impact of water salinity is small for low temperatures as encountered in the region at the time investigated here. At water temperatures of 0°C, brightness temperature sensitivity to sea surface salinity is less than 0.25 K per 1 g/kg (Lagerloef et al., 1995). The wind-induced sea surface rough-

ness accounts for about 0.2 K per 1 m/s of wind speed (Dinnat et al., 2003). Compared to brightness temperatures observed over sea ice, the variability of brightness temperatures over open water is hence much lower, i.e. the brightness temperature signal is much more stable over open water. Apart from the water brightness temperature's stability, the information that is available on the water characteristics is usually more reliable than the available information on sea ice (regarding its thickness, temperature and salinity, for example). Furthermore, the properties of water are more homogeneously distributed over the SMOS footprint than the properties of sea ice. Thus, we expect that brightness temperatures over open water are modelled more realistically with our radiation model than brightness temperatures over sea ice.

5.2.1 SMOS data selection

We include all SMOS measurements located within the two areas indicated in Figure 5.3. We expect the water temperature to decrease with time during the autumn. In order to investigate the effect of the decreasing water temperature on brightness temperatures, we divide the SMOS brightness temperature data into three periods of about 20 days: 1) 1st October – 20th October, 2) 21st October – 10th November, and 3) 11th November – 30th November. The single SMOS brightness temperature measurements for incidence angles of 5° – 65° are averaged over 5° intervals for these three time periods.

5.2.2 Model assumptions

We use the incoherent Burke model to simulate horizontally and vertically polarised brightness temperatures for an incidence angle range of 5° – 65°. The examined area is assumed to be ice-free, thus we set the ice concentration to c_{ice}= 0% in the model. For the model calculations, we assume a water salinity of S_{water}= 4 g/kg (Janssen et al., 1999). The water temperature in the model is estimated from National Oceanic and Atmospheric Administration (NOAA) Optimum Interpolation (OI) SST V2 GrADS weekly sea surface temperature data. The corresponding average value for 1st October – 30th November, 2010 is T_{water}= 5.5°C. The modelled brightness temperatures include an atmospheric correction and a correction for the uniform cosmic background radiation (see section 2.3). For comparison, we also perform simulations that neglect the atmospheric contribution, and simulations that neglect both, the atmospheric contribution and the cosmic background radiation.

5.2.3 Results

Observed SMOS brightness temperatures

For both, horizontally and vertically polarised brightness temperatures, we observe that brightness temperatures decrease with time (Figure 5.4). When averaged over all incidence angles, the horizontally polarised SMOS brightness temperatures measured from 1st October – 20th October are 1.9 K higher than the brightness temperatures

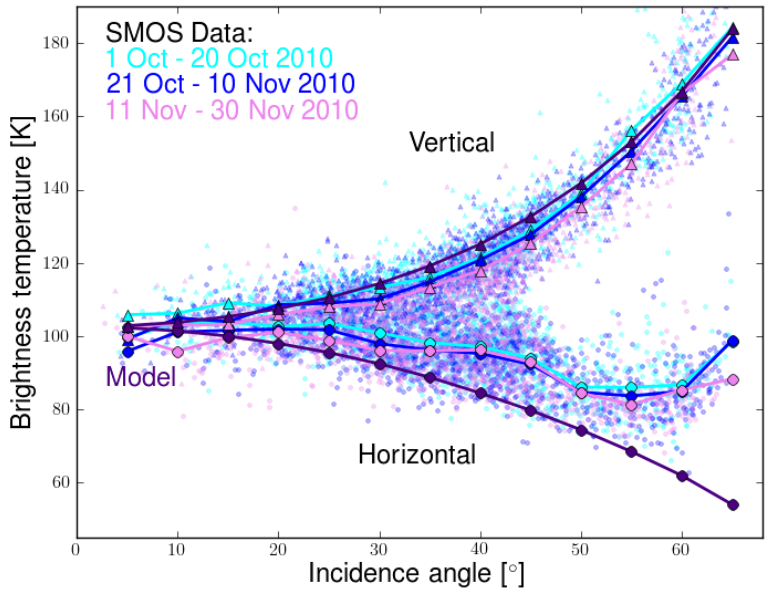

Figure 5.4: Simulated and measured brightness temperatures over open water as a function of incidence angle. Triangles indicate vertical polarisation, circles indicate horizontal polarisation. The purple curve shows the modelled brightness temperatures. The light blue, blue and pink colors indicate SMOS brightness temperatures measured during the time periods given in the figure. The small circles and triangles indicate individual SMOS measurements, the lines indicate the average values for incidence angle bins of 5°.

measured from 21st October to 10th November, and 3.4 K higher than the ones measured from 11th November to 30th November. Compared to 1st October – 20th October, SMOS brightness temperatures at vertical polarisation decrease on average by 2.6 K for 21st October – 10th November, and by 4.2 K for 11th November – 30th November.

The decrease in brightness temperature is partly explained by the decreasing water temperature. According to the NOAA OI SST V2 GrADS weekly sea surface temperature data, the average water temperature was about 7.75°C in the first time period (1st October – 20th October) and about 2.75°C in the last time period (11th November – 30th November). The expected brightness temperature decrease calculated with our radiation model is 1.9 K at horizontal polarisation (compared to the observed decrease of 3.4 K), and 2.9 K at vertical polarisation (compared to the observed decrease of 4.2 K).

For the three time periods, the root mean square deviations between single SMOS measurements and SMOS brightness temperatures averaged over 5° incidence angle intervals range between 6.8 and 7.9 K for horizontal polarisation and between 6.2 and 8.0 K for vertical polarisation, respectively. The root mean square deviations between single SMOS measurements and average SMOS brightness temperatures are thus higher than the decrease of brightness temperature with time. Therefore, we in the following consider the average brightness temperatures for the entire time period 1st

Table 5.1: Root mean square deviations (RMSD) and mean differences (ΔTB) between modelled and mean observed brightness temperatures over open water (see section 5.2)

		with correction for atmosphere and for TB_{cosm}	without correction for atmosphere	without any corrections
RMSD [K]	H-Pol	15.4	18.6	20.2
	V-Pol	3.0	2.2	3.2
ΔTB [K]	H-Pol	10.6	14.3	16.2
	V-Pol	-2.1	0.8	2.3

October – 30th November to estimate the ability of the model to reproduce brightness temperatures as observed by SMOS. The root mean square deviation between single SMOS measurements and this average SMOS brightness temperature curve is 7.3 K at horizontal and 6.5 K at vertical polarisation.

Comparison of modelled and observed brightness temperatures

The comparison of brightness temperatures measured by SMOS and brightness temperatures modelled with our radiation model (Figure 5.4) reveals that the model captures quite well the measured vertically polarised brightness temperatures, while horizontally polarised brightness temperatures are underestimated, particularly for higher incidence angles.

The root mean square deviation between average SMOS brightness temperatures and modelled brightness temperatures is 15.4 K for horizontal polarisation and 3.0 K for vertical polarisation, respectively. Averaged over the whole incidence angle range, our radiation model underestimates the measured brightness temperatures by 10.6 K for horizontal polarisation, whereas the model overestimates the measured brightness temperatures by 2.1 K at vertical polarisation (Table 5.1).

When we compare single SMOS measurements with the model, the root mean square deviation between the brightness temperatures is 14.1 K for horizontal polarisation (as compared to 15.4 K for the average SMOS brightness temperatures), and 8.1 K for vertical polarisation (as compared to 3.0 K for the average SMOS brightness temperatures). Thus, the root mean square deviations between modelled and average SMOS brightness temperatures and between modelled and single SMOS brightness temperatures are very similar for horizontal polarisation. In contrast, at vertical polarisation, the root mean square deviation from the modelled brightness temperatures is considerably higher for single SMOS measurements than for averaged SMOS brightness temperatures.

Incidence angle dependency

The deviations between modelled and observed brightness temperatures for different incidence angles are given in Table 5.2. For horizontal polarisation, the model slightly overestimates brightness temperatures for incidence angles up to 10° and underestimates brightness temperatures for higher incidence angles. This underestimation increases with increasing incidence angle; for θ= 60° the observed brightness temperatures are on average underestimated by 23.7 K. For vertical polarisation, the deviation is less than 1 K for incidence angles below 25° and reaches maximum values of 4 – 5 K at incidence angles between 35° and 50°. In section 5.4, the values given in Table 5.2 are used as correction terms for the brightness temperatures of open water.

Table 5.2: Mean differences ΔTBH and ΔTBV between modelled and mean observed brightness temperatures at horizontal and at vertical polarisation over open water for different incidence angles θ (see section 5.2)

θ	5°	10°	15°	20°	25°	30°	35°	40°	45°	50°	55°	60°
ΔTBH [K]	-2.3	-1.2	1.7	3.9	5.8	5.9	8.0	11.7	13.3	10.6	15.2	23.7
ΔTBV [K]	0.0	1.0	0.13	0.07	-1.1	-3.6	-4.4	-5.0	-5.3	-4.2	-1.8	0.1

Impact of brightness temperature corrections

In the above comparison of modelled and measured brightness temperatures, we included the atmospheric correction and the correction for the cosmic background radiation in the model (as described in section 2.3). Here, we also compare measured brightness temperatures with brightness temperatures that are modelled without the atmospheric correction, and without both the atmospheric correction and the correction for the cosmic background radiation (Table 5.1).

When we neglect both the atmospheric influence and the cosmic background radiation, horizontally polarised brightness temperatures as observed by SMOS are even more underestimated by the model: The mean difference between modelled and measured brightness temperatures increases by 5.6 K to 16.2 K, and the root mean square deviation increases by 4.8 K to 20.2 K. In contrast, at vertical polarisation, the mean difference between the model and the observations changes its sign. Instead of overestimating the SMOS brightness temperatures by 2.1 K, the model then underestimates the observed brightness temperatures by 2.3 K. The root mean square deviation at vertical polarisation remains almost constant.

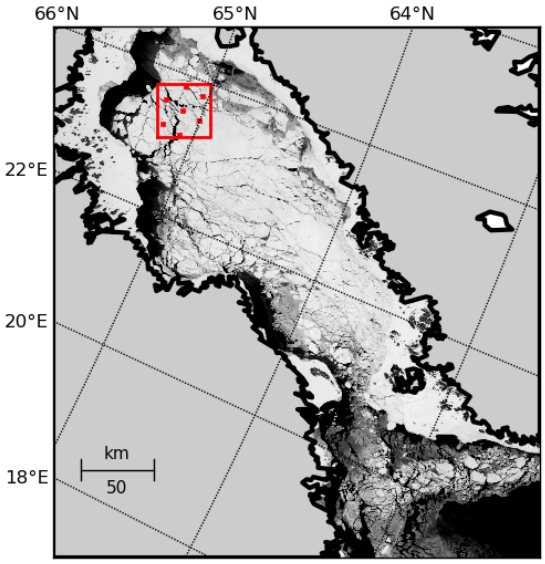

Figure 5.5: The red square box indicates the area in the Bay of Bothnia selected for the comparison of brightness temperatures as simulated with our model and as measured by SMOS over Baltic Sea ice from 1st January to 28th February, 2011. The red points indicate the centre positions of SMOS measurements located within the box. Underlayed is a MODIS image from the 9th February, 2011.

5.3 Brightness temperatures over growing sea ice

Here, we investigate whether our radiation model is able to reasonably reproduce brightness temperatures as observed by SMOS over growing sea ice. We analyse SMOS brightness temperatures measured between 1st January and 28th February, 2011 in an area located in the northern part of the Bay of Bothnia (see Figure 5.5). According to both Finnish ice charts and ice thickness maps produced by the FMI, which are based on MODIS images (Mäkynen, 2012), this area was almost completely ice-covered during the examined time period. Furthermore, the ice charts and ice thickness maps indicate that the ice thickness increased continuously from the beginning of January to the end of February.

5.3.1 SMOS data selection

We include all SMOS measurements located within the area indicated in Figure 5.5. We expect the ice thickness to increase with time during the ice growth period from the beginning of January to the end of February. In order to investigate the effect of increasing ice thickness on brightness temperatures, we divide the SMOS measurements into three different time periods: 1) 1st January – 26th January, 2) 27th January – 17th February, and 3) 18th February – 28th February. For each of these three time periods approximately the same number of SMOS measurements is available. The

single SMOS brightness temperature measurements for incidence angles of 5° – 65° are averaged over 5° intervals for these three time periods.

5.3.2 Model assumptions

We use the incoherent Burke model to simulate horizontally and vertically polarised brightness temperatures for an incidence angle range of 5° – 65°. The investigated area was almost completely ice-covered during the time period considered here, as indicated in Finnish ice charts, in MODIS-based ice thickness maps, and in ice concentration data from the ASI algorithm (Kaleschke et al., 2001; Spreen et al., 2008) applied to AMSR-E brightness temperature measurements (Figure A.5 in the appendix). Thus, we set the ice concentration to c_{ice}= 100% in the radiation model. For the model calculations, we assume a water salinity of S_{water}= 3 g/kg (Janssen et al., 1999). Water temperature is assumed to be at freezing temperature (T_{water}= -0.2°C). The ice surface temperature T_{surf} for the model calculations is estimated from the MODIS IST MOD029 product (Hall et al., 2004) (Figure A.5 in the appendix). The corresponding average value for 1st January – 28th February, 2011 is T_{surf}= -15.4°C. Ice salinity is assumed to be between 0.5 g/kg and 1.5 g/kg. Snow density is assumed to be ρ_{snow}= 350 kg/m^3.
We use the FMI's ice thickness maps based on MODIS images (Mäkynen, 2012) to estimate the ice thickness within the examined area for the three selected time periods. The average ice thicknesses are 1) d_{ice}= 25 cm for 1st January – 26th January, 2) d_{ice}= 41 cm for 27th January – 17th February, and 3) d_{ice}= 58 cm for 18th February – 28th February. The Finnish ice charts confirm that ice thickness was continuously increasing from 1st January – 28th February and that the determined ice thickness values are reasonable.
For our comparisons, we use the incoherent Burke model with one snow and one ice layer, and alternatively with one ice layer only. The thickness of the snow layer in the model is estimated from the empiric relationship between ice thickness and snow thickness given in the equations (4.8) and (4.9).
The modelled brightness temperatures include an atmospheric correction and a correction for the uniform cosmic background radiation (see section 2.3).

5.3.3 MODIS-based ice thickness maps and ice charts

In order to estimate the ice thickness in the Bay of Bothnia, we here use ice thicknesses retrieved from MODIS thermal imagery that were provided by the FMI. For the ice thickness retrieval from MODIS images, a surface heat balance equation is used to estimate ice thickness from ice surface temperature, which is obtained from MODIS measurements. The method works only for cloud-free and sufficiently cold weather conditions. The maps produced by the FMI are cloud-masked. For Baltic conditions, the maximum retrievable ice thickness is about 40 cm for air temperatures below -20°C, and reduces to about 15 cm for air temperatures between -10 and -5°C. The uncertainty is estimated to be 40 – 50% for ice thicknesses between 20 and 50 cm, and 20% for ice thicknesses between 10 and 20 cm. Thus, in our investigations with

Table 5.3: Root mean square deviations between modelled and observed brightness temperatures over Baltic Sea ice for the given time periods with estimated ice thicknesses d_{ice} and ice salinities S_{ice}. The ice surface temperature is assumed to be $T_{surface}$ = -15.4°C. The first number gives the root mean square deviation between the modelled and the average SMOS brightness temperatures (averaged over 5° incidence angle intervals), the second number refers to the root mean square deviations between modelled brightness temperatures and single SMOS measurements.

		1 Jan – 26 Jan: d_{ice}=25 cm, S_{ice}=1.5 g/kg	27 Jan – 17 Feb: d_{ice}=41 cm, S_{ice}=1.0 g/kg	18 Feb – 28 Feb: d_{ice}=58 cm, S_{ice}=1.0 g/kg
$d_{snow} \neq 0$	H-Pol	6.0 K / 14.5 K	6.1 K / 10.6 K	4.1 K / 8.1 K
	V-Pol	5.0 K / 12.3 K	3.7 K / 9.7 K	3.3 K / 7.2 K
$d_{snow} = 0$	H-Pol	33.0 K / 35.4 K	34.1 K / 34.0 K	32.7 K / 33.1 K
	V-Pol	18.8 K / 23.0 K	20.5 K / 22.9 K	17.2 K / 17.9 K

an average ice surface temperature of T_{surf}= -15.4°C and ice thicknesses around 25 to 60 cm, the uncertainty is about 40 – 50% and the maximum reliable ice thickness is 30 – 40 cm. However, the MODIS-based ice thicknesses are consistent with ice thicknesses given in Finnish ice charts. (Mäkynen, 2012)
During the ice season, the Finnish Ice Service manually produces daily ice charts for the Baltic Sea. For the ice chart production, ice analysts update previous charts using the available information from Synthetic Aperture Radar (SAR) images, drilling measurements near the coast, systematic field observations (including thickness) by the staff of icebreakers and other ships, and ice growth estimates obtained from ice models (Mäkynen, 2012).

5.3.4 Results

First, we analyse the temporal evolution of the horizontally and vertically polarised brightness temperatures as observed by SMOS for an incidence angle range of 5° to 65° (Figure 5.6). We compare these SMOS brightness temperatures with modelled brightness temperatures. In a first comparison, we estimate the ice and snow thickness, assume reasonable ice salinities, and then simulate brightness temperatures using the model with one ice and one snow layer. Thereafter, we look at single SMOS measurements and the range of ice thicknesses that is expected to occur for each time period in the examined area (Figures 5.7, 5.9, and 5.11). Additionally, we compare brightness temperatures as modelled for three different ice salinities and for model calculations that include or neglect a snow layer, respectively (Figures 5.8, 5.10, and 5.12).

Observed SMOS brightness temperatures
The average brightness temperatures as observed by SMOS clearly increase with time (Figure 5.6). The horizontally polarised mean brightness temperature, averaged over

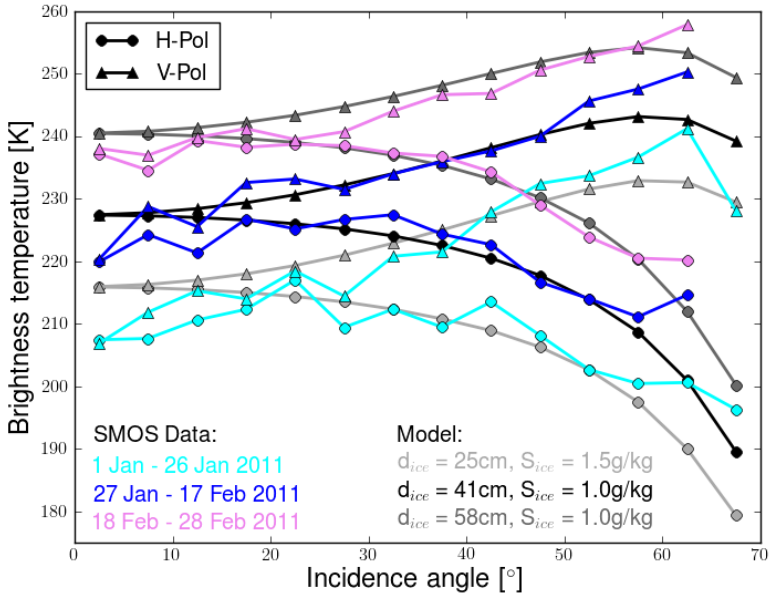

Figure 5.6: Modelled and measured brightness temperatures over Baltic sea ice as a function of incidence angle. Triangles indicate vertical polarisation, circles indicate horizontal polarisation. The light gray, black and gray lines show the brightness temperatures modelled for the ice thicknesses given in the figure. The light blue, blue and pink colors indicate SMOS brightness temperatures measured during the time periods given in the figure. All lines indicate the average values for incidence angle bins of 5°.

the considered incidence angle range, increases from 207.7 K to 221.2 K and finally to 233.0 K for the three subsequent time periods. At vertical polarisation, the average brightness temperature increases from 223.1 K to 235.6 K and finally to 245.4 K.

Comparison of modelled and observed brightness temperatures

In order to investigate the capability of our radiation model to reproduce brightness temperatures as observed by SMOS, we compare modelled brightness temperatures with measured brightness temperatures. In Figure 5.6 we assume that the ice is snow-covered and that the ice salinity is S_{ice}= 1.5 g/kg for the thin ice (d_{ice}= 25 cm) in the first time period considered here (1st January - 26th January). We assume that due to desalination processes the ice salinity decreases to S_{ice}= 1.0 g/kg for the remaining time.

The brightness temperatures modelled for these assumptions agree well with brightness temperatures measured by SMOS. At horizontal polarisation, the model slightly underestimates the observed brightness temperatures, when averaged over 5° incidence angle intervals. For the three time periods, the modelled brightness temperatures are on average 1.3 to 2.4 K lower than the observed brightness temperatures, while the root mean square deviations between the modelled and the observed brightness temperatures are between 4.1 and 6.1 K (Table 5.3). At vertical polarisation, the model slightly underestimates the observed brightness temperatures by 1.0 K for the

time period 27th January - 17th February (d_{ice}= 41 cm), while the model slightly overestimates the observed brightness temperatures by 1.0 to 1.4 K for the other two time periods (1st January - 26th January, d_{ice}= 25 cm, and 18th February - 28th February, d_{ice}= 58 cm). The root mean square deviations for vertically polarised brightness temperatures are between 3.3 and 5.0 K. For both polarisations, the root mean square deviations are smallest for the thickest ice.
Figures 5.7, 5.9, and 5.11 show modelled and observed brightness temperatures for the three time periods separately. The root mean square deviations between modelled brightness temperatures and single SMOS measurements are considerably higher than between modelled brightness temperatures and SMOS brightness temperatures averaged over 5° incidence angle intervals (Table 5.3). For horizontal polarisation, the root mean square deviations for single SMOS measurements range between 8.1 and 14.5 K (as compared to 4.1 – 6.1 K for averaged SMOS measurements). For vertical polarisation, we obtain values between 7.2 and 12.3 K (as compared to 3.3 – 5.0 K for averaged SMOS measurements). The root mean square deviation decreases with time and thus with increasing ice thickness. When we model brightness temperatures for a range of ice thicknesses of ± 10 cm around the assumed ice thickness, most of the SMOS measurements take values within this modelled range of brightness temperatures.
Additionally, we compare observed brightness temperatures with different model assumptions for the ice salinity and under the presence or absence of a snow layer (Figures 5.8, 5.10, and 5.12). The brightness temperatures modelled for snow-free ice conditions are considerably lower than the observed brightness temperatures. Depending on the assumed ice salinity (between 0.5 and 1.5 g/kg), horizontally polarised modelled brightness temperatures are on average 23 to 46 K lower than the observed brightness temperatures, and the vertically polarised modelled brightness temperatures are 11 to 34 K lower than the observations. Assuming the same ice salinity as for the model calculations that include a snow layer on ice (Figure 5.6), the root mean square deviations between modelled and average observed brightness temperatures range between 32.7 and 34.1 K at horizontal polarisation, and between 17.2 and 20.5 K at vertical polarisation for the three time periods (Table 5.3).

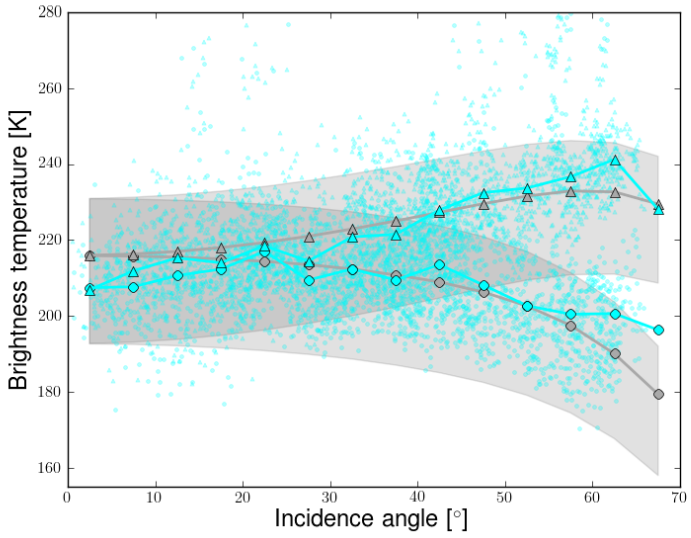

Figure 5.7: Brightness temperatures over Baltic Sea ice as a function of incidence angle. Triangles indicate vertical polarisation, circles indicate horizontal polarisation. The light gray and light blue lines are the same as the corresponding lines in Figure 5.6. The gray shaded area indicates the model's range of brightness temperatures for ice thicknesses d_{ice}= 25 cm ± 10 cm. The small circles and triangles indicate individual SMOS measurements (1st January – 26th January).

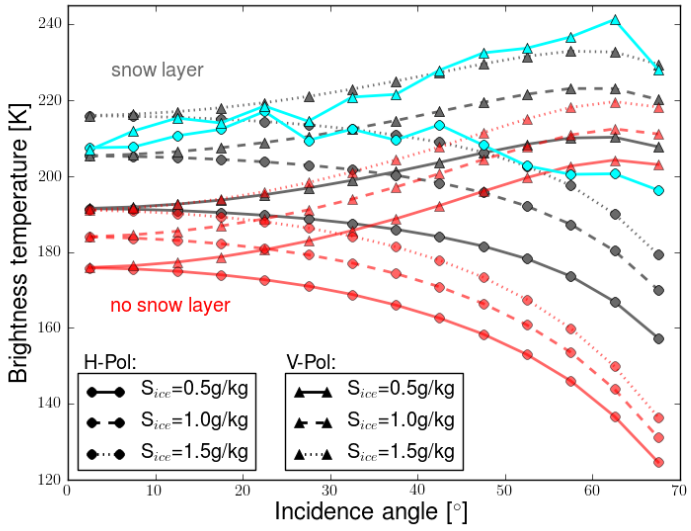

Figure 5.8: Brightness temperatures over Baltic Sea ice as a function of incidence angle. Triangles indicate vertical polarisation, circles indicate horizontal polarisation. The gray lines indicate brightness temperatures modelled for snow-covered ice, the red lines indicate brightness temperatures modelled for snow-free ice. The line styles indicate the assumed ice salinities as given in the figure. The light blue line indicates SMOS measurements from 1st January – 26th January (same as in Figures 5.6 and 5.7).

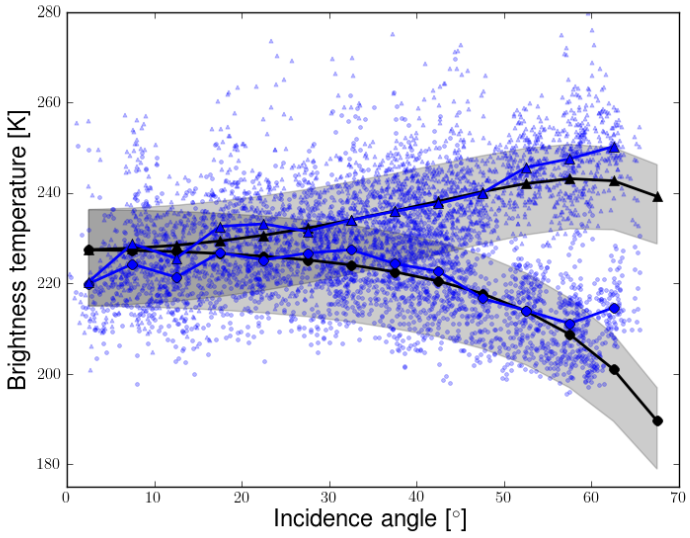

Figure 5.9: Brightness temperatures over Baltic Sea ice as a function of incidence angle. Triangles indicate vertical polarisation, circles indicate horizontal polarisation. The black and blue lines are the same as the corresponding lines in Figure 5.6. The gray shaded area indicates the model's range of brightness temperatures for ice thicknesses d_{ice}= 41 cm ± 10 cm. The small circles and triangles indicate individual SMOS measurements (27th January – 17th February).

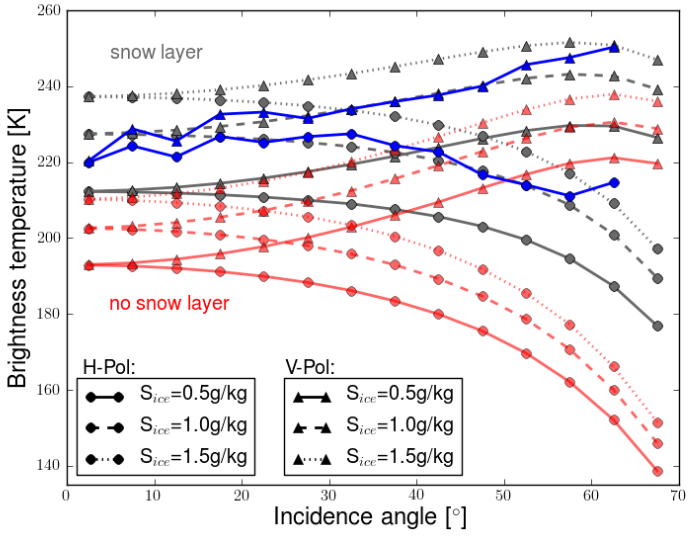

Figure 5.10: Brightness temperatures over Baltic Sea ice as a function of incidence angle. Triangles indicate vertical polarisation, circles indicate horizontal polarisation. The gray lines indicate brightness temperatures modelled for snow-covered ice, the red lines indicate brightness temperatures modelled for snow-free ice. The line styles indicate the assumed ice salinities as given in the figure. The blue line indicates SMOS measurements from 27th January – 17th February (same as in Figures 5.6 and 5.9).

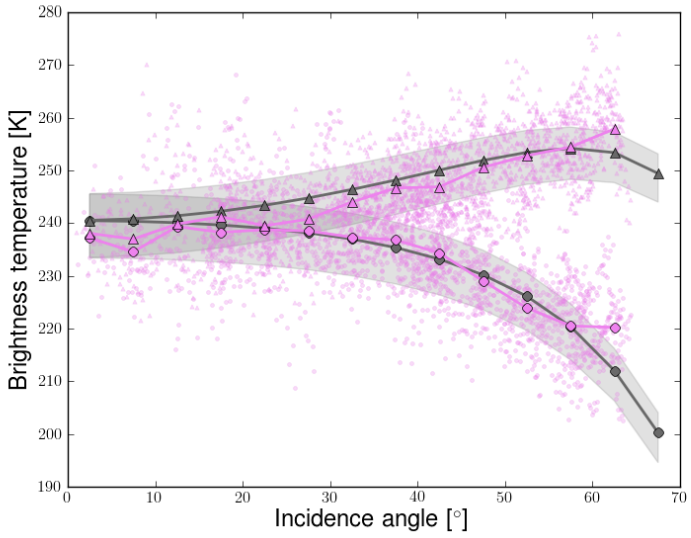

Figure 5.11: Brightness temperatures over Baltic Sea ice as a function of incidence angle. Triangles indicate vertical polarisation, circles indicate horizontal polarisation. The gray and pink lines are the same as the corresponding lines in Figure 5.6. The gray shaded area indicates the model's range of brightness temperatures for ice thicknesses d_{ice}= 58 cm ± 10 cm. The small circles and triangles indicate individual SMOS measurements (18th February – 28th February).

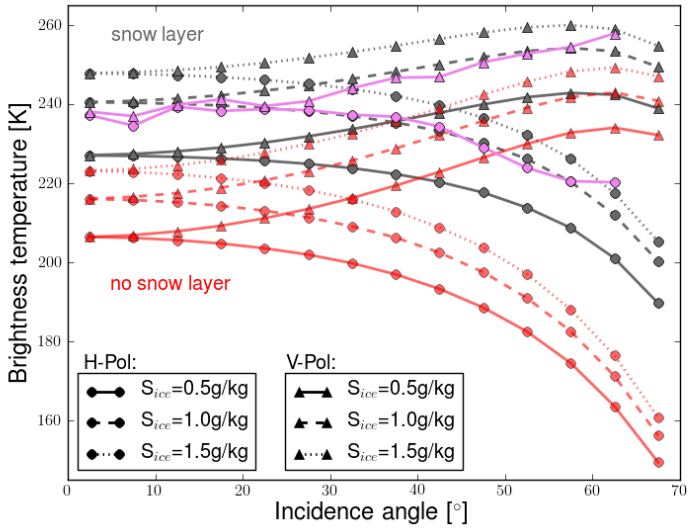

Figure 5.12: Brightness temperatures over Baltic Sea ice as a function of incidence angle. Triangles indicate vertical polarisation, circles indicate horizontal polarisation. The gray lines indicate brightness temperatures modelled for snow-covered ice, the red lines indicate brightness temperatures modelled for snow-free ice. The line styles indicate the assumed ice salinities as given in the figure. The pink line indicates SMOS measurements from 18th February – 28th February (same as in Figures 5.6 and 5.11).

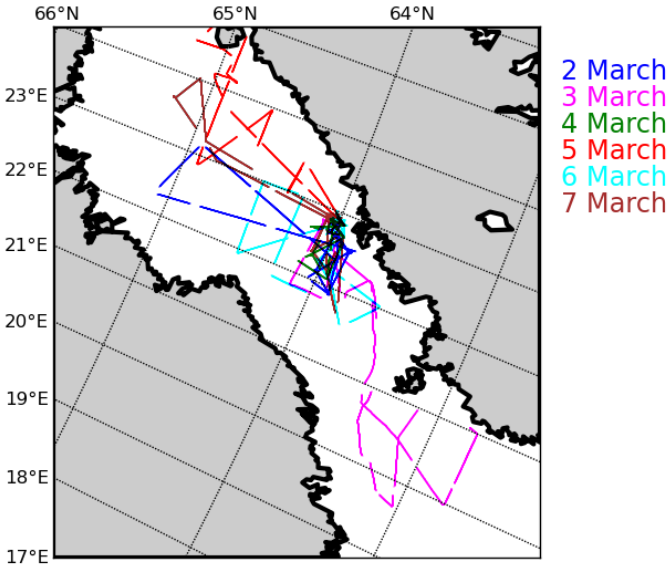

Figure 5.13: Overview of all EM Bird ice thickness flights performed during the SafeWin campaign in March, 2011. The colors indicate the date of the flights.

5.4 Validation with EM Bird measurements

In order to validate the ice thickness retrieval based on SMOS brightness temperature measurements, we here compare ice thicknesses retrieved from SMOS with ice thicknesses as measured during an airborne EM ice thickness survey in March, 2011 in the Sea and Bay of Bothnia.

5.4.1 EM Bird ice thickness measurements

For the validation of SMOS ice thicknesses, we use ice thicknesses measured during an EU SafeWin project's winter field campaign in the northern Baltic Sea. Between 2nd and 7th March, 2011 a helicopter-towed EM Bird measured the ice thickness in the Bay of Bothnia and the northern Sea of Bothnia. All flight tracks of the 11 flights that were performed during the campaign are indicated in Figure 5.13.
The EM ice thickness sounding system consists of a laser altimeter and an assembly of coils that transmit and receive low-frequency EM fields. The transmitted and received EM fields give the sensor's height above the conductive seawater surface. The laser altimeter measures the sensor's altitude above the ice or snow surface. Over sea ice the difference between the sensor's height above the ice surface and its height above the seawater corresponds to the total ice thickness, i.e. the sum of the ice and snow thickness. (Haas et al., 2009)
The EM Bird used in the SafeWin field campaign operates at a frequency of 4.06 kHz. The sampling frequency is 10 Hz, corresponding to a spacing of approximately 3 – 4 m

between subsequent measurements. The laser altimeter has a sampling frequency of 100 kHz. The EM Bird is flown 10 to 20 m above the ice surface. The strength of the measured EM field represents the average field of an area approximately 3.7 times the instrument's altitude above the ice surface, i.e. the footprint is approximately between 37 and 74 m. (Haas and Casey, 2012)
The accuracy of EM Bird ice thickness measurements over level ice is about 10 cm (Haas et al., 2009), whereas ice ridges can be underestimated by up to 50% (Haas and Jochmann, 2003). Therefore, sea ice thickness distributions obtained from EM Bird measurements are most accurate with respect to their modal thickness (Haas et al., 2010).
Because measuring ice thickness with the EM Bird is only possible due to the higher conductivity of seawater compared to sea ice, the brackish nature of the Baltic Sea provides challenging conditions for EM ice thickness measurements. Additionally, the accuracy of EM Bird ice thickness measurements in the Baltic Sea is further decreased by 1) shallow waters and by 2) freshwater layers under fast ice. 1) In brackish waters shallower than about 10 to 15 m ice thicknesses are overestimated by the EM Bird, because currents are induced in the seafloor, which is usually less conductive than seawater. 2) Freshwater layers can form under fast ice due to river runoff from land. These freshwater layers have very low conductivities. Both effects cause that the ice thickness measurements carried out over fast ice close to the coast are less reliable. In this regard, the ice thickness measurements made in the region around the Hailuoto island (approximately at the geographical coordinates 65.0°N and 24.8°E) and along the shore west of Vaasa (approximately at 63.1°N and 21.6°E) are affected most for this flight campaign. (Haas and Casey, 2012)

5.4.2 Ice thickness retrieval with SMOS

For the retrieval of ice thickness, we here use horizontally and vertically polarised brightness temperatures with incidence angles $\theta \leq 50°$. We exclude all SMOS measurements that have a land fraction of more than 10% within a square area of 40 km × 40 km around the SMOS grid cell's centre point. The land-sea mask we use to determine the land fraction is the Global Self-consistent Hierarchical, High-resolution Shoreline Database (GSHHS) (Wessel and Smith, 1996).

Model assumptions
For the retrieval of ice thickness from SMOS brightness temperatures we use the incoherent Burke model with one ice and one snow layer. The retrieval requires information on 1. ice concentration, 2. ice temperature, 3. ice salinity, 4. water salinity, 5. water temperature, and 6. snow cover:

1. **Ice concentration**: Commonly, ice concentration is retrieved from passive microwave brightness temperatures using one of the available sea ice concentration algorithms. We considered using ice concentration maps obtained from the ASI algorithm applied to AMSR-E brightness temperature measurements (Kaleschke et al., 2001; Spreen et al., 2008) with tie-points adjusted to Baltic Sea conditions (Maaß and Kaleschke, 2010). However, these ice concentration maps showed

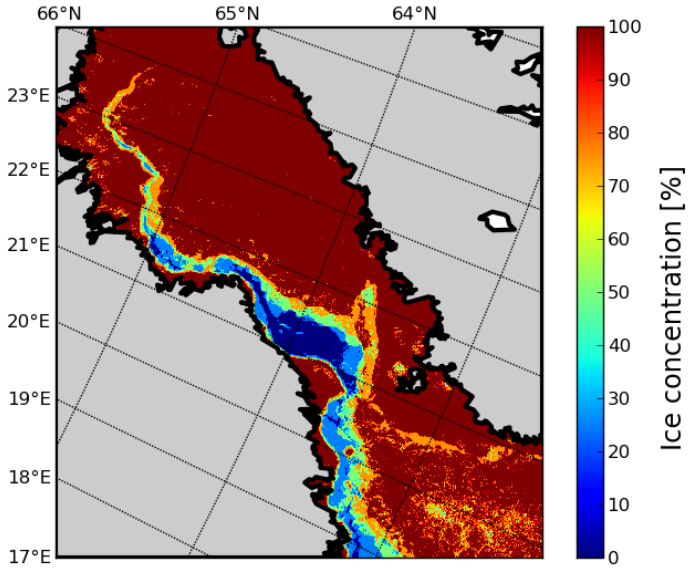

Figure 5.14: Mean ice concentration for 2nd – 7th March, 2011 obtained from averaging classified MODIS images from the 3rd, 5th, 6th, and 8th March. In the classification, each MODIS pixel (resolution 250 m x 250 m) is determined to be covered by water or ice.

lower ice concentrations than can be visually inferred from the high-resolution optical MODIS images available for the area and time period considered here. The MODIS images taken over the Bay and Sea of Bothnia on the 3rd, 5th, 6th, and 8th March are cloud-free over large areas. Thus, in this case, these images with a resolution of 250 m × 250 m enable us to determine the ice coverage more reliably than the more coarsely resolved ice concentration maps based on passive microwave measurements. We produce ice concentration maps by applying a simple classification approach to the MODIS images at band 1, which measures at wavelengths λ= 620 – 670 nm. All MODIS pixels with reflectivities $r < 0.2$ are assigned to be open water pixels; all pixels with reflectivities $r \geq 0.2$ are assigned to be ice pixels. First, we classify each available MODIS image and then we average over all days. The resulting ice concentration field (Figure 5.14) is used as input for our radiation model.

2. **Ice surface temperature**: We use the MODIS IST MOD029 ice surface temperature product (Hall et al., 2004) to estimate the ice temperature of the ice in the Bay and Sea of Bothnia during the SafeWin field campaign. The average ice surface temperature of all MODIS pixels located within the area where the EM Bird measurements took place is T_{surf}= -3.4°C. Thus, this value is used as model input for the ice surface temperature.

3. **Ice salinity**: Sea ice salinity in the Baltic Sea typically takes values between 0.2 and 2 g/kg (Hallikainen, 1992). In the Bay and Sea of Bothnia ice salinities are generally lower than in the central Baltic Sea and its western parts. Due

to desalination processes occuring in ice, we expect the ice salinity of older and thicker ice to be lower than the ice salinity of younger and thinner ice. According to Finnish ice charts, the campaign area south of approximately 63.5°N had been completely ice-covered for about one month before the EM Bird measurements were carried out from 2nd to 7th March, 2011. Most of the remaining area covered by the flight campaign had been almost completely ice-covered for more than two months, when the campaign was carried out. The ice thicknesses measured during the flight campaign are mainly between 30 and 60 cm. Thus, we suppose that S_{ice}= 0.5 g/kg is a reasonable assumption for the average ice salinity of the ice in the area and for the time period considered here.

4. **Water salinity**: Water salinity is assumed to be S_{water}= 4 g/kg (Janssen et al., 1999).

5. **Water temperature**: Water is assumed to be at freezing temperature. For an ice salinity of S_{water}= 4 g/kg, the corresponding temperature of water at the freezing point is T_{water}= -0.2°C (Fofonoff and Millard, 1983).

6. **Snow cover:** We estimate the snow thickness from the empirical relationship between ice and snow thickness for Baltic Sea conditions given in equations (4.8) and (4.9). On the one hand, we thus account for the impact of a snow cover on brightness temperatures above snow-covered ice, as investigated in Chapter 4. On the other hand, the ice thicknesses measured by the EM Bird are total ice thicknesses (ice + snow thickness). In the following comparison, we thus retrieve total ice thicknesses from SMOS brightness temperatures and compare these to total ice thicknesses measured by the EM Bird. Snow is assumed to be dry and to have a density of ρ_{snow}= 360 kg/m^3, with ρ_{snow}= 360 kg/m^3 being a representative value for an average snow density between typical values for new snow (ρ_{snow}= 225 kg/m^3) and water-soaked snow (ρ_{snow}= 450 kg/m^3) in the Baltic Sea (Saloranta, 2000).

From brightness temperatures to total ice thicknesses

In order to retrieve ice thickness from brightness temperatures measured by SMOS, we use the incoherent Burke model for one ice and one snow layer to model brightness temperatures for a range of incidence angles and a range of total ice thicknesses. The considered range of incidence angles is θ= 5°, 12.5°, 17.5°, ..., 47.5° and the range of total ice thicknesses is d_{total}= 0 cm, 6 cm, 12 cm, 18 cm, 24 cm, ..., 90 cm.

For ice concentration, ice temperature and salinity, water temperature and salinity, and the snow cover we make the assumptions as given above. In section 5.2, we found that brightness temperatures modelled for open water in the Baltic Sea differ from brightness temperatures measured with SMOS. Thus, we here include a correction for the brightness temperature contribution that originates from the water fraction within each SMOS pixel. Therefore, we add $(1 - c) \cdot \Delta TB(\theta)$ to the modelled brightness temperatures, with c being the ice concentration and $\Delta TB(\theta)$ being the correction term as given for different incidence angles in Table 5.2. Additionally, we include an atmospheric correction and a correction for the uniform cosmic background radiation (section 2.3).

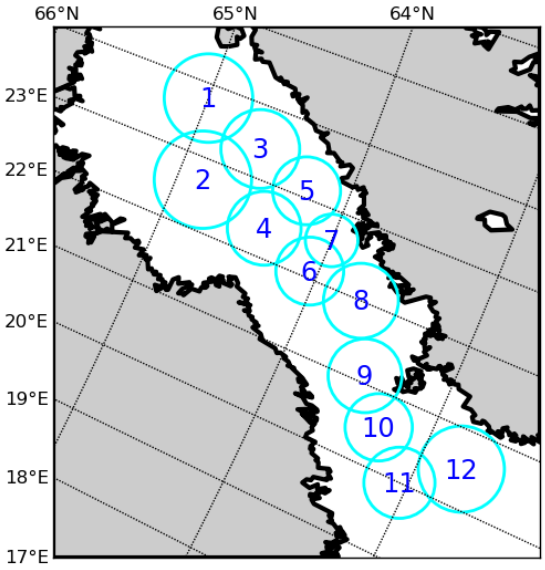

Figure 5.15: Numbering of the 12 circles used for the comparison of ice thicknesses as measured by the EM Bird and as retrieved from SMOS brightness temperatures.

For the retrieval of ice thickness, we first collect all brightness temperatures measured by SMOS during the time period 2nd – 7th March, 2011. We average all brightness temperatures with incidence angles θ between 0° and 10°; for the remaining incidence angles brightness temperatures are averaged over 5° incidence angle intervals (i.e. for 10° – 15°, 15° – 20°, ..., 45° – 50°). In a second step, we calculate the root mean square deviations between these averaged SMOS brightness temperatures and the brightness temperatures modelled for θ= 5°, 12.5°, 17.5°, ..., 47.5°. The deviations are calculated for all model calculations with different total ice thicknesses (d_{total}= 0 cm, 6 cm, 12 cm, ..., 90 cm). The ice thickness for that the root mean square deviation between measured and modelled brightness temperatures over the considered incidence angle range is lowest is then the ice thickness we retrieve from SMOS. This ice thickness is retrieved separately for horizontal and for vertical polarisation, as well as for brightness temperature intensity.

5.4.3 Validation approach 1

Comparison of ice thicknesses measured by the EM Bird and ice thicknesses retrieved from SMOS is challenging, because every SMOS measurement represents an area of about 35 – 50 km × 35 – 50 km (depending on incidence angle), while single EM Bird measurements have footprints in the order of 50 m × 50 m. In addition, SMOS measurements are located on a regular grid, while the EM Bird flight tracks are distributed irregularly. We choose to divide the area covered by the SafeWin campaign's flight tracks into 12 circular areas. We assign a number to each of the 12 circles (Figure 5.15) and assume that the ice thickness distribution within each of

these circles is reasonably represented by the EM Bird ice thicknesses (Figures 5.16 and 5.17). The centre points and the radii of the circles are given in Table A.21 in the appendix. For comparison, we show the results of a more traditional approach on the basis of a gridded field in section 5.4.4.

SMOS data selection
For each circle, we include all SMOS measurements whose centre points are located within a circular area defined by the corresponding validation circle's centre point and a radius of 0.75 times the radius of the corresponding circle (Table A.21 and Figures 5.16 and 5.17). The factor 0.75 is chosen quite arbitrarily. It is a compromise between including as many measurements as possible and excluding SMOS measurements that represent large areas outside the circle.
The EM Bird flight tracks located within circle nos. 9 and 12 are single lines through the circles rather than covering representatively the defined circular areas. Thus, for circle no. 9 we exclude the SMOS measurements located north of 63.6°N, and for circle no. 12 we exclude the SMOS measurements located south of 62.65°N.

The ice conditions
The MODIS images for the 3rd March (Figure 5.16) and the 6th March (Figure 5.17) show the dynamical behaviour of ice in the Bay and Sea of Bothnia during the examined time period. In particular, within the circle nos. 8, 10, and 12 the ice cover changes within the three days from 3rd to 6th March. According to the MODIS images, in circle no. 8, there is a large open water area on 3rd March, whereas the circular area appears to be completely ice-covered on the 6th March. In contrast, the large linear opening in the sea ice cover within the circle nos. 10 and 12 that is visible on 6th March, had been a closed ice cover on 3rd March. Thus, in these areas (circle nos. 8, 10, and 12), the assumption of a constant ice cover for the duration of the campaign may cause more difficulties than in the other areas.

Results

First, we compare the ice thickness distributions as measured by the EM Bird with ice thicknesses retrieved from SMOS brightness temperature intensities for the 12 circles (Figures 5.18 and 5.19). Thereafter, we compare the modal ice thicknesses obtained from the EM ice thickness distributions with the ice thicknesses as retrieved from SMOS brightness temperatures at horizontal and at vertical polarisation, as well as from brightness temperature intensities. (Figures 5.20 to 5.23).

EM Bird ice thickness distributions
The ice thickness distributions as measured by the EM Bird for the 12 circles have quite similar shapes (Figures 5.18 and 5.19). For most of the circles, more than two-thirds of the measured ice thicknesses take values between 0 and 1 m. The distributions have quite long, exponential tails representing ice thicknesses of up to 5 m or even more (e.g. for circle nos. 9 and 10, but ice thicknesses $d_{ice}>$ 5 m not depicted here).
For eight out of the twelve circles, 69 – 85% of the measured ice thicknesses are below

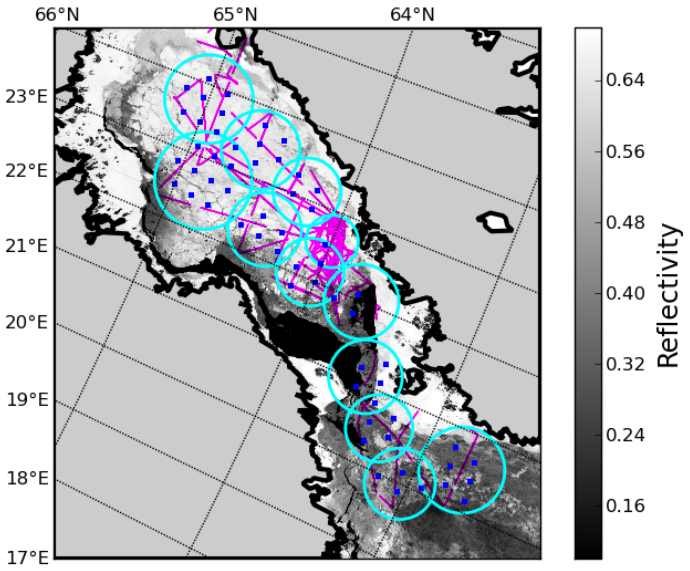

Figure 5.16: Distribution of EM Bird and SMOS measurements in the Bay and Sea of Bothnia and the 12 circular areas we choose for comparison of ice thicknesses. The pink lines indicate EM Bird flight tracks, the blue dots indicate the positions of SMOS measurements. These are overlaid on a MODIS image showing the reflectivities in band 1 (wavelength 620 – 670 nm) on 3rd March, 2011.

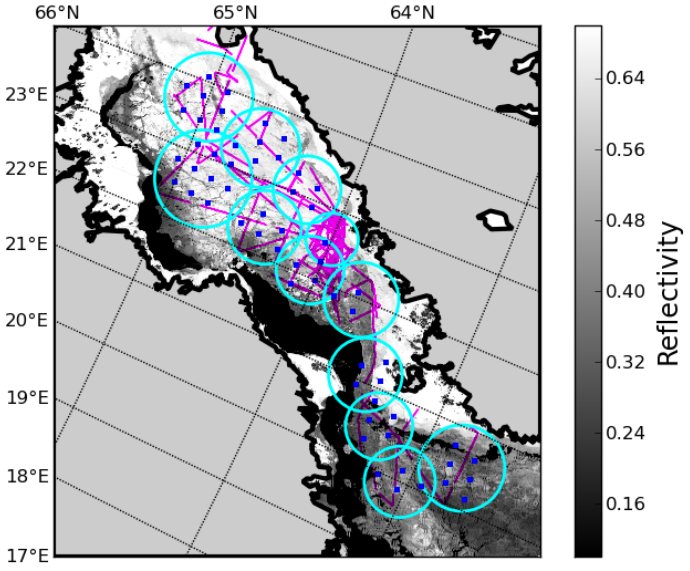

Figure 5.17: For figure description see caption of Figure 5.16, except that here the underlying MODIS image is from 6th March, 2011.

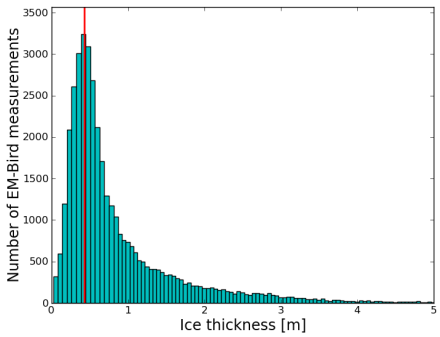

(a) Circle no. 1

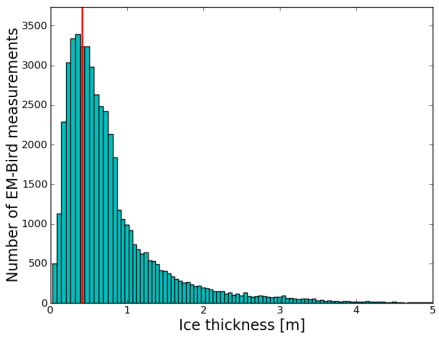

(b) Circle no. 2

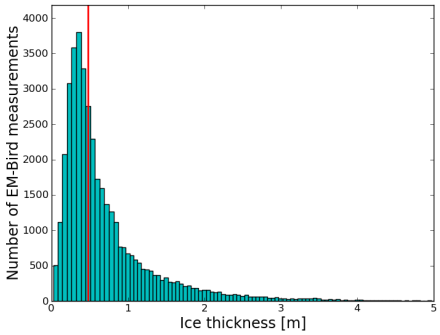

(c) Circle no. 3

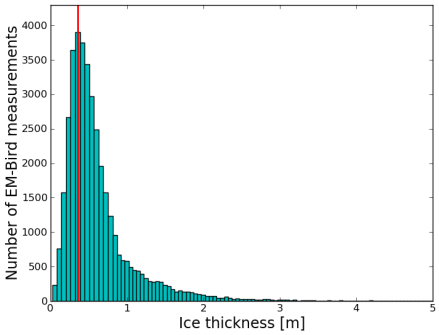

(d) Circle no. 4

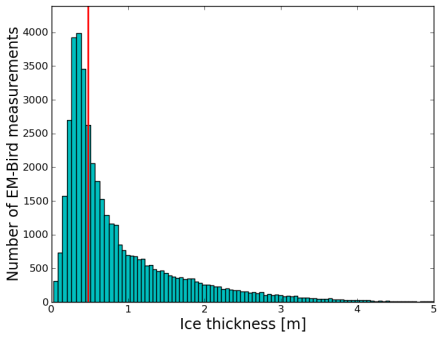

(e) Circle no. 5

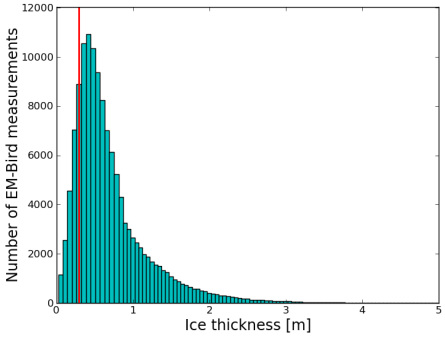

(f) Circle no. 6

Figure 5.18: Distribution of total ice thicknesses as measured by the EM Bird within the circular areas depicted in Figure 5.15. The red lines indicate ice thicknesses as retrieved from SMOS brightness temperature intensities (or vertically polarised brightness temperatures).

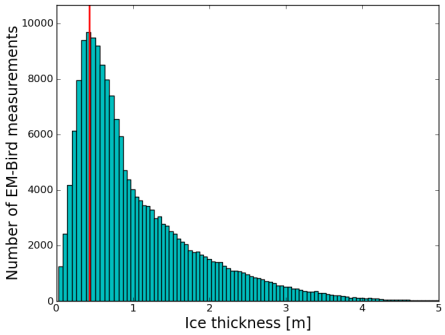

(a) Circle no. 7

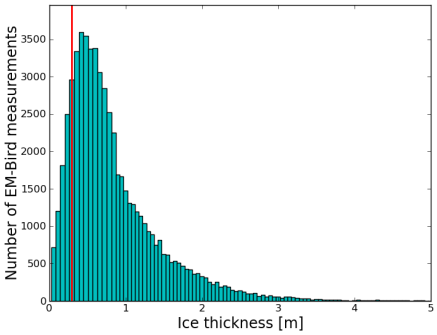

(b) Circle no. 8

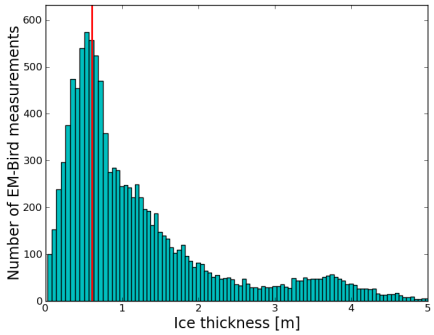

(c) Circle no. 9

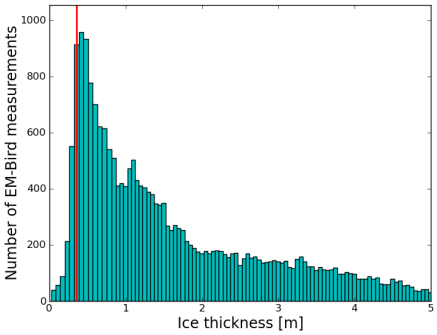

(d) Circle no. 10

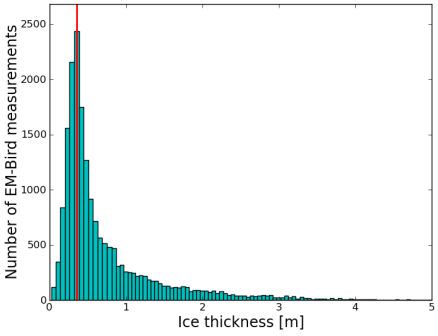

(e) Circle no. 11

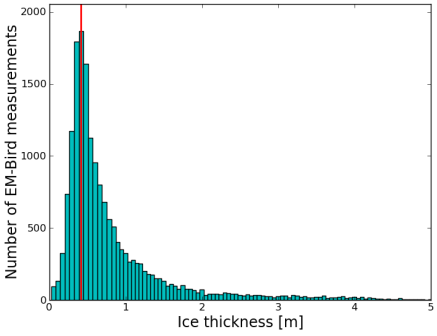

(f) Circle no. 12

Figure 5.19: For figure description see caption of Figure 5.18.

1 m, and 13 – 21% of the ice thicknesses are between 1 and 2 m (circle nos. 1 – 6, 11, 12). For the remaining four circles, circle nos. 7, 8, 9, and 10, ice thicknesses below 1 m account for 58%, 69%, 54%, and 39%, respectively; and ice thicknesses between 1 and 2 m account for 25 – 29% of the measured ice thicknesses. These four circles with the highest ice thicknesses are the four circles that are closest to the Finnish coast west of Vaasa (approximately at 63.1°N and 21.6°E). Thus, their locations coincide with the region, where the EM Bird tends to overestimate ice thickness due to shallow waters and potential freshwater layers underneath the fast ice (as indicated in section 5.4.1). However, compared to the other circles, circle no. 7 contains the highest number of EM Bird measurements and thus contains also a lot of ice thickness measurements off the coast.

Comparison of EM Bird and SMOS ice thicknesses

For the comparison of ice thicknesses retrieved from SMOS brightness temperatures and ice thicknesses measured by the EM Bird, we here use the modal value of the EM ice thickness distributions. Firstly, the modal value is considered to be the most accurate value obtained from EM Bird measurements (Haas et al., 2010). Secondly, the maximum ice thickness value that is retrievable from L-band brightness temperatures under Baltic conditions is about 1 – 2 m (Kaleschke et al., 2010). Ice thicknesses higher than this maximum value do not change the brightness temperature signal observed over ice. Thus, we expect that the ice thickness that can be retrieved from SMOS is mainly the modal ice thickness.

For each circle, the ice thickness as retrieved from SMOS brightness temperature intensities is indicated in the figures that show the ice thickness distributions measured by the EM Bird (Figures 5.18 and 5.19). The ice thickness as retrieved from SMOS brightness temperature intensities coincides with the modal ice thickness from EM Bird measurements in five out of the twelve cases (circle nos. 1, 4, 7, 11, and 12). In two cases, the SMOS ice thickness is one bin (about 6 cm) too high (circle nos. 2 and 9), in one case, the SMOS ice thickness is one bin too low (circle no. 10). In two cases, the SMOS ice thickness is two bins (about 12 cm) too high (circle nos. 3 and 5), or two bins too low (circle nos. 6 and 8). Thus, with the chosen assumptions for the model, the deviations between SMOS and EM Bird ice thicknesses are evenly distributed, and we do not observe a systematic over- or underestimation of ice thickness by SMOS, when compared to the EM Bird measurements.

Figures 5.20 to 5.23 show the spatial distributions and scatter plots of the modal EM Bird ice thicknesses and the ice thicknesses retrieved from SMOS brightness temperatures. The SMOS ice thicknesses are retrieved from horizontally polarised brightness temperatures (Figures 5.20 and 5.21), and from vertically polarised brightness temperatures and brightness temperature intensities (Figures 5.22 and 5.23). Here, the ice thicknesses retrieved from vertical polarisation and from brightness temperature intensities are identical.

The ice thicknesses retrieved from horizontal and from vertical polarisation (or from intensities) differ only slightly. The spatial distribution of the compared ice thicknesses does not reveal any distinct pattern of regional differences. The ice thicknesses that fit best are found both in the northernmost and in the southernmost circles, as well as both in the eastern part and the western part of the Bay of Bothnia. What is striking

is that the two circles with the highest positive deviation and the two circles with the highest negative deviation between SMOS and EM Bird ice thicknesses are located next to each other, respectively. For the adjacent circle nos. 3 and 5, the SMOS ice thickness is about 12 cm higher than the EM Bird modal ice thickness, while for the adjacent circle nos. 6 and 8, the SMOS ice thickness is about 12 cm lower than the EM Bird modal ice thickness.

The scatter plots for SMOS retrieved ice thicknesses and EM ice thicknesses reveal that the range of ice thicknesses that is obtained from SMOS measurements is somewhat broader than the range of ice thicknesses obtained from the modal values of the EM ice thicknesses. For example, for the SMOS retrieval based on brightness temperature intensity or on vertically polarised brightness temperatures (Figure 5.23), we obtain values between 29 and 61 cm ($2\times d_{ice}$= 29 cm, $3\times d_{ice}$= 35 cm, $4\times d_{ice}$= 41 cm, $2\times d_{ice}$= 48 cm, and $1\times d_{ice}$= 61 cm). Whereas, we obtain values between 35 and 54 cm from the EM Bird measurements ($5\times d_{ice}$= 35 cm, $6\times d_{ice}$= 41 cm, and $1\times d_{ice}$= 54 cm).

Considering all 12 circles, the root mean square deviations between EM Bird ice thicknesses and ice thicknesses retrieved from SMOS are 8.8 cm for horizontal polarisation, and 7.7 cm for vertical polarisation and for intensity. The mean ice thickness for all 12 modal values from the EM Bird ice thickness measurements is 39.9 ± 5.1 cm, compared to a mean ice thickness of 40.4 ± 8.2 cm for the SMOS ice thickness retrievals based on vertical polarisation and on intensity, and a mean ice thickness of 41.4 ± 10.0 cm for the SMOS retrieval based on horizontal polarisation.

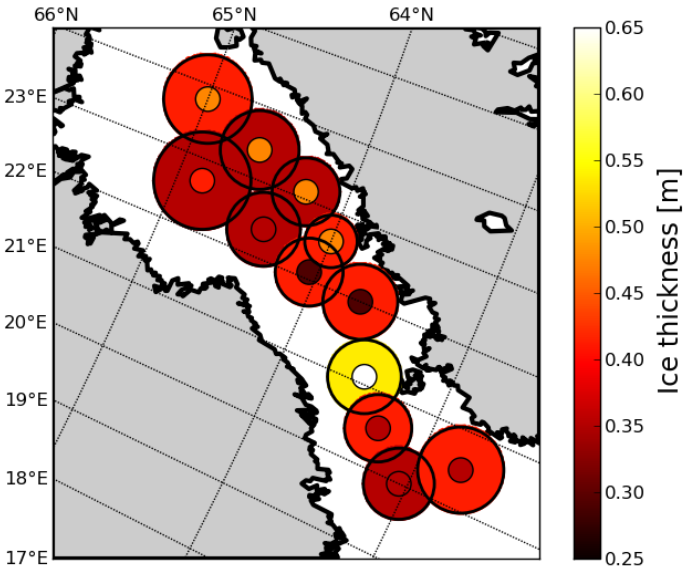

Figure 5.20: Total ice thicknesses as measured by the EM Bird and as retrieved from horizontally polarised SMOS brightness temperatures. The inner circles depict ice thicknesses as retrieved from SMOS, the outer circles depict the modal values of all ice thicknesses measured within the validation circles by the EM Bird.

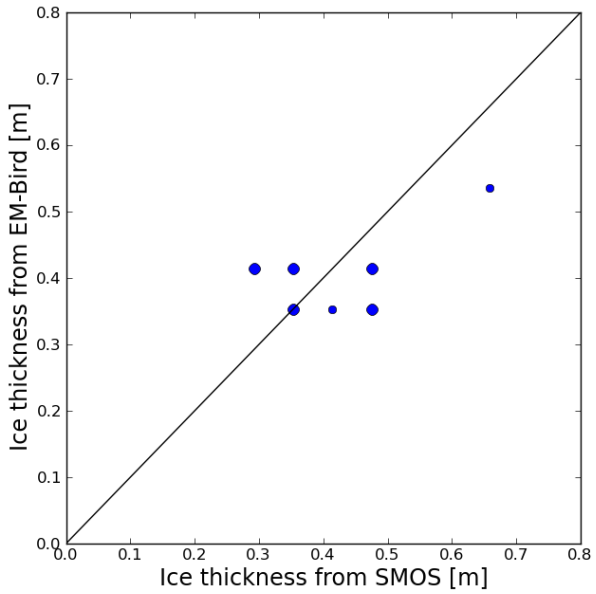

Figure 5.21: Modal ice thicknesses from the EM Bird versus ice thicknesses retrieved from horizontally polarised SMOS brightness temperatures for the 12 circles shown in Figure 5.20. The size of the points corresponds to the number of cases in that the given combination of ice thicknesses from EM Bird and SMOS coincide.

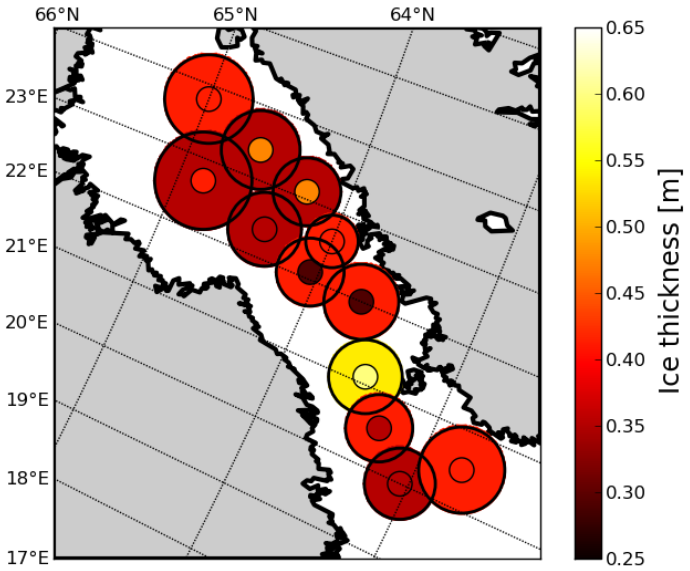

Figure 5.22: For figure description see caption of Fig.5.20, but here the SMOS ice thicknesses are retrieved from vertically polarised brightness temperatures or from brightness temperature intensities (giving the same retrieved ice thicknesses).

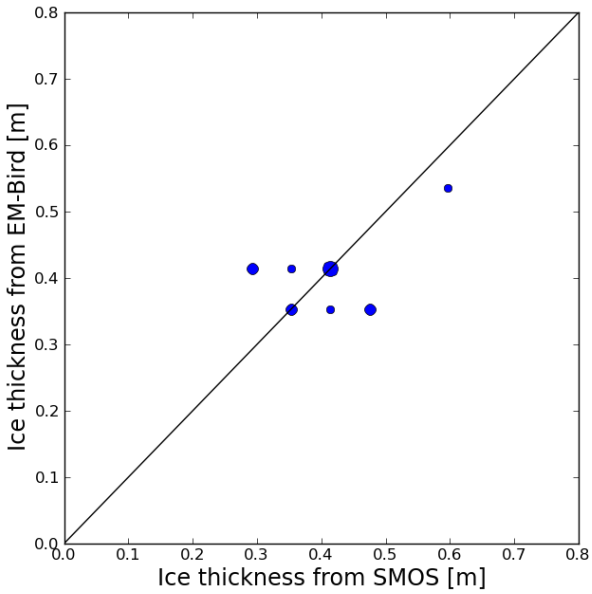

Figure 5.23: For figure description see caption of Fig.5.21, but here the SMOS ice thicknesses are retrieved from vertically polarised brightness temperatures or from brightness temperature intensities (giving the same retrieved ice thicknesses).

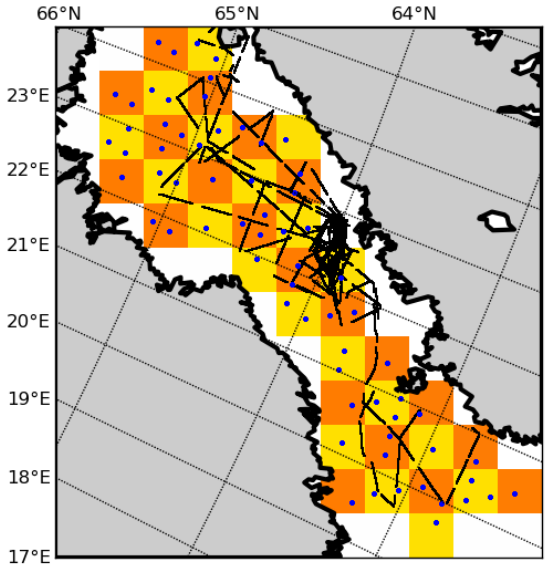

Figure 5.24: EM Bird flight tracks of the SafeWin field campaign from 2nd to 7th March, 2011 (black lines) and SMOS measurements (blue points) plotted over the 30 km × 30 km grid used in the validation approach 2 of section 5.4.4. Only the grid boxes that contain suitable SMOS brightness temperature data for a potential ice thickness retrieval are shown here. For the corresponding criteria see sections 5.4.4 and 5.4.2.

5.4.4 Validation approach 2

A common approach to compare two data sets is to define a regular grid, to select all data located within one grid cell from both data sets, and for each grid cell to compare the values obtained from one data set with the values obtained from the other data set. In this section, we show the results of such a comparison between SMOS retrieved ice thicknesses and EM Bird measurements.

Data selection

We divide the area of investigation into 12 × 11 grid cells with cell sizes of 30 km × 30 km (Figure 5.24). For the further analysis, we include all SMOS measurements whose centre points are located within an area of 0.75 times the grid cell size around the grid cell's centre point. As in section 5.4.3, the factor 0.75 is chosen quite arbitrarily and is a compromise between including as many measurements as possible and excluding SMOS measurements that represent large areas outside the grid cell. Thus, we include all SMOS measurements with their centre points being located within an area of 22.5 km × 22.5 km around the grid cell's centre point.

For the EM Bird ice thickness determination for each grid cell, we collect all EM Bird measurements located within an area of 1.25 times the grid cell size around the grid cell's centre point. Thus, for each grid cell we include all EM Bird measurements within an area of 37.5 km × 37.5 km around the grid cell's centre point. We include EM Bird measurements from a larger area (37.5 km × 37.5 km) than we do for SMOS

measurements (22.5 km × 22.5 km) because the SMOS measurements have footprint sizes of 35 – 50 km × 35 – 50 km. Thus, even with the constricted selection of SMOS measurements for each grid cell, the included SMOS measurements represent large areas outside the 22.5 km × 22.5 km area and cover at least the 37.5 km × 37.5 km area of included EM Bird measurements. As in section 5.4.3, we take the modal value of the corresponding ice thicknesses as the representative total ice thickness.
In order to avoid that we assign obviously unrepresentative values to grid cells that are only marginally covered by EM Bird measurements, we impose two requirements. These have to be fulfilled before we assign an EM ice thickness to a grid cell. Firstly, we only assign an EM ice thickness to grid cells that contain EM Bird measurements within their inner 22.5 km × 22.5 km area, i.e. in the area where the SMOS measurements' centre points have to be located in order to be included. Secondly, the grid cell has to contain more than 1000 single EM Bird measurements. According to the spacing of subsequent EM Bird measurements, 1000 single EM Bird measurements correspond to a flight track length of about 3 – 4 km.

Results

SMOS ice thickness

The ice thicknesses retrieved from SMOS show higher ice thicknesses of up to 50 - 60 cm close to the Finnish coast in the eastern part of the Bay of Bothnia (Figure 5.25). The SMOS ice thicknesses decrease further inwards the Bay of Bothnia (westward) and reach their minimum values of about 25 – 30 cm at the edge of the open water tongue that is indicated in the ice concentration map obtained from MODIS images (Figure 5.14). West of this open water tongue, close to the Swedish coast in the south-western part of the Bay of Bothnia and the Sea of Bothnia, SMOS ice thicknesses are thicker than 65 cm.

EM ice thickness

The modal ice thicknesses obtained from the EM Bird measurements show high ice thicknesses of more than 65 cm west of the coast of Vaasa (approximately at 63.1°N and 21.6°E) and ice thicknesses of about 60 cm near the island Hailuoto (Figure 5.25). These areas are expected to be areas, where the EM Bird tends to overestimate ice thicknesses, due to shallow waters and freshwater layers underneath the fast ice (see section 5.4.1). Additionally, EM ice thicknesses exceeding 65 cm are found in the north-western part of the Bay of Bothnia near the area with low ice concentrations indicated in MODIS images (Figure 5.14).

Comparison of EM and SMOS ice thicknesses

As in the validation approach 1 of the previous section, the ice thicknesses retrieved from horizontally polarised, from vertically polarised brightness temperatures, and from brightness temperature intensities are relatively similar. Thus, we here only show the results for the comparison of EM ice thicknesses and ice thicknesses retrieved from SMOS brightness temperature intensities (Figures 5.25 and 5.26).
As in the validation approach 1, we cannot identify any regions, where the EM and SMOS ice thicknesses agree particularly well or particularly poorly. The deviations

between EM and SMOS ice thicknesses are distributed evenly over the considered area (Figure 5.25).
All SMOS ice thicknesses that are compared with EM ice thicknesses here take values between 29 and 48 cm. Thus, these SMOS ice thicknesses are in the same range as for the validation approach 1, where all except of one ice thickness had values in this ice thickness range. In contrast, the EM Bird modal values for the grid-based validation approach 2 are distributed over a broader range of ice thickness values than in the validation approach 1. Here, the EM modal ice thicknesses range between 29 and 95 cm and are thus more variable than the corresponding SMOS ice thicknesses. In contrast, the range of EM ice thicknesses was 35 – 54 cm in the validation approach 1 and the EM ice thicknesses were distributed over a smaller range than the corresponding SMOS ice thicknesses.
When we average over all grid cells that contain both EM and SMOS ice thicknesses, the mean ice thickness from EM Bird measurements is 48.0 ± 16.2 cm, as compared to 38.4 ± 6.5 cm for the mean ice thickness retrieved from SMOS brightness temperature intensities. The root mean square deviation between EM Bird and SMOS ice thicknesses for the grid-based comparison here is 19.3 cm.

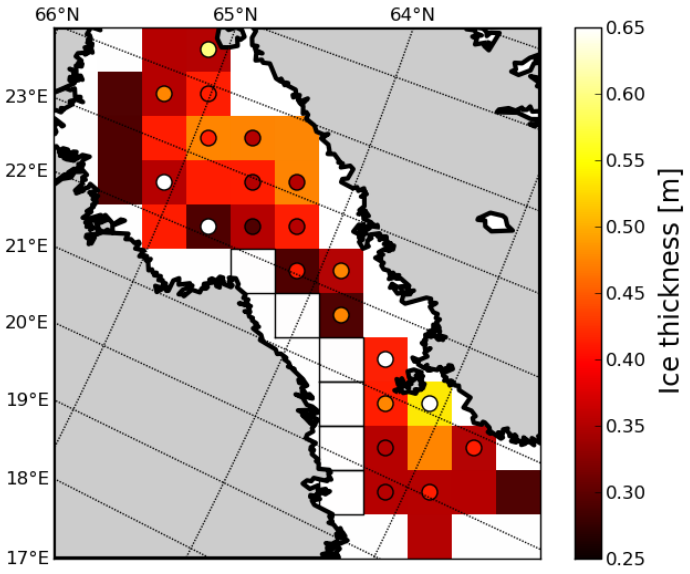

Figure 5.25: Total ice thicknesses as measured by the EM Bird and as retrieved from SMOS brightness temperature intensities. The square boxes depict ice thicknesses as retrieved from SMOS, the circles depict the modal values of all ice thicknesses measured within the square boxes by the EM Bird.

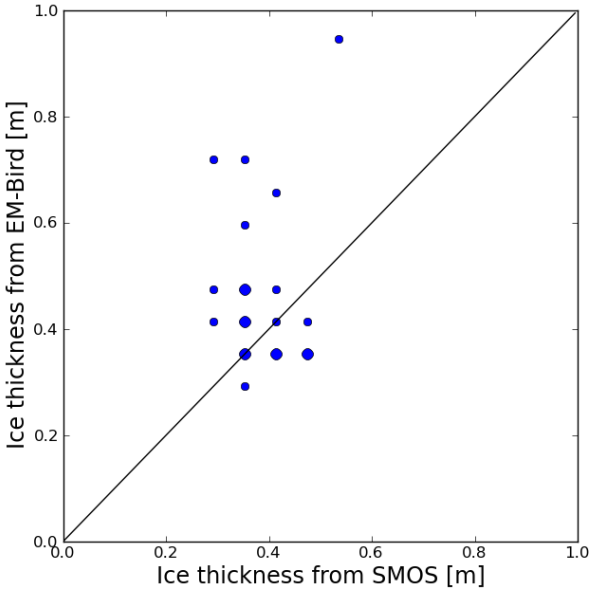

Figure 5.26: Modal ice thicknesses from the EM Bird versus ice thicknesses retrieved from SMOS brightness temperature intensities for the validation approach 2, which uses a gridded field (see Figures 5.24 and 5.25). The size of the points corresponds to the number of cases in that the given combination of ice thicknesses from EM Bird and SMOS coincide.

5.5 Summary and Discussion

In this chapter, we investigated three aspects regarding SMOS brightness temperatures in the northern parts of the Baltic Sea and the potential for sea ice thickness retrieval in the Baltic Sea: 1) We examined SMOS brightness temperatures observed over open water in the Bay and Sea of Bothnia and compared these observed brightness temperatures with our modelled brightness temperatures. 2) We examined brightness temperatures observed by SMOS over growing sea ice in the northern Bay of Bothnia and investigated whether these brightness temperatures contain information on the thickness of sea ice. 3) We applied the findings of 1) and 2) to retrieve ice thicknesses from SMOS brightness temperatures in the Baltic Sea. These ice thicknesses were validated with ice thicknesses measured by an EM Bird sounding system during a flight campaign in the Bay and Sea of Bothnia.

Brightness temperatures over open water
As expected, SMOS brightness temperatures observed over open water in October and November, 2010 in the Bay and Sea of Bothnia were quite stable with time. Over the two months considered here, brightness temperatures decreased on average by 3 – 4 K, mainly due to a decreasing water temperature. The root mean square deviations between single SMOS measurements and averaged SMOS brightness temperatures were quite high (about 6 – 8 K). Thus, we should not use single SMOS measurements for any retrievals, but rather values that have been averaged over a lot of measurements (e.g. over time and space).
We found that vertically polarised brightness temperatures observed by SMOS agreed well with our modelled brightness temperatures, while horizontally polarised brightness temperatures were considerably underestimated by our model. At vertical polarisation, the average observed brightness temperatures were overestimated by 2.1 K and the root mean square deviation between modelled and observed brightness temperatures was 3.0 K. At horizontal polarisation, brightness temperatures were on average underestimated by 10.6 K by the model, and the root mean square deviation between the model and the average observations was 15.4 K.
We used the water brightness temperature simulations and the comparison of modelled and observed brightness temperatures to investigate the performance of our atmospheric correction and of our correction for the uniform cosmic background radiation (as described in section 2.3). Regarding the root mean square deviation, the corrections had hardly any impact at vertical polarisation, but reduced the root mean square deviation by almost 5 K at horizontal polarisation (from 20.2 to 15.4 K). Regarding the mean deviation between modelled and averaged observed brightness temperatures, the corrections caused a reversal of sign at vertical polarisation: instead of a mean underestimation by 2.3 K, we obtained a mean overestimation by 2.1 K, when the corrections were applied. For horizontal polarisation, the mean deviation decreased by almost 6 K (from 16.2 to 10.6 K), when the corrections were applied. Brightness temperature intensity is the mean value of brightness temperature at horizontal and at vertical polarisation. Thus, according to our results, the mean deviation between modelled and mean observed brightness temperature intensities would be 9.25 K without the corrections, and 4.25 K with the corrections. Thus, at

least brightness temperatures at horizontal polarisation and brightness temperature intensities benefit from applying the corrections for atmospheric effects and the uniform cosmic background radiation, even when we implement only a very rough estimation of the atmospheric contribution, obtained from temperature and humidity profiles averaged over the polar regions of the Northern Hemisphere. However, the impact of the atmospheric contribution and the cosmic background radiation is smaller for brightness temperatures over sea ice than over water, because the emissivity of ice is higher than the emissivity of water. Thus, less of the downward directed atmospheric and cosmic background radiation is reflected at the ice surface than at the water surface and the contribution to the signal measured at the TOA by SMOS is smaller.
The deviations between modelled and observed water brightness temperatures discovered in this section were used as correction terms for the modelled water brightness temperatures in the last section.

Brightness temperatures over growing sea ice
Brightness temperatures observed by SMOS over sea ice in the Bay of Bothnia increased considerably over the examined time period of 1st January to 28th February, 2011. The horizontally polarised brightness temperatures, averaged over the incidence angle range of 0 – 65° and over three time periods from 1st January to 28th February, increased from 207.7 K to 221.2 K and to 233.0 K, corresponding to an overall increase by 25.3 K. The averaged vertically polarised brightness temperatures increased from 223.1 K to 235.6 K and to 245.4 K, corresponding to an overall increase by 22.3 K. We expected this increase to be caused by an increasing ice thickness. The corresponding increase of ice thickness as estimated from FMI's ice thickness maps based on MODIS images was 33 cm (from an average ice thickness d_{ice}= 25 cm for 1st January – 26th January to an average ice thickness of d_{ice}= 58 cm for 18th February – 28th February). However, there are mainly four ice properties that have the potential to cause a brightness temperature increase as it is observed in this case: 1) ice temperature, 2) ice salinity, 3) ice concentration, and 4) ice thickness.
1) **Ice temperature:** According to MODIS IST data, the ice surface temperature was always well below -5°C during the examined time period (Figure A.5 in the appendix). Our sensitivity studies in section 3.1.3 suggest that at these ice surface temperatures, brightness temperatures increase with increasing ice surface temperature. Thus, an increase of brightness temperature may only have been caused by a changing ice surface temperature, if there was a general upward trend of the ice surface temperature for the considered time period. However, the ice surface temperature data in the examined area did not show an upward (or downward) trend from 1st January to 28th February (Figure A.5 in the appendix); instead we observed rather irregular fluctuations with frequent changes between warming and cooling of the ice surface. Consequently, the brightness temperature increase with time cannot be explained by changes in ice temperature.
2) **Ice salinity:** It is difficult to exactly determine the ice salinity of the ice we examined here, but we can certainly assume that the ice salinity in the northern Bay of Bothnia is less than 2 g/kg. Our sensitivity studies in section 3.2 suggest that brightness temperatures decrease with decreasing ice salinity at ice salinities S_{ice} <

2 g/kg. Due to desalination processes that occur in growing or ageing sea ice, we expect ice salinity generally to decrease with time. Thus, according to our sensitivity studies, the brightness temperature of ice would decrease and not increase, if ice salinity changes were the main contributor to the observed brightness temperature signal. Hence, ice salinity is not likely to have caused the increase of brightness temperatures observed here.
3) **Ice concentration:** According to Finnish ice charts, to MODIS-based ice thickness maps, and to ASI ice concentration data, the investigated area was almost completely ice-covered during the whole time period considered here (Figure A.5 in the appendix). The ice coverage of the Baltic Sea is assumed to be well observed, because it is one of the busiest ship traffic areas in the world. Thus, because there was no positive trend in ice concentration, we are confident that the observed brightness temperature increase was not related to an increasing ice concentration.
4) **Ice thickness:** According to Finnish ice charts and the FMI's ice thickness maps based on MODIS images, the ice thickness gradually increased from the beginning of January to the end of February, 2011. This behaviour is in accordance with the typical evolution of ice thickness in January and February in the Bay of Bothnia (see section 5.1). Thus, the ice thickness was most likely the main contributor to the observed brightness temperature increase with time.
The deviations between modelled and measured brightness temperatures were lowest for the model calculations that include a snow layer and assume an ice salinity of S_{ice}= 1.5 g/kg for the time period 1st January – 26th January (estimated ice thickness d_{ice}= 25 cm), and an ice salinity of S_{ice}= 1.0 g/kg for the time periods 27th January – 17th February (estimated d_{ice}= 41 cm) and 18th February – 28th February (estimated d_{ice}= 58 cm). Due to the desalination processes that occur in growing or ageing sea ice, we think that these are reasonable assumptions. However, the actual values of the ice salinity are not known, and, as is also shown in section 3.2, sensitivity of brightness temperatures to ice salinity is very high for low ice salinities. Thus, the ice thickness retrieval from SMOS brightness temperatures for ice with low salinities depends on the available information on ice salinity. However, even if the ice salinity is only roughly estimated, the relative difference in the observed brightness temperatures can be used to infer information on the average ice thickness, although the absolute ice thickness values cannot be determined exactly.
We found that for all ice salinity assumptions, brightness temperatures modelled without accounting for a snow layer were considerably lower than the observed brightness temperatures. For the different ice salinities (S_{ice} between 0.5 and 1.5 g/kg), the modelled brightness temperatures were 11 – 34 K lower at vertical polarisation and 23 – 46 K lower at horizontal polarisation.
Another finding of our brightness temperature investigations over growing sea ice in the Baltic Sea was that single SMOS measurements have a high variability. The root mean square deviations between modelled and measured brightness temperatures were on average twice as high for single SMOS measurements than for SMOS measurements averaged over several days and incidence angles.
Because we were able to show that the increase of brightness temperatures, as observed by SMOS, was mainly assigned to sea ice thickness changes, we can hereby confirm that SMOS brightness temperatures provide information on ice thickness in the Baltic

Sea. For our model assumptions and a rough estimation of the ice thickness, the root mean square deviations between simulated and measured brightness temperatures were in the order of 4 – 6 K at horizontal polarisation and 3 – 5 K at vertical polarisation. The mean brightness temperatures differed by 1 – 2.5 K.

Validation of SMOS sea ice thickness retrieval in the Baltic Sea

In order to validate the sea ice thickness retrieval using SMOS, we compared ice thicknesses retrieved from SMOS brightness temperatures with ice thicknesses measured during an EM Bird flight campaign in the Bay and northern Sea of Bothnia in March, 2011. The Baltic Sea is a challenging area for the retrieval of ice thickness using SMOS. L-band brightness temperatures in the Baltic Sea region suffer from a quite high RFI contamination, and the land impact on measured brightness temperatures is relatively high in the land-enclosed Baltic Sea basin.

For the retrieval of ice thickness in the Baltic Sea, we simulated brightness temperatures for a range of incidence angles (θ= 0 – 50°). Therefore, we used the incoherent Burke model for one snow and one ice layer and assumed constant values for the model input parameters ice concentration, ice temperature and salinity, water temperature and salinity, and the density and thickness of a snow layer on top of the ice. Ice concentration was determined by the classification of MODIS reflectivities. In order to estimate the ice temperature for the model calculations, we averaged the ice surface temperatures obtained from MODIS measurements over the considered area and the time period. For ice and water salinity, water temperature, and snow density and thickness, we used typical values observed for sea ice in the Baltic Sea. While the above mentioned model parameters were set to constant values, the ice thickness was varied. We calculated the root mean square deviation between brightness temperatures observed by SMOS and brightness temperatures simulated for the different ice thicknesses. The retrieved ice thickness was then the ice thickness for that the brightness temperature simulations had the lowest deviation from the brightness temperature observations.

We showed the results for two different approaches to compare SMOS and EM Bird ice thicknesses. For the first approach (validation approach 1), we first manually defined 12 circular areas in the Bay and Sea of Bothnia. These circular areas were chosen in consideration of the EM Bird flight tracks such that we supposed every circle to be reasonably represented by the ice thicknesses measured by the EM Bird. In the next step, we then chose the matching SMOS measurements, applied our ice thickness retrieval method, and compared the resulting SMOS ice thicknesses with the EM Bird modal ice thicknesses for each of the 12 circles. The second validation approach (validation approach 2) was more governed by the distribution of the SMOS measurements. We defined a regular grid for the area of investigation. For each grid cell, we then chose the corresponding SMOS brightness temperatures and EM Bird ice thickness measurements. However, we expected the results of such a comparison to be less representative than the results of the comparison based on the circular areas (validation approach 1) for the measurements considered here. The reason is, that we here compared irregularly distributed field campaign data with satellite data distributed on a regular grid. Additionally, the footprint sizes of the two data sets were very different: single SMOS measurements have footprints of about 35 – 50 km

$\times$ 35 – 50 km, while single EM Bird measurements have footprints in the order of 50 m $\times$ 50 m.

The results of our analysis confirmed that a comparison based on a gridded field is not necessarily representative for comparison of SMOS and EM Bird measurements. For this approach (validation approach 2), the mean ice thicknesses obtained from EM Bird measurements and from the SMOS retrieval differed by almost 10 cm for mean ice thicknesses of 40 – 50 cm, and the root mean square deviation was 19.3 cm.

In contrast, ice thicknesses from the EM Bird measurements and from the SMOS retrieval agreed considerably better for the validation approach that was more oriented on the availability of the EM Bird validation data (validation approach 1). The mean EM and SMOS ice thicknesses agreed within 0.5 cm. The mean EM ice thickness, obtained from the 12 modal values, was 39.9 $\pm$ 5.1 cm. The mean SMOS ice thickness was determined to be 40.4 $\pm$ 8.2 cm for the retrieval from vertically polarised brightness temperatures and brightness temperature intensities. The corresponding root mean square deviation between EM and SMOS ice thicknesses for this validation approach was 7.7 cm. For ice thicknesses retrieved from SMOS brightness temperatures at horizontal polarisation, the agreement with EM ice thicknesses was slightly lower (the mean SMOS ice thickness being 1.5 cm higher than the EM ice thickness, and the root mean square deviation between the ice thicknesses being 8.8 cm).

Thus, we here showed that the retrieval of ice thickness from SMOS brightness temperatures is possible, even in a challenging region like the Baltic Sea. Furthermore, we demonstrated that it is important to choose an adequate approach to compare satellite-based data that are provided on a regular grid with flight campaign data that are provided along irregularly distributed flight tracks.

Chapter 6

Summary and Conclusions

In this study, we investigated how ice conditions influence the sea ice thickness retrieval from SMOS data, assessed the potential to retrieve snow thickness over thick Arctic multi-year ice from SMOS data, and validated the SMOS ice thickness retrieval for applications in the Baltic Sea. The maximum retrievable ice thickness and the accuracy of the retrieval depend on the ice conditions, which can mainly be described by ice temperature, salinity, and concentration, as well as the potential presence of a snow cover. In order to investigate the sensitivity of the ice thickness retrieval to temperature, salinity, and a snow layer on top of the ice, we here used two radiation models. These models consider the emissivity of radiation in a medium that consists of multiple layers: A coherent radiation model based on the Maxwell equations (Ulaby et al., 1981), and an incoherent model based on the radiative transfer equation (Burke et al., 1979). In addition to the theoretical considerations, we used the incoherent Burke model to compare our simulations with observations. We compared SMOS measurements with brightness temperature simulations for ice and snow thicknesses obtained from airborne measurements in the Arctic, and for ice thicknesses obtained from thermal imagery in the Baltic Sea. Furthermore, we compared snow thicknesses retrieved from SMOS with airborne snow thickness measurements in the Arctic, and ice thicknesses retrieved from SMOS with airborne EM ice thickness measurements in the Baltic Sea.

We found that for a 50 cm thick ice column, sudden temperature changes of almost 30°C at the ice surface caused a brightness temperature error of about 7 K, if we assumed a linear temperature gradient within ice, instead of accounting for the actual temperature profile. However, after four hours the difference had reduced to 3 K and was less than 0.5 K after more than eight hours. For thinner ice and less pronounced surface temperature changes, temperatures adjusted even more rapidly to the new situation. The time scales for that the error reduced significantly are in the same order of magnitude as the expected temporal deviation between SMOS measurements and possibly available surface temperature information. Thus, we conclude that we can assume a linear temperature gradient for the retrieval of ice thickness from SMOS brightness temperatures.
Brightness temperatures simulated for multiple layers and a linear temperature gradient were about 5 K higher than brightness temperatures simulated for one ice layer

and a bulk ice temperature, because the relationships between ice permittivity and ice emissivity, as well as between ice permittivity and ice temperature are non-linear. We suggest to determine a representative ice permittivity value, which can be used in a one-ice-layer-model, instead of using the time-consuming multiple-ice-layer-model. For this purpose, the ice salinity profile in ice should also be taken into account, instead of a constant bulk ice salinity, as was considered here.

We found that for typical Arctic conditions (bulk ice salinity: S_{ice}= 8 g/kg, water salinity: S_{water}= 30 g/kg, water temperature: T_{water}= -1.8°C), brightness temperature sensitivity to ice temperature is higher for thinner ice than for thicker ice, except for very high ice surface temperatures (T_{surf} > -4°C). For thin ice ($d_{ice} \leq$ 15 cm), brightness temperatures increase with increasing ice temperature, except for very high ice temperatures near the freezing point of water. For thicker ice, brightness temperatures increase with increasing ice temperature until a reversal point is reached. A further increase of ice temperature leads to a decrease of brightness temperature. For thicker ice, this reversal point occurs already at lower ice temperatures than for thinner ice. The reversal point occurred at T_{surf}= -2.8°C for an ice thickness of d_{ice} = 15 cm and at T_{surf}= -9.6°C for an ice thickness of d_{ice} = 60 cm. This reversal point was also found for the impact of ice temperature on the ice thickness retrieval: For temperatures colder than the reversal point, retrieved ice thicknesses are overestimated by about 1 cm per ice surface temperature overestimation of 1 K. For ice temperatures higher than the reversal point, retrieved ice thicknesses are considerably underestimated even for only slight overestimations in ice temperature.

According to our models, brightness temperature sensitivity to ice salinity is very high for low salinities, thus the ice thickness retrieval in brackish waters and over multi-year ice requires more accurate information on ice salinity than for ice with higher salinity. For typical Arctic conditions (T_{surf}= -15°C, S_{water}= 30 g/kg, T_{water}= -1.8°C) and ice salinities S_{ice} < 2.5 g/kg, brightness temperatures increase by more than 10 K, when ice salinities increase by 1 g/kg. For typical first-year ice salinities of 7 g/kg< S_{ice} < 10 g/kg, the sensitivity reduces and ice thickness retrieval is only slightly influenced by ice salinity. For these ice salinities, retrieved ice thicknesses are overestimated by less than 2 cm per ice salinity overestimation of 1 g/kg.

We found that, for an example case of growing sea ice during the Arctic freeze-up, the increasing ice thickness was the main contributor to the observed brightness temperature increase. Compared to the ice thickness signal, temperature and salinity variability accounted only for 21% and 11% of the observed brightness temperature intensity's variability, respectively. In contrast, the polarisation difference was more influenced by ice temperature and salinity.

The incoherent Burke model does not reproduce the proper brightness temperatures for very thin layers of ice or snow (less than a few centimeters), because the Burke model does not reduce to the emissivity of the underlying medium, when the overlying layer approaches a thickness of zero. Furthermore, the incoherent Burke model turned out to be less suitable for sea ice applications, if multiple layers in ice are considered, because it neglects higher order reflection terms. However, when we added a snow layer on top of ice, brightness temperatures modelled with the incoherent Burke model were consistent with the average values of the oscillating brightness temperatures in the coherent Ulaby model, which accounts for higher order reflection terms.

According to our radiation models, the presence of a snow layer always increased brightness temperatures above sea ice, because snow emits radiation and has a higher emissivity than ice. The dielectric properties of wet snow had more impact on brightness temperature than the dielectric properties of dry snow. Due to dry snow being almost transparent in L-band, brightness temperatures over snow-covered sea ice were only very weakly dependent on the thickness of the snow layer, when thermal insulation by snow was neglected. When neglecting the thermal insulation, the presence of a snow cover caused an increase of brightness temperatures by about 10 K at nadir view (for typical Arctic conditions). At horizontal polarisation, the increase of brightness temperature increased with increasing incidence angle θ and reached 25 K at θ= 50°. In contrast, at vertical polarisation, the increase of brightness temperatures due to the presence of a snow cover decreased with increasing incidence angle. At θ= 50°, vertically polarised brightness temperatures of snow-covered and snow-free sea ice were almost identical. Additionally to this impact by the dielectric properties of snow, thermal insulation by snow caused a further increase of brightness temperatures, when ice temperatures were below the reversal point for the ice temperature sensitivity of brightness temperature.

In accordance with the findings from our theoretical considerations, comparisons between observed and simulated brightness temperatures for snow-covered thick ice in the Arctic showed that horizontal polarisation is more affected by the presence of a snow layer than vertical polarisation. The root mean square deviation between simulated and measured horizontally polarised brightness temperatures reduced significantly, when a snow layer was included in the simulations. When only pixels with a closed ice cover and an almost constant ice surface temperature were used, the root mean square deviation was 20.0 K for the simulations without snow and 4.4 K for the simulations with snow.

When averaged over about 100 – 200 SMOS measurements, brightness temperatures observed over snow-covered thick Arctic sea ice increased with increasing snow thickness. Horizontally polarised brightness temperature observations, averaged over the whole incidence angle range provided by SMOS, agreed well with simulations, while we observed an offset of about 5 – 8 K at vertical polarisation.

Due to the dependence of brightness temperature on snow thickness caused by thermal insulation of snow, SMOS brightness temperatures at horizontal polarisation can be used to estimate snow thickness over thick Arctic multi-year ice. The performance of the snow thickness retrieval depends on the model assumptions for ice temperature, ice salinity, and snow density. For snow thicknesses measured during the IceBridge campaign, the root mean square deviations between measured and SMOS retrieved snow thicknesses ranged between 11.0 and 18.0 cm, and the average value was 12.9 cm. The correlation coefficients r^2 ranged between 0.51 and 0.64. When we constrained the comparison to snow thicknesses retrieved to be lower than 35 cm, the root mean square deviations ranged between 5.7 and 9.1 cm, and the average value was 6.9 cm. For the model assumptions with the lowest deviation from the observations, mean SMOS and IceBridge snow thicknesses differed only by 0.3 cm.

We found that over open water in the Baltic Sea, our model agreed quite well with SMOS brightness temperatures at vertical polarisation, while the model considerably underestimated brightness temperatures at horizontal polarisation. Including our

correction for atmospheric contributions, based on long-term mean atmospheric profiles, and the correction for the uniform cosmic background radiation in L-band caused simulated brightness temperatures to be, on average, almost 6 K higher than without the corrections. Thus, the corrections resulted in brightness temperatures over sea water to be less underestimated by our model at horizontal polarisation, and turned the slight underestimation of brightness temperatures at vertical polarisation into a slight overestimation. After the corrections, the mean deviation between simulated and observed open water brightness temperatures was 10.6 K at horizontal polarisation and 2.1 K at vertical polarisation.

Over sea ice with a gradually increasing ice thickness, brightness temperatures observed over two months in the Bay of Bothnia increased with time. The brightness temperatures increased in total by 22 K at vertical polarisation and by 25 K at horizontal polarisation for an estimated ice thickness increase by 33 cm. From considering the temporal evolution of ice temperature, ice salinity, and ice concentration, we concluded that the brightness temperature increase was caused by the increasing ice thickness. For realistic assumptions for ice temperature and ice salinity, the observed SMOS brightness temperatures were considerably underestimated, when the snow layer was neglected in the brightness temperature simulations. When the snow layer was included, we obtained mean deviations of 1 – 2.5 K and root mean square deviations of 4 – 6 K at horizontal polarisation and 3 – 5 K at vertical polarisation for the model assumptions with the best agreement (S_{ice}= 1.5 g/kg for younger and thinner ice of $d_{ice}\approx$ 25 cm, and S_{ice}= 1.0 g/kg for older and thicker ice of $d_{ice}\approx$ 40 – 60 cm). We stated that absolute ice thickness values are possibly difficult to retrieve exactly because of the lack of information on ice temperature and salinity and the high sensitivity of brightness temperature to ice salinity for low salinities. However, SMOS brightness temperatures contained information on the trend in ice thickness, even in a challenging region with a high impact by the surrounding land and by a potentially high level of artificial contamination in the L-band radiation signal.

We obtained a good agreement between ice thicknesses as retrieved from SMOS and as measured by an EM Bird during a flight campaign in the northern Baltic Sea in March, 2011. Comparison of ice thicknesses within 12 circular areas, which were representatively covered by both SMOS and EM measurements, revealed a root mean square deviation of 7.7 cm and a difference of 0.5 cm for the mean ice thicknesses, when we accounted for a snow layer and used SMOS brightness temperature intensities or vertically polarised brightness temperatures for the retrieval. The corresponding mean ice thicknesses were 39.9 ± 5.1 cm for the EM measurements and 40.4 ± 8.2 cm for the SMOS retrieval. The deviations were slightly higher, when we used horizontally polarised SMOS brightness temperatures for the retrieval.

The retrievals of ice and snow thickness were most successful, when the broad range of incidence angles as provided by SMOS was exploited, and when SMOS brightness temperatures were averaged over several measurements.

Here, we provided means to correct the SMOS ice thickness retrieval with regard to ice temperature, salinity, and a snow cover on ice and to determine the uncertainty of the retrieved ice thicknesses caused by these ice conditions. Furthermore, we provided the basis for producing ice thickness maps in the Baltic Sea and snow thickness maps over thick multi-year ice in the Arctic.

Appendix

A.1 Atmospheric correction

Table A.1: Atmospheric correction term $\Delta T_{B,atm}$ as defined in section 2.3.3 for different emissivities e, brightness temperatures TB, and incidence angles θ, calculated from NCEP monthly mean air temperature and relative humidity profiles for April.

e	TB [K]	$\theta = 0°$	$\theta = 20°$	$\theta = 40°$	$\theta = 60°$
0.3	80	2.82	3.00	3.67	5.59
	85	2.78	2.95	3.62	5.51
0.4	110	2.37	2.52	3.09	4.71
	100	2.45	2.61	3.20	4.87
0.5	125	2.05	2.18	2.67	4.07
	135	1.97	2.10	2.57	3.91
	130	2.01	2.14	2.62	3.99
0.6	160	1.57	1.67	2.04	3.11
	150	1.65	1.75	2.14	3.27
	140	1.73	1.84	2.25	3.43
0.7	190	1.12	1.19	1.46	2.23
	180	1.20	1.28	1.57	2.39
	170	1.28	1.36	1.67	2.55
0.8	190	0.92	0.98	1.20	1.83
	220	0.68	0.72	0.88	1.34
	200	0.84	0.89	1.09	1.66
	210	0.76	0.81	0.99	1.50
0.85	220	0.58	0.61	0.75	1.14
	230	0.50	0.53	0.65	0.98
	200	0.74	0.78	0.96	1.46
	210	0.66	0.70	0.86	1.30
0.9	240	0.31	0.33	0.41	0.62
	250	0.23	0.25	0.30	0.46
	220	0.48	0.51	0.62	0.94
	230	0.39	0.42	0.51	0.78
0.95	240	0.21	0.23	0.28	0.42
	250	0.13	0.14	0.17	0.26
	230	0.29	0.31	0.38	0.58
	260	0.05	0.06	0.07	0.10
1.0	270	-0.13	-0.14	-0.17	-0.26
	240	0.11	0.12	0.15	0.22
	250	0.03	0.03	0.04	0.06
	260	-0.05	-0.05	-0.06	-0.10

A.2 Sensitivity to ice temperature

Table A.2: Mean sensitivity of brightness temperature intensity (θ= 0 – 40°) to ice surface temperature $\frac{\partial TB}{\partial T_{surf}}$ [K/K] for Arctic conditions (S_{water}= 30 g/kg, S_{ice}= 8 g/kg, T_{water}= -1.8°C):

T_{surf} \ d_{ice}	**10 cm**	**20 cm**	**30 cm**	**40 cm**	**50 cm**
-2°C	2.1	-1.8	-2.6	-2.6	-2.6
-6°C	2.7	0.6	-0.4	-0.7	-0.9
-10°C	2.5	1.6	0.8	0.3	0.1
-14°C	1.7	1.5	1.0	0.7	0.4
-18°C	1.3	1.2	0.8	0.6	0.4

Table A.3: Mean sensitivity of brightness temperature intensity (θ= 0 – 40°) to ice thickness $\frac{\partial TB}{\partial d_{ice}}$ [K/cm] for Arctic conditions (S_{water}= 30 g/kg, S_{ice}= 8 g/kg, T_{water}= -1.8°C):

T_{surf} \ d_{ice}	**10 cm**	**20 cm**	**30 cm**	**40 cm**	**50 cm**
-2°C	1.9	0.1	0.0	0.0	0.0
-6°C	3.5	0.8	0.2	0.0	0.0
-10°C	3.9	1.3	0.4	0.2	0.0
-14°C	3.9	1.6	0.6	0.3	0.1
-18°C	3.8	1.7	0.8	0.4	0.2

Table A.4: Mean sensitivity of ice thickness, as retrieved from the mean brightness temperature intensity (θ= 0 – 40°), to ice surface temperature $\frac{\partial d_{ice}}{\partial T_{surf}}$ [cm/K] for Arctic conditions (S_{water}= 30 g/kg, S_{ice}= 8 g/kg, T_{water}= -1.8°C):

T_{surf} \ d_{ice}	**10 cm**	**20 cm**	**30 cm**	**40 cm**	**50 cm**
-2°C	1.1	-12.7	<-50	<-50	<-50
-6°C	0.8	0.8	-2.5	-15.3	<-50
-10°C	0.6	1.2	1.8	2.1	3.4
-14°C	0.4	0.9	1.6	2.5	4.9
-18°C	0.3	0.7	1.1	1.6	2.6

Table A.5: Mean sensitivity of brightness temperature intensity (θ= 0 – 40°) to ice surface temperature $\frac{\partial TB}{\partial T_{surf}}$ [K/K] for Baltic conditions (S_{water}= 6 g/kg, S_{ice}= 1 g/kg, T_{water}= -0.3°C):

T_{surf} \ d_{ice}	**20 cm**	**40 cm**	**60 cm**	**80 cm**	**100 cm**
-2°C	11.9	3.8	0.0	-1.4	-1.8
-6°C	4.1	3.9	3.	2.	1.3
-10°C	1.7	2.1	1.8	1.5	1.2
-14°C	1.0	1.3	1.3	1.1	1.0
-18°C	0.7	0.9	0.9	0.9	0.8

Table A.6: Mean sensitivity of brightness temperature intensity (θ= 0 – 40°) to ice thickness $\frac{\partial TB}{\partial d_{ice}}$ [K/cm] for Baltic conditions (S_{water}= 6 g/kg, S_{ice}= 1 g/kg, T_{water}= -0.3°C):

T_{surf} \ d_{ice}	**20 cm**	**40 cm**	**60 cm**	**80 cm**	**100 cm**
-2°C	1.8	0.4	0.1	0.0	0.0
-6°C	2.0	1.0	0.5	0.2	0.1
-10°C	1.8	1.0	0.6	0.3	0.2
-14°C	1.6	1.0	0.6	0.4	0.2
-18°C	1.5	1.0	0.6	0.4	0.3

Table A.7: Mean sensitivity of ice thickness, as retrieved from the mean brightness temperature intensity (θ= 0 – 40°), to ice surface temperature $\frac{\partial d_{ice}}{\partial T_{surf}}$ [cm/K] for Baltic conditions (S_{water}= 6 g/kg, S_{ice}= 1 g/kg, T_{water}= -0.3°C):

T_{surf} \ d_{ice}	**20 cm**	**40 cm**	**60 cm**	**80 cm**	**100 cm**
-2°C	6.5	8.7	0.0	<-50	<-50
-6°C	2.1	4.1	6.3	9.0	11.1
-10°C	1.0	2.1	3.1	4.5	5.9
-14°C	0.6	1.3	2.0	3.0	4.0
-18°C	0.4	0.9	1.4	2.1	2.9

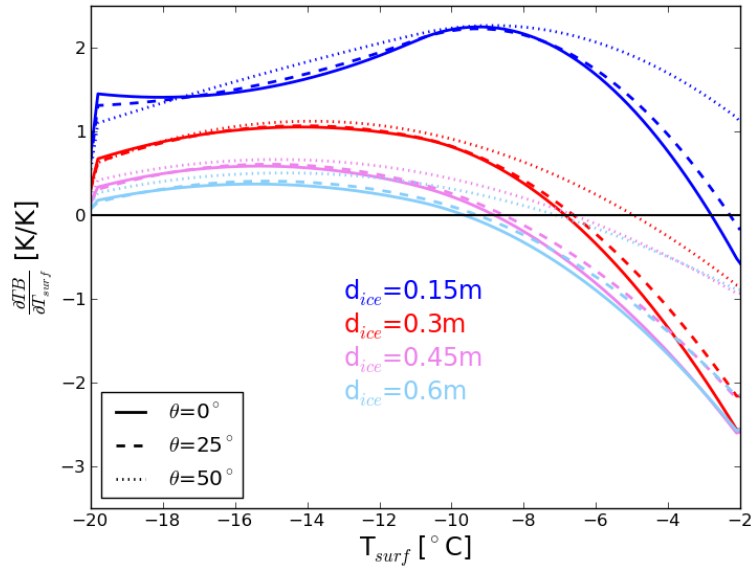

Figure A.1: Derivative of the vertically polarised brightness temperature TB with respect to ice surface temperature T_{surf} as a function of T_{surf} according to the incoherent Burke model for one ice layer. For the assumed ice conditions and the explanation of the lines see caption of Figure 3.10.

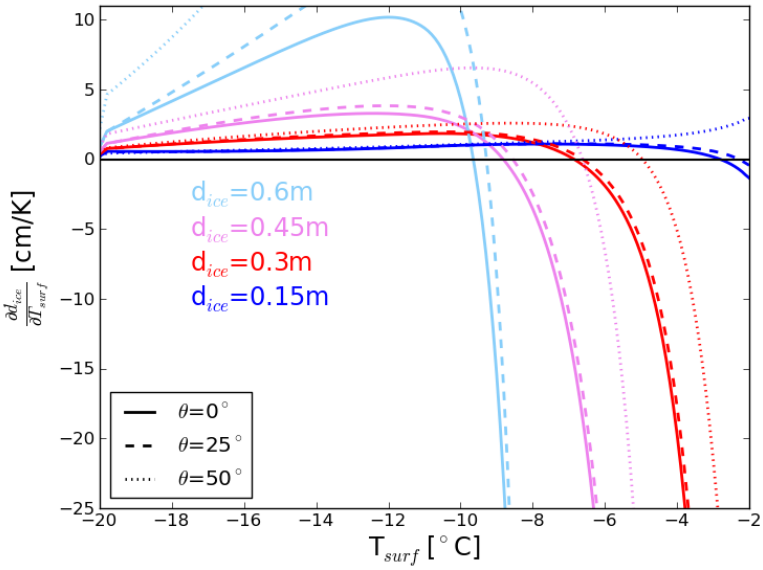

Figure A.2: Derivative of ice thickness d_{ice} with respect to ice surface temperature T_{surf} as a function of T_{surf}, when the vertically polarised brightness temperature is described as a function of ice thickness following the incoherent Burke model for one ice layer. For the assumed ice conditions and the explanation of the lines see caption of Figure 3.10.

A.3 Sensitivity to ice salinity

Table A.8: Mean sensitivity of brightness temperature intensity (θ= 0 – 40°) to ice salinity $\frac{\partial TB}{\partial S_{ice}}$ $[\frac{K}{g/kg}]$ for Arctic conditions (S_{water}= 30 g/kg, $T_{surface}$= -15°C, T_{water}= -1.8°C):

S_{ice} \ d_{ice}	**10 cm**	**20 cm**	**30 cm**	**40 cm**	**50 cm**
2 g/kg	7.8	11.1	12.2	11.9	11.0
4 g/kg	6.2	7.5	6.7	5.2	3.7
7 g/kg	4.2	3.6	2.0	0.8	0.1
10 g/kg	2.8	1.5	0.6	0.0	-0.2
13 g/kg	2.0	1.1	0.1	-0.3	-0.6

Table A.9: Mean sensitivity of brightness temperature intensity (θ=0 – 40°) to ice thickness $\frac{\partial TB}{\partial d_{ice}}$ [K/cm] for Arctic conditions (S_{water}= 30 g/kg, $T_{surface}$= -15°C, T_{water}= -1.8°C):

S_{ice} \ d_{ice}	**10 cm**	**20 cm**	**30 cm**	**40 cm**	**50 cm**
2 g/kg	2.6	1.9	1.4	1.0	0.7
4 g/kg	3.4	2.0	1.2	0.7	0.4
7 g/kg	3.8	1.8	0.8	0.4	0.2
10 g/kg	3.8	1.4	0.5	0.2	0.0
13 g/kg	3.6	1.0	0.2	0.1	0.0

Table A.10: Mean sensitivity of ice thickness, as retrieved from the mean brightness temperature intensity (θ= 0 – 40°), to ice salinity $\frac{\partial d_{ice}}{\partial S_{ice}}$ $[\frac{cm}{g/kg}]$ for Arctic conditions (S_{water}= 30 g/kg, $T_{surface}$= -15°C, T_{water}= -1.8°C):

S_{ice} \ d_{ice}	**10 cm**	**20 cm**	**30 cm**	**40 cm**	**50 cm**
2 g/kg	3.0	5.9	8.8	11.9	15.2
4 g/kg	1.8	3.7	5.5	7.1	8.5
7 g/kg	1.1	2.0	2.5	2.2	0.3
10 g/kg	0.7	1.1	1.2	-0.1	-5.5
13 g/kg	0.6	1.0	0.4	-4.4	<-50

Table A.11: Mean sensitivity of brightness temperature intensity (θ= 0 – 40°) to ice salinity $\frac{\partial TB}{\partial S_{ice}}$ [$\frac{K}{g/kg}$] for Baltic conditions (S_{water}= 6 g/kg, S_{ice}= 1 g/kg, T_{water}= -0.3°C):

S_{ice} \ d_{ice}	**20 cm**	**40 cm**	**60 cm**	**80 cm**	**100 cm**
0.5 g/kg	21.5	27.3	27.5	24.7	21.0
1 g/kg	18.5	21.5	19.5	15.5	11.9
2 g/kg	13.5	12.2	7.7	4.2	1.7
3 g/kg	9.4	5.7	1.5	-0.3	-1.2
4 g/kg	6.5	2.1	0.2	-0.7	-0.8

Table A.12: Mean sensitivity of brightness temperature intensity (θ= 0 – 40°) to ice thickness $\frac{\partial TB}{\partial d_{ice}}$ [K/cm] for Baltic conditions (S_{water}= 6 g/kg, S_{ice}= 1 g/kg, T_{water}= -0.3°C):

S_{ice} \ d_{ice}	**20 cm**	**40 cm**	**60 cm**	**80 cm**	**100 cm**
0.5 g/kg	1.5	1.0	0.7	0.5	0.3
1 g/kg	1.8	1.0	0.6	0.3	0.2
2 g/kg	2.0	0.9	0.4	0.2	0.1
3 g/kg	2.0	0.7	0.2	0.1	0.0
4 g/kg	1.8	0.5	0.1	0.0	0.0

Table A.13: Mean sensitivity of ice thickness, as retrieved from the mean brightness temperature intensity (θ= 0 – 40°), to ice salinity $\frac{\partial d_{ice}}{\partial S_{ice}}$ [$\frac{cm}{g/kg}$] for Baltic conditions (S_{water}= 6 g/kg, S_{ice}= 1 g/kg, T_{water}= -0.3°C):

S_{ice} \ d_{ice}	**20 cm**	**40 cm**	**60 cm**	**80 cm**	**100 cm**
0.5 g/kg	14.3	27.1	40.6	>50	>50
1 g/kg	10.6	21.1	32.8	45.7	>50
2 g/kg	6.8	14.0	20.2	26.0	23.1
3 g/kg	4.8	8.6	6.9	-4.5	12.2
4 g/kg	3.5	4.3	1.3	-27.5	<-50

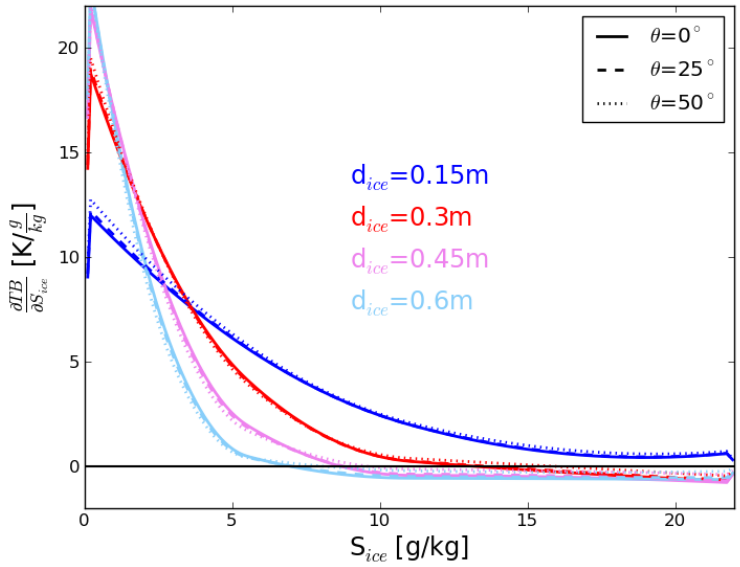

Figure A.3: Derivative of vertically polarised brightness temperature TB with respect to ice salinity S_{ice} as a function of S_{ice} according to the Burke model for one ice layer. For the assumed ice conditions and the explanation of the lines see caption of Figure 3.18.

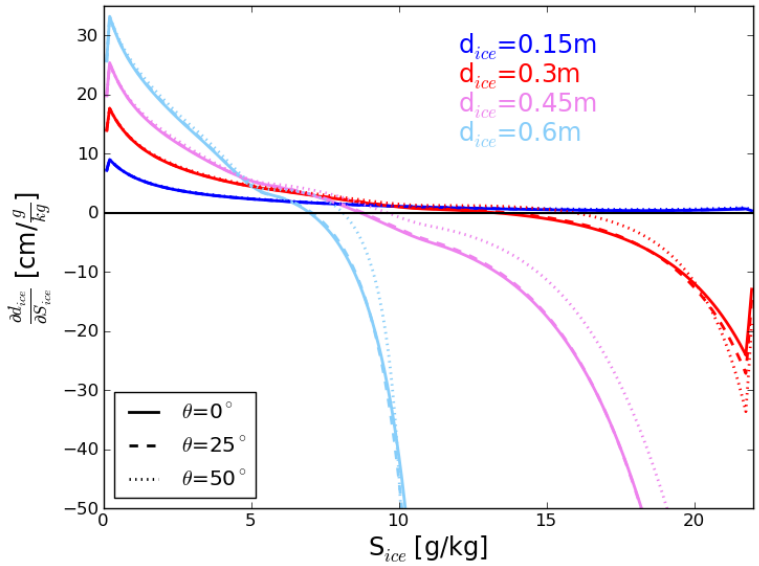

Figure A.4: Derivative of ice thickness d_{ice} with respect to ice salinity S_{ice} as a function of S_{ice}, when the vertically polarised brightness temperature is described as a function of ice thickness following the Burke model for one ice layer. For the assumed ice conditions and the explanation of the lines see caption of Figure 3.18.

A.4 Temperature reversal points

Table A.14: Reversal points of the derivatives $\frac{\partial TB}{\partial T_{surf}}$ and $\frac{\partial d_{ice}}{\partial T_{surf}}$ for the brightness temperature intensities at incidence angles θ=0 ° and θ= 40° for Arctic conditions (S_{water}= 30 g/kg, S_{ice}= 8 g/kg, T_{water}= -1.8°C):

d_{ice}	**10 cm**	**20 cm**	**30 cm**	**40 cm**	**50 cm**
$T_{surf}\left(\frac{\partial TB}{\partial T_{surf}}=0\right)[\theta=0°]$	-	-4.6°C	-6.9°C	-8.3°C	-9.2°C
$T_{surf}\left(\frac{\partial TB}{\partial T_{surf}}=0\right)[\theta=40°]$	-	-4.9°C	-7.2°C	-8.6°C	-9.4°C
$T_{surf}\left(\frac{\partial d_{ice}}{\partial T_{surf}}=0\right)[\theta=0°]$	-	-4.6°C	-	-8.3°C	-
$T_{surf}\left(\frac{\partial d_{ice}}{\partial T_{surf}}=0\right)[\theta=40°]$	-	-4.9°C	-7.2°C	-8.6°C	-9.4°C

Table A.15: Reversal points of the derivatives $\frac{\partial TB}{\partial T_{surf}}$ and $\frac{\partial d_{ice}}{\partial T_{surf}}$ for the brightness temperature intensities at incidence angles θ= 0° and θ= 40° for Baltic conditions (S_{water}= 6 g/kg, S_{ice}= 1 g/kg, T_{water}= -0.3°C):

d_{ice}	**20 cm**	**40 cm**	**60 cm**	**80 cm**	**100 cm**
$T_{surf}\left(\frac{\partial TB}{\partial T_{surf}}=0\right)[\theta=0°]$	-	-	-	-	-3.0°C
$T_{surf}\left(\frac{\partial TB}{\partial T_{surf}}=0\right)[\theta=40°]$	-	-	-2.1°C	-2.7°C	-3.1°C
$T_{surf}\left(\frac{\partial d_{ice}}{\partial T_{surf}}=0\right)[\theta=0°]$	-	-	-	-	-
$T_{surf}\left(\frac{\partial d_{ice}}{\partial T_{surf}}=0\right)[\theta=40°]$	-	-	-	-	-

A.5 Salinity reversal points

Table A.16: Reversal points of the derivatives $\frac{\partial TB}{\partial S_{ice}}$ and $\frac{\partial d_{ice}}{\partial S_{ice}}$ for the brightness temperature intensities at incidence angles θ= 0° and θ= 40° for Arctic conditions (S_{water}= 30 g/kg, T_{surf}= -15°C, T_{water}= -1.8°C):

d_{ice}	**10 cm**	**20 cm**	**30 cm**	**40 cm**	**50 cm**
$S_{ice}\left(\frac{\partial TB}{\partial S_{ice}}=0\right)[\theta=0°]$	-	-	-	10.1 g/kg	7.7 g/kg
$S_{ice}\left(\frac{\partial TB}{\partial S_{ice}}=0\right)[\theta=40°]$	-	-	13.3 g/kg	9.7 g/kg	6.8 g/kg
$S_{ice}\left(\frac{\partial d_{ice}}{\partial S_{ice}}=0\right)[\theta=0°]$	-	-	-	10.1 g/kg	7.7 g/kg
$S_{ice}\left(\frac{\partial d_{ice}}{\partial S_{ice}}=0\right)[\theta=40°]$	-	-	13.3 g/kg	9.7 g/kg	6.8 g/kg

Table A.17: Reversal points of the derivatives $\frac{\partial TB}{\partial S_{ice}}$ and $\frac{\partial d_{ice}}{\partial S_{ice}}$ for the brightness temperature intensities at incidence angles θ= 0° and θ= 40° for Arctic conditions (S_{water}= 6 g/kg, T_{surf}= -10°C, T_{water}= -0.3°C):

d_{ice}	**20 cm**	**40 cm**	**60 cm**	**80 cm**	**100 cm**
$S_{ice}\left(\frac{\partial TB}{\partial S_{ice}}=0\right)[\theta=0°]$	-	-	6.4 g/kg	3.0 g/kg	2.5 g/kg
$S_{ice}\left(\frac{\partial TB}{\partial S_{ice}}=0\right)[\theta=40°]$	-	-	4.2 g/kg	-	-
$S_{ice}\left(\frac{\partial d_{ice}}{\partial S_{ice}}=0\right)[\theta=0°]$	-	-	-	3.0 g/kg	-
$S_{ice}\left(\frac{\partial d_{ice}}{\partial S_{ice}}=0\right)[\theta=40°]$	-	-	-	-	-

A.6 Comparison with IceBridge

Table A.18: Settings of the 14 scenarios used to simulate brightness temperatures for the retrieval of snow thickness (section 4.4.5). The settings differ in the amount of days for that SMOS data are included, the range of incidence angles θ, the (snow) surface temperature T_{surf}, the snow density ρ_{snow}, the ice thickness d_{ice}, and the ice salinity S_{ice}.

No.	SMOS data	θ	T_{surf}[°C]	ρ_{snow}[kg/m^3]	d_{ice}[m]	S_{ice}[g/kg]
1	3 days	15 – 50°	-35.15	260	4	1.52
2	3 days	15 – 60°	-35.15	260	4	1.52
3	1 day	15 – 50°	-35.15	260	4	1.52
4	1 day	15 – 60°	-35.15	260	4	1.52
5	3 days	15 – 50°	-40.15	260	4	1.52
6	3 days	15 – 50°	-38.15	260	4	1.52
7	3 days	15 – 50°	-36.15	260	4	1.52
8	3 days	15 – 50°	-33.15	260	4	1.52
9	3 days	15 – 50°	-38.15	260	3	1.52
10	3 days	15 – 50°	-38.15	260	5	1.52
11	3 days	15 – 50°	-38.15	200	4	1.52
12	3 days	15 – 50°	-38.15	280	4	1.52
13	3 days	15 – 50°	-38.15	320	4	1.52
14	3 days	15 – 50°	-38.15	320	4	2.5

Table A.19: Correlation coefficients r^2 and root mean square deviations RMSD for the snow thicknesses as retrieved from horizontally polarised SMOS brightness temperature and as measured during the IceBridge campaign for the 14 scenarios given in Tab. A.18.

No.	r^2	RMSD [cm]	r^2 ($d_{snow} < 35$ cm)	RMSD [cm] ($d_{snow} < 35$ cm)
1	0.56	11.24	0.58	7.40
2	0.60	12.19	0.58	7.16
3	0.51	12.52	0.47	7.95
4	0.55	13.30	0.47	7.49
5	0.63	14.62	0.47	6.37
6	0.61	12.79	0.58	5.71
7	0.58	11.57	0.56	6.76
8	0.51	11.13	0.53	9.07
9	0.59	11.70	0.57	5.83
10	0.64	15.35	0.48	6.24
11	0.64	18.02	0.28	8.84
12	0.60	11.90	0.58	5.89
13	0.58	10.95	0.57	6.52
14	0.61	13.14	0.57	5.73

Table A.20: Correlation coefficients r^2 and root mean square deviations RMSD for the snow thicknesses as retrieved from vertically polarised SMOS brightness temperature and as measured during the IceBridge campaign for the 14 scenarios given in Tab. A.18.

No.	r^2	RMSD [cm]	r^2 ($d_{snow} < 35$ cm)	RMSD [cm] ($d_{snow} < 35$ cm)
1	0.10	16.32	-	-
2	0.08	17.18	-	-
3	0.11	16.40	-	-
4	0.09	17.28	-	-
5	0.35	12.48	0.40	12.45
6	0.25	14.28	0.28	14.29
7	0.14	15.77	-	-
8	0.03	17.03	-	-
9	0.22	15.06	-	-
10	0.25	13.75	0.30	13.71
11	0.33	12.54	0.38	12.50
12	0.23	14.70	0.24	14.71
13	0.18	15.32	-	-
14	0.23	14.48	0.27	14.49

A.7 Growing sea ice in the Bay of Bothnia

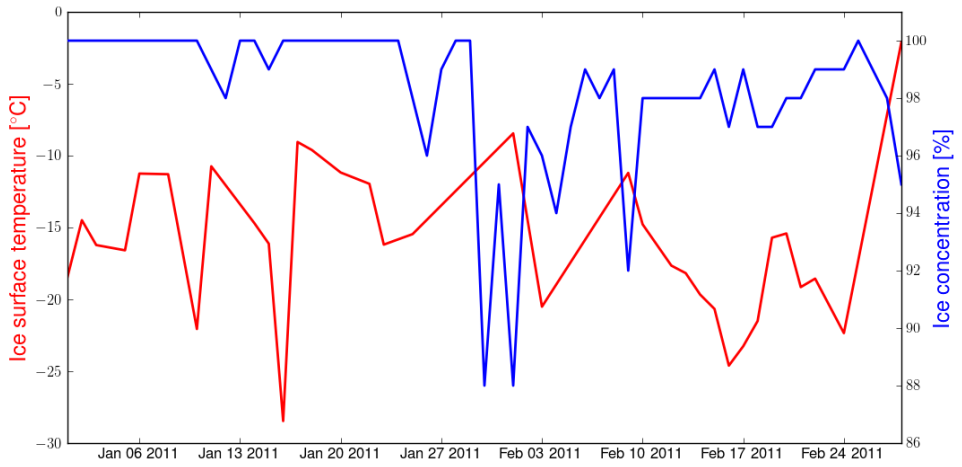

Figure A.5: Ice surface temperature and ice concentration in January and February, 2011 for the area in the Bay of Bothnia that is investigated in section 5.3. The red line indicates ice surface temperatures as obtained from the MODIS IST MOD29 product (Hall et al., 2004), the blue line indicates ice concentration as obtained from AMSR-E brightness temperatures using the ASI algorithm (Kaleschke et al., 2001; Spreen et al., 2008).

A.8 Validation of SMOS ice thickness retrieval in the Baltic Sea

Table A.21: Centre points and radii of the circles used for the validation of SMOS retrieved ice thicknesses with EM Bird ice thicknesses in section 5.4.3

Circle no.	Latitude [°N]	Longitude [°E]	Radius [km]
1	65.00	23.8	30.0
2	64.85	22.7	33.0
3	64.60	23.4	26.7
4	64.40	22.4	25.0
5	64.25	23.1	23.0
6	64.05	22.1	23.0
7	64.00	22.6	17.8
8	63.70	22.0	25.4
9	63.50	21.1	25.0
10	63.30	20.55	22.8
11	63.05	20.0	24.1
12	62.75	20.5	29.2

Acronyms

AMSR-E Advanced Microwave Scanning Radiometer for EOS

ARTIST Arctic Radiation and Turbulence Interaction STudy

ASI ARTIST Sea Ice

ATM Airborne Topographic Mapper

CDC Climate Diagnostics Center

DGG Discrete Global Grid

EM Electromagnetic induction

ESA European Space Agency

FMI Finnish Meteorological Institute

GMT Generic Mapping Tools

GSHHS Global Self-consistent Hierarchical High-resolution Shoreline database

IDCSI2 Sea Ice Freeboard, Snow Depth, and Thickness data set

ISEA 4H9 Icosahedral Snyder Equal Area projection with aperture 4, resolution 9, and shape of cells as hexagon

IST Ice Surface Temperature

KT19 KT19.85 Series II Infrared Radiation Pyrometer

MODIS MODerate Resolution Imaging Spectroradiometer

MIRAS Microwave Imaging Radiometer using Aperture Synthesis

NASA National Aeronautics and Space Administration

NCEP National Centers for Environmental Prediction

NOAA National Oceanic and Atmospheric Administration

RFI Radio Frequency Interference

SMOS Soil Moisture and Ocean Salinity

SSMIS Special Sensor Microwave Imager Sounder

TOA Top Of the Atmosphere

List of Figures

List of Tables

Bibliography

Andersen, S., Tonboe, R., Kaleschke, L., Heygster, G., and Pedersen, L. (2007). Intercomparison of passive microwave sea ice concentration retrievals over the high-concentration Arctic sea ice. *J. Geophys. Res*, 112(C8):C08.

Burke, W., Schmugge, T., and Paris, J. (1979). Comparison of 2.8- and 21-cm microwave radiometer observations over soils with emission model calculations. *Journal of Geophysical Research*, 84(C1):287 – 294.

Camps, A., Corbella, I., Vall-llossera, M., Duffo, N., Marcos, F., Martínez-Fadrique, F., and Greiner, M. (2003). The SMOS end-to-end performance simulator: Description and scientific applications. In *Proceedings IGARSS*, volume 1, pages 13 – 15.

Camps, A., Gourrion, J., Tarongi, J., Gutierrez, A., Barbosa, J., and Castro, R. (2010). RFI analysis in SMOS imagery. In *Proceedings IGARSS*, pages 2007 – 2010.

Cavalieri, D., Markus, T., and Comiso, J. (2004). AMSR-E/Aqua daily L3 12.5 km brightness temperature, sea ice concentration, and snow depth polar grids V002.

Comiso, J., Cavalieri, D., and Markus, T. (2003). Sea ice concentration, ice temperature, and snow depth using AMSR-E data. *IEEE Transactions on Geoscience and Remote Sensing*, 41(2):243–252.

Cox, G. and Weeks, W. (1974). Salinity variations in sea ice. *Journal of Glaciology*, 13(67):109–120.

Cox, G. and Weeks, W. (1983). Equations for determining the gas and brine volumes in sea ice samples. *Journal of Glaciology*, 29(102):306 – 316.

Dinnat, E., Boutin, J., Caudal, G., and Etcheto, J. (2003). Issues concerning the sea emissivity modeling at L band for retrieving surface salinity. *Radio Science*, 38(4):8060.

Doronin, Y. (1971). *Thermal interaction of the atmosphere and the hydrosphere in the Arctic*. CoronetBooks, Philadelphia.

Farrell, S., Kurtz, N., Connor, L., Elder, B., Leuschen, C., Markus, T., McAdoo, D., Panzer, B., Richter-Menge, J., and Sonntag, J. (2012). A first assessment of IceBridge snow and ice thickness data over Arctic sea ice. *IEEE Transactions on Geoscience and Remote Sensing*, 50(6):2098–2111.

Fofonoff, N. and Millard, R. (1983). Algorithms for computation of fundamental properties of seawater. Tech. Rep. 44, UNESCO, Technical Papers in Marine Science.

Giles, K., Laxon, S., Wingham, D., Wallis, D., Krabill, W., Leuschen, C., McAdoo, D., Manizade, S., and Raney, R. (2007). Combined airborne laser and radar altimeter measurements over the Fram Strait in May 2002. *Remote Sensing of Environment*, 111(2):182 – 194.

Goodberlet, M. and Mead, J. (2012). Improved Models of Soil Emission for Use in Remote Sensing of Soil Moisture. *IEEE Transactions on Geoscience and Remote Sensing*, 50(10):3991 – 3999.

Haas, C. and Casey, A. (2012). Helicopterborne EM ice thickness surveys during SafeWin 2011 field campaign. Technical report, University of Alberta.

Haas, C., Hendricks, S., Eicken, H., and Herber, A. (2010). Synoptic airborne thickness surveys reveal state of Arctic sea ice cover. *Geophysical Research Letters*, 37(9):L09501.

Haas, C. and Jochmann, P. (2003). Continuous EM and ULS thickness profiling in support of ice force measurements. In Loeset, S., Bonnemaire, B., and Bjerkas, M., editors, *Proceedings of the 17th International Conference on Port and Ocean Engineering under Arctic Conditions, POAC 03*. Department of Civil and Transport Engineering, Norwegian University of Sci. Trondheim, Norway.

Haas, C., Lobach, J., Hendricks, S., Rabenstein, L., and Pfaffling, A. (2009). Helicopterborne measurements of sea ice thickness, using a small and lightweight, digital EM system. *Journal of Applied Geophysics*, 67(3):234–241.

Hall, D., Key, J., Casey, K., Riggs, G., and Cavalieri, D. (2004). Sea ice surface temperature product from MODIS. *IEEE Transactions on Geoscience and Remote Sensing*, 42(5):1076 – 1087.

Hall, Dorothy, K. (1996). Remote sensing applications to hydrology: imaging radar. *Hydrological Sciences*, 41(4):609 – 624.

Hallikainen, M. (1989). Microwave radiometry of snow. *Advances in Space Research*, 9(1):267 – 275.

Hallikainen, M. (1992). *Microwave Remote Sensing of Sea Ice*, chapter Microwave remote sensing of low-salinity sea ice, pages 361 – 373. Washington, DC: AGU.

Heygster, G., Huntemann, M., and Wang, H. (2012). Polarization-based SMOS sea ice thickness retrieval algorithm (Algorithm II). Algorithm Theoretical Basis Document (ATBD), STSE SMOSICE.

Jackson, T. and O'Neill, P. (1986). Microwave dielectric model for aggregated soils. *IEEE Transactions on Geoscience and Remote Sensing*, 24(6):920 – 929.

Janssen, F., Schrum, C., and Backhaus, J. (1999). A climatological data set of temperature and salinity for the Baltic Sea and the North Sea. *Deutsche Hydrographische Zeitschrift*, 51:5 – 245.

Kaleschke, L., Lüpkes, C., Vihma, T., Haarpaintner, J., Bochert, A., Hartmann, J., and Heygster, G. (2001). SSM/I sea ice remote sensing for mesoscale ocean-atmosphere interaction analysis. *Canadian Journal of Remote Sensing/Journal Canadien de Teledetection*, 27(5):526 – 537.

Kaleschke, L., Maaß, N., Haas, C., Hendricks, S., Heygster, G., and Tonboe, R. (2010). A sea-ice thickness retrieval model for 1.4 GHz radiometry and application to airborne measurements over low salinity sea-ice. *The Cryosphere*, 4:583 – 592.

Kaleschke, L., Tian-Kunze, X., Maaß, N., Mäkynen, M., and Drusch, M. (2012). Sea ice thickness retrieval from SMOS brightness temperatures during the Arctic freeze-up period. *Geophysical Research Letters*, 39(L05501).

Kalnay, E., Kanamitsu, M., Kistler, R., Collins, W., Deaven, D., Gandin, L., Iredell, M., Sana, S., White, G., Woollen, J., et al. (1996). The NCEP/NCAR 40-Year Reanalysis Project. *Bull. Am. Meteorol. Soc.*, 77:437 – 471.

Kawamura, T., Shirasawa, K., Ishikawa, N., Lindfors, A., Rasmus, K., Granskog, M., Ehn, J., Leppäranta, M., Martma, T., and Vaikmäe, R. (2001). Time-series observations of the structure and properties of brackish ice in the Gulf of Finland. *Annals of Glaciology*, 33(1):1 – 4.

Kerr, Y., Waldteufel, P., Wigneron, J., Martinuzzi, J., Font, J., and Berger, M. (2001). Soil moisture retrieval from space: The Soil Moisture and Ocean Salinity (SMOS) mission. *IEEE Transactions on Geoscience and Remote Sensing*, 39(8):1729 – 1735.

Klein, L. and Swift, C. (1977). An improved model for the dielectric constant of sea water at microwave frequencies. *IEEE Transactions on Antennas and Propagation*, 25(1):104 – 111.

Kong, J. (1975). *Theory of electromagnetic waves*, volume 1. New York, Wiley-Interscience.

Krabill, W. B. (2012). IceBridge KT19 IR Surface Temperature. online. Boulder, Colorado USA: NASA DAAC at NSIDC.

Kurtz, N. (2012). *IceBridge quick look sea ice freeboard, snow depth, and thickness product manual*.

Kurtz, N. and Farrell, S. (2011). Large-scale surveys of snow depth on Arctic sea ice from operation IceBridge. *Geophysical Research Letters*, 38(20):L20505.

Kurtz, N., Studinger, M., Harbeck, J., Onana, V., and Farrell, S. (2012). IceBridge Sea Ice Freeboard, Snow Depth, and Thickness. online. Boulder, Colorado USA: NASA DAAC at NSIDC.

Kwok, R. and Cunningham, G. (2008). ICESat over Arctic sea ice: Estimation of snow depth and ice thickness. *Journal of Geophysical Research*, 113(C8):C08010.

Kwok, R., Panzer, B., Leuschen, C., Pang, S., Markus, T., Holt, B., and Gogineni, S. (2011). Airborne surveys of snow depth over Arctic sea ice. *Journal of Geophysical Research*, 116(C11):C11018.

Kwok, R. and Rothrock, D. (2009). Decline in Arctic sea ice thickness from submarine and ICESat records: 1958 – 2008. *Geophysical Research Letters*, 36(15):L15501.

Lagerloef, G., Swift, C., and LeVine, D. (1995). Sea surface salinity: The next remote sensing challenge. *Oceanography*, 8(2):44 – 50.

Laxon, S., Peacock, N., and Smith, D. (2003). High interannual variability of sea ice thickness in the Arctic region. *Nature*, 425(6961):947 – 950.

Le Vine, D. and Abraham, S. (2002). The effect of the ionosphere on remote sensing of sea surface salinity from space: Absorption and emission at L band. *IEEE Transactions on Geoscience and Remote Sensing*, 40(4):771 – 782.

Le Vine, D. and Abraham, S. (2004). Galactic noise and passive microwave remote sensing from space at L-band. *IEEE Transactions on Geoscience and Remote Sensing*, 42(1):119 – 129.

Le Vine, D., Abraham, S., Kerr, Y., Wilson, W., Skou, N., and Sobjaerg, S. (2005). Comparison of model prediction with measurements of galactic background noise at L-band. *IEEE Transactions on Geoscience and Remote Sensing*, 43(9):2018 – 2023.

Leppäranta, M. and Hakala, R. (1992). The structure and strength of first-year ice ridges in the Baltic Sea. *Cold Regions Science and Technology*, 20(3):295–311.

Leppäranta, M. and Manninen, T. (1988). The brine and gas content of sea ice with attention to low salinities and high temperatures. Internal Rep. 88-2, Finnish Institute of Marine Research, Helsinki.

Leppäranta, M. and Myrberg, K. (2009). *Physical oceanography of the Baltic Sea*. Springer Verlag.

Liebe, H., Hufford, G., and Cotton, M. (1993). Propagation modeling of moist air and suspended water/ice particles at frequencies below 1000 GHz. In *Proceedings of the AGARD 52nd Specialists' Meeting of the Electromagnetic Wave Propagation Panel*.

Maaß N. and Kaleschke, L. (2010). Improving passive microwave sea ice concentration algorithms for coastal areas: applications to the Baltic Sea. *Tellus A*, 62(4):393 – 410.

Mäkynen, M. (2012). SMOSIce-DAT user manual for the validation data. STSE-SMOS Sea Ice Retrieval Study SMOSIce contract report, European Space Agency.

Mäkynen, M. and Hallikainen, M. (2005). Passive microwave signature observations of the Baltic Sea ice. *International Journal of Remote Sensing*, 26(10):2081 – 2106.

Martin, S., Drucker, R., Kwok, R., and Holt, B. (2004). Estimation of the thin ice thickness and heat flux for the Chukchi Sea Alaskan coast polynya from Special Sensor Microwave/Imager data, 1990 – 2001. *Journal of Geophysical Research*, 109:10012 – 10012.

Maykut, G. and Untersteiner, N. (1971). Some results from a time-dependent thermodynamic model of sea ice. *Journal of Geophysical Research*, 76(6):1550 – 1575.

Maykut, G. A. (1986). *Geophysics of Sea Ice*, chapter The surface heat and mass balance, pages 395 – 463. Plenum, New York.

McMullan, K., Brown, M., Martín-Neira, M., Rits, W., Ekholm, S., Marti, J., and Lemanczyk, J. (2008). SMOS: The payload. *IEEE Transactions on Geoscience and Remote Sensing*, 46(3):594 – 605.

Menashi, J., Germain, K., Swift, C., Comiso, J., and Lohanick, A. (1993). Low-frequency passive-microwave observations of sea ice in the Weddell Sea. *Journal of Geophysical Research*, 98(C12):22569 – 22577.

Mills, P. and Heygster, G. (2011). Sea Ice Emissivity Modeling at L-Band and Application to 2007 Pol-Ice Campaign Field Data. *IEEE Transactions on Geoscience and Remote Sensing*, 49(2):612 – 627.

Misra, S. and Ruf, C. (2012). Analysis of radio frequency interference detection algorithms in the angular domain for SMOS. *IEEE Transactions on Geoscience and Remote Sensing*, 50(5):1448 – 1457.

Murray, F. (1967). On the computation of saturation vapor pressure. *Journal of Applied Meteorology*, 6(1):203 – 204.

NOAA, U. and Force, U. (1976). US standard atmosphere, 1976. *Washington, DC.*

Oliva, R., Daganzo, E., Kerr, Y., Mecklenburg, S., Nieto, S., Richaume, P., and Gruhier, C. (2012). SMOS radio frequency interference scenario: Status and actions taken to improve the RFI environment in the 1400 – 1427-MHz passive band. *IEEE Transactions on Geoscience and Remote Sensing*, 50(5):1427 – 1439.

Palosuo, E. (1961). Crystal structure of brackish and freshwater ice. *Int. Assoc. of Hydrol. Sci., Snow Ice Comm.*, 54:9 – 14.

Palosuo, E. (1963). The Gulf of Bothnia in winter. II. Freezing and ice forms. *Merentutkimuslaitoksen julkaisu/ Havsforskningsinstitutets skrift*, 209:1 – 64.

Pinori, S., Crapolicchio, R., and Mecklenburg, S. (2008). Preparing the ESA-SMOS (soil moisture and ocean salinity) mission-overview of the user data products and data distribution strategy. In *Microwave Radiometry and Remote Sensing of the Environment, MICRORAD*, pages 1 – 4. IEEE.

Pounder, E. (1965). *The physics of ice*. Oxford, Pergamon Press. The Commonwealth and International Library, Geophysics Division.

Rosenkranz, P. (1998). Water vapor microwave continuum absorption: A comparison of measurements and models. *Radio Science*, 33(4):919 – 928.

Rott, H. and Mätzler, C. (1987). Possibilities and limits of synthetic aperture radar for snow and glacier surveying. *Annals of Glaciology*, 9:195 – 199.

Sahr, K., White, D., and Kimerling, A. (2003). Geodesic discrete global grid systems. *Cartography and Geographic Information Science*, 30(2):121 – 134.

Saloranta, T. (2000). Modeling the evolution of snow, snow ice and ice in the Baltic Sea. *Tellus A*, 52(1):93 – 108.

Seinä, A. and Palosuo, E. (1996). The classification of the maximum annual extent of ice cover in the Baltic Sea 1720 – 1995. *Meri: Report series of the Finnish Institute of Marine Research (Merentutkimuslaitos)*, 27.

Spreen, G., Kaleschke, L., and Heygster, G. (2008). Sea ice remote sensing using AMSR-E 89 GHz channels. *Journal of Geophysical Research*, 113.

Tamura, T. and Ohshima, K. (2011). Mapping of sea ice production in the Arctic coastal polynyas. *Journal of Geophysical Research*, 116(C7):C07030.

Tiuri, M., Sihvola, A., Nyfors, E., and Hallikainen, M. (1984). The complex dielectric constant of snow at microwave frequencies. *IEEE Journal of Oceanic Engineering*, 9(5):377 – 382.

Tonboe, R., Dybkjær, G., and Høyer, J. (2011). Simulations of the snow covered sea ice surface temperature and microwave effective temperature. *Tellus A*, 63(5):1028 – 1037.

Ulaby, F., Moore, R., and Fung, A. (1981). *Microwave remote sensing: Active and passive*, volume 1 - Microwave remote sensing fundamentals and radiometry. Addison-Wesley.

Untersteiner, N. (1964). Calculations of temperature regime and heat budget of sea ice in the Central Arctic. *Journal of Geophysical Research*, 69(22):4755 – 4766.

Vant, M., Ramseier, R., and Makios, V. (1978). The complex-dielectric constant of sea ice at frequencies in the range 0.1–40 GHz. *Journal of Applied Physics*, 49(3):1264 – 1280.

Warren, S., Rigor, I., Untersteiner, N., Radionov, V., Bryazgin, N., Aleksandrov, Y., and Colony, R. (1999). Snow depth on Arctic sea ice. *Journal of Climate*, 12(6):1814 – 1829.

Weeks, W. and Lee, O. (1962). The salinity distribution in young sea-ice. *Arctic*, 15(2):92 – 108.

Wessel, P. and Smith, W. (1996). A global, self-consistent, hierarchical, high-resolution shoreline database. *Journal of Geophysical Research – Solid Earth*, 101(B4).

Yu, Y. and Rothrock, D. (1996). Thin ice thickness from satellite thermal imagery. *Journal of Geophysical Research*, 101(C11):25753 – 25766.

Zine, S., Boutin, J., Font, J., Reul, N., Waldteufel, P., Gabarró, C., Tenerelli, J., Petitcolin, F., Vergely, J., Talone, M., et al. (2008). Overview of the SMOS sea surface salinity prototype processor. *IEEE Transactions on Geoscience and Remote Sensing*, 46(3):621 – 645.

Acknowledgements

I am very grateful to Dr. Lars Kaleschke for the supervision of my work, helpful consultations, and constructive remarks.

Furthermore, I would like to thank Prof. Detlef Stammer for reviewing this work, and Prof. Angelika Humbert and Prof. Hartmut Graßl for being in my advisory panel.

I appreciate the helpful discussions I had with the sea ice remote sensing group of the Institute of Oceanography, Hamburg and the members of the ESA SMOSIce project.

I am very grateful to the IMPRS-ESM for funding my PhD studies and for the support during the last three years.

Thanks go to the institutions that provided the data used in this thesis:
The SMOS data were provided by the ESA Support to Science Element programme under contract 4000101476.
NCEP Reanalysis data were provided by the Physical Sciences Division, Earth System Research Laboratory, NOAA, Boulder, Colorado, from their Web site at http://www.esrl.noaa.gov/psd/.
Ice concentration data retrieved from SSMIS measurements were provided by the Integrated Climate Data Center (ICDC), CliSAP/KlimaCampus, University of Hamburg, http://icdc.zmaw.de.
IceBridge ice and snow thicknesses, and surface temperatures were provided by the NASA Distributed Active Archive Center at the National Snow and Ice Data Center, Boulder, Colorado USA. Digital media. http://nsidc.org/data/idcsi2.html.
The Baltic EM thickness campaign and analysis was conducted within the EU-funded project "Safety of winter navigation in dynamic ice" (contract SCP8-GA-2009-233884 - SAFEWIN). The partners in this project are Aalto University, Arctic and Antarctic Research Institute, Finnish Meteorological Institute, Finnish Transport Agency, ILS Oy, Stena Rederi AB, Swedish Maritime Administration, Swedish Meteorological and Hydrological Institute, Tallinn University of Technology and AS Tallink Group.
MODIS-based ice thickness maps were provided by Marko Mäkynen from the Finnish Meteorological Institute in the framework of the ESA SMOSIce project.

I thank my office mates Meike Demgen, David Bröhan, and Anja Rösel for the nice time we had, and Meike, David, Manfred Brath, Mark Carson, and Alexander Beitsch for proof-reading.

My sincere thanks go to my family, especially for their dog sitting efforts.

Finally, I thank all my colleagues of the remote sensing group of the Institute of Oceanography for the good working atmosphere and my soccer buddies for everything beyond work.



ISSN 1614-1199